

Transient disruption of vascular barriers using focused ultrasound and microbubbles for targeted drug delivery in the brain

Author: Muna Aryal

Persistent link: <http://hdl.handle.net/2345/bc-ir:104127>

This work is posted on [eScholarship@BC](#),
Boston College University Libraries.

Boston College Electronic Thesis or Dissertation, 2014

Copyright is held by the author, with all rights reserved, unless otherwise noted.

Boston College
The Graduate School of Arts and Sciences
Department of Physics

**Transient disruption of vascular barriers using
focused ultrasound and microbubbles for targeted
drug delivery in the brain**

a dissertation by
MUNA ARYAL

submitted in partial fulfillment of the requirements

for the degree of

Doctor of Philosophy

December 2014

© copyright by Muna Aryal
2014

**Transient disruption of vascular barriers using
focused ultrasound and microbubbles for targeted
drug delivery in the brain**

By: Muna Aryal

Advisors: Prof. Nathan J. McDannold

and

Prof. Cyril P. Opeil, S. J.

Abstract

The physiology of the vasculature in the central nervous system (CNS) which includes the blood–brain-barrier (BBB) and other factors, prevents the transport of most anticancer agents to the brain and restricts delivery to infiltrating brain tumors. The heterogeneous vascular permeability in tumor vessels (blood-tumor barrier; BTB), along with several other factors, creates additional hurdles for drug treatment of brain tumors. Different methods have been used to bypass the BBB/BTB, but they have their own limitations such as being invasive, non-targeted or requiring the formulation

of new drugs. Magnetic Resonance Imaging guided Focused Ultrasound (MRIgFUS), when combined with circulating microbubbles, is an emerging noninvasive method to temporarily permeabilize the BBB and BTB. The purpose of this thesis was to use this alternative approach to deliver chemotherapeutic agents through the BBB/BTB for brain tumor treatment in a rodent model to overcome the hinderances encountered in prior approaches tested for drug delivery in the CNS.

The results presented in thesis demonstrate that MRIgFUS can be used to achieve consistent and reproducible BBB/BTB disruption in rats. It enabled us to achieve clinically-relevant concentrations of doxorubicin ($\sim 4.8 \pm 0.5 \mu\text{g/g}$) delivered to the brain with the sonication parameters (0.69 MHz; 0.55 MPa; 10 ms bursts; 1 Hz PRF; 60 s duration), microbubble concentration (Definity, 10 $\mu\text{l/kg}$), and liposomal doxorubicin (Lipo-DOX) dose (5.67 mg/kg) used. The resulting doxorubicin concentration was reduced by 32% when the agent was injected 10 minute after the last sonication. Three weekly sessions of FUS and Lipo-DOX appeared to be safe in the rat brain, despite some minor tissue damage. Importantly, the severe neurotoxicity seen in earlier works using other approaches does not appear to occur with delivery via FUS-BBB disruption. The results from three weekly treatments of FUS and Lipo-DOX in a rat glioma model are highly promising since they demonstrated that the

method significantly inhibits tumor growth and improves survival. Animals that received three weekly sessions of FUS + Lipo-DOX (N = 8) had a median survival time that was increased significantly ($P < 0.001$) compared to animals who received Lipo-DOX only (N = 6), FUS only (N = 8), or no treatment (N = 7). Median survival for animals that received FUS + Lipo-DOX was increased by 100% relative to untreated controls, whereas animals who received Lipo-DOX alone had only a 16% improvement. Animals who received only FUS showed no improvement. No tumor cells were found in histology in 4/8 animals in the FUS + Lipo-DOX group, and only a few tumor cells were detected in two animals. Tumor doxorubicin concentrations increased monotonically (823 ± 600 , 1817 ± 732 and 2432 ± 448 ng/g) in the control tumors at 9, 14 and 17 days respectively after administration of Lipo-DOX. With FUS-induced BTB disruption, the doxorubicin concentrations were enhanced significantly ($P < 0.05$, $P < 0.01$, and $P < 0.0001$ at days 9, 14, and 17, respectively) and were greater than the control tumors by a factor of two or more (2222 ± 784 , 3687 ± 796 and 5658 ± 821 ng/g) regardless of the stage of tumor growth. The transfer coefficient K_{trans} was significantly ($p < 0.05$) enhanced compared to control tumors only at day 9 but not at day 14 or 17. These results suggest that FUS-induced enhancements in tumor drug delivery for Lipo-DOX are relatively consistent over time, at least in this

tumor model. These results are encouraging for the use of large drug carriers, as they suggest that even large/late-stage tumors can benefit from FUS-induced drug enhancement. Corresponding enhancements in K_{trans} were found variable in large/late-stage tumors and not significantly different than controls, perhaps reflecting the size mismatch between the liposomal drug (~100 nm) and Gd-DTPA (molecular weight: 938 Da). Overall, this thesis research provides pre-clinical data toward the development of MRIgFUS as a noninvasive method for the delivery of agents such as Lipo-DOX across the BBB/BTB to treat patients with diseases of the central nervous system.

Acknowledgements

I would like to express my deep and sincere gratitude to my supervisor and mentor, Prof. Nathan J. McDannold. His extraordinary supervision, encouragement, guidance and support throughout my graduate studies enabled me to develop a deep and comprehensive understanding of the subject matter and to succeed in the great achievement of completing my dissertation. I would like to express my sincere thanks to Rev. Cyril P. Opeil, S.J. for his great support and inspiration throughout this work. I couldn't have conducted my thesis without his constant support. I would like to thank committee members Prof. Krzysztof Kempa and Prof. Stephen Wilson for reviewing this dissertation.

Many thanks go to Prof. Micheal J. Naughton and Prof. Rein Uritam for allowing me doing research of my interest off-campus without any discontinuity of mental or financial support. I also extend my thanks to all the faculty members, staff members and graduate students of the physics department at Boston College. It has been my great luck and an honor to be a member of Focused Ultrasound Laboratory at Brigham and Women's Hospital, Harvard Medical School. I am particularly obliged to Dr. Chang-Sheng Mei for his cordial support and for introducing me to Prof. Nathan J.

McDannold. It would have been difficult for me to complete this thesis work without the skilled hands and efforts of Dr. Natalia Vykhodtseva and the members of the laboratory. I am particularly grateful to Dr. Yong-Zhi Zhang and Mrs. Chanikarn "Yui" Power for their immense help and training for the animal experiments. I am grateful to all the current and former members especially Dr. Juyoung Park, Dr. Eun Joo Park, Dr. Costas Arvanitis, Phillip Alexander, and Keiko Fujiwara.

I owe my loving thanks to my husband Dr. Binod Rizal, daughter Bina and brothers- Rajendra and Harishchandra Aryal for their love and support. I will always be indebted to my parents and parents-in-law for keeping me in their thoughts and prayers to god and of their wishes for success and joy in my life. I dedicate this dissertation to them.

Table of Contents

Acknowledgements	i
Table of Contents	iii
List of Figures.....	viii
List of Tables	x
Chapter 1: Introduction	1
1.1 Motivation.....	1
1.2 The Blood-Brain Barrier	1
1.3 The Blood Tumor Barrier	3
1.4 Methods for Drug Delivery in the Brain.....	4
1.4.1 Invasive Approaches to Brain Drug Delivery.....	4
1.4.2 Transvascular Brain Drug Therapy: Biopharmaceutical Approaches	5
1.4.3 Transvascular Brain Drug Therapy BBB Disruption.....	8
1.5 Ultrasound.....	9
1.5.1 Focused Ultrasound	11
1.5.2 Application.....	13
1.6 Ultrasound and Microbubble	15
1.6.1 Linear Bubble Vibration	15
1.6.2 Nonlinear Bubble Vibration.....	19
1.6.3 Coated Bubble Vibration	20
1.7 Acoustic Characterization	21
1.8 Application in the Brain.....	22
1.8.1 Ultrasound-Induced BBB Disruption	23
1.8.2 Effect of Ultrasound Parameters and Other Factors on BBB Disruption	25
1.8.3 Optimal Parameters for BBBD	29
1.8.4 Potential Mechanisms	30
1.8.5 Bioeffects Induced by FUS and Microbubbles.....	32

1.8.6	Delivery of Imaging/Therapeutic Agents and Tests in Animal Disease Models	37
1.8.6.1	Delivery of Imaging Tracers	37
1.8.6.2	Delivery of Therapeutics	40
1.8.6.3	Disease Models	41
1.8.7	Treatment Planning, Monitoring and Evaluation	45
1.8.7.1	Treatment Planning	45
1.8.7.2	Treatment Monitoring and Control	48
1.8.7.2.1	Acoustic Emission	49
1.8.7.3	Treatment Evaluation	51
1.9	Dynamic Contrast Enhanced Magnetic Resonance Imaging	53
1.9.1	Pharmacokinetic Analysis of DCE-MRI	53
1.9.1.1	Tofts and Kermode (TK) Model	53
1.10	Magnetic Resonance Imaging	56
1.10.1	Basic Principles of MRI	56
1.10.2	MRI Sequences	59
1.11	Doxorubicin	61
1.12	Scope of this Thesis	63
	Chapter 2: Methods and Materials	66
2.1.	Animals	66
2.2	Ultrasound Transducer	67
2.1.2.2	Transducer Characterization	68
2.1.2.3	Transducer Calibration	69
2.1.2.4	Estimated Pressure Amplitude in the Brain	71
2.3	Experimental Set-up	71
2.4	Magnetic Resonance Imaging	72
2.5	Fluorometry	74
2.6	Targeted Doxorubicin Delivery through Blood Brain and Blood Tumor Barrier using Transcranial MRI-guided Focused Ultrasound	75

2.6.1	Sonications.....	76
2.6.2	Chemotherapy.....	77
2.6.3	Effect of Drug Injection Protocol on Doxorubicin Delivery to the Brain.....	78
2.6.3.1	Fluorometric Assay.....	79
2.6.3.2	Extraction and Quantification of Doxorubicin.....	80
2.6.3.3	Statistical Analysis.....	80
2.6.4	Fluorescence Imaging.....	81
2.6.4.1	Tissue Preparation.....	81
2.7	Multiple Sessions of Liposomal Doxorubicin and Ultrasound-Mediated Blood-Brain Barrier Disruption: A Safety Study in the Rat Brain.....	82
2.7.1	Study Design.....	82
2.7.2	Magnetic Resonance Imaging.....	83
2.7.3	Histology.....	84
2.8	Multiple Treatments with Liposomal Doxorubicin and Ultrasound-Induced Disruption of Blood-Tumor and Blood-Brain Barriers Improve Outcomes in a Rat Glioma Model.....	84
2.8.1	Cell Culture.....	85
2.8.2	Tumor Implantation.....	85
2.8.3	Study Design.....	86
2.8.4	Sonication.....	87
2.8.5	Chemotherapy.....	88
2.8.6	Magnetic Resonance Imaging.....	88
2.8.7	Image Analysis.....	89
2.8.8	Histology.....	89
2.8.9	Statistical Analysis.....	90
2.9	Enhancement in Blood-Tumor Barrier Permeability and Delivery of Liposomal Doxorubicin using Focused Ultrasound and Microbubbles: Evaluation during Tumor Progression in a Rat Glioma Model.....	90
2.9.1	Bilateral Tumor Implantation.....	91
2.9.2	Study Design.....	91
2.9.3	Magnetic Resonance Imaging.....	92

2.9.4	Fluorometric Assay and Doxorubicin Extraction	93
2.9.5	Data Analysis	94
2.9.6	Statistical Analysis	95
2.9.7	Histology.....	95
2.9.5	Acoustic Emission	96
Chapter 3: Targeted Lipo-DOX Delivery through Blood-Brain and Blood-Tumor Barriers using Transcranial MRI-Guided Focused Ultrasound		97
3.1	Results.....	97
3.1.1	Permeabilization of BBB/BTB	97
3.1.2	Effect of Lipo-DOX Injection Protocol on doxorubicin Delivery to the Brain	98
3.1.3	Fluorescence Imaging	100
3.2	Discussion.....	103
Chapter 4: Multiple Sessions of Focused Ultrasound Blood-Brain Barrier Disruption to Enhance Delivery of Liposomal Doxorubicin: A Safety Study		106
4.1	Results.....	107
4.1.1	BBB Permeabilization	107
4.1.2	Histological Findings	109
4.2	Discussion.....	112
Chapter 5: Multiple Treatments with Liposomal Doxorubicin and Ultrasound-Induced Disruption of Blood-Tumor and Blood-Brain Barriers Improve Outcomes in a Rat Glioma Model		117
5.1	Results.....	117
5.1.1	BBB/BTB Permeabilization.....	117
5.1.2	Tumor progression	120
5.1.3	Histological Findings	124
5.1.4	Survival Analysis	130
5.2	Discussion.....	131
Chapter 6: Enhancement in Blood-Tumor Barrier Permeability and Delivery of Liposomal Doxorubicin using Focused Ultrasound and Microbubbles: Evaluation during Tumor Progression in a Rat Glioma Model.....		138
6.1	Results.....	140

6.1.1	Bilateral Tumor Progression and BBB/BTB Disruption	140
6.1.2	Doxorubicin Concentration and Kinetics of BBB/BTB Permeability Changes 142	
6.1.3	Histological findings.....	147
6.2	Discussion.....	149
6.3	Acoustics Emission.....	152
6.3.1	Acoustic Emissions vs. MRI.....	153
6.3.2	Discussion.....	155
Chapter 7:Conclusions and Future Work		156
7.1	Conclusions.....	156
7.2	Future work.....	162
References.....		166
Appendix.....		186-1867

List of Figures

Chapter 1

Figure 1. 1 Diagram of a focused ultrasound transducer.....	11
Figure 1. 2 The axial intensity distribution from a focused transducer.....	13
Figure 1. 3 Energy level splitting of a nucleus of spin $I = 1/2$	57
Figure 1. 4 Fluorescence spectra for doxorubicin in aqueous solution.....	62

Chapter 2

Figure 2. 1 A single-element, spherically curved,.....	68
Figure 2. 2 Characteristic beam plots for the 0.69-MHz transducer.....	69
Figure 2. 3 Schematic of the MRI-guided focused ultrasound system.....	72
Figure 2. 4 Calibration curves for fluorometric measurements.....	75

Chapter 3

Figure 3. 1 Visualization of BBB/BTB permeabilization.....	98
Figure 3. 2 Doxorubicin concentration corresponding to doxorubicin injection ...	100
Figure 3. 3 Contrast-Enhanced T1-weighted imaging.....	102
Figure 3. 4 Contrast-Enhanced T1-weighted imaging.....	102

Chapter 4

Figure 4. 1 MRI-images acquired during three weekly treatments:.....	109
Figure 4. 2 The representative examples of T2*-weighted images.....	111
Figure 4. 3 The T2*- weighted images and corresponding histological.....	111
Figure 4. 4 An example of adverse effect on the brain surface of FUS+doxorubicin..	112

Chapter 5

Figure 5. 1 Treatment overview.....	119
Figure 5. 2 MRI appearance of the tumors and their growth over time.....	123
Figure 5. 3 Appearance of 9L gliosarcoma in the three control groups in histology.	128
Figure 5. 4 Histological appearance of the brain in three of the animals.....	129
Figure 5. 5 Kaplan–Meier survival curves for the four experimental groups.....	131

Chapter 6

Figure 6. 1 MRI appearance of bilateral 9L gliosarcoma.....	141
Figure 6. 2 Example of signal intensity changes in sonicated tumor.....	144
Figure 6. 3 Mean K_{trans} estimates (\pm S.D.) before and after FUS.....	145
Figure 6. 4 Mean K_{trans} estimates and doxorubicin concentrations (\pm S.D.).....	147
Figure 6. 5 Appearance of two 9L gliosarcoma at different days.....	148

Figure 6. 6A-B Acoustic emissions during tumor sonication and MRI.154

List of Tables

Chapter 1

Table1. 1 Different methods investigated to get around the BBB.....9

Table1. 2 Reported effects of different parameters on BBB disruption via FUS.....28

Table1. 3 Example different tracers that have been delivered across the BBB.....39

Table1. 4 Example therapeutic agents that have been delivered across the BBB44

Chapter 2

Table 2. 1 Acoustic efficiency of air-backed single-element transducer.....70

Chapter 3

Table 5. 1 Outcomes in FUS+doxorubicin group.....124

Table 5. 2 Survival analysis.....131

Chapter 1: Introduction

1.1 Motivation

Since the time immemorial there researchers have pondered over the vast empire of the brain. The central nervous system (CNS) has remained a focus of research and continued to hold some of the greatest mysteries in science and in medicine because it is challenging to utilize most drugs due to the presence of vascular barriers that prevent their delivery. For the treatment of brain-borne ailments in general, and tumors in particular, several techniques have been investigated to overcome these barriers, and new innovations are yet in process. In these other techniques, there have been significant shortcomings, such as invasiveness, non-targetedness, or the requirement and expense of new drug formulation. The central inclination of this dissertation was to study an alternative approach with the potential to overcome the hinderances encountered in these other techniques to deliver a chemotherapeutic agent across the blood-brain barrier (BBB) and the blood-tumor barrier (BTB) for brain tumor treatments in a rodent model..

1.2 The Blood-Brain Barrier

The blood-brain barrier (BBB) is a specialized non-permeable barrier in

cerebral microvessels consisting of endothelial cells connected together by tight junctions, a thick basement membrane, and astrocytic endfeet. The tight junctions between the endothelial cells, together with an ensemble of enzymes, receptors, transporters, and efflux pumps of the multidrug resistance (MDR) pathways, control and limit access of molecules in the vascular compartment to the brain by paracellular or transcellular pathways [1]. The BBB normally protects the brain from toxins and helps to maintain the delicate homeostasis of the neuronal microenvironment. However, it also excludes 98% of all small-molecule drugs and approximately 100% of large-molecule neurotherapeutics from reaching the brain parenchyma [2,3]. Only small-molecule drugs with high lipid solubility and a molecular mass under 400-500 Daltons (Da) can cross the BBB in pharmacologically significant amounts, resulting in effective treatments for only a few diseases such as depression, affective disorders, chronic pain, and epilepsy. Given the paucity of small-molecule drugs that have been shown to be effective for the majority of CNS disorders, it is clear that the BBB is a primary limitations for the development and use of drugs in the brain. Overcoming this hindrance could mean potential therapies for a wide range of disorders, including Alzheimer's and Huntington's disease, amyotrophic lateral sclerosis (ALS), neuro-AIDS, stroke, brain or spinal cord trauma, autism, lysosomal storage disorders, fragile

X syndrome, inherited ataxias, and blindness.

1.3 The Blood Tumor Barrier

Tumors of the brain, also face challenges for effective drug delivery. While the blood vessels of primary and metastatic brain tumors are often somewhat permeable from the lack of a fully formed BBB, infiltrating cancer cells at the tumor margins and small metastatic seeds may be protected by the BBB of the surrounding normal tissue [4]. Glioblastomas in particular, are highly infiltrative, and commonly recurring after localized treatments such as conformal radiotherapy or surgery. Relapse usually occurs within a few centimeters of the treatment site [5–7]. Furthermore, their vasculature permeability is heterogeneous, and additional barriers to drug delivery include increased interstitial pressures [8] and drug efflux pumps that contribute to their multidrug resistance phenotype [9]. As for metastatic tumors, work in mice suggests that the BTB is only partially compromised in breast adenocarcinoma brain metastases, and that toxic concentrations of chemotherapy agents are only achieved in a small subset of tumors that are highly permeable [10]. Also, systemic drug accumulation in brain metastases can be substantially less than in extracranial metastases [10]. Thus, the BTB is a hindrance of effective drug delivery in addition to the BBB.

1.4 Methods for Drug Delivery in the Brain

In order to overcome these limitations, it is necessary to either bypass these vascular barriers altogether, or to facilitate passage across it via controlled exploitation of endogenous transport mechanisms. Different methods have been explored to bypass the BBB (or the BTB) (Table 1.1) [11–13]. While these methods are promising, they also have limitations.

1.4.1 Invasive Approaches to Brain Drug Delivery

High local drug concentrations can be achieved by inserting a needle or catheter into the brain and directly injecting or infusing drugs or by implanting drug-exuding devices. With such techniques, therapeutic benefits have been shown for brain tumors and other disorders [14–17]. Because of their invasiveness, there are some risks of infection or brain trauma, and they may not be amenable for repeated treatments or for drug delivery to large areas of the brain. It can also be a challenge to control the drug distribution, as drug concentrations decrease exponentially from the injection or implantation site [18]. When convection-enhanced diffusion is used, the infused agents are delivered preferentially along white matter tracts [19], which may not be desirable.

Another approach for bypassing the BBB is to introduce drugs into the cerebrospinal fluid (CSF) via intrathecal or intraventricular routes. It then follows the flow patterns of the CSF and enters the brain parenchyma via diffusion. This approach has been successful in cases where the target is in the subarachnoid space [20], but drug diffusion drops off exponentially from the brain surface and penetration into the brain parenchyma can be limited [11]. It is also possible to deliver drugs transnasally from the submucous space into the olfactory CSF [21–24]. This approach has advantages of being noninvasive and being relatively easy to administer. However, only small drug volumes can be delivered and interindividual variability and other factors may pose challenges to this procedure [24]. Nevertheless, the technique is a promising route to bypass the BBB and is currently being investigated by numerous researchers.

1.4.2 Transvascular Brain Drug Therapy: Biopharmaceutical Approaches

A number of approaches have been investigated to develop drugs that can cross the BBB or to modify or encapsulate existing drugs so they can. While these methods are highly promising and offer the ability to easily administer drugs to the

CNS as in other organs, they do require the expense and time of developing new agents, and they result in drugs being delivered to the entire brain, which may not always be desirable. Converting water-soluble molecules that would not ordinarily cross the BBB into lipid-soluble ones is one approach to brain drug therapy. This can be achieved by the addition of lipid groups, or functional groups such as acetate to block hydrogen bonding. The molecule would then undergo passive diffusion across the BBB. An example of this is the conversion of morphine to heroin by the acetylation of two hydroxyl groups, which results in the removal of the molecule from hydrogen bonding with its aqueous environment [25]. Although utilized by the pharmaceutical industry, this approach has limited applicability to drugs greater than 400-450 Da [26,27].

Another approach involves utilizing the large variety of solute carrier proteins (SLC) on the endothelial surface that specifically transport many essential polar and charged nutrients such as glucose, amino acids, vitamins, small peptides, and hormones transcellularly across the BBB [28]. These transporters move the solute into the cytoplasm where they await another SLC at the opposite cell membrane to exocytose them into the brain parenchyma. An example of an SLC used for brain drug

therapy is the large neutral amino acid transporter type 1 (LAT1), which transports the amino acid Parkinson's drug L-dopa across the BBB. Once across, it is converted to dopamine by aromatic amino acid decarboxylase, and can then bind to its target receptor. Dopamine being water-soluble cannot cross the BBB [26,29].

Finally, the molecular targeting of endothelial-surface receptors, colloquially termed the "Trojan Horse" approach, is yet another paradigm in drug transport across the BBB. This involves using a targeting ligand such as a serum protein, monoclonal antibody, or other high affinity targeting molecule that binds to its receptor and activates endocytosis of the complex into a vesicle that is transported across to, and released from the opposite pole (i.e., transcytosis). In theory, if the ligand is chemically linked to a drug or drug carrier, it too is transported across the BBB. Over the last two decades, a number of animal studies have suggested the transport of antineoplastic drugs, fusion proteins, genetic therapies (plasmid vectors, siRNA), liposomes, and nanoparticles by this mechanism [30–33]. For transcytosis to occur, it requires that the endosome not fuse with lysosomes while in the cytoplasm, which would degrade the internalized macromolecules. Unlike other tissues, endothelial cells in brain capillaries appear to have low levels of endosome fusion with lysosomes,

facilitating transport of necessary substances through the transcellular route [34–36].

1.4.3 Transvascular Brain Drug Therapy BBB Disruption

Others have investigated methods to temporarily disrupt the BBB to enable CNS delivery of circulating agents. One such technique investigated intensively for several decades is the use of intraarterial injection of a hyperosmotic solutions such as mannitol. This causes shrinkage of the endothelial cells and consequent stretching of the tight junctions [37–40], through which drug may pass. This method has been shown repeatedly to enhance delivery of therapeutic agents to brain tumors, and several promising clinical trials have been performed [41–46]. Other agents, such as bradykinin, have also been investigated [47–50]. While such methods can be an effective means to deliver drugs to large brain regions, they are invasive procedures that require general anesthesia, and can have side effects. For example, one study reported focal seizures in 5% of osmotic BBB disruption [41], and others have noted vasovagal response with bradycardia and hypotension [40]. As I describe below, to overcome limitations of invasive and biopharmaceutical approaches of brain drug delivery, focused ultrasound (FUS) combined with circulating microbubbles has been investigated by numerous researchers.

Table1. 1 Different methods investigated to get around the BBB to deliver drugs to the brain

Method	Advantages	Disadvantages
Direct injection, convection-enhanced delivery, implantable devices	High local drug concentrations can be achieved; systemic administration avoided.	Invasive; side effects; challenging to control; not readily repeatable.
Intrathecal, intraventricular injection	Effectively delivers drugs to subarachnoid space, brain surface.	Little drug penetration beyond brain surface; invasive.
Trans-nasal delivery	Noninvasive; easy to administer; repeatable.	Small volume of drug delivered; interindividual variability.
BBB disruption via arterial injection of osmotic solution or other agents	Effectively delivers drugs to large brain regions; large clinical experience.	Invasive; requires general anesthesia; side effects; not readily repeatable.
Modification of drugs to cross barrier through endogenous transport mechanisms	Easily administered; delivered to whole brain.	Requires systemic administration; expensive; each drug requires new development; clinical data lacking.
BBB disruption via FUS and microbubbles	Noninvasive; readily repeatable; can target drug delivery to desired volumes; can control "magnitude" of disruption; can be combined with drug-loaded microbubbles or magnetic particles for additional targeting.	Requires systemic administration; currently technically challenging; large volume/whole brain disruption unproven; no clinical data.

1.5 Ultrasound

Ultrasound is a mechanical wave which can be generated by applying an oscillating electrical voltage to a piezoelectric material, such as certain crystals or ceramics, which respond with mechanical deformation in proportion to the applied voltage. The expansion or contraction of the material due to the electric potential causes the compression or rarefaction of its surrounding medium, such as air or water. When an oscillating voltage produces pressure waves with frequencies higher than upper limit (~18 kHz) of human hearing frequency, it is called ultrasound. The

piezoelectric effect also works in reverse: mechanical stress can conversely induce an electric voltage across the material. Thus piezoelectric transducers can be used both to generate and receive ultrasonic signals. In medical ultrasound, these frequencies typically range between 200 kHz and 10 MHz. The wavelength λ of the ultrasound is determined by the frequency f

$$\lambda = c / f \quad 1.1$$

where c is the speed of sound in the tissue. Typically sound velocity in soft tissue is $c \approx 1540$ m/s. In soft tissues, this wave is primarily longitudinal, but shear waves can be generated under some circumstances, such as at soft tissue-bone interfaces.

When ultrasound wave propagates through a medium (tissue) its amplitude ($P(z)$) is attenuated according to:

$$P(z) = P_0 e^{-\mu z} \quad 1.2$$

where μ is the amplitude attenuation coefficient per unit path length and P_0 is the incident peak rarefactional pressure amplitude at the surface. The attenuation coefficient depends on both absorption (μ_a) and scattering (μ_s) coefficients as

$$\mu = \mu_a + \mu_s \quad 1.3$$

Both the absorption and scattering of ultrasound energy can produce heating in the medium [51]. Ultrasound has a relatively low absorption rate in soft tissue, enabling it to propagate into even deep tissue structures. For example ultrasound with 1.0 MHz, having an approximate wavelength of 1.5 mm, can penetrate up to 10 cm [52].

1.5.1 Focused Ultrasound

Focused ultrasound is an application of ultrasound in which the wave energy is concentrated to provide high gains and localized energy deposition. Ultrasound can be focused using a curved transducer geometry, a lens or reflector, or via electronic focusing. A diagram of a single element spherically curved transducer is as shown in

Figure1. 1

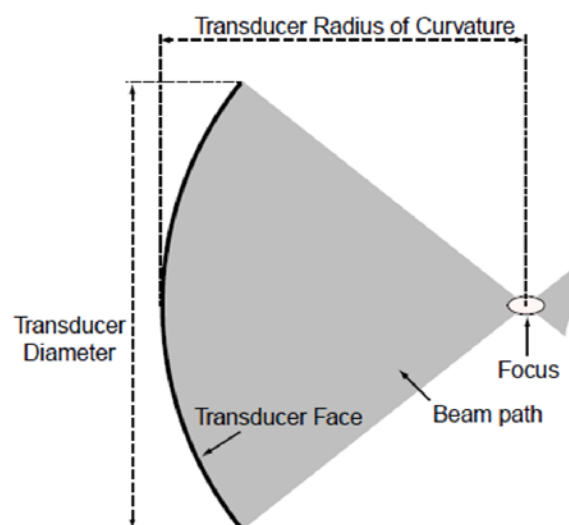


Figure1. 1 Diagram of a focused ultrasound transducer

In this case, intensity at point x on its axis can be written as

$$I(x) = I(0) \left\{ \left[\frac{R}{(R-x)} \right] \sin \left[\frac{(\pi d^2 (R-x))}{(8\lambda x R)} \right] \right\}^2 \quad 1.4$$

where $I(0)$ is the average intensity over the radiating surface, d is the diameter of the transducer, and R is the radius of curvature [51].

At the geometrical focus, $x \sim R$, the intensity can be approximate as

$$I(x) = I(0) \left(\frac{\pi d^2}{8R\lambda} \right)^2 \quad 1.5$$

The acoustic pressure profile near the focal plane can be approximated by

$$p(R, \theta) = \frac{p(R, 0) 2J_1(z)}{z} \quad 1.6$$

where $z = k a \sin \theta$, $p(R, 0)$ is the acoustic pressure on the axis, and J_1 is the first order Bessel function [51]

The shape of the focus is long and narrow, and these dimensions depend on the focusing properties of the transducer, i.e. the transducer's F-number ($F = R/d$), and the ultrasound frequency [51]. For constant values of ultrasound frequency and transducer diameter, the position of focus and intensity gain can be changed with R . The maximum intensity can be pushed deeper into the tissue by increasing R . However, a high value of R reduces the focusing effect of transducer as a result the

focal region becomes longer and peak intensity smaller. Finally, the value of intensity becomes less than 1. Figure 1. 2 shows the distribution of intensity along the axis of focused transducer with fixed value of d and frequency for different value of R . Moreover, the sharpness of the focus depends on the frequency. Ultrasound with higher frequencies can achieve tighter foci, while lower frequencies can produce wider focal regions.

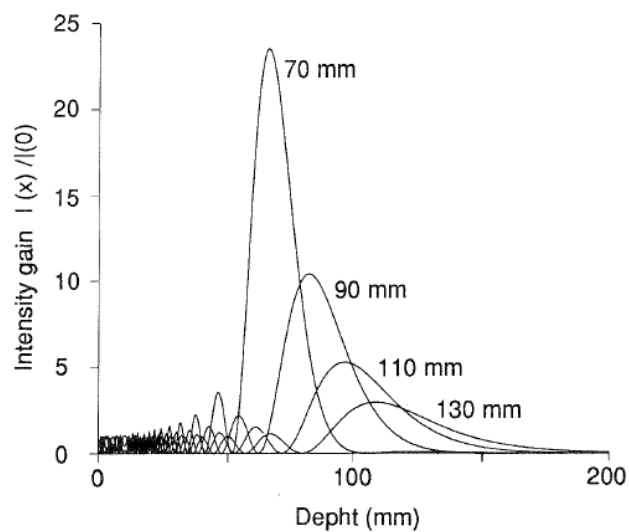


Figure 1. 2 The axial intensity distribution from a focused transducer (diameter 60mm, frequency 1MHz) for various values of radius of curvature calculated in tissue (attenuation 10 Npm-1).

1.5.2 Application

Ultrasound technology has been used for both diagnostic as well as therapeutic

applications. In diagnostic imaging, it is most notably used for fetal imaging and echocardiography. Low acoustic pressures (< 0.5 MPa peak-rarefactional) and short pulse lengths are used for this application. Typically, pulses are only a few cycles long, but are rapidly emitted to acquire real-time images at a rate of 10 to 30 frames per second. For current medical applications, diagnostic ultrasound is considered a safe imaging device that is routinely used to diagnose disease. Therapeutic applications of FUS can be achieved with both thermal and mechanical effects. For thermal application, the induced temperature is raised high enough over a short period of time (\sim seconds) to cause cell death by protein denaturation and coagulative necrosis (tissue ablation), while in hyperthermia, an induced temperature change of only a few degrees for an extended period of time (\sim minutes) can sensitize tissue to radiation and chemotherapy.

In addition to thermal effects, it can induce mechanical effects in biological tissue. In cavitation, the interaction of a gas bubble with the acoustic field, whether by radial oscillation (stable cavitation) or violent collapse (inertial cavitation), can significantly enhance absorption and heating effects in tissue [53]. Gas bubbles can form spontaneously in tissue during exposure to high intensity FUS, or pre-formed

gas bubbles, such as those found in ultrasound contrast agents, can be introduced into the acoustic field by intravenous injection. The microbubbles formed in the tissue concentrate the ultrasound effects in the microvasculature, thus greatly reducing the FUS exposure levels needed to produce bioeffects. The success of this technique has prompted its investigation in diverse medical applications, including tumor and tissue ablation [54,55], hemostasis [56], vessel occlusion [57], thrombolysis [58] and BBB disruption for drug and gene therapy in brain tissue. The specific application across the BBB will be discussed in greater detail in section 1.8.

1.6 Ultrasound and Microbubble

When microbubbles interact with ultrasound, different phenomena take place such as scattering, absorption of ultrasound and bubble oscillation. The oscillation will be either linear or nonlinear depending on the magnitude of applied acoustic pressure. At low acoustic pressures, the instantaneous radius oscillates linearly with amplitude of the applied external pressure field. For higher amplitudes of the external field, the pulsation of the bubbles becomes nonlinear.

1.6.1 Linear Bubble Vibration

In tissues, microbubbles are constrained within blood vessels or in small

regions of water within different tissue structures. Modeling the bubble behavior under such constraints is complex. A good understanding can be achieved by making some simple assumptions:

1. A bubble is considered spherical and surrounded by a liquid of infinite extent and a constant viscosity. The bubble volume is defined by a single variable, the radius, and the motion of bubble is spherically symmetric.
2. The wavelength of the ultrasound field is much larger than the bubble diameter, and only the motion of the bubble surface is of interest. The vapor pressure remains constant during the compression and expansion phase, and that there is no rectified diffusion during the short period of exposure to ultrasound.
3. The gas inside the bubble is assumed to be ideal and compression and expansion takes place according to the gas law.
4. At small excitation levels, the displacement of the bubble wall can be compared to the displacement of a simple one-dimensional mass spring oscillator. The oscillator is defined by its mass, restoring force, damping, and applied force.

The equation of bubble motion can be modeled as:

$$m \frac{d^2 x}{dt^2} + \beta \frac{dx}{dt} + Sx = F_{driv} \quad 1.7$$

where m is the mass of the bubble–liquid system, β is the mechanical resistance related to the dissipation, S is the stiffness of the system, $F_{driv}(t)$ is the driving force, and $x(t)$ is the radial displacement of the bubble wall relative to the initial radius R_0 , according to $x(t) = R(t) - R_0$.

For undamped simple harmonic oscillation the resonance frequency of bubble can be written as

$$f_R = \frac{1}{2\pi R} \sqrt{\frac{S}{m}} \quad 1.8$$

For gas bubbles in a liquid, the stiffness is that of the enclosed volume of gas that acts like a spring when the bubble is disturbed from its equilibrium radius. The inertia is principally due to the mass of the liquid surrounding the bubble that oscillates with it. The derived value of the mass, the mechanical resistance, and the stiffness are [59]

$$m = 4\pi R_0^3 \rho, \quad \beta = \delta_{tot} \omega m, \quad S = 12\pi \kappa P_0 R_0 \quad 1.9$$

where ρ is the density of the surrounding medium, δ_{tot} is the total damping, ω is the

angular frequency, κ is the heat capacity ratio (C_p/C_v), and P_0 is the ambient pressure.

The total damping δ_{tot} is sum of reradiation damping (δ_{tot} rad), damping due to viscosity of the surrounding fluid (δ_{tot} vis) and thermal damping (δ_{tot} th) i.e.

$$\delta_{tot} = \delta_{tot} \text{ rad} + \delta_{tot} \text{ vis} + \delta_{tot} \text{ th} \quad 1.10$$

The damping coefficients depend on the bubble size and the frequency of the acoustic field and are nominally on the order of 0.1 for bubbles with a diameter between 1 and 10 μm . Exact expressions for the different damping components can be found in [60].

Substitution of value m , β , and S into equation 1.8 above gives the final expression for the resonance frequency for a bubble motion without losses.

$$f_R = \frac{1}{2\pi R} \sqrt{\frac{3\kappa P}{\rho}} \quad 1.11$$

This equation shows that the resonant frequency is inversely proportional to the radius.

For an encapsulated bubble, the surrounding shell causes an additional restoring force. This can increase the resonance frequency [61] of the bubble.

$$f_{re}^2 = f_R^2 + \frac{S_{shell}}{4\pi^2 m} \quad 1.12$$

where f_{re} is the resonance frequency of the encapsulated bubble, f_R is the resonance frequency for a free gas bubble, and S_{shell} the stiffness due to the shell. The shell is assumed to be homogeneous, of constant thickness, and perfectly elastic. The shell influences the surface tension and probably also the thermal damping.

1.6.2 Nonlinear Bubble Vibration

For large acoustic pressure fields equation 1.7 it is thought to be inadequate to fully model the bubble vibration phenomenon and a more sophisticated model is needed. In developing the initial model Rayleigh made following assumptions:

5. The bubble is spherical, and is surrounded by an incompressible liquid with constant viscosity to infinite extent.
6. The gas in the bubble is compressed and expanded according to the gas law with the polytropic exponent remaining constant during the vibration.
7. Pressure at the bubble wall is at equilibrium. Combining the Rayleigh–Plesset equation and the polytropic gas law with the boundary condition, Nico-de Jong

$$\rho_1 \left(R \frac{d^2 R}{dt^2} + \frac{3}{2} \left(\frac{dR}{dt} \right)^2 \right) = \left(p_0 + \frac{2\sigma}{R_0} \right) \left(\frac{R}{R_0} \right)^{-3\kappa} \left(1 - \frac{3\kappa}{C} \left(\frac{dR}{dt} \right) \right) - \frac{2\sigma}{R} - \frac{4\mu}{R} \left(\frac{dR}{dt} \right) - p_0 - P_{ac}(t) \quad 1.13$$

where R , dR/dt , dR^2/dt^2 represent the radius, velocity and acceleration of the bubble wall, ρ_1 is the density of the liquid, p_0 is the ambient pressure, σ is the surface tension, κ is the polytropic gas exponent, μ is the viscosity of the surrounding water, c is the speed of sound, and $P_{ac}(t)$ is the applied acoustic field. For simplicity only the viscous damping caused by the surrounding liquid has been taken into account.

1.6.3 Coated Bubble Vibration

Encapsulation of the bubbles dramatically changes their acoustical behavior. The shell causes an increase in resonance frequency due to its stiffness and an increase in damping due to its viscosity. Encapsulated microbubbles were first modeled by De Jong et al. [61] and De Jong and Hoff [62] incorporating experimentally determined elasticity and friction parameters into the Rayleigh–Plesset model. Church [63] used linear visco-elastic constitutive equations to describe the shell. Since then many models have been defined to investigate the influence of the shell on the bubble's vibration, e.g. [64–67] including Marmottant model for

phospholipid-coated bubbles [68] where he proposed three parameters to describe the properties of the shell: a buckling radius, the compressibility of the shell, and a break-up shell tension. These three regimes can be expressed as following which add σ term in equation 1.13, $\sigma(R)$ is equal to zero if $R \leq R_{\text{buckling}}$, $\sigma(R) = \chi \left(\frac{R^2}{R_{\text{buckling}}^2} - 1 \right)$ if $R_{\text{buckling}} \leq R \leq R_{\text{break-up}}$ and $\sigma(R)$ becomes $\sigma(\text{water})$ if $R \geq R_{\text{ruptured}}$. Buckling radius (R_{buckling}) is a state that naturally occurs with dissolution of gas, or that can be accelerated by repeated pulses.

1.7 Acoustic Characterization

As mentioned previously, when bubbles interact with ultrasound they absorb as well as scatter energy. Both absorbed and scattered energy can be determined by using different kinds of measurement techniques [69]. The scattered power of a free microbubble can be determined by its scattering cross-section and can be expressed as [61]:

$$\sigma_s = \frac{4\pi R^2}{\left(\frac{f_r}{f} - 1\right)^2 + \delta_{\text{tot}}^2} \quad 1.14$$

where σ_s is scattering cross-section and f is applied ultrasound field.

In case of coated bubble, there exists an additional damping constant due to

shell viscocity [70]

$$\delta_s = \frac{12\eta S d S_e}{\omega_0 \rho a^3} \quad 1.15$$

The expressions for other three damping constants are the same as equation 1.10. However, the resonance frequency of the bubble depends on the shell properties, and this alters the value of damping constant. It was observed that encapsulated bubbles could scatter energy with different harmonics such as n-harmonics, sub-and ultraharmonics [69] Like in case of scattering, absorption cross section also depends on damping coefficient as:

$$\sigma_a = \sigma_s \left(\frac{\delta}{\delta_{rad}} - 1 \right) \quad 1.16$$

where σ_a is absorption cross section. The total energy loss for an acoustic beam travelling through bubble solution is determined by the sum of scattering and absorption cross sections.

1.8 Application in the Brain

FUS has been investigated since the 1940's for noninvasive ablation in the brain as a potential alternative to surgical resection and radiosurgery [71–74]. Until recently, clinical testing required a craniotomy to allow for ultrasound propagation

into the brain [75,76] because of ultrasonic heating of the skull bone and beam aberration caused by the skull's irregular shape and large acoustic impedance. In the past decade, FUS thermal ablation systems have been developed that overcome these obstacles produced by the skull [77]. They reduce skull heating through active cooling of the scalp and a transducer design with a large aperture to distribute the ultrasound energy over a large skull region, and they correct for beam aberrations using a phased array transducer design. When combined with methods that use acoustic simulation based on CT scans of the skull bone to determine the phase and amplitude corrections for the phased array [78,79] and MRI temperature imaging (MRTI) to monitor the heating [80], a completely noninvasive alternative to surgical resection in the brain becomes possible. These systems, use very high intensities to enable thermal ablation through the human skull, and are currently in initial human trials [81,82], .

1.8.1 Ultrasound-Induced BBB Disruption

Since the early years of investigation into ultrasound bioeffects on the brain, several studies have noted localized BBB disruption, either accompanied with tissue necrosis or without evident tissue damage [73,83–88]. None of these early studies

however, elucidated sonication parameters that could repeatably and reliably produce BBB disruption without occasionally producing lesions or necrosis.

In 2000 our laboratory discovered that if short ultrasound bursts are preceded by an intravenous injection of a microbubble ultrasound contrast agent, the BBB can be consistently opened without the production of lesions or apparent neuronal damage [89]. The circulating microbubbles appear to concentrate the ultrasound effects to the blood vessel walls, causing BBB disruption through widening of tight junctions and activation of transcellular mechanisms, with little effect on the surrounding parenchyma [90]. Furthermore, the opening occurs at acoustic power levels orders of magnitude lower than was previously used, making this method substantially easier to apply through the intact skull. For BBB disruption, the sonications have been typically applied as short (~1-20 ms) bursts at a low duty cycle (1-5%) for 0.5-1 min. With a few simple modifications to enable low-intensity bursts, existing clinical brain FUS systems can be used for BBB disruption [91]. Clinical translation may also be possible using simpler FUS systems [92].

1.8.2 Effect of Ultrasound Parameters and Other Factors on BBB

Disruption

A number of sonication parameters can be varied in ultrasonic BBB disruption. Each parameter variation may impact the threshold pressure amplitude needed to disrupt the BBB, along with the magnitude of its disruption, and the resultant drug quantity delivered to the brain parenchyma. As determined from a number of studies, parameter variations and their effects are listed in Table 1. 2. These studies used an MRI contrast agent, fluorescent probe, or drug to evaluate the BBB disruption. Given the large parameter space, and different techniques and criteria used to evaluate the disruption (each with different sensitivities), it can be challenging to compare results from different laboratories. Such comparisons are additionally confounded by uncertain accuracies in estimates of acoustic pressure amplitude when sonicating through the skull [93]. However, general trends can be observed.

For a fixed set of parameters, as one increases the pressure amplitude, the magnitude of the BBB disruption increases, and at some level it appears to saturate [94–96]. Below some value, no disruption is detected, and at some higher pressure threshold, vascular damage is produced along with the disruption (see below).

Such studies repeated while varying a different parameter have shown that the threshold for BBB disruption depends strongly on the ultrasound frequency [97] and burst length [98]. Most experiments have been done with commercially-available ultrasound contrast agents that consist of microbubbles with a wide range of diameters. Experiments with microbubbles with narrow size distributions suggest that the BBB disruption threshold can also be reduced by using larger microbubbles [99–101]. Pulse repetition frequency can also influence the magnitude of disruption up to a point [102,103], but other studies have seen no dependence [98]. Finally, the magnitude of the disruption can be increased by increasing the sonication duration [96] or by repeating the sonication after some delay [104,105], but excessive durations may result in tissue damage [105,106]. Factors such as using an infusion instead of a bolus injection of microbubbles [107] and choice of anesthesia protocol [108] may also influence the resulting disruption. Other factors such as the delay between the microbubble injection and the start of sonication, and whether the drug or tracer is administered before or after the sonication may also be expected to have an effect. Additive effects have been observed when FUS-induced BBB disruption is combined with agents that affect vascular permeability [109–111].

These trends observed in parametric studies are difficult to interpret with confidence since the exact mechanism by which microbubble-enhanced FUS induces BBB disruption is currently unknown (see below). They are perhaps consistent with the following notions. First, for BBB disruption to occur, the microbubbles oscillations may need to reach a certain minimal radius, which can be achieved by increasing the pressure amplitude or by using larger microbubbles, and assuming the bubbles grow during each burst via rectified diffusion, by decreasing the ultrasound frequency or increasing the burst length. Next, in addition to depending on the bubble size during its oscillation, the magnitude of the disruption depends on the number of sites on which the microbubbles interact with the vasculature. The number of these sites can be increased by increasing the microbubble dose, or by increasing the sonication duration and/or number of bursts. Data showing a strong dependence on burst length may also suggest that the threshold and magnitude of the disruption depend on the amount of time the microbubbles interact with the blood vessels during each burst. Pulse repetition frequency may have an influence if the microbubbles are being fragmented or destroyed-time may be needed to replenish them if that is the case [112]. Finally, it appears that the magnitude of the disruption can saturate at some level, and increasing the different parameters has no additional effect.

Table 1. 2 Reported effects of different parameters on BBB disruption via FUS and microbubbles.

Parameter	Effect on BBB disruption
Pressure amplitude	Increase in BBB disruption magnitude as pressure amplitude increases; saturation at some point [94–96] ; vascular damage produced at high pressure amplitudes.
Ultrasound frequency	Decrease in BBB disruption threshold as frequency decreases; some evidence of improved safety for lower frequencies [97]
Burst length	For burst lengths less than 10 ms, BBB disruption threshold increases and BBB disruption magnitude decreases as burst length is reduced [98,102,103,113]; little or no increase in disruption magnitude for longer bursts [93,102,114].
Pulse repetition frequency	BBB disruption magnitude increases as repetition frequency increases up to a point [102]. Other works have observed no effect on BBB disruption magnitude [98].
Ultrasound contrast agent dose	Magnitude of BBB disruption increases with dose [102,115–117] ; other experiments have reported no effect [98].
Sonication duration	Longer durations [96] or repeated sonication [105,118], increase magnitude of BBB disruption; damage reported with excessive sonication [96,105] .
Microbubble diameter	Threshold for BBB disruption lower for larger microbubbles; disruption magnitude increased with larger microbubbles [100,101,119] .
Ultrasound contrast agent	Similar outcomes reported for Optison [®] and Definity [®] microbubbles [120]. Sonovue [®] microbubbles and research agents are also commonly used.

1.8.3 Optimal Parameters for BBB

Overall, these studies have made it clear that BBB disruption is possible over a wide range of exposure parameters. Disruption has been demonstrated at frequencies between 28 kHz [121] and 8 MHz [113], burst lengths as low as a few ultrasound cycles [102,103,122] up to 100 ms [114], and over a range of pulse repetition frequencies, microbubble doses, and sonication times. It is not clear what the “optimal” parameters are, or what criteria to use to establish them. In our view, the primary consideration could be to find parameters that maximize the window in acoustic pressure amplitude where robust BBB disruption is possible without producing vascular damage. It will be challenging to precisely estimate the pressure amplitude in the human brain after transcranial sonication, and having the widest safety margin possible will be desirable for clinical translation. How close the FUS frequency is to the “resonant size” of the microbubbles may have an impact on the width of this safe window. Additional important criteria would be to optimize the frequency and transducer geometry to produce the desired focal spot size, to effectively focus through the skull with minimal distortion, and if a phased array transducer is used, to be able to steer the focal region throughout the brain. It may also

be desirable to find parameters that enable BBB disruption in the shortest possible sonication time so that multiple targets can be targeted in a reasonable amount of time, and to maintain a safe dose of microbubbles.

1.8.4 Potential Mechanisms

Even though FUS exposures combined with microbubbles have been investigated to disrupt the BBB in numerous studies, the exact mechanism to open BBB still remains unknown. It does appear that two known effects that can be induced by FUS, bulk heating and inertial cavitation, are not responsible. Initial studies on the method utilized MRI-based temperature imaging [114] during the sonications, and no measureable heating was observed. Studies that recorded the acoustic emissions during the sonications [123–125] have found that BBB disruption can be achieved without wideband acoustic emission, which is a signature for inertial cavitation [74]. It may not also be the same mechanism utilized for so-called “sonoporation”, where transient pores in cell membranes created by sonication with microbubbles enable drugs to enter [126]. Those pores are rapidly resolved, while FUS-induced BBB disruption lasts for several hours.

Fundamentally, one does not know if the FUS/microbubble interactions

physically modify the vessel walls, or if they are triggering a physiological response that includes temporary BBB breakdown. As described below, electron microscopy studies have shown delivery of tracers through widened tight junctions [90,127], which could be consistent with a direct physical force pulling them apart, as well as active transport [90,128]. Other work has shown the sonications can induce vascular spasm [129,130]. While the role of this spasm is not clear, it does make clear that the sonications can trigger a physiological response.

In the absence of bulk heating and inertial cavitation, mechanical effects induced during the microbubble oscillations in the ultrasound field are likely sources for the disruption. A number of effects are produced with potential to induce the observed BBB disruption. Microbubbles tend to move in the direction of the wave propagation via acoustic radiation force [131], which will bring them in contact with vessel endothelium. During oscillation, the shell of the microbubble can break, the bubbles can be fragmented into smaller bubbles, and they can grow via rectified diffusion. Microstreaming due to microbubble oscillations can induce biologically-significant shear stresses on the neighboring endothelium, and the oscillations produce inward forces that in extreme cases can pull the vessel wall inward [132].

Clearly, the behavior of a microbubble in an acoustic field is complex, and it can be different in free fluid than when constrained within a capillary [133].

1.8.5 Bioeffects Induced by FUS and Microbubbles

The BBB disruption occur almost immediately with sonication [130] and appears to decay exponentially over several hours thereafter [94,114,118,134]. The amount of agent delivered across the barrier appears to be much larger in grey matter than in white matter, presumably due to differences in vascular density [91]. Several studies have found that the barrier appears to be largely restored in approximately 4-6 hours [94,114,118,128,134,135]; other experiments have observed low-level disruption at 24 hours after sonication or longer [101]. The source of this discrepancy is not clear, but it could be simply that more sensitive detection methods such as high-field MRI combined with large doses of MRI contrast agent are capable of detecting low-level disruption missed in other works. The duration of the opening to different tracers appears to be reduced for larger tracers [134].

This window in time where the barrier is open is thought to be good for the prospect of delivering even long-circulating drugs, but not so long as to produce concern of toxicity arising from chronic BBB breakdown. Indeed, the appearance of

the brain after BBB disruption in light microscopy appears to be normal [136], even after repeated weekly sessions [91]. The only major feature that has been observed in many studies is the presence of tiny clusters of extravasated red blood cells (petechiae) [137,138]. It is thought that these petechiae are formed during inertial cavitation, and experiments where no wideband emissions (a signature for inertial cavitation) were observed, no such extravasations were observed [139]. Some have suggested that wideband emissions can be observed without producing such petechiae [140]. While the presence of these petechiae is undesirable, their impact on the brain may be minimal. Investigations looking for apoptosis or ischemia, which may be expected if serious vascular damage were occurring, failed to anything more than a few individual damaged neurons, and long-term effects have not found evidence of neuronal damage with such sonications [137,138,141]. However, as I show in section 4.1.2, this vascular damage might be exacerbated by a chemotherapy agent. At excessive exposure levels, more severe vascular damage, parenchymal damage, and neuronal loss can occur [114,142].

Transmission electron microscopy (TEM) investigations have demonstrated an increase of cytoplasmic vesicles in endothelium and pericytes (suggestive of

transcytosis), formation of trans-endothelial fenestrae, widened tight junctions, and transport of serum components across the BBB [90]. The use of a 44 kDa tracer molecule helped elucidate arterioles as the major site of trans-endothelial vesicle transport (followed by capillaries then venules), and showed extensive tracer deposition in the endothelial paracellular space, basement membrane, and surrounding brain parenchyma [128]. Finally, using immunogold labeling, the disappearance of tight junction (TJ) proteins occludin, claudin-5, and ZO-1 were shown, along with opened endothelial junctions and tracer leakage at 1-4 hours post-sonication [127]. The TJ proteins reappeared at 6 and 24 hours. Other work has shown down-regulation of the same TJ proteins along with their mRNA, and recovery to normal levels at 12 hours post-sonication [143]. Reorganization of connexin gap junction proteins have also been reported [144]. An increase of endothelial vesicles in normal [145] and tumor microvessels [146] have also been observed on TEM with an up-regulation of caveolin proteins/mRNA, suggesting that caveolae-mediated transcytosis (CMT) as a contributing mechanism for permeability. These researchers also found increased phosphorylation of Src and caveolin-1/2, noting that Src-induced phosphorylation of caveolins is a trigger for CMT [147].

Intracellular signaling cascades in response to mechanical stimulation by FUS-induced BBB disruption is likely, but has only recently been addressed. Increased phosphorylation of Akt and its downstream molecule GSK3 β has been shown in neurons flanking the BBB disruption at 24 hours, well after tight junction reassembly [148]. Akt phosphorylation has been implicated in neuroprotection after stroke [149], while activation of the p38 JNK MAP kinases promote neuronal apoptosis [150,151]. Alonso *et al.* showed increased protein ubiquitination in neurons not glia post sonication, no increase in heat shock proteins, and limited neuronal apoptosis at 24 hours in areas staining positive for extravasated albumin [152]. Ca²⁺ signaling has also been suggested as being stimulated by FUS-induced BBB disruption. Specifically, temporary disruption of the endothelial plasma membrane (i.e., sonoporation) can induce immediate transient changes of intracellular Ca²⁺ concentration in cells with direct contact with microbubbles, and delayed fluctuations in nearby cells [153]. When factoring in fluid shear induced in an *in vitro* flow channel (intended to mimic cerebral vessels), the membrane disruption and Ca²⁺ transients were much lower [154].

Multiphoton microscopy (MPM) has provided useful insights into the

bioeffects of FUS-induced BBB disruption. Initial work with this technique demonstrated arteriolar vasospasm in 14/16 mice lasting up to 5 minutes, and interrupted cerebral blood flow [129]. Although this could cause ischemic injury, it has been noted that mice have enhanced vasomotor excitability over other rodents, such as rats [155]. Indeed, a similar study in rats showed vasospasm in only 25% of the vessels examined [130]. Initial work has also noted two forms of vessel dye leakage, rapid focal microdisruptions (3-9 seconds) that were prevalent at vessel bifurcations, and slow disruptions that were observed as a gradual increase in extravascular signal intensity [156]. Subsequent work noted three rather than two leakage types: (1) fast, characterized by rapid increase to peak intensity and rapid decrease, (2) sustained, described as rapid increase to peak which persisted for up to an hour, and (3) slow, a gradual increase to peak intensity [130]. The authors noted that differing vessel calibers have preferences for different leakage types, and interestingly, that distinct peak negative pressures also show preference for leakage types. Continuing work suggested correlation between fast leakage, common with high pressure amplitudes, and detachment of astrocyte endfeet from the vessel walls [157].

1.8.6 Delivery of Imaging/Therapeutic Agents and Tests in Animal Disease Models

1.8.6.1 Delivery of Imaging Tracers

One advantage of this method for targeted drug delivery in the brain is that it appears to be “drug neutral” – that is, it appears that many agents with a wide range of properties can be successfully delivered across the BBB and/or the BTB. A large number of imaging tracers Table 1. 3 and therapeutic agents Table 1. 4 which normally do not cross the BBB have been delivered to the brain or to brain tumor models with FUS and microbubbles. The amount of substance delivered and the distance from the blood vessels that it penetrates appears to depend on its size. For example, less delivery of an albumin-bound MRI contrast agent (MW: ~67 kDa) was evident compared to a standard agent (MW: 928 Da) in a macaque [91]. This is even clearer in another study, where fluorescent Dextran with different molecular weights are delivered to the mouse hippocampus. For 3,000 Da Dextran, a relatively uniform fluorescence was observed; for the larger 70 kDa tracer, it was more concentrated near the blood vessels, and a 2000 kDa was found not to penetrate at all [158]. This result points to a need for close examination of how the delivery of large agents

occurs – it may not be enough to look for the presence of the agent, but to also investigate whether it is delivered far enough from the vasculature at a high enough concentration to reach the desired target at a therapeutic level. Low-resolution methods such as MRI may not be sufficient for this purpose. It may be possible, for example, for agents to make it past the endothelial cells but get trapped at the basement membrane [159].

Table 1. 3 Example different tracers that have been delivered across the BBB

Agent	Size	Use
Lanthanum chloride	139 Da	Electron microscopy tracer [127]
^{99m} Tc-Diethylenetriaminepentaacetic pentaacetate	492 Da	SPECT agent [160]
Omniscan [®] (Gd-DTPA-BMA)	574 Da	MRI contrast agent [101]
Magnevist [®] (Gd-DTPA)	928 Da	MRI contrast agent [114]
Trypan blue, Evans blue	~67 kDa	Tissue dyes (binds to albumin) [91,161]
Ablavar [®] (Gadofosveset trisodium)	~67 kDa	MRI contrast agent (binds to albumin) [91]
Horseradish peroxidase	40 kDa	Electron microscopy tracer [90]
Dextran	3-70 kDa	Fluorescent tracer [158]
Immunoglobulin G	~150 kDa	Endogenous antibodies [162]
pCMV-EGFP ¹	?	Plasmid DNA [163]
MION-47	20 nm	MRI contrast agent [141]
Gold nanoparticles	50 nm	Carrier for drugs or imaging [164]
Gold nanorods	10×40 nm	Photoacoustic imaging contrast agent [165]
Dotarem, P846, P792, P904, P03680	1-65 nm	MRI contrast agents [134]

1.8.6.2 Delivery of Therapeutics

A large number of therapeutic agents have also been delivered to the brain and to brain tumor models (Table 4). Many of the studies so far have investigated the delivery of chemotherapy agents, such as BCNU [166], doxorubicin [118], methotrexate [167], cytarabine [168], and temozolomide [169]. Enhanced delivery of chemotherapy packaged in liposomes [95,170], targeted liposomes [171] and magnetic particles [172–174], which allow for MRI-based tracking and enhanced delivery via magnetic targeting have also been demonstrated. Other works have shown Trastuzumab, an antibody-based agent used for HER2-positive breast cancer [175,176], and boronophenylalanine, which is used for boron neutron capture therapy, can be delivered to the brain and to brain tumor models [177,178]. FUS-induced BBB disruption has also been shown to improve the delivery of natural killer cells in a brain tumor model [179]. Finally, a number of experiments have loaded chemotherapy and other agents into the microbubbles used for the disruption [163,174,180–182], which offers the possibility of achieving even higher local payload at the targeted region. Delivering agents for neurodegenerative diseases, such as Alzheimer's, Huntington's, and Parkinson's disease, have also been an active

area of research by several groups. A number of therapies for neurodegenerative diseases such as neuroprotective agents [181,183] , antibodies [162,184], plasmid DNA [163], and siRNA [157] have all been successfully delivered across the BBB using FUS and microbubbles. Other investigations have shown that circulating neural progenitor cells [185] or viral vectors for gene therapy [186–188] can be delivered to the sonicated regions after FUS-induced BBB disruption.

1.8.6.3 Disease Models

While delivery of these agents is promising, one also needs to demonstrate that the amount of drug delivered – and the drug penetration – is sufficient to produce a therapeutic response. In some cases it is also important to demonstrate that the drug reaches the desired target and is active after it is delivered [183]. Several studies have shown that FUS enhancement of the BTB can slow tumor growth and/or improve survival in orthotopic murine models of primary or metastatic brain tumors [166,170,172,173,189–191] . While in some cases the response has been modest, several of these studies have seen substantial improvements. Using multiple treatments may be necessary to achieve a pronounced improvement [170]. One factor

that has not been investigated in depth so far is to confirm that drugs can successfully be delivered to infiltrating tumor cells, which are a major feature in glioma and other primary tumors, and to metastatic “seeds”. Both can be protected by the normal BBB. The orthotopic models investigated so far do generally not have large infiltrating zones, and the benefit observed in studies so far may have been primarily due to FUS-enhanced permeability of the BTB. It may be challenging to get therapeutic levels to distant regions that are protected by the BBB. Some agents may have neurotoxic effects on the normal brain that may limit this ability.

Beyond brain tumors, a study by Jordao *et al.* showed that delivery of antibodies targeted to amyloid plaques can reduce the plaque burden in Alzheimer’s disease model mice [192]. While the decrease was modest, with multiple treatment sessions this may be an effective treatment strategy. In an intriguing follow-up study, the same group recently showed that FUS-induced BBB disruption alone can reduce the size of the plaques, perhaps through the delivery of endogenous antibodies [193]. We anticipate that these studies are only the beginning, and that FUS has a large potential for Alzheimer’s disease and other neurodegenerative disorders. Issues regarding the feasibility and safety of disrupting the BBB in large brain regions (or

the whole brain – perhaps repeatedly) may be need further investigation, however.

Table1. 4 Example therapeutic agents that have been delivered across the BBB or BTB

Therapeutic Agent	Size	Use	Delivered to
Temozolomide	194 Da	Chemotherapy	Glioma model (9L)¹ [194]
1,3-bis(2-chloroethyl-1-nitrosourea (BCNU) ²	214 Da	Chemotherapy	Glioma model (C6) ¹ [180,195]
Cytarabine	243 Da	Chemotherapy	Normal brain [168]
Boronophenylalanine	330 Da	Agent for boron neutron capture therapy	Glioma models (GBM 8401 [177]; 9L [178])
Doxorubicin	540 Da	Chemotherapy	Normal brain [118]
Methotrexate	545 Da	Chemotherapy	Normal brain [167]
siRNA	~13 kDa	Huntington's disease therapy	Normal brain [157]
Glial cell line-derived neurotrophic factor (GDNF) ²	24 kDa	Neuroprotective agent	Normal brain [181]
Brain-derived neurotrophic factor (BDNF)	27 kDa	Neuroprotective agent	Normal brain ³ [183]
Herceptin (Trastuzumab)	148 kDa	Anti-cancer antibody	Normal brain [175]; Breast cancer brain met. model (BT474) ¹ [190]
BAM-10 A β targeted antibodies	~150 kDa	Therapeutic antibody for Alzheimer's Disease	TgCcrND8 Alzheimer's model mice ¹ [184]
BCNU-VEGF ²	~150 kDa	Antiangiogenic-targeted chemotherapy	Glioma model (C6) ¹ [182]
Plasmid DNA (pBDNF-EGFP) ²	~3600 kDa ⁴	Gene therapy	Normal brain [163]
Epirubicin in Magnetic nanoparticles	~12 nm	Magnetic targeted chemotherapy	Glioma model (C6) ¹ [196]
Doxorubicin in magnetic nanoparticles ²	~6-10 nm	Magnetic targeted chemotherapy	Glioma model (C6) [174]
BCNU in magnetic nanoparticles	~10-20 nm	Magnetic targeted chemotherapy	Glioma model (C6) ¹ [173]
Adeno-associated Virus (AAV)	~25 nm	Gene therapy vector	Normal brain [186–188]
Liposomal doxorubicin (Lipo-DOX)	90 nm	Chemotherapy	Normal brain [115]; Glioma model (9L) ¹ [170,191]
Interleukin-4 receptor targeted Lipo-DOX	100-120 nm	Chemotherapy	Glioma model (8401) [171]
Neural progenitor cells	7-10 μ m	Stem cell	Normal brain [185]
Natural killer cells (NK-92)	~10 μ m	Cell therapy for brain tumor	Breast cancer brain met. model (MDA-MB-231-HER2) [179]

¹ Also showed improved outcomes with FUS-induced BBB disruption;

² Used drug-loaded microbubbles;

³ Also showed drug activity after delivery;

⁴ Assumed 660 Da per base pair (bp), 760 bp for BDNF, and 4700 bp for pEGFP-N1

1.8.7 Treatment Planning, Monitoring and Evaluation

As described above, FUS-induced BBB disruption utilizes the mechanical interactions between microbubbles oscillating in the ultrasound field and the vasculature. These interactions critically depend on the exposure parameters as well as the vascular density and perhaps other properties of the vascular bed. The latter, can affect the local concentration of microbubbles, how they interact with the ultrasound field [133], and, more importantly, how much drug will be delivered to the brain [91]. Unfortunately, many of these parameters are difficult to predict and are expected to vary significantly across different patients and diseases. Thus, methods are needed to (i) determine what parameters to use (treatment planning), (ii) refine them during sonication to ensure BBB disruption without overexposure (treatment monitoring), and (iii) evaluate the treatment effects (treatment evaluation).

1.8.7.1 Treatment Planning

In most cases, experiments evaluating FUS-induced BBB disruption in animal models have used a fixed set of acoustic parameters determined from prior experience and simple, geometrically-focused transducers. In general, accurate targeting can be

achieved with such systems using stereotactic frames [197] if image-guidance is not available, and fairly repeatable results can be obtained with sonication through the thin skull in mice and rats, or in larger animals through a craniotomy. Methods to avoid standing waves [93] that take into account variations in skull thickness [198] can improve repeatability in small animal studies where transcranial sonication is used. Such approaches may be challenging to translate to human subjects, where the thicker skull is complex (a layer of trabecular bone surrounded by layers of cortical bone) and can vary substantially between individuals (3.5-9.5 mm) [199]. The skull, which has a substantially higher acoustic impedance than soft tissue, will reflect most of the ultrasound beam, and the amount transmitted will depend strongly on the angle between the bone and the face of the transducer [200]. Its irregular shape can also deflect and distort the beam, and reflections within the skull cavity need to be taken into account. To correct for beam-aberrations introduced by thick skulls, phased arrays composed of more than 1000 elements combined with skull aberration correction algorithms that utilize CT data are employed [78,79]. These arrays can also be programmed to rapidly steer the beam electronically to multiple targets enabling coverage of tissue volumes [91], and different portions of the array can be disabled to reduce internal reflections or exclude certain structures.

While these approaches that use acoustic simulations and CT scans are effective in restoring the focusing of the array after transmission through the skull, clinical experience with them for thermal ablation have shown that one still needs to correct for small errors (~1-2 mm) in targeting [81,82]. To achieve this correction, one needs to be able to visualize the focal region at exposure levels that do not induce damage or other unwanted effects. Currently, this can be achieved using MRI-based methods that can visualize low-level (1-2°C) focal heating [80,201] or map small tissue displacements of a few microns induced by radiation force [202]. Ensuring accurate targeting will be most important if one aims to precisely disrupt the BBB at discrete locations. In addition, since the strength of the total microbubble activity, as well as magnitude of the disruption will depend on the vascularity of the targeted tissue (gray vs. white matter, for example [91]), it will be important to know exactly where the target is located. It might also be desirable to avoid direct sonication on large blood vessels. If one is uncertain about the targeting of the focal region, it may be challenging to understand whether a poor or unexpected result is due to an incorrect exposure level or to mistargeting. Pre-treatment imaging delineating vascularity, perfusion, or other vascular properties may prove useful for planning the treatment. It may also be useful to combine these measurements with models of the

microbubble oscillations within the microvasculature [133,203].

Accurate control of the focal pressure is critical to ensure BBB disruption is produced while preventing inertial cavitation. The thick and complex human skull makes accurate focal pressure estimations extremely challenging. While the acoustic modeling methods developed for aberration correction may provide estimates of the focal pressure amplitude, it has not been validated to my knowledge. It may be possible to use the MRI-based methods mentioned above that can visualize focal displacements or heating to ensure a predictable focal pressure amplitude. Marty et al., for example, used MRI acoustic radiation force imaging to ensure a consistent exposure level between subjects in BBB disruption experiments in rats [134]. However, one needs to take the underlying tissue properties (which may be unknown for tumors or other abnormalities) into account or test it in proximal normal brain locations.

1.8.7.2 Treatment Monitoring and Control

Given the challenges in predicting the focal pressure amplitude when sonicating transcranially, it is anticipated that effective monitoring of the procedure will be important if this technology is to be translated to clinical use. At minimum,

such monitoring should provide an indication that the exposure level is sufficient to induce BBB disruption and alert the user if inertial cavitation is occurring. One could use MRI methods for this purpose. Contrast-enhanced imaging can be used to visualize when the disruption occurs, and T2*-weighted or susceptibility-weighted MRI can be used to detect petechiae produced by inertial cavitation [114,138]. These methods could be used now for control over the procedure in initial clinical tests of FUS-induced BBB disruption with experienced users. However, performing multiple MRI acquisitions would be time-consuming and may require to use excessive amounts of both US and MRI contrast agents, thus real-time and, perhaps, more direct methods are desirable for the prospect of widespread clinical implementation.

1.8.7.2.1 Acoustic Emission

Acoustic cavitation describes the oscillations of either vapour or gas filled cavities within a liquid. Acoustic emissions from the oscillating microbubbles offer a potential way to guide and monitor bubble activities during ultrasound exposure in biological tissue. Harmonic (nf_0 , $n = 1, 2, 3, \dots$, $f_0 =$ fundamental frequency) signal components can arise from different sources such as tissue, coupling media and microbubbles. Conversely, subharmonic ($f_0/2$) and ultraharmonic ($3f_0/2, 5f_0/2, \dots$)

emissions can arise only from bubble emissions and are indicators of stable cavitation [204]. Acoustic cavitation can be detected both actively and passively. Active techniques use a pulse echo transducer to monitor the region where cavitation is expected. If transient cavitation occurs the diagnostic pulse will reflect off of the generated bubble cloud and a change in the backscattered signal will be detected. The same technique can be used to detect changes in backscattered signal following the injection of microbubbles. Alternatively, a passive transducer can be used to monitor the field and record the signal following sonications from the active transducer [125].

The spectral content and strength of the recorded emissions is sufficient to characterize and subsequently control the microbubble oscillations. Inertial cavitation is manifested in the frequency domain of the acoustic emission as a broadband signal [74], and has generally been associated with the production of vascular damage during BBB disruption [123,125], although other studies have suggested that it can occur without damage [124]. Harmonic and/or sub- and ultra-harmonic acoustic emissions in the absence of broadband signal are indicative of stable volumetric oscillations, which consistently have been associated with safe BBB disruption [123–125]. Arvanitis et.al have explored the strength of the harmonic

emissions as a basis for such a controller, as they have found that one can reliably detect it before inertial cavitation occurs and that it is correlated with the magnitude of the BBB disruption measured via MRI contrast enhancement [123,125]. If one can integrate a large number of receivers into the FUS system, one can use passive reconstruction methods [205,206] to create two- or even three-dimensional maps of the microbubble activity to ensure that it is occurring at the expected location.

1.8.7.3 Treatment Evaluation

As described above, contrast-enhanced imaging and T2*- or susceptibility-weighted imaging can be used to verify that BBB disruption has occurred and whether significant vascular damage has occurred, respectively. For tumors, it may be necessary to compare the signal enhancement after contrast injection to measurements obtained before FUS. However, as I show in section 6.1.2, the permeability changes to a small molecule MRI contrast agent may be minimal for late stage tumors. Other imaging modalities may also be useful [207]. If the contrast-enhanced imaging is obtained before the therapeutic agent is injected, one can confirm that the BBB disruption is only occurring at the targeted locations before administering the drug, providing another level of control to ensure that drugs are delivered only to desired

regions.

Post-treatment imaging could be more useful if one could use it to estimate drug uptake and penetration in the brain tissue. This can be achieved directly by labeling the drug with a contrast agent for MRI or other modality [174]. It might also be possible to use a standard contrast agent as a surrogate measurement. A number of studies have related signal intensity changes of contrast-enhanced MRI at the end of the sonication with tissue drug concentrations [95,175,208]. More quantitative and repeatable techniques, such as estimating contrast agent concentrations via T1-mapping [134,209] or vascular transfer coefficients via analysis of dynamic contrast-enhanced MRI (DCE-MRI) [99] have been used to perform spatial and temporal characterization of BBB permeability. DCE-MRI can also predict the resulting payload of drugs [118] and in some cases in tumors [209]. I explored this method with a liposomal agent in section 1.9. If one understands the relationship between the concentrations of the therapeutic and the imaging contrast agent, which can perhaps be established in animals, one might be able to titrate the drug administration to achieve a desired level in the brain. However, this may be challenging in tumors, where the vascular permeability can change over time [209].

1.9 Dynamic Contrast Enhanced Magnetic Resonance Imaging

The technique of dynamic contrast enhanced magnetic resonance imaging (DCE-MRI), in which multiphase MRI scans are taken following the intravenous injection of a contrast agent. It has broadly been used in past studies to compute the permeability in applications such as embolic stroke, various types of cancer and injuries, both in humans [210–212] and animals [209,213–215].

1.9.1 Pharmacokinetic Analysis of DCE-MRI

There are many kinetic models; however, the Toft and Kermode (TK) model is usually used in clinical studies [216–218]. This model provides information about the influx forward volume transfer constant from plasma into the extravascular extracellular space (EES) and fractional volume of EES per unit volume of tissue.

1.9.1.1 *Tofts and Kermode (TK) Model*

The TK model is one of the popular compartment models, which assumes the equilibrium of contrast media between the plasma and the EES and the isodirectional permeability therefore, the equilibrium is described by

$$dC_t / dt = K_{trans} (C_p - C_t / v_e) \quad 1.17$$

where t is the time, C_t is the concentration of contrast media (CM) in tissue, C_p is the concentration of CM in plasma, K_{trans} is the influx forward volume transfer constant (into EES from plasma), and v_e is the fractional volume of EES per unit volume of tissue.

The original TK model (one-compartment, two parameter model) assumes the concentration of the CM is derived from the EES components and the plasma component is negligible:

$$C_t(t) = K_{trans} \int_0^t C_p(t') \exp\left[-\frac{K_{trans}(t-t')}{v_e}\right] dt'. \quad 1.18$$

The modified TK model (two-compartment, three parameter model) assumes the concentration of the CM is derived from the EES and plasma

$$C_t(t) = K_{trans} \int_0^t C_p(t') \exp\left[-\frac{K_{trans}(t-t')}{v_e}\right] dt' + v_p C_p(t), \quad 1.19$$

where v_e is the fractional volume of plasma per unit volume of tissue.

Substituting C_t and C_p in equation (1.19) variables (K_{trans} , v_p , v_e) can be estimated.

Patlak analysis was used to estimate K_{trans} and v_p which assumed the value of the exponential term is unity because either the back diffusion rate K_{trans}/v_e is small, $t-t'$ is small or both. Under this condition equation (1.19) becomes

$$C_i(t) = K_{trans} \int_0^t C_p(t') dt' + v_p C_p(t), \quad 1.20$$

Dividing entire equation by $C_p(t)$ gives a linear equation and its slope and intercept gives the value of K_{trans} and v_p , respectively. For this analysis the required value of C_t can be obtained from DCE-MRI. However, the relationship between the signal intensity (SI) and the concentration of the CM is not linear, so the conversion of the SI into the concentration of CM is needed. In our case, the agent Gd-DTPA (Magnevist, Gd-DTPA; Bayer Healthcare; 0.25 ml/kg) as a CM was used.

The Gd-DTPA concentration was estimated as a function of time at each image voxel with the following equation:

$$1/T_1 = 1/T_{10} + R_1 C \quad 1.21$$

where T_{10} is T_1 relaxation time before injection of Gd-DTPA, T_1 is T_1 relaxation times during the dynamic sequence (during and after injection of Gd-DTPA), R_1 is a constant (relaxation rate) of Gd-DTPA, which is $4.39 \text{ s}^{-1} \text{ mM}^{-1}$ [219] and C is the concentration of Gd-DTPA during the dynamic sequence. Maps of T_{10} were generated by fitting the signal intensity of a spoiled gradient echo (SPGR) sequence acquired at multiple flip angles as described elsewhere [220]. $T_1(t)$ was estimated using a SPGR sequence with the following expression:

$$\frac{1}{T_1(t)} = -\frac{1}{TR} * \log\left[\frac{1-A}{1-\cos\alpha * A}\right], \text{ where}$$

1. 22

$$A = \frac{1 - \exp\left(-\frac{TR}{T_{10}}\right)}{1 - \cos\alpha * \exp\left(-\frac{TR}{T_{10}}\right)} * \frac{S(t)}{S(0)}$$

where α and TR are the flip angle and repetition time of the SPGR sequence, respectively (more detail in chapter 1.13). S(t) is the signal intensity of the sequence as a function of time, and S(0) indicating the signal intensity before the contrast injection.

The concentration of Gd-DTPA in plasma Cp(t) can be written as Cp(t) = Cb(t) / (1-Hematocrit) where Cb(t) could be obtained by choosing a region of interest in a vascular unit (ophthalmic artery or transverse sinus) and value of hematocrit in rat was adjusted for a 45% capillary hematocrit level [220].

1.10 Magnetic Resonance Imaging

1.10.1 Basic Principles of MRI

In the presence of external magnetic field B₀ along z axis, a spin 1/2 nucleus can have one of two energy states Figure 1. 3 with corresponding energies [221]

$$E = -\mu_z B_0 = -m_I \hbar \gamma B_0 \quad 1. 23$$

where $m_l = \pm 1/2$ are the values of z-component of angular moment of the nucleus, γ is gyromagnetic ratio with a typical value for hydrogen nucleus is $2.675 \times 10^8 \text{ s}^{-1} \text{ tesla}^{-1}$, and $\hbar = 1.05 \times 10^{-34} \text{ J s}$ is the Dirac constant.

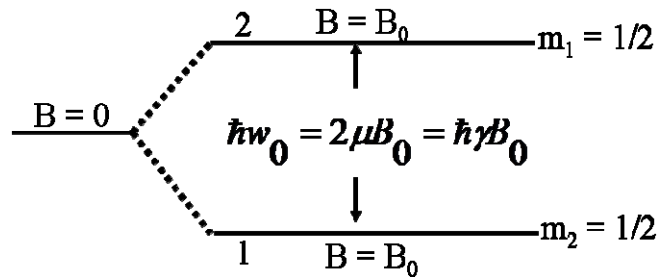


Figure1. 3 Energy level splitting of a nucleus of spin $I = 1/2$ in a static magnetic field B_0

The two energy levels of the spin $1/2$ nucleus depend on the relative orientation of spin with respect to applied magnetic field. The nuclei with parallel and anti-parallel spin orientations have low and high energies, respectively. The energy difference (ΔE) between two levels depend on the applied magnetic field as

$$\Delta E = \hbar\gamma B_0 \quad 1.24$$

The corresponding electromagnetic frequency $\nu = \gamma B_0$ is called Larmor frequency (42.6 MHz/Tesla) and at this frequency atomic nucleus precess in the magnetic field. The value of magnetization in the direction of the applied field (longitudinal magnetization) is the sum of z-component of the nuclear magnet within unit volume and at thermal equilibrium this can be obtained by using Boltzman statistics

$$M_0 = N(\hbar\gamma)^2 \left(\frac{B_0}{4kT} \right) \quad 1.25$$

where N is spin density. For MRI purpose, the most used spin 1/2 nuclus is hydrogen nucleus due to its abundance in animals. The magnetization due to the hydrogen nuclus is the source of signal in a MRI. For the detection of the magnetization, its direction is tilted away from B_0 by applying radio frequency signals with frequency equals to Larmor frequency. When RF pulses are applied, the nuclear magnets start to distribute equally over the two energy states and gain the phase coherence. The magnetization can be tilted completely in transverse direction (perpendicular to B_0) when the RF pulse is applied for long time. Immediately after RF pulse application, the spins start to return to thermal equilibrium and lose phase coherence. As a result the transverse magnetization (M_{\perp}) begins to decay exponentially as

$$M_{\perp}(t) = M_0 e^{-\frac{t}{T2}} \quad 1.26$$

where T2 is called the spin-spin relaxation time. In case of the inhomogeneous applied magnetic field, an additional decay in magnetization happened with time constant T2'. In this case overall time constant is called T2* relaxation which can be written as

$$\frac{1}{T2^*} = \frac{1}{T2} + \frac{1}{T2'} \quad 1.27$$

At the same time, the value of longitudinal magnetization (M_z) start to increase as

$$M_z(t) = M_0(1 - e^{-\frac{t}{T1}}) \quad 1.28$$

where T1 is called spin-lattice relaxation. The T1 and T2 relaxation times depend on the medium and are responsible for much of the tissue contrast exploited in standard MRI imaging sequences.

1.10.2 MRI Sequences

One of the most useful properties of MRI is to visualize the specific structure of biological tissue. The signal intensity depends on many parameters, including proton density, T1 and T2 relaxation times. Different pulse sequence parameters such as repetition time (TR) and echo time (TE) can vary with different biological tissues. TR is the time between two consecutive RF pulses measured in milliseconds. For a given type of nucleus in a given environment, TR determines the contributions to image contrast arising from the spin-lattice relaxation time T1. The longer the TR, the more the longitudinal magnetisation is recovered. Tissues with short T1 have greater signal intensity than tissues with a longer T1 at a given TR. A long TR allows more

magnetization to recover and thus reduces differences in the contribution of T1 to the image contrast. Signals with differing T1 values will therefore not be reduced in intensity to differing extents, giving rise to little or no T1-weighted contrast. TE is the time from the application of an RF pulse to the measurement of the MRI signal. TE determines how much decay of the transverse magnetisation is allowed to occur before the signal is read. It therefore controls the spin-spin relaxation time T2 and signal intensities in images will be weighted according to T2 values. The application of RF pulses at different TRs and the receiving of signals at different TEs produces variation in contrast in MRI images. A number of pulse sequences have been (and continue to be) developed. Here, we briefly discuss two basic sequences that illustrate the generation of T1-, T2- and T2*-weighted images. (1) The spin echo (SE) sequence is the most commonly used pulse sequence to create T1- and T2-weighted images. The sequence comprises two radiofrequency pulses - the 90 degree pulse that creates the detectable magnetisation and the 180 degree pulse that refocuses it at TE. The selection of TE and TR determines resulting image contrast. (2) Gradient echo (GRE) sequences can be generated by means of reversal of a pulsed field gradient, rather than by the introduction of a 180 degree pulse. Gradient echoes are commonly used in rapid imaging sequences; they generate T2*-weighted images.

1.11 Doxorubicin

Doxorubicin (molecular weight: 580Da) is a commonly-used anticancer drug for treatment of a wide range of cancers. Also known as Adriamycin, it is an anthracycline antibiotic derived from daunorubicin, which was isolated from the pigment producing bacteria *Streptomyces peucitis* [222]. Doxorubicin is active against leukemias and many solid tumours, including breast, endometrial, ovarian and bladder cancers, as well as adult and pediatric sarcomas, either alone or more commonly in combination with other drugs [223]. Typically administered as infusions of 50 mg/m² repeated every four weeks, the dose and frequency of administration are limited by acute myelosuppression, the occurrence of which is correlated with the integral of the plasma doxorubicin concentrations over time [224]. Figure 1. 4 shows that intratumoral Doxorubicin concentration is strongly correlated ($R^2 = 0.90$) with patient response rate, irrespective of the type of cancer [225]. However, it has not typically used for brain related diseases because it can not pass through the BBB. Walter et.al [226], showed that direct intratumoral infusion of Doxorubicin prolonged the survival time in glioma patients. It is believed that doxorubicin's antitumour effect is due to its localization in the nucleus of tumour cells where it binds to topoisomerase II and prevents resealing of the double helix during

DNA synthesis, leading to growth arrest and apoptotic cell death. This process also causes the unwanted death of normal cells.

In order to reduce the toxic effect, encapsulation of Doxorubicin within microscopic (~100 nm) phospholipids vesicles, known as liposomes, has been used. Liposomally encapsulated doxorubicin (Lipo-DOX) also prolongs the circulation time [227] in the vasculature. Due to these benefits, Lipo-DOX is commonly used in clinics instead of free doxorubicin.

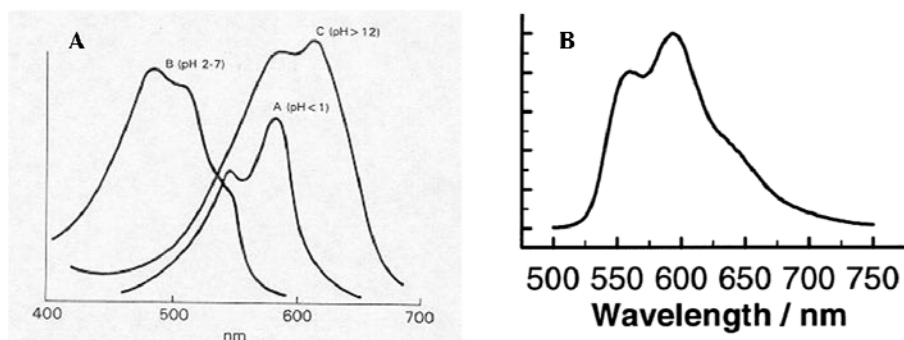


Figure1. 4 Fluorescence spectra for doxorubicin in aqueous solution. *A*, Absorption spectrum shows maximum absorption at 480 nm (curve *B*, pH 2-7) [228]. *B*, Emission spectrum with excitation at 479 nm shows maximum emission near 595 nm [229].

For quantification of Doxorubicin one can use optical spectroscopy since it has emission peaks at 554 nm and 585 nm when excited at wavelengths of 470-490

nm [228,229].

1.12 Scope of this Thesis

Prior research work demonstrated that FUS can enhance the delivery of Lipo-DOX in normal brain through the BBB using high frequency (1.6 MHz) ultrasound with a long exposure time [95]. In addition, a single treatment with FUS and Lipo-doxorubicin in glioma tumor model showed an improvement ~24% compared to untreated controls [115]. However, detailed quantification of the drug delivery through BBB and therapeutic efficacy of multiple treatments have not been studied. The overall objective of this thesis work was to investigate effect of low frequency (0.69 MHz) transcranial FUS (similar to that used clinically) on the permeability of the BBB/BBB, the pharmacokinetics of Lipo-DOX, and the therapeutic efficacy and safety profile of multiple treatments with FUS+Lipo-DOX in an animal model.

The first set of experiments were focused on the study of the distribution and quantification of Lipo-DOX and the released free doxorubicin, both on a macroscopic and a microscopic level. Here the doxorubicin concentrations after BBBB were compared for cases when the agent was administered before and after ultrasound. The findings of this study helped to establish the drug injection protocol to increase the

local penetration of Lipo-DOX across the BBB to achieve a high concentration of doxorubicin for subsequent drug delivery experiments.

In the second set of experiments using the developed protocol for drug injection, the effect of multiple sessions of FUS-induced BBB disruption with and without Lipo-DOX were compared in the normal rat. Variations in the acoustic power required to disrupt the BBB were established over three weeks to take into account the thickening of the skull as the rats grew. This safety study showed that FUS-BBBD can be used for treatment at multiple times based on histological evaluation, and it identified potential risks related to inertial cavitation.

Using the parameters established in the above safety study, the therapeutic efficacy of multiple treatment sessions with FUS-BBBD and Lipo-DOX was explored in the 9L rat glioma model. These treatments were compared to control animals and to animals who received treatments with FUS-BBBD or Lipo-DOX only. The impact of multiple treatments on tumor growth rates, survival times and histology were compared among these four groups.

The usefulness of MRI as a monitoring and feedback tool for the delivery of Lipo-DOX was explored by comparing the transfer coefficient K_{trans} for the MRI

contrast agent Gd-DTPA, which was measured using DCE-MRI, to the resulting doxorubicin concentration in the tumor. Moreover, acoustic monitoring of bubble activity during sonication was correlated with signal intensity of Gd-DTPA after sonication.

Overall, these results provide evidence that the multiple treatments with this ultrasound-enhanced drug delivery technique has a good potential to enable the effective use of Lipo-DOX for the treatment of brain tumor.

Chapter 2: Methods and Materials

2.1. Animals

The experiments performed in our laboratory were approved by our institutional animal committee. The test subjects used were male Sprague-Dawley rats (200-400 g) acquired from Charles River Laboratories (Boston, Massachusetts). In preparation for imaging, surgery or sonication, the rats were anesthetized by i.p. administration of ketamine (90 mg/kg) and xylazine (10 mg/kg) per hour, or as needed. The hair covering the dorsal surface of the skull was removed with depilatory lotion. For experiments requiring i.v. administration of contrast agents or chemotherapy, a 24-gauge catheter was inserted into the tail vein.

All animals were cared for in accordance with our institutional animal care policy. For animals in experiments of ultrasound-mediated drug delivery, animals were euthanized by transcardiac methods with normal saline 1-4 h after the last sonication. For animals which were implanted with glioma for the survival study, euthanasia of those exhibiting severely impaired activity or weight loss exceeding 20% within one week, tumor dimensions exceeding 10–11 mm, or if treatment-related severe adverse events occurred that caused pain or distress and that could not be

ameliorated. Euthanasia in these animals was conducted by transcardial perfusion with saline followed by 10% phosphate-buffered formalin while under deep anesthesia. The animals employed in the safety study that did not exhibit such poor outcomes were euthanized approximately seven weeks after the last treatment by transcardial perfusion with saline followed by 10% phosphate-buffered formalin while under deep anesthesia.

2.2 Ultrasound Transducer

For all experiments, the ultrasonic fields were generated by a single-element, spherically curved, air-backed piezoelectric (PZT-Lead zirconium titanate) transducer (manufactured in-house) with a diameter of 100 mm, radius of curvature of 80 mm, and resonant frequency of 0.690 MHz (Figure 2. 1). The electrical impedance of the transducer was matched to the output impedance of the amplifier by means of an inductor-capacitor circuit contained within an external matching box. The function generator, amplifier, power meter, and matching circuit were part of the MRI-compatible FUS system described below in section 2.1.3

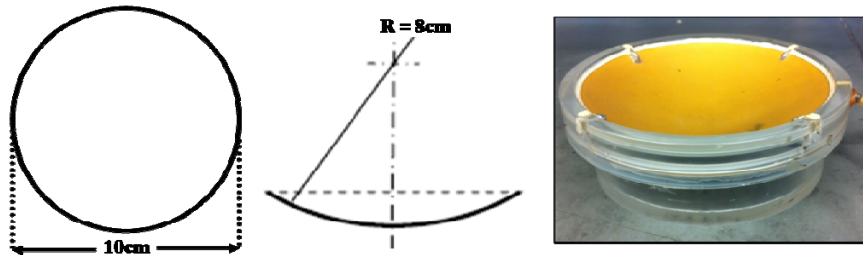


Figure 2. 1 A single-element, spherically curved, air-backed piezoelectric transducer with a diameter of 100 mm, radius of curvature of 80 mm, and resonant frequency of 0.690 MHz.

2.1.2.2 Transducer Characterization

Figure 2. 2 shows the characteristic beam plots of the 0.690 MHz transducer, which produced a ellipsoid focal spot with diameter and length of 2.3 mm and 12 mm, respectively, at half-maximum pressure amplitude. The plots were created by scanning a needle hydrophone (ONDA, Sunnyvale,CA) in a raster pattern perpendicular (top) and parallel (bottom) to the direction of the ultrasound beam.

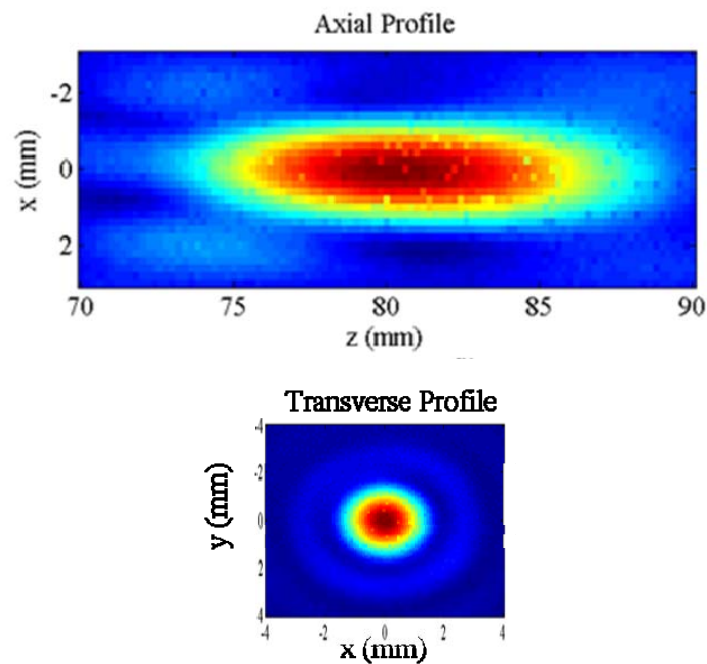


Figure 2. 2 Characteristic beam plots of the intensity for the 0.69 MHz transducer

2.1.2.3 Transducer Calibration

The transducer efficiency was measured using an acoustic radiation force balance system [51]. The system is based on the principle that an acoustic wave exerts a force F on an absorbing target that is proportional to the total ultrasonic power (P) intercepted by the target surface. The radiation force (F) is

$$F = \frac{DP}{v} \quad 2.1$$

where v is the propagation velocity of the wave in water and D is a constant that depends on the type of interaction between the target and beam. For a perfect absorber $D = 1$. If R is the radius of curvature of the transducer, L is the focal length, and the angle of incidence is zero degrees, then the force measured along the beam axis is

$$F = \left(\frac{P}{v}\right)\left(\frac{2L}{R}\right)^2[(R^2 + L^2)^{\frac{1}{2}} - L] \quad 2.2$$

The transducer was immersed in degassed, deionized water ($pO_2 < 1$ ppm) and driven at peak-to-peak voltages ranging from 0.01-0.09 V in 10 mV steps. A densely bristled brush was used as the absorbing target to encompass the complete acoustic beam emitted by the transducer. The brush was suspended in the water by a thin wires

attached to an electronic scale so that its face lay directly opposite the transducer. For each voltage, the acoustic power output of the transducer was calculated from the force exerted on the brush, which was measured by the change in weight of the absorbing brush. The output acoustic power was averaged over three measurements was divided by the input electrical power to compute the efficiency of the transducer (Table 2.1). Measurements made at the lowest applied voltage were disregarded.

Table 2. 1 Acoustic efficiency of air-backed single-element transducer. Frequency: 0.69 MHz; Radius of curvature: 80 mm; Diameter: 100 mm; F number: 0.8.

Applied Voltage (V)	Electrical Power (W)	Acoustic Power (W)	Efficiency (%)
0.01	0.025	0.0059	23
0.02	0.112	0.089	80
0.03	0.25	0.19	76.5
0.039	0.42	0.39	76.9
0.04	0.44	0.41	78
0.041	0.46	0.42	77
0.042	0.48	0.44	78.5
0.043	0.5	0.47	78
0.044	0.53	0.48	77.7
0.045	0.56	50	76
0.05	0.68	0.53	77.6
0.06	0.99	0.76	77.5
0.07	1.36	1.05	76.9
0.08	1.77	1.35	76
0.09	2.25	1.56	70.6

2.1.2.4 Estimated Pressure Amplitude in the Brain

Throughout this thesis, the reported exposure levels are absolute peak negative pressure amplitudes measured in water with a membrane hydrophone (Marconi; 0.5 mm diameter). Attenuation by the brain and rat skull is expected to reduce the pressure amplitude by ~30% at this frequency [198] with additional uncertainty arising from standing waves within the skull and increases in skull thickness as the animal ages [230].

2.3 Experimental Set-up

The sonication system was operated within a clinical 3T MRI scanner (Signa; GE Healthcare). The transducer was immersed in a small tank of degassed, deionized water and attached to an MRI-compatible, manually-operated positioning system (Figure 2. 3). The animal was laid supine on a tray above this tank, with a water bag providing an acoustic path to the dorsal surface of the head. The animal's body temperature was maintained with a heated water pad. Before treatment, the heating in a silicone phantom was visualized using temperature-sensitive MRI to localize the acoustic focal point in the MRI coordinate space.

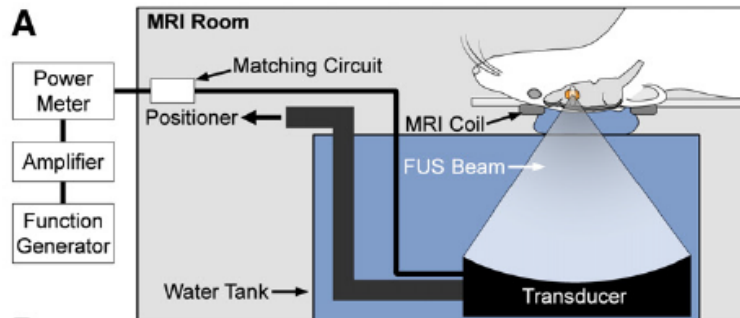


Figure 2. 3 Schematic of the MRI-guided FUS system. Inside the MRI magnet room, the transducer was mounted on a manual MRI-compatible 3-D positioning system and immersed in a water tank integrated into the MRI table. Outside the magnet room, a network consisting of a function generator, power amplifier, power meter, and dual directional coupler served to control the transducer. The animal was laid supine on a tray above this tank, with a water bag providing an acoustic path to the dorsal surface of the head.

2.4 Magnetic Resonance Imaging

The experimental set-up shown in Figure 2-3 was integrated into the table of a 3-Tesla clinical MRI scanner (Signa; General Electric Healthcare) for image guidance and evaluation. Each animal was placed on the table in the supine position with the dorsal surface of the head centered on a 7.5-cm-diameter transmit/receive surface coil (constructed in-house).

For all BBB disruption experiments, two-dimensional T2-weighted fast spin-echo (FSE) images were acquired in three orthogonal planes to plan the sonications (parameters: repetition time (TR): 2000 ms; echo time (TE): 79.7 ms; echo train

length (ETL): 8; matrix size: 256×256; slice thickness/spacing: 1 mm/interleaved; field of view (FOV): 8 cm; number of excitations/averages (NEX): 2; bandwidth: 15.63 kHz). The target site for BBB disruption was identified on the MR images and the transducer repositioned accordingly. Sonications were performed through the opening of the surface coil, which was filled with a plastic bag [poly(vinyl chloride), thickness ~75 μm] containing degassed water. After ultrasound-mediated BBB disruption was completed, a bolus of gadopentatate dimeglumine (Gd-DTPA) MRI contrast agent (Magnevist; Berlex Laboratories, Wayne, NJ; 0.125 mmol/kg; 0.25 mL/kg; molecular weight: 938 Da) was injected into the tail vein and T1-weighted fast spin-echo (FSE) images (repetition/echo time (TR/TE): 500/17 ms; echo train length (ETL): 4; matrix size: 256 x 256; slice thickness: 1 mm; field of view (FOV): 8 cm; number of excitations (NEX): 2; flip angle (FA): 90 degrees) brain were acquired in three orthogonal planes to confirm BBB permeabilization. Axial three-dimensional T2*-weighted fast spoiled gradient echo images were also acquired (TR/TE: 33.3/19 ms; matrix size: 256×256×28; slice thickness: 0.8 mm; FOV: 8 cm; NEX: 1; flip angle: 15°; bandwidth: 15.63 kHz). These images are sensitive to small susceptibility changes and were used for detecting iron-containing petechiae caused by excessive FUS [114] and hemorrhagic regions within the tumor and additional images were

acquired as needed.

2.5 Fluorometry

A benchtop cuvette fluorometer (VersaFluor; Bio-Rad Laboratories, Hercules, California) with changeable filters was used to quantify doxorubicin accumulation in brain tissue. Because doxorubicin absorbs the most light between approximately 473 nm and 494 nm and emits maximal fluorescent light at about 590 nm [229,231], fluorescence measurements were performed using filters with excitation and emission wavelengths of 480 ± 10 nm and 590 ± 5 nm, respectively.

To calibrate the fluorometer for doxorubicin quantification, a serial dilution of doxorubicin in acidified alcohol was used to measure the fluorescent signal of the extracted supernatant. The gain of the VersaFluor fluorometer was set to medium for doxorubicin concentrations of 100-1000 ng/mL. For lower doxorubicin concentrations of 10-100 ng/mL, the fluorometer was not sensitive enough to differentiate small differences in concentration using medium gain, so the gain was set to high. For each experiment, a freshly prepared solution of acidified alcohol was used as a "blank" to zero the fluorometer. Figure 2. 4 shows the calibration curves used to convert the fluorometric readings to doxorubicin concentration.

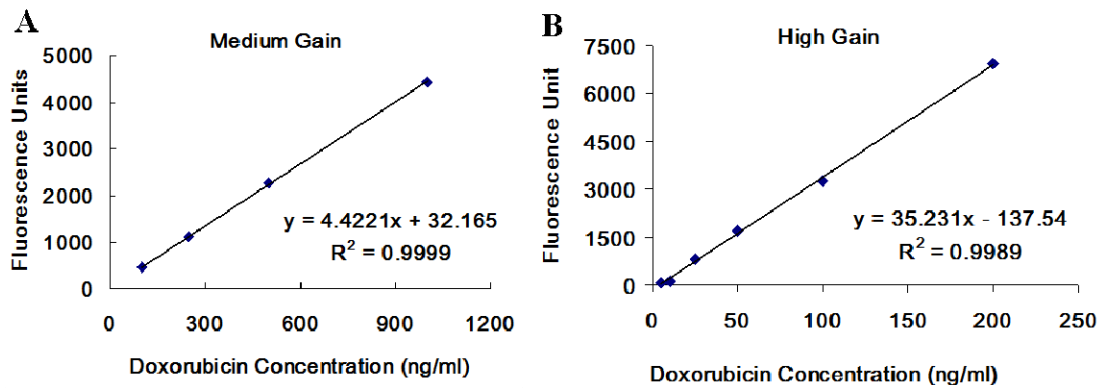


Figure 2. 4 Calibration curves for fluorometric measurements of doxorubicin concentration showing a strong linear correlation between the arbitrary fluorometric units and the doxorubicin concentration for medium gain ($R^2 = 0.99$) in A and high gain ($R^2 = 0.99$) in B. The calibration coefficients were obtained after forcing each linear fit through zero.

2.6 Targeted Doxorubicin Delivery through Blood Brain and Blood Tumor Barrier using Transcranial MRI-guided Focused Ultrasound

The first step towards developing a protocol for targeted drug delivery across the BBB/BTB in a standard pre-clinical rodent model was the modification of the ultrasound parameters needed to achieve reproducible, localized BBB/BTB disruption in rats. Although ultrasound is strongly attenuated in bone, past studies had shown that the skull of the rat is thin enough to permit the focusing of the ultrasound beam

sufficient to induce localized BBB opening [Refs].

2.6.1 Sonications

Energy was delivered in pulsed sonications with burst length of 10 ms and pulse repetition frequency of 1 Hz (i.e., 10 ms ON followed by 990 ms OFF; duty cycle: 1%) for 60 s. Each sonication was accompanied by a bolus of a microbubble-based ultrasonic contrast agent (Definity, Lantheus Medical Imaging; N. Billerica, MA) 0.01 mL/kg) into the tail vein catheter. Each mL of Definity contains a maximum of 1.2×10^{10} microbubbles, which are composed of octafluoropropane gas-filled lipid shells with a mean diameter of $1.1\text{-}3.3 \times 10^{-6}$ m. The administration of 0.01 mL/kg Definity was as a bolus approximately 9 s before sonication, followed by a 0.2 mL saline flush. To facilitate the injections of such a small volume, the Definity was diluted to 0.1× normal concentration in phosphate buffered saline (PBS). Multiple sonications in an individual rat were spaced 3-5 min apart to allow time for vascular clearance of most of the Definity, which has a pulmonary elimination half-life of 1.9 min in humans.

The pressure amplitude 0.4 MPa was initially set based on a prior study in rats with this device [232] for BBB disruption. The range from 0.55 to 0.81 MPa based

on empirical observations on the exposure level needed to achieve a consistent level of BBB disruption as the age and weight of the animals increased. This observation was made in our initial treatments and is similar to previous reports that demonstrated that the skull becomes thicker as the animal ages [198].

Once the parameters for consistent BBB disruption by transcranial sonication were modified as needed, the technique to aid in the targeted delivery of Lipo-DOX in the rat brain was adapted. In the first set of experiment, the central aim was to develop a drug injection protocol for ultrasound-mediated BBB disruption which would allow Lipo-DOX to accumulate at sufficient levels in the normal in rat brain to have a therapeutic effect and in the second set, to visualize and quantify the resulting doxorubicin distribution at the focal plane.

2.6.2 Chemotherapy

In our experiments, a chemotherapy agent was administered intravenously. Doxorubicin hydrochloride encapsulated in long-circulating pegylated liposomes (Dox-NP; Avanti POLAR LIPIDS, INC., Alabaster, AL; 5.67 mg/kg, Half life in plasma: 2-3 days) was selected for targeted delivery through the blood-brain barrier. In this form, greater than 90% of the drug is encapsulated within the liposomes. Once

the liposomes pass from the vascular compartment to the parenchyma, the liposome is degraded by endogenous enzymatic processes, and the encapsulated doxorubicin is released in the tissue. In the first set of experiments, a drug injection protocol which would deliver a therapeutic level of Lipo-DOX through the BBB was sought to be identified.

2.6.3 Effect of Drug Injection Protocol on Doxorubicin Delivery to the Brain

The experimental set-up of the first study was used. A peak negative pressure amplitude of 0.55 MPa was used to provide BBB disruption to deliver Lipo-DOX to the brain. The sonications were delivered at 3-5 min intervals in a grid pattern (spacing: 1-1.5 mm) to 9 targets.

In the first set, the rats were assigned in two groups: (A) Lipo-DOX injection before FUS (N = 5), (B) Lipo-DOX injection after FUS (N = 4). For the animals in group A, both hemispheres were sonicated. A full dose of Lipo-DOX (5.67 mg/kg) was divided into a 9 fractions in the first sonicated hemisphere; one fraction was administered before each sonication in this hemisphere. Since Lipo-DOX has such a long circulation time, we assumed that a full dose was already in the circulatory

system of the subject, so we did not administer any additional drug before sonication in the contralateral hemisphere. For the animals in group B, only one hemisphere was sonicated and the other hemisphere served as a control. A full dose of Lipo-DOX was administered 10 minute after the sonications.

2.6.3.1 Fluorometric Assay

Trypan blue (Aldrich Chemical Company, Inc. Milwaukee, WI, USA; 2.5ml/kg) was administered through the tail vein after the completion of the sonications and imaging to further confirm successful BBB disruption and to mark the target site of sonication for tissue harvesting. Each animal was put into a state of deep anesthesia with an overdose of ketamine and xylazine. To flush unabsorbed Lipo-DOX from the cerebral vasculature, the brain was perfused by transcardiac methods with normal saline 4 h after the last sonication. The site of BBB disruption, identifiable by its trypan blue stain, was harvested along with nonsonicated control tissue. The concentration of Lipo-DOX of each tissue sample was determined by taking the average of at least three fluorometric readings on a benchtop fluorometer.

2.6.3.2 *Extraction and Quantification of Doxorubicin*

A preparation of acidified alcohol (0.3 N HCl in 50% EtOH) was used to extract doxorubicin from harvested tissue samples for fluorometric quantification [233]. For these minute samples, the tissue density was assumed to be approximately 1 g/cm³. Thus, the mass of each sample was equal to its volume. The mass of each sample was measured and cut down until was approximately 30 mg. Each sample was put into a 1.5-mL centrifuge tube with 20 volumes (400-500 μ L) of acidified alcohol, then homogenized with a tissue blender (Next Advance, Averill Park, NY), refrigerated for 24 hours at 4°C. Samples were then centrifuged at 16,000 \times g for 25 min. at 4°C. The supernatant was extracted for immediate fluorometric reading using a benchtop fluorometer (VersaFluor; Bio-Rad Laboratories, Hercules, CA; Ex/Em: 480/590 nm) or stored at -80°C.

2.6.3.3 *Statistical Analysis*

Sonicated and contralateral control paired samples were compared using a two-tailed paired student's t-test. Values of $p < 0.05$ were considered statistically significant. Additional analyses included least-squares linear regression and calculation of correlation coefficients.

2.6.4 Fluorescence Imaging

In the second set of experiments, a fluorescent microscope was used to visualize the distribution of doxorubicin in the brain after treatment with ultrasound-induced focal BBB/BTB disruption and intravenous Lipo-DOX administration. Doxorubicin has excitation maximum of 480 nm and emission maximum at 590 nm respectively. Fluorescence images were acquired using a fluorescent microscope Observer.Z1 with the X-Cite 120Q series light source and a AxioCam MRm mounted camera (Zeiss, Germany) with 10× objective, 1.6x optovar, and a 500 ms exposure time. High resolution images of different tissue sections were obtained in tiles using a motorized stage so that the distribution of doxorubicin was obtained for the entire tissue section.

2.6.4.1 Tissue Preparation

The rat brain was flash frozen in dry ice with 2-methylbutane (Fisher, Pittsburgh PA). For tissue sectioning, the frozen rat brain was mounted with a minimal amount of optimal cutting medium (OCT) compound (the owner of the cryostat did not want OCT to come into contact with the cryotome blade), and sectioned at a 20µm thickness using a Microm HM550 cryostat (Mikron Instruments

Inc, Vista, CA). The specimen temperature was set at -19°C and the chamber temperature at -20°C. Tissue sections were thaw-mounted on microscope glass slides (Fisher, Pittsburgh PA) for fluorescence imaging.

2.7 Multiple Sessions of Liposomal Doxorubicin and Ultrasound-Mediated Blood-Brain Barrier Disruption: A Safety Study in the Rat Brain

After the identification of the Lipo-DOX injection protocol that could deliver a therapeutic level of Lipo-DOX through the BBB and showed the doxorubicin distribution in the sonicated area with fluorescence microscope, the safety profile of this delivery was investigated in normal rat brain.

2.7.1 Study Design

Lipo-DOX (5.67mg/kg) was administered intravenously. That dosage was selected on the basis of prior work testing this agent in rats [234]. Nine rats were assigned to one of two groups: (1) three weekly treatments with FUS and concurrent chemotherapy (FUS+Lipo-DOX) (N=5), (2) three weekly treatments with FUS only (N=4). After determining the coordinates of the focal point within the MRI space, treatment planning MRI was acquired, and the focal region was positioned so its center was 2 mm lateral to the midline and 4 mm deep from the dorsal brain surface.

They were centered 2.5 mm anterior to the bregma in the striatum. The striatum was of interest because that was the place where 9L-rat glioma tumors were grown and treated [170]. Sonications (0.69 MHz; 0.55-0.81 MPa; 10 ms bursts; 1 Hz PRF; 60s duration) were performed in a grid pattern at 5, 9, and 12 targets, respectively. Before each sonication, ultrasonic contrast agent (Definity, Lantheus Medical Imaging; 0.01 mL/kg) was administered intravenously. To facilitate the injections of such a small volume, the agent was diluted to 0.1× normal concentration in PBS. It was injected as a bolus approximately 9 s before each sonication, followed by a 0.2 mL saline flush. Lipo-DOX was administered intravenously over multiple slow injections just before each sonication.

2.7.2 Magnetic Resonance Imaging

MRI was used to evaluate and monitor treatment effects. T2-weighted imaging was used to plan the treatments. BBB disruption was evaluated using T1-weighted imaging acquired before and after administration of the MRI contrast agent gadopentatate dimeglumine (Magnevist Gd-DTPA; Bayer Healthcare; 0.25 mL/kg). T2*-weighted imaging was used to confirm that petechiae, which are produced by excessive FUS exposures, did not occur [114].

2.7.3 Histology

All of the animals from FUS-Only and FUS+Lipo-DOX were sacrificed seventy days from the first treatment to evaluate the histological effects. The animal was deeply anesthetized with ketamine/xylazine, sacrificed, and the brain fixed via transcardial perfusion (0.9% NaCl, 100 mL; 10% buffered formalin phosphate, 250 mL). The brain was then removed, embedded in paraffin, and serially sectioned at 5 μm sections in the axial plane (perpendicular to the direction of ultrasound beam propagation). Every 50th section (250 μm apart) was stained with hematoxylin and eosin (H&E). The author who evaluated the histology was blind to the FUS exposure parameters.

2.8 Multiple Treatments with Liposomal Doxorubicin and Ultrasound-Induced Disruption of Blood-Tumor and Blood-Brain Barriers Improve Outcomes in a Rat Glioma Model

The therapeutic efficacy of the technique was investigated in rats with implanted aggressive glioma using the same parameters used in the experiments where the safety profile for multiple treatments with FUS only and FUS + doxorubicin were investigated. The following steps were involved in this work.

2.8.1 Cell Culture

9L rat gliosarcoma cells (passage number 3, obtained from the Neurosurgery Tissue Bank at University of California-San Francisco) were grown in Minimum Essential Medium (1×) with Earle's salts, supplemented with 10% fetal bovine serum, 1% L-glutamine, 1% MEM nonessential amino acids, and 0.1% gentamicin in a 5% CO₂ chamber held at 37°C.

2.8.2 Tumor Implantation

In the anesthetized rat, the dorsal surface of the skull was sterilized with an iodine swab. A 5-mm skin incision was made and a 1-mm burr hole was drilled into the skull approximately 1 mm anterior to the bregma and 2 mm lateral to the midline. A 4 µl volume of cell suspension (1×10^5 cells) was injected into the right caudate putamen at a depth of 3.5 mm relative to the dural surface using a 10 µl gas-tight syringe (Hamilton). The cells were injected over a period of 5 min. Two min later, the needle was retracted slowly over another 5 min, and the skin was closed with 5-0 silk sutures (Ethicon, Somerville, New Jersey). The rat recovered from anesthesia under observation. Each animal was given a one-time dose of antibiotic (Baytril, 2.5 mg/kg; Bayer HealthCare, Wayne, New Jersey) and analgesic (Buprenex, 0.05 mg/kg; Reckitt

Benckiser Healthcare, Hull, England, UK) every 12 h for 24 h following surgery by i.p. administration. The sutures were removed 5 days later, and treatment began on day 7 or 8, at which point the tumor had an MRI-evident diameter between 1 and 3 mm.

2.8.3 Study Design

The rats were randomly assigned to one of four groups: (1) no treatment (Control) (N=7), (2) three weekly treatments with FUS-induced BBB/BTB permeabilization (FUS-Only) (N=8), (3) three weekly treatments with liposomal doxorubicin (Lipo-DOX-Only) (N=6), and (4) three weekly treatments with FUS and concurrent chemotherapy (FUS+Lipo-DOX) (N=8). The animals were monitored regularly to evaluate the treatment effects on survival and tumor growth. Animals surviving 6 weeks after treatment were considered long-term survivors. However, some were followed for longer periods for later histological examination, as they appeared healthy. The animals were euthanized if they exhibited severely impaired activity, weight loss exceeding 20% within one week, tumor dimensions exceeding 10–11 mm, or if treatment-related severe adverse events occurred that caused pain or distress and that could not be ameliorated. The animals were euthanized via

transcardial perfusion with saline followed by 10% phosphate-buffered formalin while under deep anesthesia. The brain was removed and immersed in 10% phosphate-buffered formalin for histological preparation. To avoid skin infections that were observed in two animals (Table 5. 1), animals receiving FUS and chemotherapy were treated with an antibiotic Baytril (Bayer; 2.5 mg/kg).

2.8.4 Sonication

Animals in group 2 (FUS only) and 4 (FUS+Lipo-DOX) were provided treatment with microbubble-enhanced MRI-guided FUS. After determining the coordinates of the focal point within the MRI space, treatment planning MRI was acquired, and the focal region was positioned within the tumor. Sonication parameters were the same as in the safety study and consisted of multiple points in and around the tumor combined with microbubbles. The sonications were delivered at 5 min intervals in a grid pattern (spacing: 1 or 1.5 mm, depending on tumor volume) to 5-20 targets, with the number of locations increasing over the three weeks as the tumor volume increased. The central aim was to permeabilize the BTB in the entire tumor and the BBB in a surrounding rim of at least 1 mm.

2.8.5 Chemotherapy

Animals in group 3 (Lipo-DOX Only) and 4 (FUS+Lipo-DOX) were administered chemotherapy. For chemotherapy, 5.67 mg/kg of Lipo-DOX was administered intravenously. In initial experiments (5 rats in Lipo-DOX Only group; 5 in FUS + Lipo-DOX group), DOXIL (Centocor Ortho-Biotech) was used. Due to a current national shortage of this agent that occurred during these experiments, Lipo-Dox (TTY Biopharm) was used for the remaining animals (1 rat in the Dox-Only group; 3 in the FUS+Lipo-DOX group). For the FUS+Lipo-DOX group, chemotherapy was administered over multiple slow injections administered just before each sonication. For the Lipo-DOX Only group, the agent was administered over 5 slow injections at 5 min intervals. This scheme was adopted from chapter 2.6.3. Each injection was followed by a 0.2 mL saline flush.

2.8.6 Magnetic Resonance Imaging

T2-Weighted imaging was used to plan the treatments and measure tumor volumes. BBB/BTB disruption was evaluated using T1-weighted imaging acquired before and after administration of the MRI contrast agent gadopentatate dimeglumine (Magnevist Gd-DTPA; Bayer Healthcare; 0.25 mL/kg). T2*-Weighted imaging was

used to investigate whether petechiae, which are produced by excessive FUS exposures, did not occur [114] and to evaluate hemorrhagic regions in the tumors.

2.8.7 Image Analysis

Non-contrast MRI imaging was performed weekly ($\pm 1-3$ days depending on MRI availability). Tumor boundaries were manually segmented in axial T2-weighted images using ImageJ; the volume was calculated by the sum of the areas multiplied by the image thickness. In weeks 1-2, the tumors appeared as clearly circumscribed volumes, which were sometimes surrounded by hyperintense regions (presumably edema). These boundaries were sometimes not evident at later times in the FUS+Lipo-DOX group, and it was not clear whether MRI abnormalities were residual/recurring tumor or treatment-related effects. To be conservative, such cases were included in the volume calculations.

2.8.8 Histology

Representative examples from the Control (4/7 animals) and FUS-Only (5/8 animals) groups were selected for histological examination. The treatment response varied for animals in the Lipo-DOX Only and FUS+Lipo-DOX groups (see Table 5.

1) and all brains from these animals were examined. Tissue blocks containing the tumor were embedded in paraffin and cut into 4–6 μm serial sections perpendicular to the direction of ultrasound propagation. Sections with the largest evident tumor were stained with H&E for examination in light microscopy.

2.8.9 Statistical Analysis

Tumor volumes for the four groups were compared using one-way ANOVA. The Kaplan–Meier method was used to compare survival of animals in each group. Significance was calculated by using log-rank test with Yates' correction. These analyses were performed using Matlab (MathWorks) and Microsoft Excel. The Bonferroni method was used to compare multiple pairs of groups [235]. With four treatment groups (including controls) and with six possible paired comparisons, pair-wise P values less than the Bonferroni-corrected threshold of $0.05/6 = 0.0083$ were considered statistically significant.

2.9 Enhancement in Blood-Tumor Barrier Permeability and Delivery of Liposomal Doxorubicin using Focused Ultrasound and Microbubbles: Evaluation during Tumor Progression in a Rat Glioma Model

After the therapeutic efficacy of the technique was investigated in a rat glioma

model, DCE-MRI was used to characterize the FUS-induced permeability changes of the BBB/BTB at different times after implantation, and these changes were related to the doxorubicin concentrations.

2.9.1 Bilateral Tumor Implantation

The previously described techniques for tumor cell implantation were adopted for a bilateral tumor model where 9L rat gliosarcoma cells were injected into both the right and left caudate putamen at a depth of 3.5 mm relative to the dural surface. Tumors on both hemispheres were observed in MRI on day 7 or 8. Animals were included in the study if the tumors on both hemispheres were approximately the same size: a diameter between 1-3 mm on day 7 or 8. The animals were euthanized if they exhibited severely impaired activity, weight loss exceeding 20% within one week, or tumor dimensions exceeding 10-11 mm.

2.9.2 Study Design

The rats were randomly assigned to one of three groups where FUS was applied on day 9, day 14, or day 17 after implantation (N=5 for each group). After determining the coordinates of the focal point within the MRI space, the focal region

was positioned in the tumor in the right hemisphere. The nonsonicated left tumors served as controls. Ultrasound bursts were then applied at multiple points in and around the tumor at pressures amplitudes ranging from 0.55-0.81 MPa (burst length: 10 ms, pulse repetition frequency: 1 Hz, duration: 60 s). Before each sonication, ultrasonic contrast agent (Definity, Lantheus Medical Imaging; 0.01 mL/kg) was administered intravenously. To facilitate the injections of such a small volume, the agent was diluted to 0.1× normal concentration in PBS. It was injected as a bolus approximately 9 s before each sonication, followed by a 0.2 mL saline flush. The sonications were delivered at 5 min intervals in a grid pattern (spacing: 1.5 mm) to 5-20 targets, depending on the tumor volume. The goal was to permeabilize the BTB in the entire tumor and the BBB in a surrounding rim of at least 1 mm. For drug delivery, 5.67 mg/kg of Lipo-DOX was administered in fractions over multiple slow injections intravenously just before each sonication. Each injection was followed by a 0.2 mL saline flush.

2.9.3 Magnetic Resonance Imaging

T2, T1-contrast and T2* weighted images were obtained as described above. In addition, DCE-MRI was performed before and after the sonications. For T1-mapping,

a spoiled gradient echo (SPGR) sequence (TR/TE: 9.9/4.8 ms; matrix size: 256×256; slice thickness: 2 mm; FOV: 8 cm; Scan time for each flip angle: 15.3s; bandwidth: 31.25 kHz) acquired at multiple flip angles (30/20/15/10/2°). For the DCE imaging, eight pre-contrast sets of SPGR images (TR/TE: 9.9/4.8 ms; matrix size: 256×256; slice thickness: 2 mm; FOV: 8 cm; Scan time: 534.6s flip angle: 35°; bandwidth: 31.25 kHz) were acquired. Then, a bolus of Gd-DTPA (2x 0.25 mL/kg) was administered I.V. and an additional 62 sets of SPGR images were acquired with a temporal resolution of 7.6 s for 8 min. A double dose of Gd-DTPA was used in order to secure the presence of a bolus peak in the vascular system to determine the arterial input function (AIF) and to obtain accurate tissue concentrations [236]. Identical slice locations were used for T1 mapping and DCE-MRI. These measurements were made before and after FUS-BBBD in the right tumor. The time interval between measurements was at least an hour to avoid excessive Gd-DTPA accumulation.

2.9.4 Fluorometric Assay and Doxorubicin Extraction

After the completion of the sonication and imaging session, Trypan Blue was administered through the tail vein to mark the regions where the BBB was disrupted and to improve visualization of the tumors. Animals were deeply anaesthetized with

ketamine/xylazine and euthanized about two hours after the last sonication. After transcardial perfusion with normal saline (0.9% NaCl, 250 mL) to flush unabsorbed doxorubicin from the cerebral vasculature, the brain was removed. Small tissue volumes (approximately 30 mg) from both tumor sites which were identified by its trypan blue stain were harvested. Samples were homogenized in a tissue blender with acidified ethanol (50% ethanol in 0.3 N HCl), refrigerated for 24 hours at 4°C, and centrifuged at 16,000×g for 25 min. at 4°C. The concentration in each tissue sample was determined by taking the average of at least of three readings.

2.9.5 Data Analysis

Tumor boundaries were manually segmented in axial T2-weighted images using ImageJ; the volume was calculated by the sum of the areas multiplied by the image thickness. On day 9, 14 and 17, the tumors appeared as clearly circumscribed volumes, which were sometimes surrounded by hyperintense regions (presumably edema). The TOPPCAT software package [220] was used to calculate maps of the coefficient K_{trans} that describes transport of Gd-DTPA across the BBB/BTB, and the vascular volume fraction, f_v . The entire tumor was manually segmented in these maps in Matlab (MathWorks), and the mean value was calculated. Rats that had regions

within either tumor with little or no signal enhancement after Gd-DTPA administration were excluded, as these regions were assumed to be necrotic.

2.9.6 Statistical Analysis

Tumor volumes, measurements of K_{trans} and f_v , and doxorubicin concentrations for the sonicated and non-sonicated tumors were compared using unpaired, two-tailed t-tests. Comparisons of K_{trans} and f_v before and after sonication were made using a paired t-test. Other analysis included linear least-squares regression and calculation of correlation coefficients. Data analysis was performed using Matlab and Microsoft Excel.

2.9.7 Histology

Two additional animals, one animal with tumors at day 9 and one at day 14, were sacrificed 4 hours after the last sonication via transcardial perfusion with 0.9% NaCl solution followed by 10% phosphate-buffered formalin while under deep anesthesia with ketamine and xylazine. Brains were harvested and fixed in formalin. Tissue blocks containing the tumor were embedded in paraffin and cut into 4-6 μm serial axial sections. The section with biggest tumor was stained with hemotoxylin

and eosin (H&E) for examination of light microscopy. Lipo-DOX and trypan blue were not administered in the animals used for the histology study.

2.9.5 Acoustic Emission

The acoustic emissions were recorded using a piezoelectric passive cavitation detector (center frequency: 3.5 MHz, bandwidth: $\pm 30\%$, diameter: 8 mm, Smart Materials, Sarasota, FL) transducer for every 10 ms burst. The procedure for measurement and analysis of the emissions are described in detail elsewhere [125]. Briefly, the passive cavitation detector was mounted next to the transducer and aimed at the focal region to monitor the acoustic emission produced during sonication. The signals from the detector were amplified, filtered, and recorded to a computer using a high-speed digitizing card (PXI-5124; National Instruments). The time signal, frequency spectra, and magnitude of the emission at different harmonics were displayed in real-time during each sonication using software developed in-house in Matlab and stored for later analysis.

Chapter 3: Targeted Lipo-DOX Delivery through Blood-Brain and Blood-Tumor Barriers using Transcranial MRI-Guided Focused Ultrasound

3.1 Results

3.1.1 Permeabilization of BBB/BTB

BBB permeabilization and the presence or lack of petechiae were confirmed using contrast-enhanced and T2*-weighted MRI, respectively. All animals demonstrated hyperintense regions in contrast enhanced T1-weighted images after FUS, confirming BBB permeabilization. In several cases, one or more hypointense spots were observed in T2*-weighted MRI at the brain surface in the cortex, demonstrating the presence of petechiae. Such spots were observed in both hemispheres near the brain surface in 4 of the 5 animals in the animals where doxorubicin concentrations were measured and that received Lipo-DOX before or during after sonication. They were not observed in animals who received Lipo-DOX after sonication.

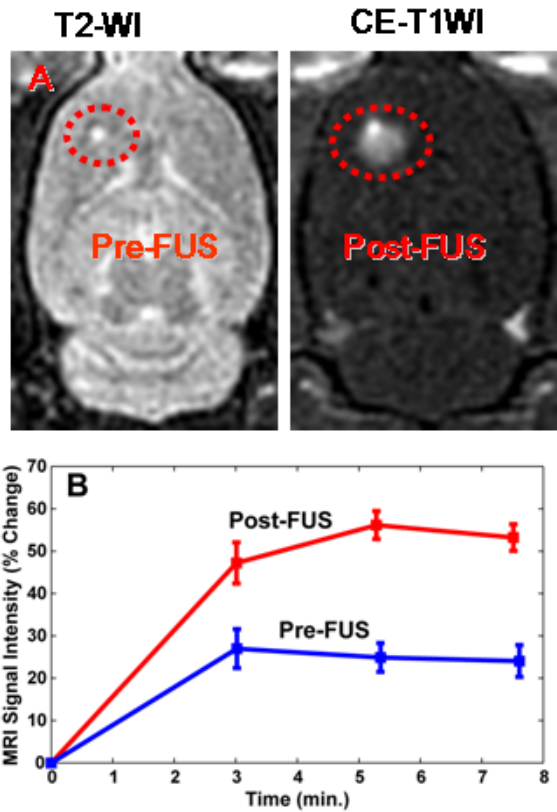


Figure 3. 1 Visualization of BBB/BTB permeabilization. (A) Axial images acquired before (left) and after (right) the FUS-BBBD showing the signal enhancement in T1-weighted MRI after Gd-DTPA injection. Before FUS, the tumor was a small enhancing area (red circle). The magnitude and extent of this enhancement were increased after FUS. (B) Signal enhancement in this example as a function of time.

3.1.2 Effect of Lipo-DOX Injection Protocol on doxorubicin Delivery to the Brain

Doxorubicin concentrations were compared for cases when the Lipo-DOX was injected before or after sonication Figure 3. 2. In group A, both hemispheres were sonicated. In the right hemisphere, Lipo-DOX was administered in 9 fractions, one before each sonication whereas in the left, sonications were performed without

additional Lipo-DOX administration. In group B, the sonications were performed only in one hemisphere, and the total dose of Lipo-DOX was injected in bolus 10 min later. The sonication time was approximately 30 min for the 9 targets.

In group A, the mean doxorubicin concentrations in the right and left hemispheres were 4.7 ± 0.5 and 4.8 ± 0.5 $\mu\text{g/g}$, respectively; they were not significantly different ($p > 0.05$). In group B, the doxorubicin concentration was significantly less ($p < 0.001$) than in both hemispheres in group A. The mean concentration in these animals was 3.2 ± 0.3 $\mu\text{g/g}$, 32% less compared to the volumes in group A. The doxorubicin concentrations were significantly enhanced in all cases ($p < 0.001$) compared to the control tissue. In addition, in every case the doxorubicin concentrations in the sonicated areas exceeded our goal of 0.819 ± 0.482 $\mu\text{g/g}$, a value reported to correlate with a clinical response for human tumors [237].

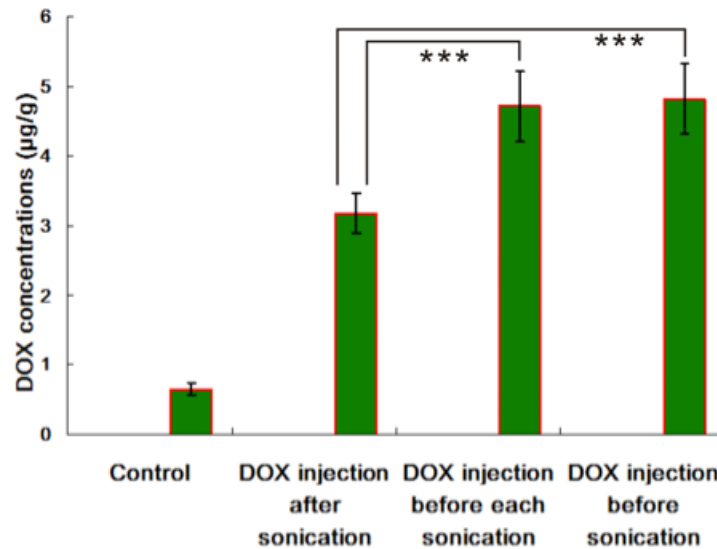


Figure 3. 2 Doxorubicin concentrations corresponding to different Lipo-DOX injection protocols. The doxorubicin concentration was 4.7 ± 0.5 and 4.8 ± 0.5 $\mu\text{g/g}$, when the agent was administered in fractions during the sonications and when it was injected before sonication, respectively; these values were not significantly different from each other ($p > 0.05$). This concentration was reduced by 32% to a value of 3.2 ± 0.3 $\mu\text{g/g}$ when Lipo-DOX was administered 10 min after the last sonication. This reduction was significant ($p < 0.001$). In all groups, the doxorubicin concentration was significantly larger than in control tissue that did not receive FUS-BBBD. The concentrations in all sonicated volumes were above our goal of 0.819 ± 0.482 $\mu\text{g/g}$, a value reported to correlate with a 39% clinical response rate in human tumors (Cummings and McArdle 1986).

3.1.3 Fluorescence Imaging

Fluorescence microscopy was used to investigate the distribution of doxorubicin in the normal brain and in a tumor. Example results from animals euthanized xxx-xxx h after Lipo-DOX administration and FUS-BBBD are shown in Figures (3.3) and (3.4) respectively. In the normal brain, the pattern of extravasation of the fluorescent drug matched well with the focal contrast enhancement on T1-weighted MRI and focal trypan blue staining evident on tissue blocks. High

concentrations were observed around a site of capillary damage. Otherwise, drug was observed in a relatively homogeneous region. In the tumor, it appeared that the sonications enhanced the delivery more at the edge of the tumor than in the center. This may reflect the high cell density and increased interstitial pressure that makes drug delivery in tumors challenging [238]. Overall, using fluorescence in this way is promising for evaluating drug distributions and penetration. The development of this protocol can be utilized in the future by our laboratory to characterize and optimize the procedure.

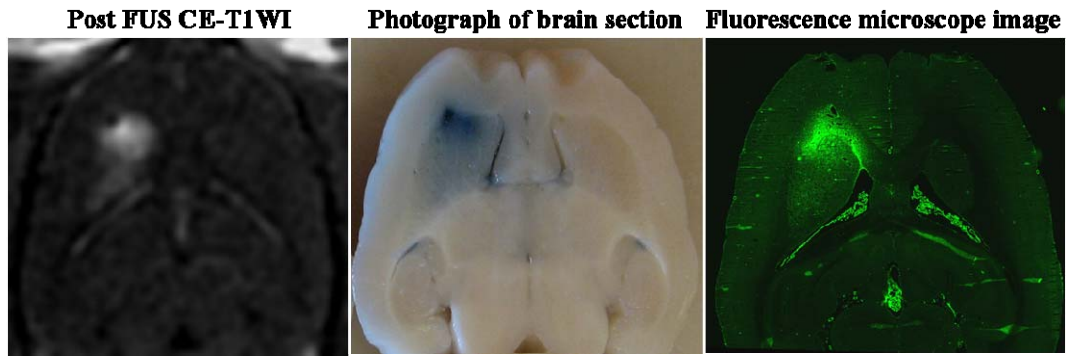


Figure 3.3 Left: Contrast-Enhanced T1-weighted imaging (CE-T1WI); Middle: Photograph of post mortem brain tissue stained with Trypan blue; Right: image showing doxorubicin fluorescence. CE-T1WI verified the BBB permeabilization immediately after the sonications (0.69 MHz; 0.55-0.81 MPa; 10 ms bursts; 1 Hz PRF; 60s duration, 10 μ l/kg Definity microbubbles), which were performed in a grid pattern at 5 targets with intravenous injection of Lipo-DOX (5.67mg/kg). The animal was euthanized 2 h later. The areas where the MRI contrast agent, Trypan blue, and doxorubicin were observed agreed well, with the greatest levels near a small area with capillary damage.

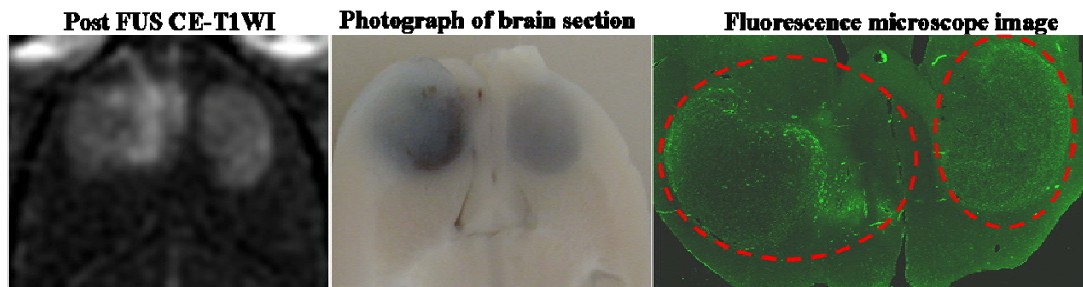


Figure 3.4 Contrast-Enhanced T1-weighted imaging (CE-T1WI); Middle: Photograph of post mortem brain tissue stained with Trypan blue; Right: image showing doxorubicin fluorescence. Sonications (0.69 MHz; 0.55-0.81 MPa; 10 ms bursts; 1 Hz PRF; 60s duration, definity) were performed in a grid pattern at 5 targets with intravenous injection of Lipo-DOX (5.67mg/kg) on the tumor on the left side of the images. The animal was euthanized 2 h later. The three methods agreed well in visualizing the areas with the greatest delivery. The highest doxorubicin levels were observed in the sonicated tumor at the margins.

3.2 Discussion

It has been demonstrated that ultrasound and microbubbles can enhance the delivery of Lipo-DOX into the healthy rat brain parenchyma and the 9L glioblastoma rat tumor model. If this result can be translated, it would have some advantages over other drug delivery methods. For example, being able to use the currently approved drug removes the need and expense of developing and testing new drug formulations. The method is noninvasive and restricts the drug delivery only to desired brain regions.

While a high doxorubicin concentration was achieved in each group, higher concentrations were achieved when we injected Lipo-DOX before sonication (group A) rather than afterwards (group B). This finding may have been due to partial BBB restoration in group B. With the acoustic parameters used in this study, Park et al. reported an exponential decay in permeability to Gd-DTPA (molecular weight: 938 Da) after FUS-BBBD with half-life of 2.2 hours [118]. With this time, the barrier permeability would be reduced by approximately 20% for the first target that was sonicated 40 min before Lipo-DOX administration. Others have shown that this

restoration is faster for larger agents and suggested that an agent the size of Lipo-DOX (100 nm) would have a half-life of only a few minutes [134].

This finding might also reflect transient effects occurring during sonication that actively transported Lipo-DOX out of the blood vessels. A number of studies on “sonoporation” have shown that sonication with microbubbles can drive drugs across cell membranes through the creation of pores that are present for a short time [239]. It may also be possible that the microbubble-enhanced sonications lysed the ~100 nm liposomes, releasing free doxorubicin which was readily transported through the BBB disruption. Others have shown that microbubble collapse can cause such a release when the liposomes are attached to the microbubbles [240], and perhaps something similar happened here. Additional experiments would be necessary however to determine whether the exposure levels used here could release doxorubicin.

Another unexpected finding was that surface damage was observed in the animals in group A in the doxorubicin concentration study, but not in group B. This finding could suggest that the presence of Lipo-DOX, which was in circulation during the sonications in group A, somehow reduced the inertial cavitation threshold. The mechanism by which this lowering could have been produced is unknown. This

finding needs to be verified.

My investigation into using fluorescence to map the released doxorubicin into the rat brain and into a tumor was promising for future work. It would also be interesting to fluorescently tag Lipo-DOX and examine in microscopy how far the intact liposomes, and at a later time the released doxorubicin, penetrates into the brain after FUS-BBBD. In addition, it would be interesting to repeat these experiments using a smaller drug or a drug with a short plasma half-life. The dependence on the order of the sonication and the drug administration on the delivered drug concentrations may be different in such cases.

Chapter 4: Multiple Sessions of Focused Ultrasound Blood-Brain Barrier Disruption to Enhance Delivery of Liposomal Doxorubicin: A Safety Study

An effective drug treatment for an invasive brain tumor such as glioma will require chemotherapy delivery to the normal tissues at the tumor margin, where the BBB protects infiltrating tumor cells, in addition to the semipermeable solid tumor. In a patient with a glioma, this infiltrative margin can extend several centimeters [241]. While an earlier study of FUS-BBBD and Lipo-DOX found that a single drug delivery session did not result in the normal brain tissue damage in rats [191], it is possible that multiple treatments could produce side effects such as those observed in our survival study tumor-bearing rats (see section 5.1.3 below). Furthermore, early studies with mannitol BBB disruption and free doxorubicin suggested that this drug is significantly neurotoxic, even at small concentrations [242,243]. Others have observed concentration-dependent neurotoxicity when free doxorubicin or Lipo-DOX was infused into the brain via convection-enhanced delivery [244].

For these reasons, we tested whether multiple sessions of Lipo-DOX administration and FUS-mediated BBB disruption (FUS-BBBD) can induce severe

adverse events in the normal brain tissue. Sonicating multiple targets in the normal brain over three weeks, we evaluated whether multiple sessions of FUS-BBBD and Lipo-DOX produced significant brain tissue damage. For these experiments, we aimed to use sonications similar to our tumor survival study described in section 2.8.4. We sonicated multiple overlapping brain targets to induce BBB disruption in regions that increased in volume over the three weeks. The tissue effects were compared in histology to animals who received FUS-BBBD or Lipo-DOX alone.

In the previous chapter, the results showed that FUS-BBBD and Lipo-DOX can deliver clinically-relevant concentrations of doxorubicin, and we found that injecting the agent before or during sonication was more effective than administering it afterwards. Thus, we used these parameters in this chapter and throughout the rest of the work described in this thesis.

4.1 Results

4.1.1 BBB Permeabilization

BBB permeabilization and the presence or lack of petechiae were confirmed using contrast-enhanced and T2*-weighted MRI, respectively (Fig 4.1). A higher pressure amplitude (0.81 vs. 0.55 MPa) was needed for the third session to induce

consistent BBB permeabilization, presumably because of an increase in skull or dura thickness as the rats grew [198]. All animals demonstrated hyperintense regions in contrast enhanced T1-weighted images after each session, confirming BBB permeabilization. In several cases, one or more hypointense spots were observed in T2*-weighted MRI in the focal plane or at the brain surface in the cortex, demonstrating the presence of petechiae. Such spots were observed after the second or third session in 4 of the 5 animals who received both FUS-BBBD and Lipo-DOX and in 3 of the 4 animals who received FUS-BBBD alone. They were not seen in animals who received MRI at day 53 or 67. In addition to these hypointense spots in the focal plane, hypointense spots were also observed in the cortex at the brain surface in every animal except one who received FUS-BBBD alone.

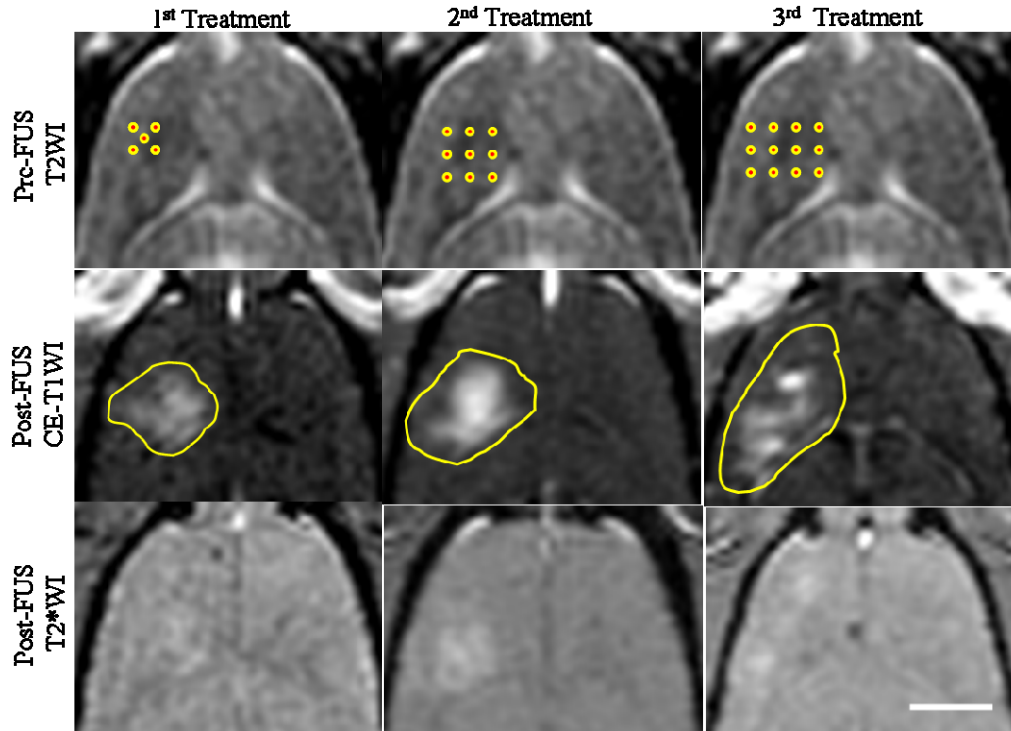


Figure 4. 1 MRI-images acquired during three weekly treatments: T2-weighted imaging (T2WI) used for treatment planning; Contrast-Enhanced T1-weighted imaging (CE-T1WI) verified the BBB permeabilization; T2*-weighted imaging (T2*WI) detected tissue damage. The targeted spots are indicated in dots; the yellow curves outlined extent of MRI contrast enhancement due to BBB permeabilization. Sonications (0.69 MHz; 0.55-0.81 MPa; 10 ms bursts; 1 Hz PRF; 60s duration) were performed in a grid pattern at 5, 9, and 12 targets, respectively, mimicking the three weekly treatments, which were administered in the tumor treatment study described in section 2.8.4. (bars: 5mm)

4.1.2 Histological Findings

All animals that received FUS-BBBD alone were found to be unaffected in the targeted plane in the striatum (Figure 4.2). However, four of the five rats who received FUS-BBBD and Lipo-DOX had small regions with evidence of prior damage in the focal plane (Figure 4.3). In three of these animals, this was evidenced by the presence of small scars with largest dimensions of 0.5-2.0 mm. These scars

consisted of infiltrating macrophages and activated astroglial cells. In the fourth animal, a small (1.0×2.0 mm) cyst formation was observed. No changes were observed in the control hemisphere that received Lipo-DOX only (black boxes in Figure 4.3).

Evidence of more severe prior damage was observed in the cortex near the brain surface in four of the five animals who received FUS-BBBD and Lipo-DOX and in one of the four animals who received FUS-BBBD alone. The effects were similar in appearance to those in the striatum, but the dimensions of the affected areas, which ranged from 0.5-2.5 mm, were larger. Examples of these effects are shown in Figure 4.4.

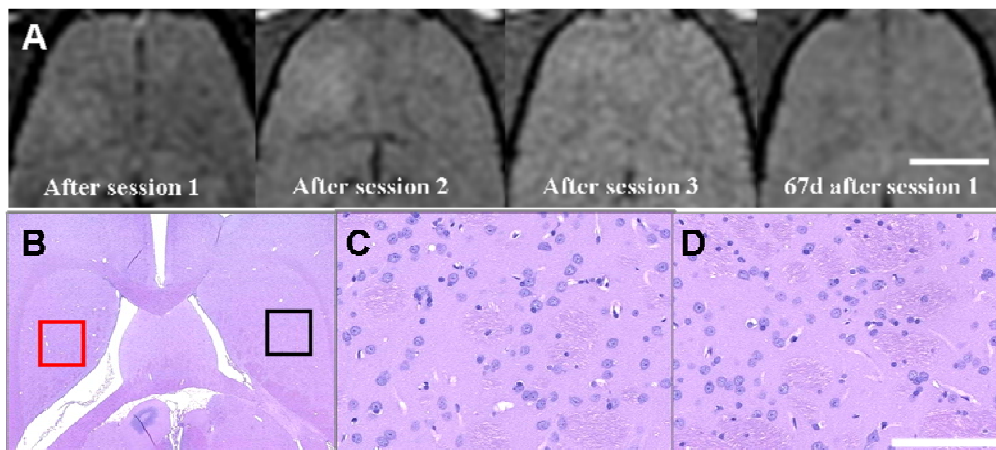


Figure 4. 2 T2*-weighted MRI and corresponding histological appearance of a brain after three weekly sessions with FUS-BBBD alone. The samples for histology (H&E stained sections) were obtained 70 days after the first FUS-BBBD session. T2*-weighted imaging (A) appeared normal in this example. Some signal enhancement was observed in the T2*-weighted imaging after the three treatments. This enhancement was due to MRI contrast, which was administered earlier. The histological appearance of the sonicated regions (C) was indistinguishable from the corresponding non-sonicated regions in the

other hemisphere (D). The regions shown in C and D are indicated in B by the red and black squares, respectively. (bars: 5 mm in A-B; 200 μ m in C-D).

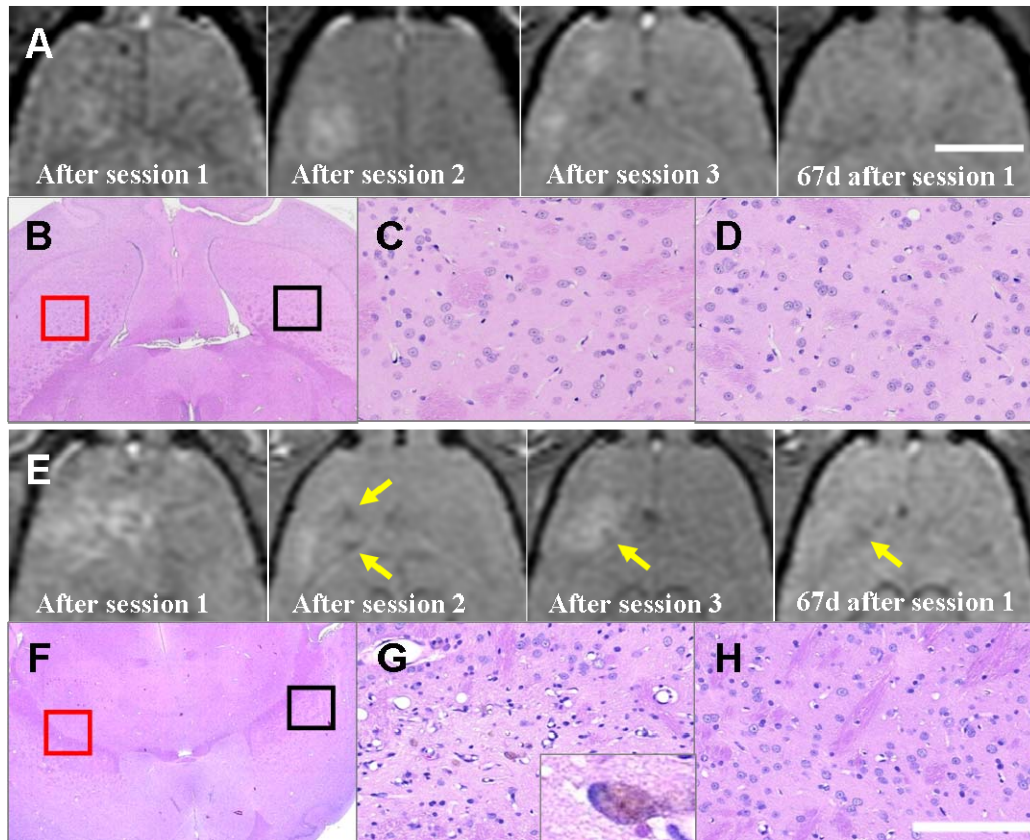


Figure 4. 3 Representative examples of T2*- weighted images and histology (H&E stained sections) in the focal plane for rats who received three weekly sessions of FUS-BBBD and Lipo-DOX. Histology was obtained 70 days after the first FUS-BBBD session. (A-D) Example where the treated regions appeared unaffected in both T2*-weighted MRI (A) and histology (B-D). The histological appearance of the sonicated regions (C) was indistinguishable from the corresponding non-sonicated regions in the other hemisphere (D). The regions shown in C and D are indicated in B by the red and black squares, respectively. (E-H) Example where hypointense areas (arrows) were evident in T2*-weighted MRI after session 2 and a scar was observed in histology (G). Note that the location of the scar was evident in the area that was hypointense in T2*-weighted imaging. A small cluster of hemosiderin (inset) was observed, likely remnants from earlier petechiae. No changes were observed in the control location in the other hemisphere (H). The regions shown in C and D are indicated in B by the red and black squares, respectively. Some signal enhancement was observed in the T2*-weighted imaging (A,E) after the three treatments. This enhancement was due to MRI contrast, which was administered earlier. . (bars: 5 mm in A,B, E,F; 200 μ m in C-D, G-H).

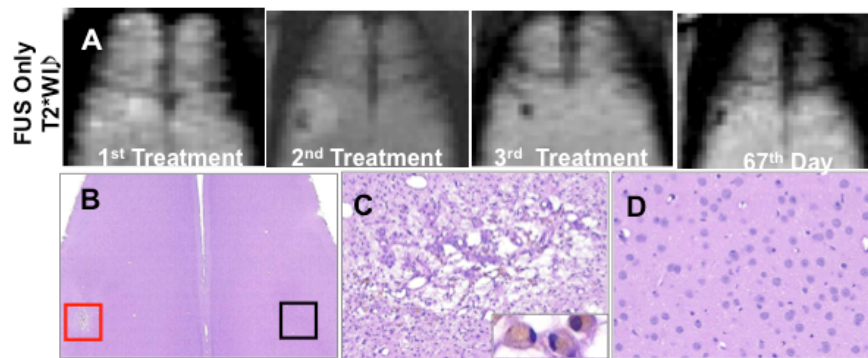


Figure 4. 4 An example of adverse effects in the cortex near the brain surface in an animal that received three sessions of FUS-BBBD and Lipo-DOX. A: Hypointense spots (arrows) were detected in T2*-weighted imaging after the second treatment. Tissue necrosis (C) is evident in the area that appeared hypointense in T2*-weighted imaging. Hemosiderin (yellowish brown granular pigments formed by breakdown of hemoglobin) was observed in macrophages within the necrotic area (inset in C). No changes were found in the contralateral hemisphere that did not receive FUS-BBBD. These adverse effects, which were evident in four of the five animals who received FUS-BBBD and Lipo-DOX and in one of the four animals who received FUS-BBBD alone, were probably due to the long focal length of the transducer (full-width, half maximum of the pressure field: 12 mm) compared to thickness of the rat brain (10-12 mm) and reflections within the skull. (bars: 5 mm in A-B; 200 μ m in C-D).

4.2 Discussion

Regardless of the order of the sonication, it is clear that the sonication parameters used here effectively resulted in a clinically-relevant doxorubicin concentration in the normal brain. However, the severe neurotoxicity that was observed in earlier studies was not observed here. Early work on the toxicity of intracarotid administration of free doxorubicin in rats and dogs following osmotic BBB modification revealed that this agent can be significantly neurotoxic, even at small concentrations [242,243]. In that study, the animals developed neurological

deficits including seizures, with corresponding necrosis and hemorrhagic infarcts observed in histopathology. Other experiments using convection-enhanced delivery have also observed extensive necrosis when high concentrations of doxorubicin or Lipo-DOX were infused into the brain [244]. These studies, along with effects we observed previously at the tumor margins [170], prompted the current study to investigate whether FUS-BBBD and Lipo-DOX can induce such extensive damage. Such effects were not observed.

Evidence for small regions of minor prior tissue damage, however, was detected in this work. We suspect these regions were due capillary damage induced during the sonications. The exposure levels used were the same as in our prior study in tumors and were somewhat aggressive, as evidenced by the presence of hypointense spots in T2*-weighted imaging in most animals. Prior work suggests that these dark spots are caused by the presence of iron-laden particles from petechiae [245] presumably caused by capillary damage caused by inertial cavitation [123]. Based on other studies examining long-term effects of FUS-BBBD, such minor capillary damage is not expected to result in significant long-term effects [94,137], and indeed this was the case here for the animals who did not receive

Lipo-DOX. In contrast, evidence of small areas of prior tissue damage was observed in most of the animals who received FUS-BBBD and Lipo-DOX. The cause of this difference is not known, but it is possible that excessive doxorubicin concentrations resulted around capillaries damaged by inertial cavitation. It may also be possible that doxorubicin impaired repair or otherwise exacerbated such capillary damage that could have resolved over time without the drug. Based on these results we anticipate that while sonication with low-level inertial cavitation may be acceptable – or even desirable – when the focal region is inside a solid tumor, such aggressive exposure levels may not be appropriate for delivering Lipo-DOX to the surrounding normal brain tissue.

An unexpected finding of this work was that more severe damage was evident in both MRI and histology near the brain surface in the cortex. This damage could have been the result of the low frequency and a long focal region – longer than the thickness of the rat brain – that was used in this study. This frequency was chosen to be similar to the transcranial FUS system that is currently being used in clinical trials [246] and it is known that such a frequency can result in reflections and standing waves when sonicating transcranially in a rat [93]. However, the lack of tissue

damage in the far-field close to the skull base, where one might expect the pressure amplitude to be highest due to reflection, suggests that perhaps something else caused these surface effects. Perhaps the microbubble concentration was sufficiently large in the highly vascular cortex to produce shielding, resulting in a lower pressure amplitude at the focal point. While future work is needed to verify this speculation, if it were correct, it may be possible that under some circumstances elevating the exposure level of the sonications can lead to diminishing returns in FUS-BBBD at the focal plane.

Another unexpected finding was that surface damage was observed in the animals in group A in the doxorubicin concentration study, but not in group B. This finding could suggest that the presence of Lipo-DOX, which was in circulation during the sonications in group A, somehow reduced the inertial cavitation threshold. The mechanism by which this lowering could have been produced is unknown. This finding needs to be verified.

This study had some limitations. The sample size was relatively small, and more work is needed to verify the link between the capillary damage produced during some of the sonications and the small areas of downstream tissue damage that

were evident here with the delivery of Lipo-DOX. We also only considered a single dose of Lipo-DOX and a single set of sonication parameters, and we examined the tissue effects only at a single time point using standard light microscopy and H&E stained sections. A larger study using more sensitive methods may find minor tissue effects that were missed here. However, the relevance of such potential minor effects is questionable in the context of a glioma treatment.

Chapter 5: Multiple Treatments with Liposomal Doxorubicin and Ultrasound-Induced Disruption of Blood–Tumor and Blood–Brain Barriers Improve Outcomes in a Rat Glioma Model

The purpose of this work was to evaluate whether multiple treatment sessions can effectively improve the therapeutic effect of Lipo-DOX in a rat glioma model.

Previous work has shown that a single treatment with FUS-enhanced delivery of this agent to orthotopically-implanted 9L rat gliosarcoma model had a modest improvement in survival and tumor growth [191]. Here we examined whether three weekly sessions can provide a more pronounced treatment effect in this tumor model.

We also utilized low-frequency FUS to better match an existing clinical FUS device [81].

5.1 Results

5.1.1 BBB/BTB Permeabilization

BBB/BTB permeabilization and a lack of significant FUS-induced tissue damage were confirmed using contrast-enhanced and T2*-weighted MRI, respectively. A higher pressure amplitude (0.81 vs. 0.55 MPa) was needed for the third treatment to

induce consistent BBB/BTB permeabilization, presumably because of an increase in skull or dura thickness as the rats grew [198]. To confirm that the sonications increased the vascular permeability in the tumor, contrast-enhanced imaging before and after the sonications in several animals was performed (Figure 5. 1 A-B). Sonication targets were applied in a grid to cover the tumor evident in T2-weighted imaging plus a surrounding margin (C). Weekly MRI examination was used to monitor the tumor progression. Representative examples from each experimental group over the first three weeks and the tumor volume measurements are shown in Figure 5.2.

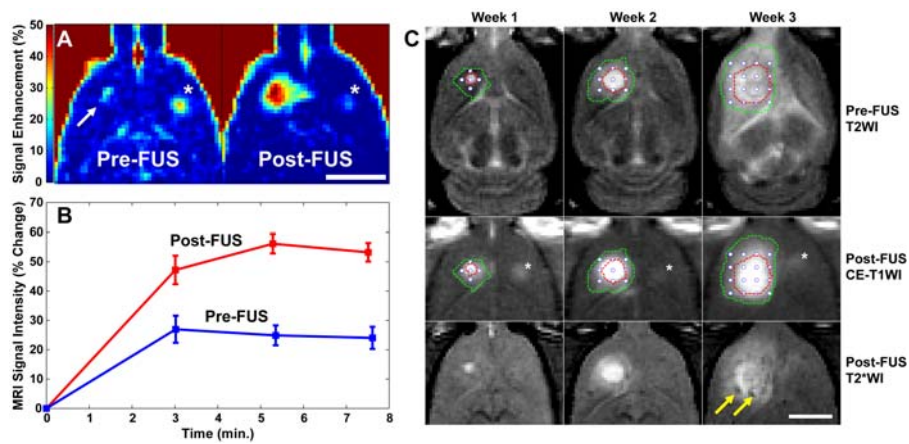


Figure 5. 1 Treatment overview. (A) Axial images acquired before (left) and after (right) the first FUS + Lipo-DOX treatment showing the signal enhancement in T1-weighted MRI after Gd-DTPA injection. Before FUS, the tumor was a small enhancing area (arrow). The magnitude and extent of this enhancement were increased after FUS. (B) Signal enhancement in this example as a function of time. (C) T2-weighted imaging (T2WI) used for treatment planning, contrast-enhanced T1-weighted imaging (CE-T1WI) used to verify the BBB/BTB permeabilization, and post-FUS T2*-weighted imaging (T2*WI) acquired during three weekly FUS+Lipo-DOX treatments. The location of the tumor in treatment planning is indicated by the solid line, and the extent of MRI contrast enhancement is indicated by the dotted line. The coordinates of the sonication targets are also noted (white circles). Two hypointense spots (arrows) were evident after the third treatment in T2*-weighted imaging. The enhancing area evident in the other hemisphere in (A) and (C) (asterisk) was a location in the brain that was sonicated before the first Gd-DTPA injection to confirm the accurate targeting of the FUS beam. Bars: 5 mm.

5.1.2 Tumor progression

In most animals in the three control groups, the tumor grew rapidly over this time Figure 5.2 (A) resulting in significant midline shift and compression of the lateral ventricles. Hypointense regions were often evident within the tumor in T2*-weighted imaging in all groups. Eleven of fifteen rats (73%) in these groups either died or were euthanized before the third treatment due either to tumor dimensions exceeding 10–11 mm or poor health conditions (weight loss exceeding 20% or severely impaired activity). The rest died or were euthanized for these reasons before week 4. One rat in the Lipo-DOX Only group was euthanized before the third treatment; the rest were euthanized shortly after week 3.

All animals in the FUS + Lipo-DOX group received all three treatments, and no rat in this group was euthanized before week 4 Figure 5.2 (B–C). The tumor volume reached a maximum at weeks 3 or 4, after which they began to shrink. The outcomes for the eight animals in this group varied and are summarized in Table 5.1. The maximum tumor volume varied substantially, with some tumors reaching volumes similar to the control group, and others never reaching 100 mm³. The mean tumor volume in the FUS + Lipo-DOX group was less than in the three control groups

at weeks 2–3 Figure 5.2 (C). These differences were not found to be significant.

The first two rats treated in the FUS + Lipo-DOX group (Rats 1 and 2 in Table 5. 1) exhibited local skin toxicity (inflammation, peeling; minor bleeding) on the scalp and the front and hind paws beginning on or after week two. These two animals developed a skin infection and were euthanized at days 34 and 35. In their last imaging session, one of these animals had no tumor evident in MRI, and the other had a small tumor that appeared to be responding to the treatment. Subsequent animals were treated prophylactically with antibiotics. While skin irritation or mild inflammation was observed, they did not develop infections.

Three animals (Rats 3, 4 and 8 in Table 5. 1) did not exhibit any evident morbidity. They gained weight and behaved normally. These animals were followed for 9 or more weeks, at which time they were euthanized for histological examination. One of these long-term survivors was euthanized at day 66; the other two were observed for longer periods (136 and 142 days). Tumors in these animals grew to a substantial volume (greater than 300 mm³) before they began to resolve. MRI from one of these animals is shown in (Figure 5.2B). After the tumors disappeared, brain tissue loss at the former tumor site was evident in MRI, along with damage in

adjacent tissues and enlarged ventricles. Tissue damage appeared as highly hyperintense regions in T2-weighted imaging. In some regions, within this damaged area, discrete hyperintense zones in both T2* and T2-weighted imaging were seen. Two animals in the FUS + Lipo-DOX group (Rats 5 and 7 in Table 5. 1) were euthanized due to poor health at days 32 and 36, respectively. At the time of sacrifice, one of these animals exhibited only a small hyperintense region in T2-weighted imaging, and no tumor was evident in histology (see below). The other had an extensive hyperintense area in T2-weighted imaging, but only a small cluster containing a few tumor cells was found in histology. Finally, in one animal (Rat 6 in Table 5. 1), a large hypointense region was observed in T2*-weighted imaging at week 4 that was assumed to be intratumoral hemorrhage. This animal also exhibited impaired activity and was euthanized at this time.

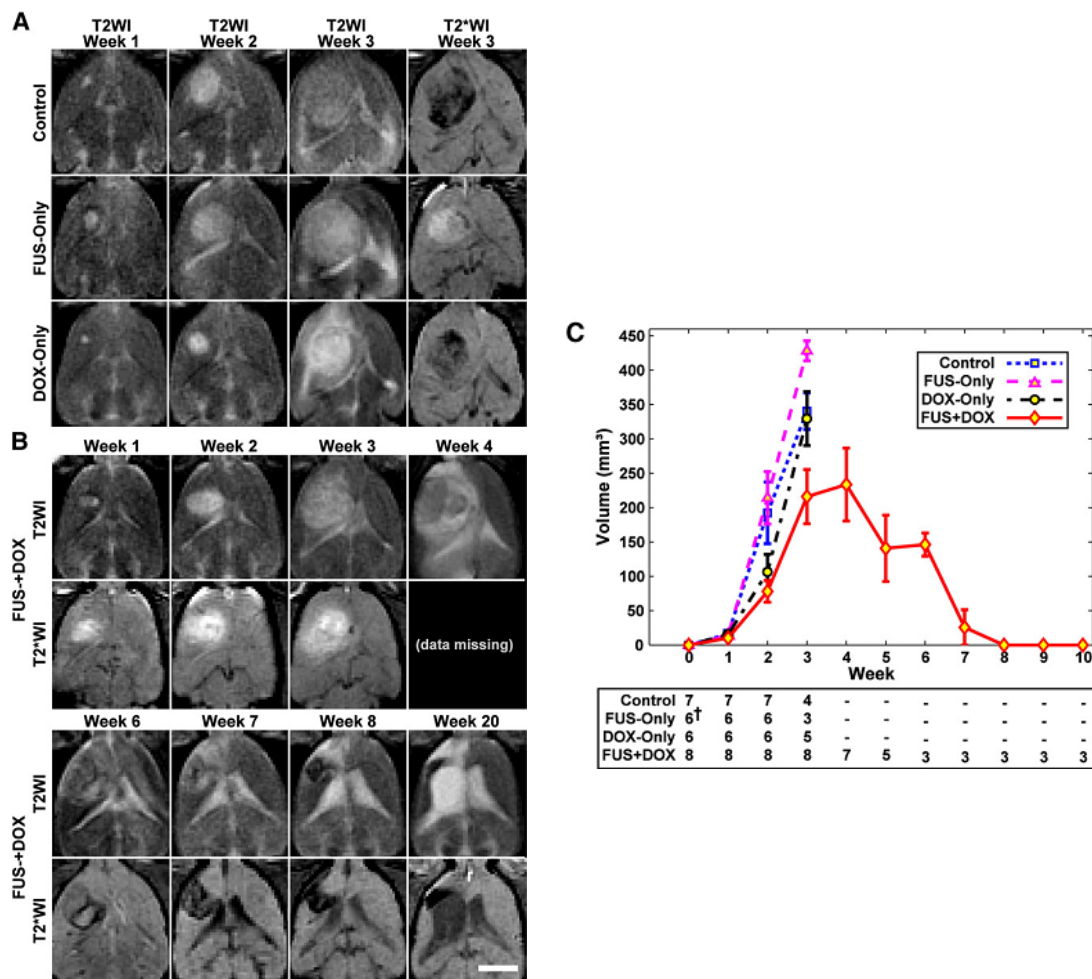


Figure 5. 2 MRI appearance of the tumors and their growth over time. (A) MRI for the three control groups for weeks 1–3. The rapid growth that was observed in most of the rats in these groups is evident in T2-weighted imaging (T2WI). Hypointense areas were often observed within the tumor in T2*-weighted MRI (T2*WI). (B) Serial MRI for a long-term survivor in the FUS + Lipo-DOX group (Rat 4 in Table 5. 1) showing rapid tumor growth and subsequent resolution. The volume was maximum at week four, at which time it covered a significant portion of one hemisphere. It then began to shrink, and from week 8 onwards it was no longer evident. Brain tissue loss at the former site was evident, and the lateral ventricle was enlarged and filled much of this space. Tissue adjacent to the former tumor mass was highly hyperintense in T2-weighted imaging, and presumably damaged. A hypointense region was observed at the former tumor site in T2*-weighted imaging starting at weeks 6–7, which slowly shrunk over time. Imaging between weeks 8 and 20 was mostly similar. Note that the T2*-weighted imaging in the FUS-Only and FUS + Lipo-DOX animals was acquired after Gd-DTPA in weeks 1–3; contrast enhancement was observed in the tumor and surrounding brain. Bar: 5 mm. (C) MRI-measured tumor volumes as a function of time for each experimental group. Tumors were implanted at week 0. The number of surviving animals at each week is noted below the plot (MRI from two animals in the FUS-Only group was not included in this analysis due to poor image quality). Mean \pm S.E. is shown.

Table 5. 1 Outcomes in FUS+Lipo-DOX group

Rat	Survival (days)	Maximum vol. in MRI (mm ³)	Vol. in MRI at euthanasia (mm ³)	Tumor found in histology	Outcome
1	34	244	63	Yes	Skin infection, euthanized
2	35	52	0	No	Skin infection, euthanized
3	66	358	0	No	Long-term survivor
4	142	365	0	No	Long-term survivor
5	32	424 ²	424 ²	Yes ¹	Poor health, euthanized
6	31	312	312	Yes	Intratumoral hemorrhage, euthanized
7	36	96	40	No	Poor health, euthanized
8	136	312	0	Yes ¹	Long-term survivor

¹Only an small cluster containing a few tumor cells was found

²A well-defined tumor margin was not evident in T2-weighted MRI at week 3-4 in this animal; only a large hyperintense region was observed (see Figure 4F). The volume of this hyperintense region was included in the volume measurements, as if this region was with tumor or edema could not be determined.

5.1.3 Histological Findings

Tumors in the Control and FUS-Only groups appeared at days 15–23 as solid masses that replaced large amounts of brain tissue (Figure 5. 3A). The tumor bulk consisted of viable and rapidly dividing spindle-shaped cells interspersed with multiple small necrotic sites. Microvessels that were necrotic, dilated, and congested with erythrocytes were observed throughout and were surrounded by necrotic zones (Figure 5. 3B). Small hemorrhagic regions were also found. Blood cells in these regions and in congested blood vessels were consistent with the hypointense regions observed in T2*-weighted imaging. In the largest tumors, numerous necrotic and hemorrhagic areas accompanied by cell necrosis and apoptosis were found scattered throughout the tumor mass. Rapid tumor growth and invasion displaced and

compressed the surrounding brain tissue, resulting in ischemia and cell death (infarction) in some adjacent brain regions (Figure 5. 3C). A narrow (0.5–1 mm) band of invading/infiltrating cells was evident at the tumor margin (Figure 5. 3D).

The tumor appearance in the Lipo-DOX Only group varied. Although viable and dividing cells were generally present, a reduced cellularity compared to the other control groups, along with unhealthy-appearing tumor cells and an intensely vacuolated matrix was evident in this group (Figure 5. 3E). Large regions of necrosis were observed in some cases, but some viable tumor cells were always found within these necrotic areas. Substantial hemorrhage was evident at the periphery of some tumors, accompanied by infarction in the surrounding brain. Tumor cell invasion along perivascular tracts and tumor cell clusters were observed at sites as far as 1–2 mm from the edge of the solid tumor mass (Figure 5. 3F). In one animal (euthanized at day 26 due to impaired activity), no tumor cells were found in histology.

In contrast to the controls, all but one of the animals in the FUS + Lipo-DOX group exhibited a strong treatment response, with no tumor mass detected in 6/8 animals. However, in two of these animals a few residual or recurrent tumor cells were found in the former tumor site. In one rat, which was euthanized due to skin

infection at day 34, a tumor was found to be shrunken compared to its maximum size in MRI and partly destroyed. The central area contained a viable tumor mass, and a surrounding rim of tissue appeared to be damaged. Only one animal (Rat 6 in Table 5. 1) had a large tumor like most rats in the control groups. This animal, in which intratumoral bleeding was suspected in MRI, was euthanized at week 4. Histological examination confirmed hemorrhagic infarction in a region of tumor necrosis. This region was restricted to the tumor mass; no blood was found inside the adjacent ventricular space.

Example histological findings from the FUS + Lipo-DOX group are shown in Figure 5. 4. In the three long-term survivors, where the tumors grew to a substantial volume before beginning to resolve, brain tissue loss was evident at the former tumor site (Figure 5. 4A). The adjacent lateral ventricle was significantly enlarged and filled this missing area. A region in the adjacent brain was necrotic, with an appearance consistent with infarct (Figure 5. 4B). A small cyst was observed within this necrotic zone. The hypointense regions evident in MRI contained hemosiderin — either in clusters or taken up by macrophages (inset in Figure 5. 4B). In one long-term survivor, a small cluster of recurring or residual tumor cells was found.

Findings from two animals from the FUS + Lipo-DOX group that were euthanized for impaired activity are shown in (Figure 5. 4C–H). In one case (euthanized at day 36) only a small necrotic area with macrophage infiltration was found at the former tumor site (Figure 5. 4C–E). In the second animal (euthanized at day 32), a larger necrotic area was found at the former tumor site, and affected or damaged tissue was observed in the surrounding brain that was hyperintense in T2-weighted MRI (Figure 5. 4F–H). A tiny cluster of tumor cells was found in this example (inset in Figure 5. 4G).

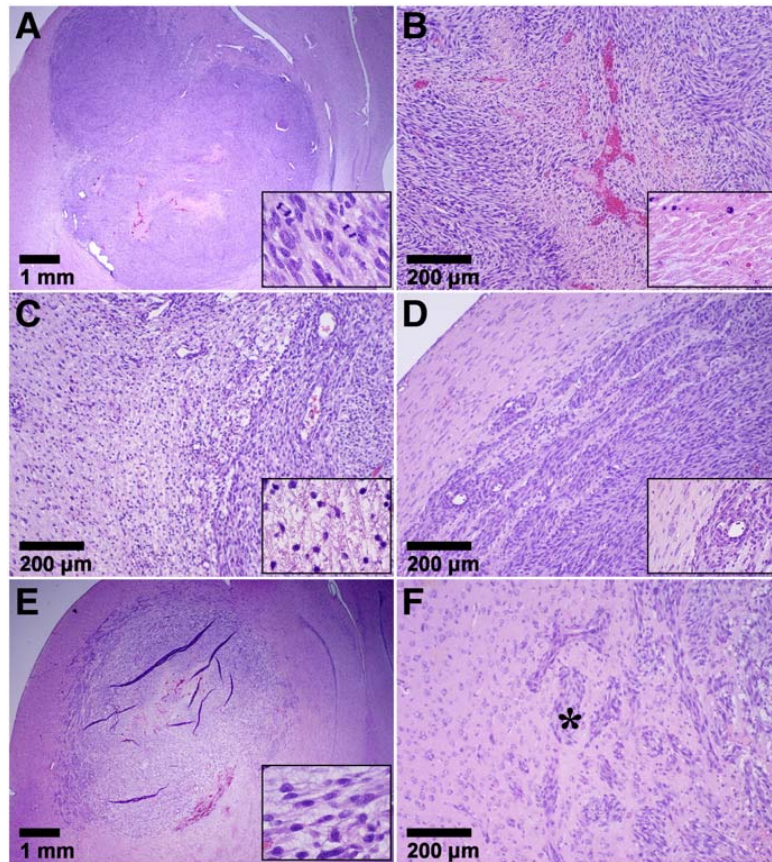


Figure 5. 3 Appearance of 9L gliosarcoma in the three control groups in histology. Animals receiving no treatment or FUS-Only (A–D) all had a similar appearance. The tumor appeared as a solid mass that replaced large volumes of brain tissue (A). The bulk of the tumors consisted of viable and rapidly dividing spindle-shaped cells (inset in A). Congested blood vessels were observed throughout, surrounded by necrotic tissue (B). Some regions of adjacent brain tissue were severely damaged, presumably from ischemia (C). There was a rim of infiltrating cells at the margin (D). Most tumors in the Lipo-DOX Only group (E–F) were also large masses of tumor cells with an infiltrating margin (E). However, unlike the other two control groups, they had a lower cellularity, unhealthy tumor cells, and intensely vacuolated matrix (inset in E). Tumor cell invasions along perivascular tracts and tumor cell clusters were observed at distant sites up to 2 mm from the edge of the solid tumor. The vacuolation evident in the tumor mass was often not observed in the infiltrating margin (* in F).

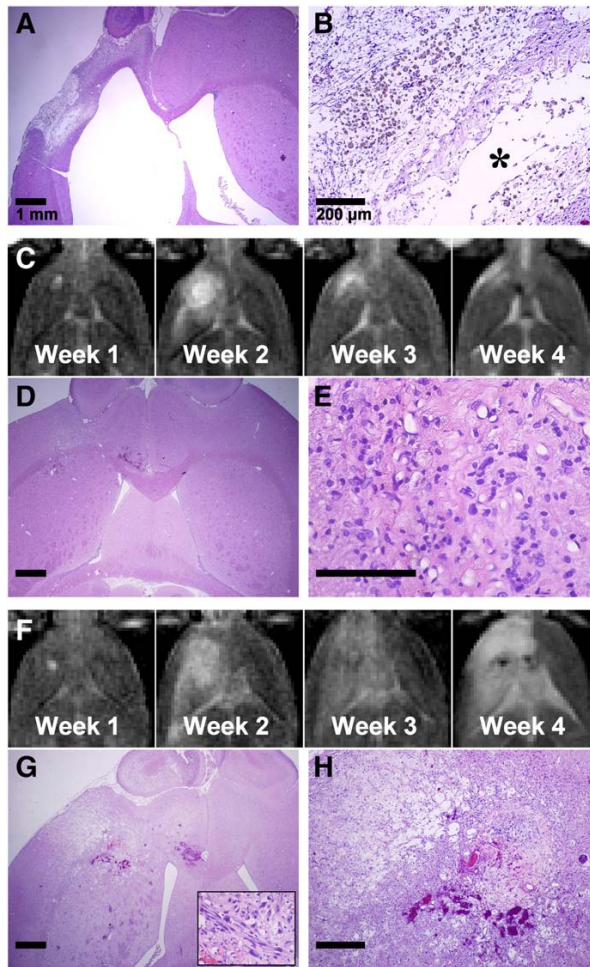


Figure 5. 4 Histological appearance of the brain in three of the animals from the FUS + Lipo-DOX group. (A–B) Long-term survivor (see xxxB for MRI). No tumor cells were found. Brain tissue loss at the former tumor site was evident, and the lateral ventricle was enlarged and filled this space. Tissue necrosis (infarct) was observed in the adjacent tissue, presumably from ischemia. Hemosiderin, either in clusters or inside macrophages was observed within the necrotic area. A small cyst (*) was also observed. (C–E) Example frogman animal, whose tumor was resolved, but the animal was euthanized at day 36 due to poor health. (C) T2-weighted MRI showing tumor growth and shrinkage. At week 4, only a small hyperintense region was visible. (D–E) A small necrotic area with macrophage infiltration was found at the former tumor site. (F–H) Another animal with a strong treatment response, but that was euthanized due to poor health at day 32. In this animal, the tumor grew to a relatively large size over weeks 1–2. At week 4, an extensive hyperintense area was observed in T2-weighted imaging (F). A necrotic area with micro-hemorrhages was found in histology at the former tumor site (G–H). Damaged or necrotic brain tissue was evident in the area that was hyperintense in T2-weighted imaging. A small cluster of tumor cells remained (inset in G).

5.1.4 Survival Analysis

Kaplan–Meier survival analysis is shown in Figure 5. 5; the corresponding statistical data are summarized in Table 5. 1. The median survival time for the animals in both the Control and FUS-Only groups was about 18 days. For animals in the Lipo-DOX Only group, it was 20.3 days - a 16% improvement over the animals in the Control group. However, this difference was not significant ($P = 0.16$). In contrast, the animals in the FUS + Lipo-DOX group showed a significant survival benefit ($P < 0.001$) compared to the other three groups. The median survival time was 35 days, a 100% and 72% improvement over the Control and Lipo-DOX Only groups, respectively. Note that this analysis did not censor the two animals euthanized early due to skin infection. If one assumes those animals did not die from their tumor and censors them, the estimated median survival of the FUS + Lipo-DOX group would be longer than 142 days, as more than 50% of the remaining animals survived until this time.

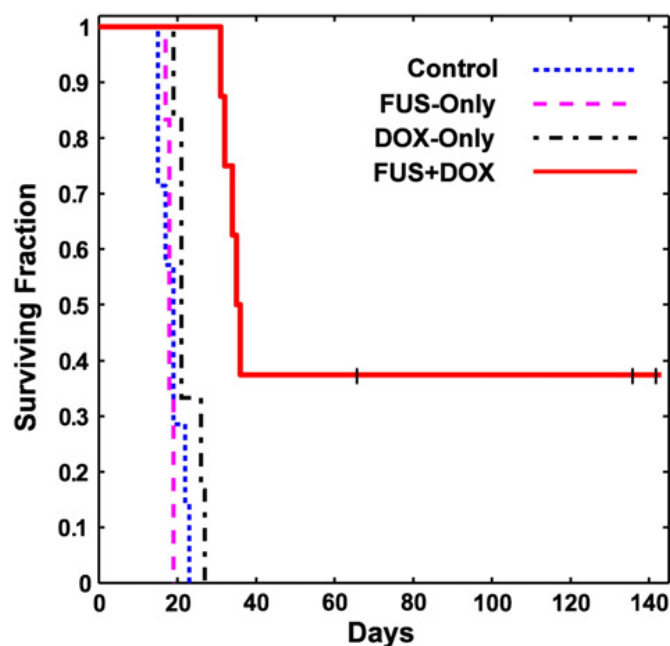


Figure 5. 5 Kaplan–Meier survival curves for the four experimental groups. Three long-term survivors, who did not exhibit impaired activity, were euthanized at different times (tick marks). Afterwards they were censored.

Table 5. 2 Survival analysis

Treatment Group	N rats	Max. survival (days)	Median survival (days)	ISTmedian (%)	Mean survival \pm S.D. (days)	P-value, Hazard ratio
Control	7	23	17.5	18.6 \pm 3
FUS-Only	8	21	18.0	2.9	18.9 \pm 1	0.85, 1.16
Lipo-DOX Only	6	27	20.3	16.2	22.5 \pm 3	0.16, 1.18
FUS+Lipo-DOX	8	>142	35.0	100.0	64.0 \pm 48	0.00031, 5.36

Note - Increase in Survival Time [IST_{median} (%)], P-value, and Hazard ratio are relative to the Control group. P-value and Hazard ratio from Log-Rank test between FUS+Lipo-DOX and Dox-Only group are 0.00057, 4.52 respectively.

5.2 Discussion

Doxorubicin is a commonly-used anticancer drug for treatment of a wide

range of cancers. While its effectiveness against glioma has been shown in vitro [247] and in vivo when injected directly into the tumor [226,248], systemic administration has not been effective clinically [249], presumably reflecting insufficient delivery [250]. A number of drug formulations have been developed to enhance the delivery of doxorubicin in animal glioma models [251–255] and at least one clinical trial is ongoing with such an agent [256]. Here, ultrasound and microbubbles can effectively improve outcomes in a rat glioma model using an existing liposomal agent, removing the need to develop and test new drug formulation was demonstrated. The method is noninvasive and restricts the drug delivery only to desired brain regions. While more work is needed to optimize the treatment and to better understand its safety profile, these results are promising for the development of new treatment options for glioma patients. They join several other studies that showed this FUS method can enhance drug delivery and improve outcomes in brain tumor models [166,167,172,173,190,191,257].

This study also demonstrates the importance of multiple treatments. Previously, a modest survival improvement (24%) compared to untreated controls was observed with a single treatment in this tumor model [191]. With three weekly

treatments, median survival was increased by 100% compared to the controls, and it was observed that 72% survival improvement compared to treatment with chemotherapy only. While the drug alone produced some treatment effects, it did not significantly improve survival or stop tumor proliferation in most cases. Histological examination of the tumors in this group showed a heterogeneous response to the treatment, with necrotic areas interspersed with viable tumor cells — perhaps consistent with heterogeneous vascular permeability and insufficient drug delivery to some regions. It also appeared that perhaps the drug did not reach the infiltrating tumor cells, as the matrix vacuolation evident in the tumor mass was not seen around the tumor cells at the tumor margin. In contrast, all but one of the tumors in the FUS + Lipo-DOX group exhibited a strong treatment effect

Several adverse events were observed. Three rats with little or no tumor evident in histology – one in the Lipo-DOX Only group and two in the FUS + Lipo-DOX group were euthanized due to impaired activity after three treatments. This finding may suggest that we used an aggressive treatment schedule that may not be tolerated by all subjects. Doxorubicin, even when encapsulated, has multiple known side effects, some of them severe. Use of medications to reduce the symptoms of

these side effects may help to avoid the impairment we observed. In one animal (shown in Figure 5. 4F–H), damaged brain tissue was evident over a large portion of the treated hemisphere. Brain tissue loss and necrosis in the surrounding brain in the three long-term survivors in the FUS + Lipo-DOX group was observed. It was not known whether these effects were due to the FUS + Lipo-DOX treatment or to the extensive tumor burden that could have damaged the surrounding brain due to mass effects. The results in Chapter 4 suggest that the amount of doxorubicin delivered across the BBB in the normal brain with these sonication parameters would not result in such severe neurotoxicity.

A potentially significant adverse event was the extensive intratumoral hemorrhagic area that occurred in one animal one week after the last FUS + Lipo-DOX treatment. While frank bleeding (such as into the ventricles) was not observed, vascular risks associated the treatment should be examined in more detail. This hemorrhage may have resulted from necrosis of the vessel wall in a large tumor vessel. Others have reported hemorrhages in this tumor model with different doxorubicin formulations [255,258]. Skin toxicity was observed, a finding that may not be surprising since such toxicity, particularly in the hands and feet, is a known side effect

of doxorubicin [259]. However, it might be prudent to confirm that the sonications do not increase drug delivery into the scalp. The focal region of our transducer overlapped the small rat skull, and the intensity on the scalp may have been relatively high. While the intensity on the scalp is expected to be less in humans, this issue might still be important, as large tumors may require sonication at hundreds of individual targets, and any low-level effects may accumulate. Reflections from the skull bone can exacerbate this effect.

This study had several limitations. One limitation was our tumor model. While the 9L rat gliosarcoma model is highly aggressive and the robust survival improvement observed here is certainly encouraging, future work is needed with models that are genetically similar to human GBM and that have similar growth patterns. The 9L glioma model is not considered to be highly infiltrating [260] and only a relatively narrow infiltrating zone was observed. The disruption of the BBB in the surrounding brain tissue may not have played as large a role in our outcomes as might be anticipated clinically. Targeting infiltration is anticipated to be critically important with human GBM, and based on clinical patterns of recurrence [5,6,261], a margin extending several centimeters into the “normal” brain may require BBB

disruption for effective therapy. Additional work in a more infiltrating tumor model is needed to ensure that such regions can safely and effectively be targeted. Finally, this model has been reported to be immunogenic [260], which may have led to more improved outcomes than would be achieved in non-immunogenic tumor model.

Another limitation was to use two different drug formulations in some animals due to a national shortage of doxorubicinIL. While they had similar liposome properties, there may have been differences unknown to us that may have impacted our results. The sample size was also relatively small, and more work is needed to better characterize the effectiveness of the treatment and the rate of adverse events. More consistent results may be obtained using online methods to optimize the exposure levels. While the exposure levels based on the animal age and weight were modified, retreatment of regions where MRI contrast enhancement was poor to attempt to achieve a uniform level of enhancement was performed. The monitoring the microbubble dynamics in real-time using online acoustic emission monitoring [139,204] and re-treating areas with poor contrast enhancement can improve the local delivery and perhaps allow for a reduced systemic dose was being anticipated. Here, only one dose of liposomal doxorubicin was evaluated. By utilizing

post-treatment MRI contrast imaging, which can be correlated to drug concentrations [95,118], along with online methods to control the exposures was expected, the optimization of the drug dose delivered to the tumor and the surrounding brain tissue. If one understands the relationship between the concentrations of the therapeutic and the imaging contrast agent, which can perhaps be established in animals, one might be able to titrate the drug administration to achieve a desired level in the brain. However, this may be challenging in tumors, where the vascular permeability can change over time. This relationship was explored in work described in the next Chapter.

**Chapter 6: Enhancement in Blood-Tumor Barrier Permeability
and Delivery of Liposomal Doxorubicin using Focused
Ultrasound and Microbubbles: Evaluation during
Tumor Progression in a Rat Glioma Model**

It would be desirable to demonstrate that the amount of drug delivered and its penetration into the brain parenchyma is sufficient to produce a therapeutic response.

Ideally, this would be performed for each patient. Post-treatment imaging could provide this assurance by labeling the drug with a contrast agent for MRI or other imaging modality [174]. It might also be possible to use a standard contrast agent as a surrogate measurement, which would be advantageous since it could be used with existing drugs. A number of studies have related signal intensity changes in contrast-enhanced MRI after BBB disruption with tissue drug concentrations [95,175,208].

More quantitative and repeatable techniques, such as estimating contrast agent concentrations via T1-mapping [134,209] or vascular transfer coefficients via analysis of dynamic contrast-enhanced MRI (DCE-MRI) [99] have been used to perform spatial and temporal characterization of BBB permeability after FUS. DCE-MRI can also be investigated to predict the resulting payload of drugs to the

brain [118] and in tumors [262].

Despite these promising findings, one needs to be careful when expanding to different patient populations or if different drugs are used. The relationship between the delivery of a contrast agent and a therapeutic can be complicated. For example, a relationship found in the normal brain may not translate to patients with CNS disorders. This challenge could be particularly difficult in tumors where the vascular properties can change over time [238]. Further complications may arise when the therapeutic has a different size or other chemical property than the contrast agent.

Here, the usefulness of MRI as a monitoring and feedback tool for the drug delivery procedure was explored. I measured the transfer coefficient K_{trans} of the MRI contrast agent Gd-DTPA with DCE-MRI for cases with and without sonication and Lipo-DOX administration. I then compared K_{trans} to the resulting doxorubicin concentrations in tumors. Moreover, I performed this characterization at three time points to investigate if this relationship changes over time as the tumor blood vessels become more degenerate. Finally, a feasibility study was performed where acoustical monitoring of bubble activity during sonication was correlated with signal intensity changes in contrast-enhanced MRI was investigated.

6.1 Results

6.1.1 Bilateral Tumor Progression and BBB/BTB Disruption

The MRI appearance of the bilateral tumors on day 9, 14, and 17 were monitored in MRI where they grew rapidly over time (Figure 6. 1A), resulting in significant midline shift and compression of the lateral ventricles. The tumor volumes in the right hemisphere were 14.5, 113.8 and 151.4 mm³ at days 9, 14, and 17 respectively. The corresponding volumes of the left tumors were 16.0, 110.8, and 143.8 mm³, and were not significantly different (P=0.9) from those on the right (Figure 6. 1B). A higher pressure amplitude (0.81 vs 0.55 MPa) was needed at day 17 to induce consistent BBB/BTB permeabilization, presumably because of an increase in skull or dura thickness as the rats grew [198]. The sonication pattern was similar to the studies in earlier chapters, where 5-20 targets were applied in a grid (spacing: 1.5 mm) to cover the entire tumor and a rim of surrounding brain tissue. Post-FUS T2*-weighted images were used to detect small petechiae which would appear in this imaging as hypointense spots.

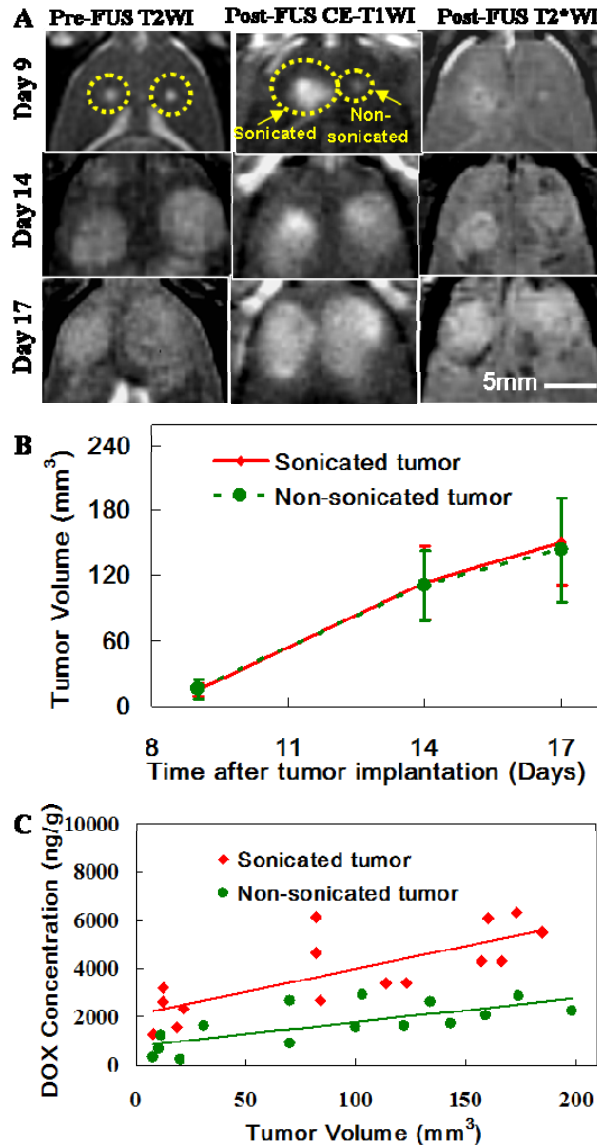


Figure 6. 1 MRI appearance of bilateral 9L gliosarcoma, their growth curves, and doxorubicin concentrations measured approximately 2 hours after the ultrasound experiments as a function of tumor volume. (A) Axial views of MRI at day 9, 14, and 17 after implantation. The rapid growth of tumor was evident in T2-weighted MRI (T2WI), changes of BBB/BTB permeabilization were observed in contrast-enhanced T1-weighted images (CE-T1WI) after gadolinium injection, and FUS-induced tissue damage was evaluated in T2*-weighted images (T2*WI) which would appear as hypointense spots in images. (B) The growth curves shows no significant difference between the volumes of the sonicated and non-sonicated tumors ($P=0.9$). (C) Doxorubicin concentrations measured in the tumors post mortem in tumor tissue were correlated to tumor volume ($R^2=0.58, 0.51$ for the sonicated and non-sonicated tumors, respectively). Doxorubicin concentration in the sonicated tumor was generally larger than the non-sonicated tumor.

6.1.2 Doxorubicin Concentration and Kinetics of BBB/BTB Permeability Changes

Lipo-DOX was administered in fractions immediately before each sonication, and its concentration in the tumors was measured about two hours later. The doxorubicin concentration measured post mortem via fluorometry increased monotonically as a function of tumor volume in both the left (non-sonicated) and right (sonicated) tumors (Figure 6. 1C). A good correlation ($R^2 = 0.58$ and 0.51 for the left and right tumors, respectively) was observed between doxorubicin concentration and tumor volume (Fig.2C). The concentration in the sonicated tumor (2222 ± 784 , 3687 ± 796 and 5658 ± 821 ng/g) was generally greater than in the non-sonicated tumor (823 ± 600 , 1817 ± 732 and 2432 ± 448 ng/g).

In most animals, DCE-MRI was obtained before and after FUS-induced BBB/BTB to calculate the transfer coefficient K_{trans} for Gd-DTPA. Example maps of K_{trans} and changes of signal intensity before and after sonication are shown in (Figure 6. 2). After FUS, the signal intensity on sonicated tumor was increased significantly ($P < 0.05$), at day 9 but not at day 14 or 17 compared with before FUS (Figure 6. 2A-C). Before FUS, the K_{trans} values for the both tumors appeared similar on days 9, 14

and 17. They increased, particularly at day 9, for the sonicated tumors (shown by the arrow in Figure 6. 2D). Comparisons of mean K_{trans} before and after sonication are shown in Figure 6. 3. In the non-sonicated tumor, the mean K_{trans} values (\pm S.D) before FUS were 0.0068 ± 0.0027 , 0.0088 ± 0.0026 and $0.012 \pm 0.0086 \text{ min}^{-1}$ at day 9, 14 and 17, respectively; after the sonications these values were 0.0044 ± 0.0018 , 0.0103 ± 0.0047 and $0.0115\pm 0.0015 \text{ min}^{-1}$ (Figure 6. 3A). In the sonicated tumors, the mean K_{trans} values before FUS were 0.0077 ± 0.0053 , 0.0082 ± 0.0025 , and 0.01006 ± 0.0019 at day 9, 14, and 17, respectively. After FUS they were 0.0129 ± 0.0064 , 0.0128 ± 0.0062 and 0.0116 ± 0.0018 (Figure 6. 3B). No significant difference ($P>0.05$) was observed in the mean K_{trans} between the two DCE-MRI acquisition for the non-sonicated tumor at any day. However, for the sonicated tumor, K_{trans} was significantly increased ($P < 0.05$) at day 9 but not at day 14 or 17.

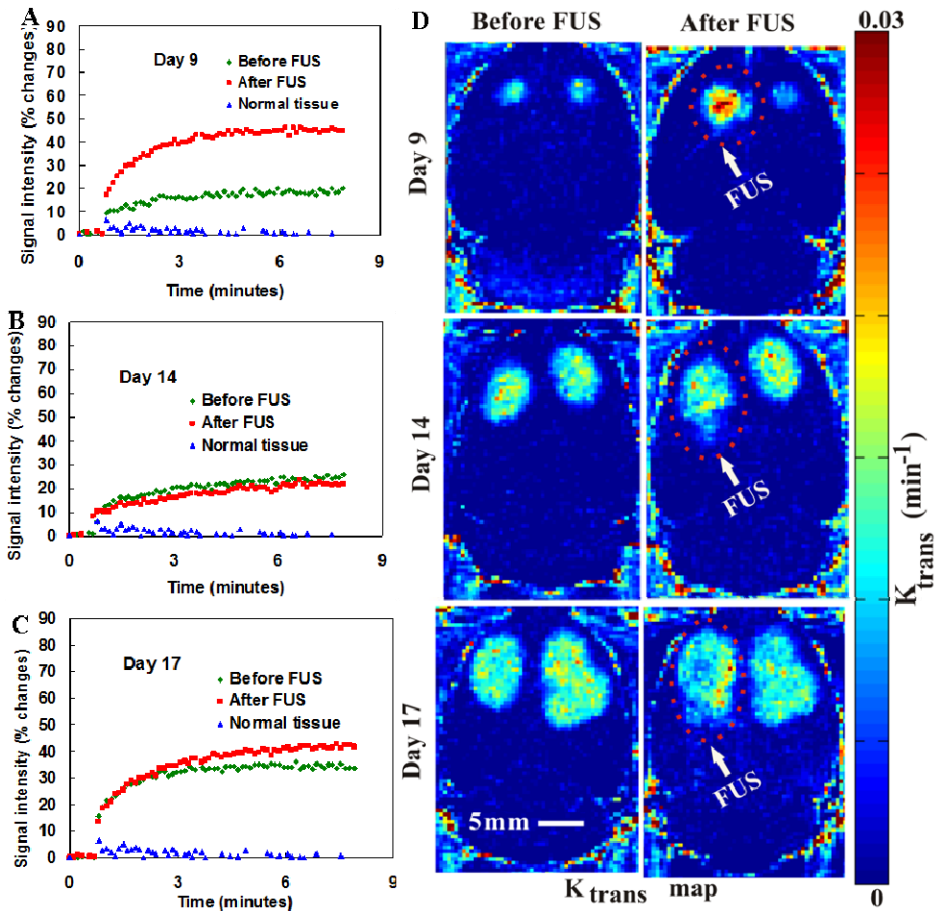


Figure 6. 2 Example of signal intensity changes in sonicated tumor and permeability maps in the bilateral tumors at different stages of tumor growth before and after FUS. (A-C) Change of signal intensity of Gd-DTPA on sonicated tumor was measured (before and after FUS) at three different days (9, 14 and 17 days after implantation) during DCE-MRI. After FUS, the signal intensity of Gd-DTPA on sonicated tumor was increased significantly ($P < 0.05$), at day 9 but not at day 14 or 17 compared with before FUS. (D) Maps of K_{trans} for Gd-DTPA obtained after two separate injections (before and after FUS) on three different days (9, 14 and 17 days after implantation). Before FUS, the K_{trans} values for the both tumors appeared similar on days 9, 14 and 17. They increased, particularly at day 9, for the sonicated tumors (shown by arrow in Fig. 3D). K_{trans} values are indicated in the color bar.

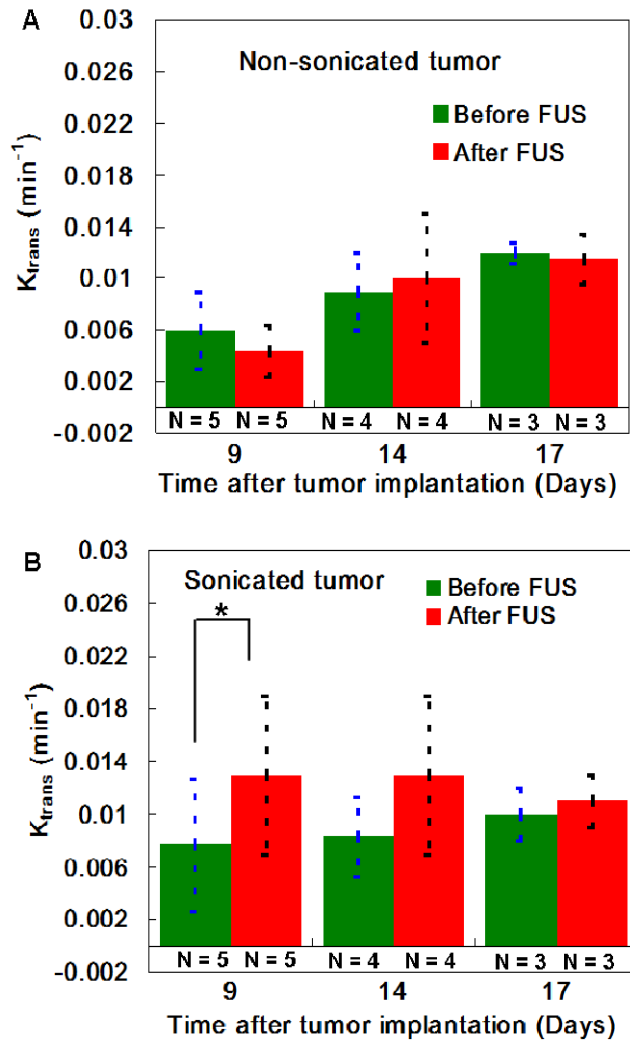


Figure 6. 3 Mean K_{trans} estimates (\pm S.D.) before and after FUS for the sonicated and control (non-sonicated) tumors at different stages of tumor growth. (A) The K_{trans} measurements in non-sonicated tumors were not significantly enhanced between the two DCE-MRI acquisitions (before and after FUS) at any day. (B) For the sonicated tumors, mean K_{trans} was significantly increased ($P < 0.05$) at day 9 but not at day 14 or 17. (* $P < 0.05$)

Figure 6. 4 shows the comparison of K_{trans} and doxorubicin concentration between the sonicated and non-sonicated tumors obtained DCE-MRI after sonication of one of the tumors. Similar to the results shown in Figure 6. 3, K_{trans} was significantly greater ($P < 0.05$) at day 9, but not at days 14 or 17. The mean ratio of

K_{trans} between the sonicated and non-sonicated tumors was 1.7 ± 1.2 , 1.6 ± 2 , 1.1 ± 2 , and, respectively, at days 9, 14, and 17 (Figure 6. 4A). In contrast, the doxorubicin concentration was enhanced significantly at all days ($P < 0.05$ at day 9, $P < 0.01$ at day 14 and $P < 0.0001$ at day 17) (Fig. 5B). The ratio of doxorubicin concentration between the sonicated and non-sonicated tumors was 2.7 ± 1.3 , 2.03 ± 1.08 , and 2.33 ± 1.8 for days 9, 14, and 17 respectively (Figure 6. 4B). Other than a moderate correlation ($R^2=0.44$) at day 9, there was no clear relationship between doxorubicin concentration and K_{trans} after FUS-induced BBB disruption. No significant difference ($P > 0.05$) was observed in f_v between measurements made before and after FUS or between the sonicated and non-sonicated tumors.

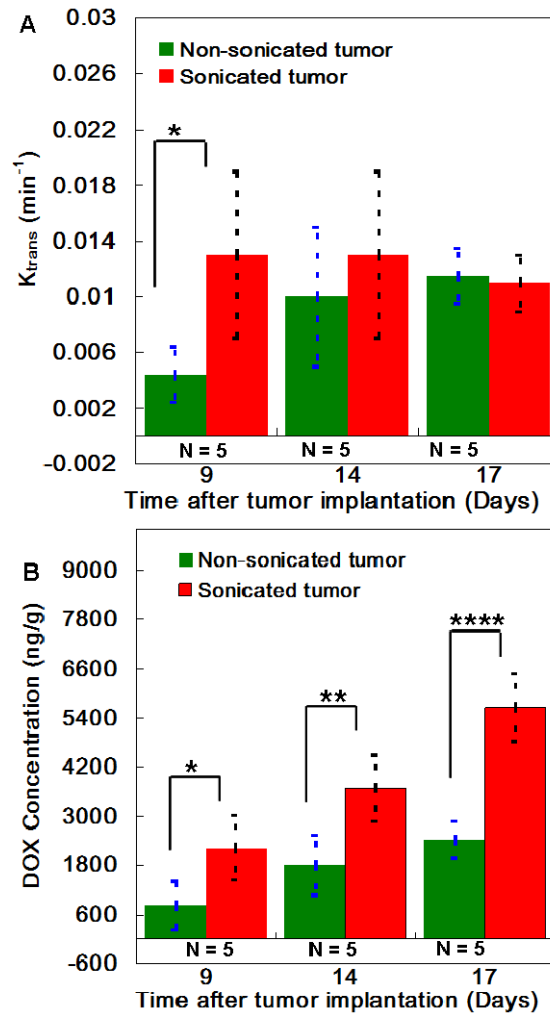


Figure 6. 4 Mean K_{trans} estimates and doxorubicin concentrations (\pm S.D.) at different stages of tumor growth for the sonicated and control (non-sonicated) tumors. (A) The K_{trans} measurements in the sonicated tumors were significantly enhanced compared those in the controls at day 9 but not at day 14 or 17. (B) Doxorubicin concentration was significantly enhanced at all days. (* $P<0.05$; ** $P<0.01$; **** $P<0.0001$)

6.1.3 Histological findings

Histological examination was performed on two rats after sonication at day 9 and 14. Tumors in both groups appeared as solid masses that replaced large amounts of brain tissue (Figure 6. 5A-B). The tumor bulk consisted of viable and rapidly

dividing spindle-shaped cells. Tiny necrotic sites scattered throughout the tumor were observed on day 14 but not on day 9 (yellow square in Figure 6. 5B). Those sites were comparatively smaller than the rest of the tumor mass. The sonicated tumors appeared unaffected in the H&E stained sections. The only effect of note was a small number of tiny clusters of extravasated erythrocytes (petechiae) that were scattered throughout the sonicated tumor regions (Figure 6. 5C-D, magnified view of red squares).

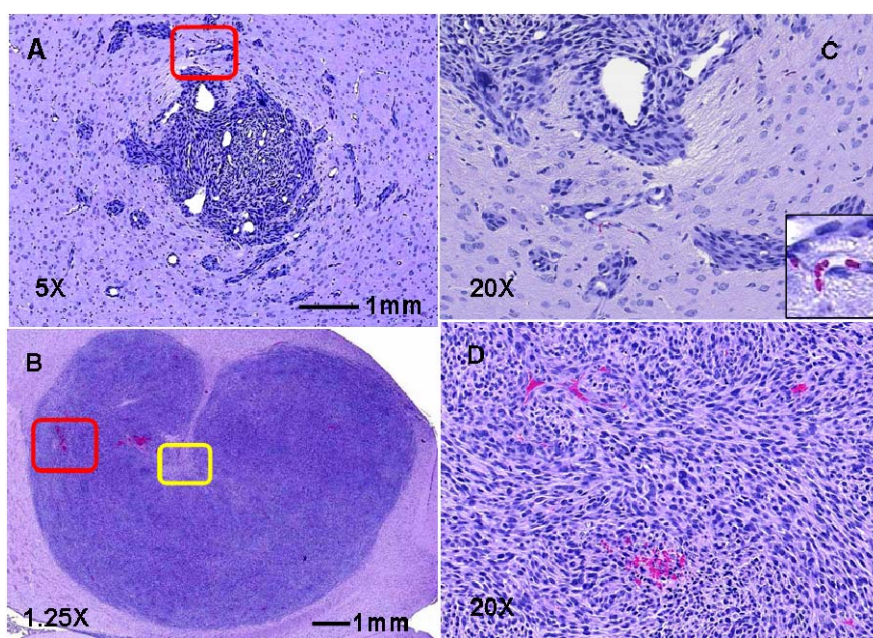


Figure 6. 5 Appearance of two 9L gliosarcoma at different days after implantation in histology. (A-B) Appearance of the tumors in an H&E stained section at day 9 (5 \times) and 14 (1.25 \times). The tumors appeared as solid masses that replaced large volumes of brain tissue. The bulk of the tumors consisted of rapidly dividing spindle-shaped cells with some small necrotic zones evident on day 14 (yellow square in B). (C-D) Magnified views (20x) of the red boxes. Most of the sonicated region appeared unaffected, but in a few areas tiny petechiae were observed.

6.2 Discussion

This study investigated the pharmacokinetic characteristics of small and large-molecule agents at different stages of tumor growth after BBB/BTB permeabilization with microbubble-enhanced FUS. Gd-DTPA (938 Da) and DCE-MRI were used to noninvasively provide semiquantitative measures of transport across these vascular barriers, and the concentration of doxorubicin, which was administered in ~100 nm liposomes, was measured in the tumor post mortem. Microbubble-enhanced FUS succeeded in increasing doxorubicin concentration by a factor of two or more regardless of the stage of tumor growth, but the enhanced delivery of Gd-DTPA, reflected in transport coefficient K_{trans} measured in DCE-MRI, was significantly enhanced only at the early stage of tumor growth. K_{trans} was slightly elevated compared to the non-sonicated tumors at later time points, but there was substantial variation and the increases were not statistically significant. That finding is consistent with the results of a study by Chu et al., who also found that microbubble-enhanced sonication could increase delivery of Gd-DTPA in early, but not in late-stage tumors [209]

If this finding that K_{trans} for Gd-DTPA of late-stage tumors cannot be significantly increased is correct, it suggests that there could be a size-dependent

maximum level enhancement in BTB permeability that can be achieved by FUS and microbubbles. In contrast to Gd-DTPA, the sonication-induced enhancement in doxorubicin delivery increased at days 14 and 17. However, future work investigating agents with a range of different sizes would be necessary to understand whether these results are true in general. In addition, the 9L gliosarcoma is a highly aggressive tumor model; it would be interesting to investigate less aggressive models to further understand how tumor development influences the ability to enhance delivery of drugs of different sizes.

The fact that FUS appeared to be more effective in delivering a drug encapsulated in a large carrier regardless of the tumor stage is encouraging, as it suggests that even late-stage tumors can benefit from FUS-induced drug enhancement. Many promising drug carriers such as liposomes and various other nano-carriers are being developed that may be useful for brain tumors if the challenges created by the BTB and BBB can be overcome. These agents can be more targeted and have fewer side effects compared to the broad-spectrum chemotherapy agent doxorubicin. However, more work is needed to confirm that drug penetration away from the blood vessels, which can be relatively small for large particles, is sufficient to achieve a

therapeutic response. Prior work with liposomal doxorubicin and brain tumor models [170,191], and the development of “brain-penetrating” nano-carriers [263] are encouraging in this regard.

Unfortunately, a good correlation with doxorubicin delivery and K_{trans} measurements with the commonly-used MRI contrast agent Gd-DTPA was not seen, which would have been useful since it could enable one to noninvasively estimate drug concentrations. Several studies have found a good correlation between signal intensity changes in contrast enhanced MRI and that of a drug or tracer in the normal brain or in tumor models [208,264,265]. Most relevant to this study, Treat et al. compared MRI signal enhancement after Gd-DTPA injection and doxorubicin concentration in the normal rat brain after FUS-BBBD [95]. Unlike in this work those experiments, which also used liposomal doxorubicin, a good correlation was observed between these two measurements. This discrepancy was likely due to differences between normal brain and tumor blood vessels. In contrast to the normal brain, where FUS-induced permeability changes to the BBB might be expected to be relatively reproducible, the vascular permeability in a tumor can vary widely and can change over time, and it is likely that predicting the sonication-induced changes to the

BTB is not straightforward. This discrepancy is likely to be particularly stark when the drug and contrast agent have a large difference in size or in other chemical properties. It would be interesting to repeat this study with liposomal MRI contrast agent.

6.3 Acoustics Emission

Previous work has demonstrated that the acoustic emissions recorded during sonication can be used to characterize the microbubble activity, which can be useful for monitoring FUS-BBBD [124,125,139,204]. This work has shown that signatures for robust stable cavitation – strong harmonics, subharmonics, or ultraharmonics – are produced when the microbubbles are sonicated at an intensity that results in BBBD. In contrast, when wideband emissions are produced, which are a signature for inertial cavitation [74], vascular damage is produced in addition to FUS-BBBD [139]. As I showed in Chapter 4, avoiding this vascular damage in the brain outside the tumor margins can be important for avoiding permanent brain damage. To date, nobody has investigated this approach in tumors.

Thus, in addition to above-mentioned DCE-MRI method, we performed a feasibility study where analysis of acoustic emission of microbubbles were compared

to extravasation of the MRI contrast agent Gd-DTPA.

6.3.1 Acoustic Emissions vs. MRI

The acoustic emission and MRI findings of a tumor sonication are as shown in figure Figure 6. 6. A total of nine sonications were applied in a rat with an implanted 9L rat glioma. First, emissions signals were acquired without microbubbles at each target. We then acquired data with microbubbles at the same exposure levels. The emissions were recorded with a passive cavitation detector (a hydrophone) using a high-speed digitizer card. We then examined the spectra (calculated via FFT) of the data acquired with microbubbles normalized to baseline data, as described earlier [125]. The spectrum shown in Figure 6. 6 was typical of what was observed. After normalizing the microbubble-enhanced data to that acquired without microbubbles, all that remained was strong harmonic emissions. The average strength of the harmonics was then calculated for each target, using metrics described earlier [125].

Contrast enhanced MRI was also acquired before and after the sonications. A contrast enhanced image acquired after FUS is shown in Figure 6. 6; the inset shows a map of the enhancement after sonication normalized to that obtained before

sonication. The locations of the sonicated targets is evident in this enhancement map.

Superimposed on this map is the strength of the harmonic activity measured from the acoustic emission. A correlation between the two measurements is evident.

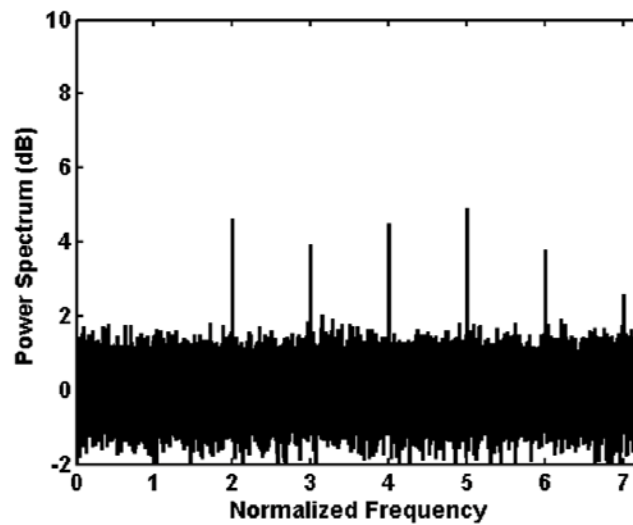
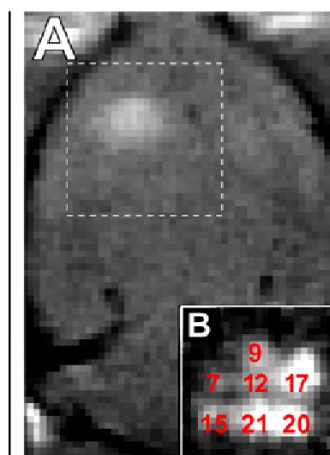


Figure 6. 6A Acoustic emissions acquired during sonications in a tumor-bearing rat. This example is a typical power spectra showing strong harmonic emissions. No broadband emission was evident. The emissions recorded during sonication with microbubbles were normalized to baseline data obtained during identical sonications without microbubbles.



Post-FUS CE-T1W

Figure 6. 6B MRI acquired after sonication of a tumor in a rat brain. (A) Contrast-enhanced T1-weighted MRI acquired after the sonications. The same imaging was acquired before the sonications as well. To examine the changes induced by the sonications, we normalized the post-sonication enhancement to the pre-sonication values. The changes in enhancement in the tumor are shown in (B). The individual sonication locations are evident. The superimposed numbers are the strength of the harmonic emissions acquired during these sonications. A correlation between the amount of enhancement induced by the sonications and the harmonic emissions recorded during the sonications is clearly evident.

6.3.2 Discussion

While we clearly need to repeat this study in more animals, these results are encouraging for the prospect of controlling FUS-BBBD. Our laboratory found previously that the strength of the harmonic emissions is correlated with the strength of BBB disruption in nonhuman primates [125], and using this as a method to control FUS-BBBD to ensure that it is safe and effective. The present results suggest that the strength of the harmonic emissions, may also be related to the change in vascular permeability in a tumor. If these results are verified, it could be an important development for the clinical translation of this technology.

Chapter 7: Conclusions and Future Work

7.1 Conclusions

In this thesis, MRgFUS technology was used to induce BBB/BTB permeabilization for the targeted delivery of a chemotherapy agent that normally does not reach the brain at all and that normally is not effectively delivered to brain tumors. The BBB/BTB and their limitations for brain drug delivery have prompted several different techniques to overcome these limitations, including invasive methods, biopharmaceutical approaches, and different methods to transiently disrupt the BBB distruption. These methods, including FUS, have different advantages and disadvantages, as I discussed in Chapter 1. Additionally, the underlying mechanisms due to interaction of microbubble with ultrasound were described briefly in that chapter. Furthermore, the working principles of MRI and DCE-MRI method used to observe the BBB/BTB permeability change due to FUS were outlined.

An overview of common methods and materials used in this dissertation was discussed in Chapter 2. In that chapter I described the animal preparation protocol, my experimental set up for MRI-guided FUS, the chemotherapy agent I used, the methods I used for transducer calibration, the MRI sequences I used to guide the procedure and

evaluate the results, and the fluorometry and fluorescent microscopy techniques I employed to visualize and measure drug concentrations.

Ultrasound-mediated Lipo-DOX delivery through BBB and its concentration in the brain were described in Chapter 3. Clinically relevant concentrations of doxorubicin ($\sim 4.8 \pm 0.5 \mu\text{g/g}$) were delivered to the brain with the sonication parameters (0.69 MHz; 0.55 MPa; 10 ms bursts; 1 Hz PRF; 60s duration), microbubble concentration (Definity, 10 $\mu\text{l/kg}$), and Lipo-DOX dose (5.67 mg/kg) I used. I found that I could achieve a clinically-relevant concentration, which I based on a study that compared doxorubicin concentrations in human tumors with clinical outcomes [237]. I also found that the resulting concentration was reduced by 32% when the agent was injected 10 minute after the last sonication. These results are encouraging for the prospect of using this drug delivery technique in an invasive glioma, where we will need to deliver drugs across the intact BBB to reach cancer cells infiltrating into the normal brain, and for optimizing the procedure.

The safety of using multiple sessions of FUS-BBBD and Lipo-DOX in the normal brain was investigated in Chapter 4. From histological analysis, we found that after three weekly treatments, the sonicated brain tissue in the focal plane was

unaffected in rats that received FUS-BBBD only, despite MRI evidence that minor vascular damage occurred during some of the sonications. In contrast, only one out of four rats that received FUS-BBBD and Lipo-DOX appeared completely unaffected at focal plane; the other three evidence of prior tissue damage (small scars and a small cyst in one case). The result indicates that while delivery of Lipo-DOX to the rat brain can result in minor damage, the severe neurotoxicity seen in earlier works [266] does not appear to occur with delivery via FUS-BBB disruption. While future work is needed, the results suggest that Lipo-DOX can exacerbate damage resulting from inertial cavitation. I base this speculation on the fact that MRI evidence suggested that vascular damage was produced during the sonications in the animals that both did and did not receive Lipo-DOX, while evidence of permanent prior damage was only observed in the rats who received Lipo-DOX. Based on these findings, I would recommend caution when sonicating the margin around a tumor.

The therapeutic efficacy of three weekly sessions of FUS and Lipo-DOX in the 9L rat glioma model has been demonstrated in chapter 5. Animals that received FUS and Lipo-DOX (N=8) had a median survival time that was increased significantly ($P < 0.001$) compared to animals who received Lipo-DOX only (N = 6),

FUS only (N=8), or no treatment (N=7). The median survival for animals that received FUS and Lipo-DOX was increased by 100% relative to untreated controls, whereas animals who received Lipo-DOX alone had only a 16% improvement. Animals who received only FUS showed no improvement. No tumor cells were found in histology in 4/8 animals in the FUS + Lipo-DOX group, and in two animals, only a few tumor cells were detected. Overall, this work demonstrates that multiple sessions using this FUS technique to enhance the delivery of Lipo-DOX can result in a pronounced therapeutic effect, at least in this rat glioma model. I would recommend continuing this work in a better tumor model that is genetically similar to a human glioma and that is more infiltrative. Methods to minimize the systemic dose and to avoid side-effects also should be pursued.

Changes in vascular permeability in a rat glioma model resulting from FUS and microbubbles were investigated as a function of time after tumor implantation using dynamic contrast-enhanced MRI (DCE-MRI) in Chapter 6. The transfer coefficient (K_{trans}) describing the extravasation of the MRI contrast agent Gd-DTPA was measured via DCE-MRI before and after sonication. I then euthanized the animal and measured doxorubicin concentration in the tumors. Tumor doxorubicin

concentrations increased monotonically (823 ± 600 , 1817 ± 732 and 2432 ± 448 ng/g) in non-sonicated control tumors at 9, 14 and 17 days respectively. With FUS-induced BTB permeabilization, the Lipo-DOX concentrations were enhanced significantly ($P<0.05$, $P<0.01$, and $P<0.0001$ at days 9, 14, and 17, respectively) and were greater than the control tumors by a factor of two or more (2222 ± 784 , 3687 ± 796 and 5658 ± 821 ng/g) regardless of the stage of tumor growth. In contrast, the transfer coefficient K_{trans} was significantly ($p<0.05$) enhanced compared to control tumors only at day 9 but not at day 14 or 17. These results suggested that FUS-induced enhancements in Lipo-DOX delivery are relatively consistent over time, at least in this tumor model. These results are also encouraging for the use of large drug carriers, as they suggest that even large/late-stage tumors can benefit from FUS-induced drug enhancement. The corresponding enhancements in K_{trans} , however, were found to be variable in large/late-stage tumors and not significantly different than controls. This difference perhaps reflects the size mismatch between the liposomal drug (~100 nm) and Gd-DTPA (molecular weight: 938 Da) and is unfortunate since it could be helpful to be able to use the MRI contrast agent as a drug surrogate to predict drug delivery. It may be necessary to use a larger MRI contrast agent to effectively evaluate the sonication-induced enhanced permeabilization in large/late-stage tumors when a large

drug carrier such as a liposome is used. In addition to DCE-MRI method, I investigated the feasibility of using recordings of the acoustic emissions produced by the microbubbles can be related to the extravasation of Gd-DTPA, as has been done previously in normal brain tissue [123,125]. While more work beyond this feasibility study is clearly needed, a correlation was evident between these two measurements suggesting that such methods can be useful for monitoring the sonications. Such methods are important when considering clinical translation. Ultimately we want to move this procedure out of the MRI environment. Having a method to reliably control the exposure level to ensure an adequate level of BBB/BBB permeabilization can enable this translation.

This work shows that FUS is a unique technology that can induce BBB or BTB permeabilization that is targeted, noninvasive and transient. It can enable the delivery of therapeutics (even nanocarriers such as a liposome) that normally do not reach the brain, enhance their delivery to brain tumors, and improve outcomes in a tumor model. When inertial cavitation is avoided, the sonications do not appear to have any deleterious effects on the brain, and the method is readily repeatable. I demonstrated that multiple treatments with FUS and Lipo-DOX significantly

inhibited tumor growth, increased survival, and appeared to completely eradicate the tumor in an aggressive rat gliosarcoma model. I also showed how MRI and acoustic methods can help to plan, monitor, and evaluate the treatment which offers the possibility of having control over the locations where drugs are delivered and concentrations of the drugs used. Importantly, my work has demonstrated that such methods can become more complicated in tumors and when a chemotherapy drug is used. When such methods are being developed, one cannot simply evaluate them in normal brain with imaging tracers.

7.2 Future work

The ultimate goal of this research is to translate ultrasound-mediated drug delivery technology from an animal model to human patients of with disorders of the CNS. Further research works need to be done before this technology becomes practical for widespread clinical trials. The results of the work in this thesis can help guide this future research.

Preliminary optical imaging results presented in Chapter 3 offer interesting findings on the likely cellular colocalization of doxorubicin in the brain after ultrasound-enhanced chemotherapy. While these results are not conclusive, it is clear

that this method has promise to further improve and optimize the procedure. For example, it is known that high interstitial pressures and a dense extracellular matrix can impede the delivery of drugs far enough from the vasculature to reach tumor cells, which can survive even in a hypoxic state [238]. By visualizing the drug and by staining blood vessels, we can investigate and even quantify this penetration depth [267]. We can then investigate different sonication parameters and other factors that we can use to improve drug penetration in addition to simply getting the drugs out of the blood vessels.

The experiments with FUS and Lipo-DOX in Chapters 4 and 5 showed that multiple treatments can have significant therapeutic outcomes while avoiding serious neurotoxicity. More consistent results may be obtained using online methods to optimize the exposure levels. Microbubble dynamics in real-time using online acoustic emission can be monitored [139,204] and re-treating areas with poor contrast enhancement can improve the local delivery and perhaps allow for a reduced systemic dose. It would also be interesting to investigate whether the sonications can release the doxorubicin from the liposomes, and has been observed by others with liposome-coated microbubbles [240]. While the 9L rat gliosarcoma model is highly

aggressive and the robust survival improvement observed here is certainly encouraging, future work is needed with models that are genetically similar to human GBM and that have similar growth patterns. Additional work in a more infiltrating tumor model is needed to ensure that we can safely and effectively target such regions. Since 9L has been shown to be immunogenic [260], it would be helpful to show that one can reproduce similar outcomes in non-immunogenic model.

In Chapter 6, if my finding that the transfer coefficient K_{trans} for Gd-DTPA of late-stage tumors cannot be significantly increased is correct, it suggests that there could be a size-dependent maximum level enhancement in BTB permeability that can be achieved by FUS and microbubbles. In contrast to Gd-DTPA, the sonication-induced enhancement in doxorubicin delivery increased at days 14 and 17. However, future work investigating agents with a range of different sizes would be necessary to understand whether these results are true in general. It would also be interesting to repeat this study with liposomal MRI contrast agent with size similar to Lipo-DOX. In addition, the 9L gliosarcoma is a highly aggressive tumor model; it would be interesting to investigate less aggressive models to further understand how tumor development influences the ability to enhance delivery of drugs of different sizes.

Finally, beyond its ability to enhance drug delivery for brain tumors, FUS can induce a number of different effects through mechanical, thermal, and vascular interactions. I am fascinated by the wide array of transient and irreversible bioeffects that we can induce using FUS in the brain. These bioeffects can be employed to develop new therapies and to probe brain function. I am particularly interested in studying the physiological response of the brain to ultrasound exposure in more detail. For example, it would be interesting to investigate the effects of ultrasound on the local concentrations of neurotransmitters/neuroinhibitors in different brain structures. If we can use FUS to modulate these substances in a controllable and predictable way, we will have a valuable tool that can open up entirely new directions for neuroscience. Targeted drug delivery is just the beginning.

References

- [1] E. A. Neuwelt, B. Bauer, C. Fahlke, G. Fricker, C. Iadecola, D. Janigro, L. Leybaert, Z. Molnár, M. E. O'Donnell, J. T. Povlishock, N. R. Saunders, F. Sharp, D. Stanimirovic, R. J. Watts, and L. R. Drewes, *Nat. Rev. Neurosci.* **12**, 169 (2011).
- [2] N. J. Abbott and I. A. Romero, *Mol. Med. Today* **2**, 106 (1996).
- [3] W. M. Pardridge, *Mol. Biotechnol.* **30**, 57 (2005).
- [4] A. F. Eichler, E. Chung, D. P. Kodack, J. S. Loeffler, D. Fukumura, and R. K. Jain, *Nat. Rev. Clin. Oncol.* **8**, 344 (2011).
- [5] G. Minniti, D. Amelio, M. Amichetti, M. Salvati, R. Muni, A. Bozzao, G. Lanzetta, S. Scarpino, A. Arcella, and R. M. Enrici, *Radiother. Oncol. J. Eur. Soc. Ther. Radiol. Oncol.* **97**, 377 (2010).
- [6] M. C. Dobelbower, O. L. Burnett Iii, R. A. Nordal, L. B. Nabors, J. M. Markert, M. D. Hyatt, and J. B. Fiveash, *J. Med. Imaging Radiat. Oncol.* **55**, 77 (2011).
- [7] M. C. Chamberlain, *J. Neurooncol.* **101**, 319 (2011).
- [8] D. Fukumura and R. K. Jain, *J. Cell. Biochem.* **101**, 937 (2007).
- [9] A. Régina, M. Demeule, A. Laplante, J. Jodoin, C. Dagenais, F. Berthelet, A. Moghrabi, and R. Béliveau, *Cancer Metastasis Rev.* **20**, 13 (2001).
- [10] P. R. Lockman, R. K. Mittapalli, K. S. Taskar, V. Rudraraju, B. Gril, K. A. Bohn, C. E. Adkins, A. Roberts, H. R. Thorsheim, J. A. Gaasch, S. Huang, D. Palmieri, P. S. Steeg, and Q. R. Smith, *Clin. Cancer Res. Off. J. Am. Assoc. Cancer Res.* **16**, 5664 (2010).
- [11] D. R. Groothuis, *Neuro-Oncol.* **2**, 45 (2000).
- [12] W. M. Pardridge, *Drug Discov. Today* **12**, 54 (2007).
- [13] J. P. Blumling Iii and G. A. Silva, *Curr. Pharm. Biotechnol.* **13**, 2417 (2012).

- [14] T. Tomita, *J. Neurooncol.* **10**, 57 (1991).
- [15] R. H. Bobo, D. W. Laske, A. Akbasak, P. F. Morrison, R. L. Dedrick, and E. H. Oldfield, *Proc. Natl. Acad. Sci. U. S. A.* **91**, 2076 (1994).
- [16] C. Guerin, A. Olivi, J. D. Weingart, H. C. Lawson, and H. Brem, *Invest. New Drugs* **22**, 27 (2004).
- [17] H. Brem and P. Gabikian, *J. Control. Release Off. J. Control. Release Soc.* **74**, 63 (2001).
- [18] L. K. Fung, M. Shin, B. Tyler, H. Brem, and W. M. Saltzman, *Pharm. Res.* **13**, 671 (1996).
- [19] J. Voges, R. Reszka, A. Gossmann, C. Dittmar, R. Richter, G. Garlip, L. Kracht, H. H. Coenen, V. Sturm, K. Wienhard, W.-D. Heiss, and A. H. Jacobs, *Ann. Neurol.* **54**, 479 (2003).
- [20] G. Fleischhack, U. Jaehde, and U. Bode, *Clin. Pharmacokinet.* **44**, 1 (2005).
- [21] L. Illum, *J. Control. Release Off. J. Control. Release Soc.* **87**, 187 (2003).
- [22] L. Illum, *Drug Discov. Today* **7**, 1184 (2002).
- [23] M. I. Ugwoke, R. U. Agu, N. Verbeke, and R. Kinget, *Adv. Drug Deliv. Rev.* **57**, 1640 (2005).
- [24] A. Pires, A. Fortuna, G. Alves, and A. Falcão, *J. Pharm. Pharm. Sci. Publ. Can. Soc. Pharm. Sci. Société Can. Sci. Pharm.* **12**, 288 (2009).
- [25] W. H. Oldendorf, S. Hyman, L. Braun, and S. Z. Oldendorf, *Science* **178**, 984 (1972).
- [26] N. J. Abbott, A. A. K. Patabendige, D. E. M. Dolman, S. R. Yusof, and D. J. Begley, *Neurobiol. Dis.* **37**, 13 (2010).
- [27] W. M. Pardridge, *Drug Discov. Today* **12**, 54 (2007).
- [28] E. Y. Zhang, G. T. Knipp, S. Ekins, and P. W. Swaan, *Drug Metab. Rev.* **34**, 709 (2002).

- [29] W. M. Pardridge, *Mol. Interv.* **3**, 90 (2003).
- [30] W. M. Pardridge, *Pharm. Res.* **24**, 1733 (2007).
- [31] P. Blasi, S. Giovagnoli, A. Schoubben, M. Ricci, and C. Rossi, *Adv. Drug Deliv. Rev.* **59**, 454 (2007).
- [32] J.-C. Olivier, *NeuroRx J. Am. Soc. Exp. Neurother.* **2**, 108 (2005).
- [33] A. Schnyder and J. Huwyler, *NeuroRx J. Am. Soc. Exp. Neurother.* **2**, 99 (2005).
- [34] R. D. Broadwell, B. J. Balin, and M. Salzman, *Proc. Natl. Acad. Sci. U. S. A.* **85**, 632 (1988).
- [35] I. Mellman, *Annu. Rev. Cell Dev. Biol.* **12**, 575 (1996).
- [36] S. Mukherjee, R. N. Ghosh, and F. R. Maxfield, *Physiol. Rev.* **77**, 759 (1997).
- [37] S. I. Rapoport, *Am. J. Physiol.* **219**, 270 (1970).
- [38] S. I. Rapoport, *Expert Opin. Investig. Drugs* **10**, 1809 (2001).
- [39] R. A. Kroll and E. A. Neuwelt, *Neurosurgery* **42**, 1083 (1998).
- [40] M.-A. Bellavance, M. Blanchette, and D. Fortin, *AAPS J.* **10**, 166 (2008).
- [41] N. D. Doolittle, M. E. Miner, W. A. Hall, T. Siegal, E. Jerome, E. Osztie, L. D. McAllister, J. S. Bubalo, D. F. Kraemer, D. Fortin, R. Nixon, L. L. Muldoon, and E. A. Neuwelt, *Cancer* **88**, 637 (2000).
- [42] W. A. Hall, N. D. Doolittle, M. Daman, P. K. Bruns, L. Muldoon, D. Fortin, and E. A. Neuwelt, *J. Neurooncol.* **77**, 279 (2006).
- [43] K. Jahnke, D. F. Kraemer, K. R. Knight, D. Fortin, S. Bell, N. D. Doolittle, L. L. Muldoon, and E. A. Neuwelt, *Cancer* **112**, 581 (2008).
- [44] L. Angelov, N. D. Doolittle, D. F. Kraemer, T. Siegal, G. H. Barnett, D. M. Peereboom, G. Stevens, J. McGregor, K. Jahnke, C. A. Lacy, N. A. Hedrick, E. Shalom, S. Ference, S. Bell, L. Sorenson, R. M. Tyson, M. Haluska, and E. A. Neuwelt, *J. Clin. Oncol. Off. J. Am. Soc. Clin. Oncol.* **27**, 3503 (2009).

- [45] J. A. Boockvar, A. J. Tsiouris, C. P. Hofstetter, I. Kovanlikaya, S. Fralin, K. Kesavabhotla, S. M. Seedial, S. C. Pannullo, T. H. Schwartz, P. Stieg, R. D. Zimmerman, J. Knopman, R. J. Scheff, P. Christos, S. Vallabhajosula, and H. A. Riina, *J. Neurosurg.* **114**, 624 (2011).
- [46] D. J. Guillaume, N. D. Doolittle, S. Gahramanov, N. A. Hedrick, J. B. Delashaw, and E. A. Neuwelt, *Neurosurgery* **66**, 48 (2010).
- [47] T. Inamura, T. Nomura, K. Ikezaki, M. Fukui, G. Pöllinger, and K. L. Black, *Neurol. Res.* **16**, 125 (1994).
- [48] M. Gutman, R. Laufer, A. Eisenthal, G. Goldman, A. Ravid, M. Inbar, and J. M. Klausner, *Cancer Immunol. Immunother. CII* **43**, 240 (1996).
- [49] K. L. Black and C. C. Chio, *Neurol. Res.* **14**, 402 (1992).
- [50] H. E. de Vries, M. C. Blom-Rosemalen, M. van Oosten, A. G. de Boer, T. J. van Berkel, D. D. Breimer, and J. Kuiper, *J. Neuroimmunol.* **64**, 37 (1996).
- [51] K. Hynynen and Gautherie M, in *Biophys. Technol. Ultrasound Hyper-Thermia* (New York: Springer-Verlag, 1990), pp. 61–115.
- [52] K. Hynynen and B. A. Lulu, *Invest. Radiol.* **25**, 824 (1990).
- [53] T. G. Leighton, *The Acoustic Bubble* (Academic Press Limited, San Diego, CA, 1994).
- [54] C. J. Diederich, R. J. Stafford, W. H. Nau, E. C. Burdette, R. E. Price, and J. D. Hazle, *Med. Phys.* **31**, 405 (2004).
- [55] N. McDannold, C. M. Tempany, F. M. Fennessy, M. J. So, F. J. Rybicki, E. A. Stewart, F. A. Jolesz, and K. Hynynen, *Radiology* **240**, 263 (2006).
- [56] S. Vaezy, R. Martin, and L. Crum, *Echocardiogr. Mt. Kisco N* **18**, 309 (2001).
- [57] C. Delon-Martin, C. Vogt, E. Chignier, C. Guers, J. Y. Chapelon, and D. Cathignol, *Ultrasound Med. Biol.* **21**, 113 (1995).
- [58] M. J. Borrelli, W. D. O'Brien Jr, E. Hamilton, M. L. Oelze, J. Wu, L. J. Bernock, S. Tung, H. Rokadia, and W. C. Culp, *J. Vasc. Interv. Radiol. JVIR*

- 23**, 1677 (2012).
- [59] H. Medwin, *Ultrasonics* **15**, 7 (1977).
- [60] N. de Jong, A. Bouakaz, and P. Frinking, *Echocardiogr. Mt. Kisco N* **19**, 229 (2002).
- [61] N. de Jong, L. Hoff, T. Skotland, and N. Bom, *Ultrasonics* **30**, 95 (1992).
- [62] N. de Jong and L. Hoff, *Ultrasonics* **31**, 175 (1993).
- [63] C. C. Church, *J. Acoust. Soc. Am.* **97**, 1510 (1995).
- [64] J. S. Allen and M. M. Rashid, *J. Appl. Mech.* **71**, 195 (2004).
- [65] Hoff, Sontum, and Hovem, *J. Acoust. Soc. Am.* **107**, 2272 (2000).
- [66] K. E. Morgan, J. S. Allen, P. A. Dayton, J. E. Chomas, A. L. Klibaov, and K. W. Ferrara, *IEEE Trans. Ultrason. Ferroelectr. Freq. Control* **47**, 1494 (2000).
- [67] K. Sarkar, W. T. Shi, D. Chatterjee, and F. Forsberg, *J. Acoust. Soc. Am.* **118**, 539 (2005).
- [68] P. Marmottant, S. van der Meer, M. Emmer, M. Versluis, N. de Jong, S. Hilgenfeldt, and D. Lohse, *J. Acoust. Soc. Am.* **118**, 3499 (2005).
- [69] N. de Jong, M. Emmer, A. van Wamel, and M. Versluis, *Med. Biol. Eng. Comput.* **47**, 861 (2009).
- [70] L. Hoff, *Acoustic Characterization of Contrast Agents for Medical Ultrasound Imaging* (Kluwer Academic, 2001).
- [71] J. G. Lynn and T. J. Putnam, *Am. J. Pathol.* **20**, 637 (1944).
- [72] W. J. FRY and F. J. FRY, *IRE Trans. Med. Electron.* **ME-7**, 166 (1960).
- [73] H. T. BALLANTINE Jr, E. BELL, and J. MANLAPAZ, *J. Neurosurg.* **17**, 858 (1960).
- [74] P. P. Lele, in *Ultrasound*, edited by M. H. Repacholi, M. Grandolfo, and A. Rindi (Springer US, Boston, MA, 1987), pp. 275–306.

- [75] R. MEYERS, W. J. FRY, F. J. FRY, L. L. DREYER, D. F. SCHULTZ, and R. F. NOYES, *J. Neurosurg.* **16**, 32 (1959).
- [76] R. F. Heimbürger, *Indiana Med. J. Indiana State Med. Assoc.* **78**, 469 (1985).
- [77] K. Hynynen and N. McDannold, *Int. J. Hyperth. Off. J. Eur. Soc. Hyperthermic Oncol. North Am. Hyperth. Group* **20**, 725 (2004).
- [78] G. T. Clement and K. Hynynen, *Phys. Med. Biol.* **47**, 1219 (2002).
- [79] J. F. Aubry, M. Tanter, M. Pernot, J. L. Thomas, and M. Fink, *J. Acoust. Soc. Am.* **113**, 84 (2003).
- [80] Y. Ishihara, A. Calderon, H. Watanabe, K. Okamoto, Y. Suzuki, K. Kuroda, and Y. Suzuki, *Magn. Reson. Med. Off. J. Soc. Magn. Reson. Med. Soc. Magn. Reson. Med.* **34**, 814 (1995).
- [81] N. McDannold, G. T. Clement, P. Black, F. Jolesz, and K. Hynynen, *Neurosurgery* **66**, 323 (2010).
- [82] E. Martin, D. Jeanmonod, A. Morel, E. Zadicario, and B. Werner, *Ann. Neurol.* **66**, 858 (2009).
- [83] L. BAKAY, H. T. BALLANTINE Jr, T. F. HUETER, and D. SOSA, *AMA Arch. Neurol. Psychiatry* **76**, 457 (1956).
- [84] N. Vykhodtseva, 5th Int. Symp. Ultrasound Biol Med Puschino Russ. (1981).
- [85] J. T. Patrick, M. N. Nolting, S. A. Goss, K. A. Dines, J. L. Clendenon, M. A. Rea, and R. F. Heimbürger, *Adv. Exp. Med. Biol.* **267**, 369 (1990).
- [86] N. I. Vykhodtseva, K. Hynynen, and C. Damianou, *Ultrasound Med. Biol.* **21**, 969 (1995).
- [87] A. H. Mesiwala, L. Farrell, H. J. Wenzel, D. L. Silbergeld, L. A. Crum, H. R. Winn, and P. D. Mourad, *Ultrasound Med. Biol.* **28**, 389 (2002).
- [88] N. McDannold, N. Vykhodtseva, F. A. Jolesz, and K. Hynynen, *Magn. Reson. Med. Off. J. Soc. Magn. Reson. Med. Soc. Magn. Reson. Med.* **51**, 913 (2004).
- [89] K. Hynynen, N. McDannold, N. Vykhodtseva, and F. A. Jolesz, *Radiology* **220**,

- 640 (2001).
- [90] N. Sheikov, N. McDannold, N. Vykhodtseva, F. Jolesz, and K. Hynynen, *Ultrasound Med. Biol.* **30**, 979 (2004).
- [91] N. McDannold, C. D. Arvanitis, N. Vykhodtseva, and M. S. Livingstone, *Cancer Res.* **72**, 3652 (2012).
- [92] F. Marquet, Y.-S. Tung, T. Teichert, V. P. Ferrera, and E. E. Konofagou, *PloS One* **6**, e22598 (2011).
- [93] M. A. O'Reilly, Y. Huang, and K. Hynynen, *Phys. Med. Biol.* **55**, 5251 (2010).
- [94] K. Hynynen, N. McDannold, N. A. Sheikov, F. A. Jolesz, and N. Vykhodtseva, *NeuroImage* **24**, 12 (2005).
- [95] L. H. Treat, N. McDannold, N. Vykhodtseva, Y. Zhang, K. Tam, and K. Hynynen, *Int. J. Cancer J. Int. Cancer* **121**, 901 (2007).
- [96] R. Chopra, N. Vykhodtseva, and K. Hynynen, *ACS Chem. Neurosci.* **1**, 391 (2010).
- [97] N. McDannold, N. Vykhodtseva, and K. Hynynen, *Ultrasound Med. Biol.* **34**, 834 (2008).
- [98] N. McDannold, N. Vykhodtseva, and K. Hynynen, *Ultrasound Med. Biol.* **34**, 930 (2008).
- [99] F. Vlachos, Y.-S. Tung, and E. E. Konofagou, *Phys. Med. Biol.* **55**, 5451 (2010).
- [100] J. J. Choi, J. A. Feshitan, B. Baseri, S. Wang, Y.-S. Tung, M. A. Borden, and E. E. Konofagou, *IEEE Trans. Biomed. Eng.* **57**, 145 (2010).
- [101] G. Samiotaki, F. Vlachos, Y.-S. Tung, and E. E. Konofagou, *Magn. Reson. Med. Off. J. Soc. Magn. Reson. Med. Soc. Magn. Reson. Med.* **67**, 769 (2012).
- [102] J. J. Choi, K. Selert, Z. Gao, G. Samiotaki, B. Baseri, and E. E. Konofagou, *J. Cereb. Blood Flow Metab.* **31**, 725 (2011).
- [103] J. J. Choi, K. Selert, F. Vlachos, A. Wong, and E. E. Konofagou, *Proc. Natl.*

- Acad. Sci. **108**, 16539 (2011).
- [104] J. Park, Y. Zhang, N. Vykhodtseva, F. A. Jolesz, and N. J. McDannold, *J. Control. Release Off. J. Control. Release Soc.* **162**, 134 (2012).
- [105] F.-Y. Yang, Y.-S. Lin, K.-H. Kang, and T.-K. Chao, *J. Control. Release Off. J. Control. Release Soc.* **150**, 111 (2011).
- [106] R. Chopra, N. Vykhodtseva, and K. Hynynen, *ACS Chem. Neurosci.* **1**, 391 (2010).
- [107] M. A. O'Reilly, A. C. Waspe, M. Ganguly, and K. Hynynen, *Ultrasound Med. Biol.* **37**, 587 (2011).
- [108] N. McDannold, Y. Zhang, and N. Vykhodtseva, *Ultrasound Med. Biol.* **37**, 1259 (2011).
- [109] J. Wang, Y. Liu, L. Liu, C. Xia, Z. Zhang, and Y. Xue, *J. Neurooncol.* **102**, 213 (2011).
- [110] Z. Zhang, C. Xia, Y. Xue, and Y. Liu, *J. Neurosci. Res.* **87**, 2282 (2009).
- [111] Z. Zhang, Y. Xue, Y. Liu, and X. Shang, *Neurosci. Lett.* **481**, 21 (2010).
- [112] D. E. Goertz, C. Wright, and K. Hynynen, *Ultrasound Med. Biol.* **36**, 916 (2010).
- [113] K. F. Bing, G. P. Howles, Y. Qi, M. L. Palmeri, and K. R. Nightingale, *Ultrasound Med. Biol.* **35**, 1298 (2009).
- [114] K. Hynynen, N. McDannold, N. Vykhodtseva, and F. A. Jolesz, *Radiology* **220**, 640 (2001).
- [115] L. H. Treat, N. McDannold, N. Vykhodtseva, Y. Zhang, K. Tam, and K. Hynynen, *Int. J. Cancer J. Int. Cancer* **121**, 901 (2007).
- [116] J.-C. Weng, S.-K. Wu, W.-L. Lin, and W.-Y. I. Tseng, *Magn. Reson. Med. Off. J. Soc. Magn. Reson. Med. Soc. Magn. Reson. Med.* **65**, 802 (2011).
- [117] F.-Y. Yang, W.-M. Fu, W.-S. Chen, W.-L. Yeh, and W.-L. Lin, *Ultrason. Sonochem.* **15**, 636 (2008).

- [118] J. Park, Y. Zhang, N. Vykhodtseva, F. A. Jolesz, and N. J. McDannold, *J. Control. Release Off. J. Control. Release Soc.* **162**, 134 (2012).
- [119] F. Vlachos, Y.-S. Tung, and E. Konofagou, *Magn. Reson. Med. Off. J. Soc. Magn. Reson. Med. Soc. Magn. Reson. Med.* **66**, 821 (2011).
- [120] N. McDannold, N. Vykhodtseva, and K. Hynynen, *Ultrasound Med. Biol.* **33**, 584 (2007).
- [121] H.-L. Liu, C.-H. Pan, C.-Y. Ting, and M.-J. Hsiao, *Ultrasound Med. Biol.* **36**, 325 (2010).
- [122] M. A. O'Reilly, A. C. Waspe, M. Ganguly, and K. Hynynen, *Ultrasound Med. Biol.* **37**, 587 (2011).
- [123] N. McDannold, N. Vykhodtseva, and K. Hynynen, *Phys. Med. Biol.* **51**, 793 (2006).
- [124] Y.-S. Tung, F. Vlachos, J. J. Choi, T. Deffieux, K. Selert, and E. E. Konofagou, *Phys. Med. Biol.* **55**, 6141 (2010).
- [125] C. D. Arvanitis, M. S. Livingstone, N. Vykhodtseva, and N. McDannold, *PloS One* **7**, e45783 (2012).
- [126] C. X. Deng, F. Sieling, H. Pan, and J. Cui, *Ultrasound Med. Biol.* **30**, 519 (2004).
- [127] N. Sheikov, N. McDannold, S. Sharma, and K. Hynynen, *Ultrasound Med. Biol.* **34**, 1093 (2008).
- [128] N. Sheikov, N. McDannold, F. Jolesz, Y.-Z. Zhang, K. Tam, and K. Hynynen, *Ultrasound Med. Biol.* **32**, 1399 (2006).
- [129] S. B. Raymond, J. Skoch, K. Hynynen, and B. J. Bacskai, *J. Cereb. Blood Flow Metab. Off. J. Int. Soc. Cereb. Blood Flow Metab.* **27**, 393 (2007).
- [130] E. E. Cho, J. Drazic, M. Ganguly, B. Stefanovic, and K. Hynynen, *J. Cereb. Blood Flow Metab. Off. J. Int. Soc. Cereb. Blood Flow Metab.* **31**, 1852 (2011).
- [131] P. Dayton, A. Klibanov, G. Brandenburger, and K. Ferrara, *Ultrasound Med.*

- Biol. **25**, 1195 (1999).
- [132] H. Chen, W. Kreider, A. A. Brayman, M. R. Bailey, and T. J. Matula, *Phys. Rev. Lett.* **106**, 034301 (2011).
- [133] E. Sassaroli and K. Hynynen, *Phys. Med. Biol.* **50**, 5293 (2005).
- [134] B. Marty, B. Larrat, M. Van Landeghem, C. Robic, P. Robert, M. Port, D. Le Bihan, M. Pernot, M. Tanter, F. Lethimonnier, and S. Meriaux, *J. Cereb. Blood Flow Metab.* **32**, 1948 (2012).
- [135] G. P. Howles, K. F. Bing, Y. Qi, S. J. Rosenzweig, K. R. Nightingale, and G. A. Johnson, *Magn. Reson. Med. Off. J. Soc. Magn. Reson. Med. Soc. Magn. Reson. Med.* **64**, 995 (2010).
- [136] B. Baseri, J. J. Choi, Y.-S. Tung, and E. E. Konofagou, *Ultrasound Med. Biol.* **36**, 1445 (2010).
- [137] N. McDannold, N. Vykhodtseva, S. Raymond, F. A. Jolesz, and K. Hynynen, *Ultrasound Med. Biol.* **31**, 1527 (2005).
- [138] H.-L. Liu, Y.-Y. Wai, W.-S. Chen, J.-C. Chen, P.-H. Hsu, X.-Y. Wu, W.-C. Huang, T.-C. Yen, and J.-J. Wang, *Ultrasound Med. Biol.* **34**, 598 (2008).
- [139] N. McDannold, N. Vykhodtseva, and K. Hynynen, *Phys. Med. Biol.* **51**, 793 (2006).
- [140] Y.-S. Tung, F. Vlachos, J. J. Choi, T. Deffieux, K. Selert, and E. E. Konofagou, *Phys. Med. Biol.* **55**, 6141 (2010).
- [141] K. Hynynen, N. McDannold, N. Vykhodtseva, S. Raymond, R. Weissleder, F. A. Jolesz, and N. Sheikov, *J. Neurosurg.* **105**, 445 (2006).
- [142] H.-L. Liu, Y.-Y. Wai, P.-H. Hsu, L.-A. Lyu, J.-S. Wu, C.-R. Shen, J.-C. Chen, T.-C. Yen, and J.-J. Wang, *J. Cereb. Blood Flow Metab. Off. J. Int. Soc. Cereb. Blood Flow Metab.* **30**, 674 (2010).
- [143] X. Shang, P. Wang, Y. Liu, Z. Zhang, and Y. Xue, *J. Mol. Neurosci. MN* **43**, 364 (2011).

- [144] A. Alonso, E. Reinz, J. W. Jenne, M. Fatar, H. Schmidt-Glenewinkel, M. G. Hennerici, and S. Meairs, *J. Cereb. Blood Flow Metab. Off. J. Int. Soc. Cereb. Blood Flow Metab.* **30**, 1394 (2010).
- [145] J. Deng, Q. Huang, F. Wang, Y. Liu, Z. Wang, Z. Wang, Q. Zhang, B. Lei, and Y. Cheng, *J. Mol. Neurosci. MN* **46**, 677 (2012).
- [146] C. Xia, Y. Liu, P. Wang, and Y. Xue, *J. Mol. Neurosci. MN* **48**, 281 (2012).
- [147] A. N. Shajahan, C. Tirupathi, A. V. Smrcka, A. B. Malik, and R. D. Minshall, *J. Biol. Chem.* **279**, 48055 (2004).
- [148] S. Jalali, Y. Huang, D. J. Dumont, and K. Hynynen, *BMC Neurol.* **10**, 114 (2010).
- [149] H. Zhao, R. M. Sapolsky, and G. K. Steinberg, *Mol. Neurobiol.* **34**, 249 (2006).
- [150] R. Nath, K. McGinnis, S. Dutta, B. Shivers, and K. K. Wang, *Cell. Mol. Biol. Lett.* **6**, 173 (2001).
- [151] J. Harada and M. Sugimoto, *Jpn. J. Pharmacol.* **79**, 369 (1999).
- [152] A. Alonso, E. Reinz, M. Fatar, J. Jenne, M. G. Hennerici, and S. Meairs, *Neuroscience* **169**, 116 (2010).
- [153] J. Park, Z. Fan, R. E. Kumon, M. E. H. El-Sayed, and C. X. Deng, *Ultrasound Med. Biol.* **36**, 1176 (2010).
- [154] J. Park, Z. Fan, and C. X. Deng, *J. Biomech.* **44**, 164 (2011).
- [155] C. Ayata, H. K. Shin, S. Salomone, Y. Ozdemir-Gursoy, D. A. Boas, A. K. Dunn, and M. A. Moskowitz, *J. Cereb. Blood Flow Metab. Off. J. Int. Soc. Cereb. Blood Flow Metab.* **24**, 1172 (2004).
- [156] S. B. Raymond, J. Skoch, K. Hynynen, and B. J. Bacskai, *J. Cereb. Blood Flow Metab. Off. J. Int. Soc. Cereb. Blood Flow Metab.* **27**, 393 (2007).
- [157] A. Burgess, Y. Huang, W. Querbes, D. W. Sah, and K. Hynynen, *J. Control. Release Off. J. Control. Release Soc.* **163**, 125 (2012).
- [158] J. J. Choi, S. Wang, Y.-S. Tung, B. Morrison 3rd, and E. E. Konofagou,

- Ultrasound Med. Biol. **36**, 58 (2010).
- [159] L. L. Muldoon, M. A. Pagel, R. A. Kroll, S. Roman-Goldstein, R. S. Jones, and E. A. Neuwelt, *AJNR Am. J. Neuroradiol.* **20**, 217 (1999).
- [160] K.-J. Lin, H.-L. Liu, P.-H. Hsu, Y.-H. Chung, W.-C. Huang, J.-C. Chen, S.-P. Wey, T.-C. Yen, and I.-T. Hsiao, *Nucl. Med. Biol.* **36**, 853 (2009).
- [161] F.-Y. Yang, H.-E. Wang, G.-L. Lin, H.-H. Lin, and T.-T. Wong, *Int. J. Nanomedicine* **7**, 723 (2012).
- [162] S. B. Raymond, L. H. Treat, J. D. Dewey, N. J. McDannold, K. Hynynen, and B. J. Bacsikai, *PloS One* **3**, e2175 (2008).
- [163] Q. Huang, J. Deng, F. Wang, S. Chen, Y. Liu, Z. Wang, Z. Wang, and Y. Cheng, *Exp. Neurol.* **233**, 350 (2012).
- [164] A. B. Etame, R. J. Diaz, M. A. O'Reilly, C. A. Smith, T. G. Mainprize, K. Hynynen, and J. T. Rutka, *Nanomedicine Nanotechnol. Biol. Med.* **8**, 1133 (2012).
- [165] P.-H. Wang, H.-L. Liu, P.-H. Hsu, C.-Y. Lin, C.-R. C. Wang, P.-Y. Chen, K.-C. Wei, T.-C. Yen, and M.-L. Li, *J. Biomed. Opt.* **17**, 061222 (2012).
- [166] H.-L. Liu, M.-Y. Hua, P.-Y. Chen, P.-C. Chu, C.-H. Pan, H.-W. Yang, C.-Y. Huang, J.-J. Wang, T.-C. Yen, and K.-C. Wei, *Radiology* **255**, 415 (2010).
- [167] J. Mei, Y. Cheng, Y. Song, Y. Yang, F. Wang, Y. Liu, and Z. Wang, *J. Ultrasound Med. Off. J. Am. Inst. Ultrasound Med.* **28**, 871 (2009).
- [168] H.-Q. Zeng, L. Lü, F. Wang, Y. Luo, and S.-F. Lou, *J. Chemother. Florence Italy* **24**, 358 (2012).
- [169] K.-C. Wei, P.-C. Chu, H.-Y. J. Wang, C.-Y. Huang, P.-Y. Chen, H.-C. Tsai, Y.-J. Lu, P.-Y. Lee, I.-C. Tseng, L.-Y. Feng, P.-W. Hsu, T.-C. Yen, and H.-L. Liu, *PloS One* **8**, e58995 (2013).
- [170] M. Aryal, N. Vykhodtseva, Y.-Z. Zhang, J. Park, and N. McDannold, *J. Controlled Release* **169**, 103 (2013).

- [171] F.-Y. Yang, T.-T. Wong, M.-C. Teng, R.-S. Liu, M. Lu, H.-F. Liang, and M.-C. Wei, *J. Control. Release Off. J. Control. Release Soc.* **160**, 652 (2012).
- [172] H.-L. Liu, M.-Y. Hua, H.-W. Yang, C.-Y. Huang, P.-C. Chu, J.-S. Wu, I.-C. Tseng, J.-J. Wang, T.-C. Yen, P.-Y. Chen, and K.-C. Wei, *Proc. Natl. Acad. Sci. U. S. A.* **107**, 15205 (2010).
- [173] P.-Y. Chen, H.-L. Liu, M.-Y. Hua, H.-W. Yang, C.-Y. Huang, P.-C. Chu, L.-A. Lyu, I.-C. Tseng, L.-Y. Feng, H.-C. Tsai, S.-M. Chen, Y.-J. Lu, J.-J. Wang, T.-C. Yen, Y.-H. Ma, T. Wu, J.-P. Chen, J.-I. Chuang, J.-W. Shin, C. Hsueh, and K.-C. Wei, *Neuro-Oncol.* **12**, 1050 (2010).
- [174] C.-H. Fan, C.-Y. Ting, H.-J. Lin, C.-H. Wang, H.-L. Liu, T.-C. Yen, and C.-K. Yeh, *Biomaterials* **34**, 3706 (2013).
- [175] M. Kinoshita, N. McDannold, F. A. Jolesz, and K. Hynynen, *Proc. Natl. Acad. Sci. U. S. A.* **103**, 11719 (2006).
- [176] E.-J. Park, Y.-Z. Zhang, N. Vykhodtseva, and N. McDannold, *J. Control. Release Off. J. Control. Release Soc.* **163**, 277 (2012).
- [177] F.-Y. Yang, Y.-W. Chen, F.-I. Chou, S.-H. Yen, Y.-L. Lin, and T.-T. Wong, *Future Oncol. Lond. Engl.* **8**, 1361 (2012).
- [178] R. D. Alkins, P. M. Brodersen, R. N. S. Sodhi, and K. Hynynen, *Neuro-Oncol.* **15**, 1225 (2013).
- [179] R. Alkins, A. Burgess, M. Ganguly, G. Francia, R. Kerbel, W. S. Wels, and K. Hynynen, *Cancer Res.* **73**, 1892 (2013).
- [180] C.-Y. Ting, C.-H. Fan, H.-L. Liu, C.-Y. Huang, H.-Y. Hsieh, T.-C. Yen, K.-C. Wei, and C.-K. Yeh, *Biomaterials* **33**, 704 (2012).
- [181] F. Wang, Y. Shi, L. Lu, L. Liu, Y. Cai, H. Zheng, X. Liu, F. Yan, C. Zou, C. Sun, J. Shi, S. Lu, and Y. Chen, *PloS One* **7**, e52925 (2012).
- [182] C.-H. Fan, C.-Y. Ting, H.-L. Liu, C.-Y. Huang, H.-Y. Hsieh, T.-C. Yen, K.-C. Wei, and C.-K. Yeh, *Biomaterials* **34**, 2142 (2013).
- [183] B. Baseri, J. J. Choi, T. Deffieux, G. Samiotaki, Y.-S. Tung, O. Olumolade, S.

- A. Small, B. Morrison, and E. E. Konofagou, *Phys. Med. Biol.* **57**, N65 (2012).
- [184] J. F. Jordão, C. A. Ayala-Grosso, K. Markham, Y. Huang, R. Chopra, J. McLaurin, K. Hynynen, and I. Aubert, *PloS One* **5**, e10549 (2010).
- [185] A. Burgess, C. A. Ayala-Grosso, M. Ganguly, J. F. Jordão, I. Aubert, and K. Hynynen, *PloS One* **6**, e27877 (2011).
- [186] E. Thévenot, J. F. Jordão, M. A. O'Reilly, K. Markham, Y.-Q. Weng, K. D. Foust, B. K. Kaspar, K. Hynynen, and I. Aubert, *Hum. Gene Ther.* **23**, 1144 (2012).
- [187] A. Alonso, E. Reinz, B. Leuchs, J. Kleinschmidt, M. Fatar, B. Geers, I. Lentacker, M. G. Hennerici, S. C. de Smedt, and S. Meairs, *Mol. Ther. Nucleic Acids* **2**, e73 (2013).
- [188] P.-H. Hsu, K.-C. Wei, C.-Y. Huang, C.-J. Wen, T.-C. Yen, C.-L. Liu, Y.-T. Lin, J.-C. Chen, C.-R. Shen, and H.-L. Liu, *PloS One* **8**, e57682 (2013).
- [189] K.-C. Wei, P.-C. Chu, H.-Y. J. Wang, C.-Y. Huang, P.-Y. Chen, H.-C. Tsai, Y.-J. Lu, P.-Y. Lee, I.-C. Tseng, L.-Y. Feng, P.-W. Hsu, T.-C. Yen, and H.-L. Liu, *PloS One* **8**, e58995 (2013).
- [190] E.-J. Park, Y.-Z. Zhang, N. Vykhodtseva, and N. McDannold, *J. Controlled Release* **163**, 277 (2012).
- [191] L. H. Treat, N. McDannold, Y. Zhang, N. Vykhodtseva, and K. Hynynen, *Ultrasound Med. Biol.* **38**, 1716 (2012).
- [192] J. F. Jordão, C. A. Ayala-Grosso, K. Markham, Y. Huang, R. Chopra, J. McLaurin, K. Hynynen, and I. Aubert, *PloS One* **5**, e10549 (2010).
- [193] J. F. Jordão, E. Thévenot, K. Markham-Coultes, T. Scarcelli, Y.-Q. Weng, K. Xhima, M. O'Reilly, Y. Huang, J. McLaurin, K. Hynynen, and I. Aubert, *Exp. Neurol.* **248**, 16 (2013).
- [194] K.-C. Wei, P.-C. Chu, H.-Y. J. Wang, C.-Y. Huang, P.-Y. Chen, H.-C. Tsai, Y.-J. Lu, P.-Y. Lee, I.-C. Tseng, L.-Y. Feng, P.-W. Hsu, T.-C. Yen, and H.-L. Liu, *PLoS ONE* **8**, e58995 (2013).

- [195] H.-L. Liu, M.-Y. Hua, P.-Y. Chen, P.-C. Chu, C.-H. Pan, H.-W. Yang, C.-Y. Huang, J.-J. Wang, T.-C. Yen, and K.-C. Wei, *Radiology* **255**, 415 (2010).
- [196] H.-L. Liu, M.-Y. Hua, H.-W. Yang, C.-Y. Huang, P.-C. Chu, J.-S. Wu, I.-C. Tseng, J.-J. Wang, T.-C. Yen, P.-Y. Chen, and K.-C. Wei, *Proc. Natl. Acad. Sci. U. S. A.* **107**, 15205 (2010).
- [197] J. J. Choi, M. Pernot, S. A. Small, and E. E. Konofagou, *Ultrasound Med. Biol.* **33**, 95 (2007).
- [198] M. A. O'Reilly, A. Muller, and K. Hynynen, *Ultrasound Med. Biol.* **37**, 1930 (2011).
- [199] S. Pichardo, V. W. Sin, and K. Hynynen, *Phys. Med. Biol.* **56**, 219 (2011).
- [200] P. J. White, G. T. Clement, and K. Hynynen, *Ultrasound Med. Biol.* **32**, 1085 (2006).
- [201] K. Hynynen, N. I. Vykhodtseva, A. H. Chung, V. Sorrentino, V. Colucci, and F. A. Jolesz, *Radiology* **204**, 247 (1997).
- [202] N. McDannold and S. E. Maier, *Med. Phys.* **35**, 3748 (2008).
- [203] N. Hosseinkhah and K. Hynynen, *Phys. Med. Biol.* **57**, 785 (2012).
- [204] M. A. O'Reilly and K. Hynynen, *Radiology* **263**, 96 (2012).
- [205] V. A. Salgaonkar, S. Datta, C. K. Holland, and T. D. Mast, *J. Acoust. Soc. Am.* **126**, 3071 (2009).
- [206] M. Gyöngy and C.-C. Coussios, *J. Acoust. Soc. Am.* **128**, EL175 (2010).
- [207] F.-Y. Yang, H.-E. Wang, G.-L. Lin, M.-C. Teng, H.-H. Lin, T.-T. Wong, and R.-S. Liu, *J. Nucl. Med. Off. Publ. Soc. Nucl. Med.* **52**, 478 (2011).
- [208] F.-Y. Yang, S.-C. Horng, Y.-S. Lin, and Y.-H. Kao, *J. Magn. Reson. Imaging JMRI* **32**, 593 (2010).
- [209] P.-C. Chu, W.-Y. Chai, H.-Y. Hsieh, J.-J. Wang, S.-P. Wey, C.-Y. Huang, K.-C. Wei, and H.-L. Liu, *BioMed Res. Int.* **2013**, 627496 (2013).

- [210] H. C. Roberts, T. P. Roberts, R. C. Brasch, and W. P. Dillon, *AJNR Am. J. Neuroradiol.* **21**, 891 (2000).
- [211] L. W. Turnbull, *NMR Biomed.* **22**, 28 (2009).
- [212] L. Z. Li, R. Zhou, H. N. Xu, L. Moon, T. Zhong, E. J. Kim, H. Qiao, R. Reddy, D. Leeper, B. Chance, and J. D. Glickson, *Proc. Natl. Acad. Sci. U. S. A.* **106**, 6608 (2009).
- [213] Q. Jiang, J. R. Ewing, G. L. Ding, L. Zhang, Z. G. Zhang, L. Li, P. Whitton, M. Lu, J. Hu, Q. J. Li, R. A. Knight, and M. Chopp, *J. Cereb. Blood Flow Metab. Off. J. Int. Soc. Cereb. Blood Flow Metab.* **25**, 583 (2005).
- [214] R. A. Knight, T. N. Nagaraja, J. R. Ewing, V. Nagesh, P. A. Whitton, E. Bershad, S. C. Fagan, and J. D. Fenstermacher, *Magn. Reson. Med. Off. J. Soc. Magn. Reson. Med. Soc. Magn. Reson. Med.* **54**, 813 (2005).
- [215] D. M. Cohen, C. B. Patel, P. Ahobila-Vajjula, L. M. Sundberg, T. Chacko, S.-J. Liu, and P. A. Narayana, *NMR Biomed.* **22**, 332 (2009).
- [216] P. S. Tofts, *J. Magn. Reson. Imaging JMRI* **7**, 91 (1997).
- [217] P. S. Tofts, G. Brix, D. L. Buckley, J. L. Evelhoch, E. Henderson, M. V. Knopp, H. B. Larsson, T. Y. Lee, N. A. Mayr, G. J. Parker, R. E. Port, J. Taylor, and R. M. Weisskoff, *J. Magn. Reson. Imaging JMRI* **10**, 223 (1999).
- [218] M. O. Leach, B. Morgan, P. S. Tofts, D. L. Buckley, W. Huang, M. A. Horsfield, T. L. Chenevert, D. J. Collins, A. Jackson, D. Lomas, B. Whitcher, L. Clarke, R. Plummer, I. Judson, R. Jones, R. Alonzi, T. Brunner, D. M. Koh, P. Murphy, J. C. Waterton, G. Parker, M. J. Graves, T. W. J. Scheenen, T. W. Redpath, M. Orton, G. Karczmar, H. Huisman, J. Barentsz, A. Padhani, and Experimental Cancer Medicine Centres Imaging Network Steering Committee, *Eur. Radiol.* **22**, 1451 (2012).
- [219] K. L. Li, X. P. Zhu, J. Waterton, and A. Jackson, *J. Magn. Reson. Imaging JMRI* **12**, 347 (2000).
- [220] D. P. Barboriak, in (McLean VA, 2004).

- [221] C. Kittel, *Introduction to Solid State Physics*, Seventh (John Wiley & Sons, n.d.).
- [222] G. Minotti, P. Menna, E. Salvatorelli, G. Cairo, and L. Gianni, *Pharmacol. Rev.* **56**, 185 (2004).
- [223] J. Holland and E. Frei, *Cancer Medicine*, 8th ed. (People's Publishing House, Shelton, Connecticut, 2010).
- [224] D. A. Gewirtz, *Biochem. Pharmacol.* **57**, 727 (1999).
- [225] J. Cummings and C. S. McArdle, *Br. J. Cancer* **53**, 835 (1986).
- [226] K. A. Walter, R. J. Tamargo, A. Olivi, P. C. Burger, and H. Brem, *Neurosurgery* **37**, 1128 (1995).
- [227] J. W. Park, *Breast Cancer Res. BCR* **4**, 95 (2002).
- [228] E. Hodgson, J. Bend, R. Philpot, and editors, *Reviews in Biochemical Toxicology* (Elsevier Biochemical, New York, 1984).
- [229] K. K. Karukstis, E. H. Thompson, J. A. Whiles, and R. J. Rosenfeld, *Biophys. Chem.* **73**, 249 (1998).
- [230] M. A. O'Reilly, A. Muller, and K. Hynynen, *Ultrasound Med. Biol.* **37**, 1930 (2011).
- [231] T. Htun, *J. Fluoresc.* **14**, 217 (2004).
- [232] M. Pilatou, N. Vykhodtseva, and N. McDannold, in (Washington, DC, 2008).
- [233] N. R. Bachur, A. L. Moore, J. G. Bernstein, and A. Liu, *Cancer Chemother. Rep.* **54**, 89 (1970).
- [234] R. D. Arnold, D. E. Mager, J. E. Slack, and R. M. Straubinger, *Clin. Cancer Res. Off. J. Am. Assoc. Cancer Res.* **11**, 8856 (2005).
- [235] J. M. Bland and D. G. Altman, *BMJ* **310**, 170 (1995).
- [236] F. Vlachos, Y.-S. Tung, and E. E. Konofagou, *Phys. Med. Biol.* **55**, 5451 (2010).

- [237] J. Cummings and C. S. McArdle, *Br. J. Cancer* **53**, 835 (1986).
- [238] R. K. Jain, K. Schlenger, M. Hockel, and F. Yuan, *Nat. Med.* **3**, 1203 (1997).
- [239] I. Lentacker, I. De Cock, R. Deckers, S. C. De Smedt, and C. T. W. Moonen, *Adv. Drug Deliv. Rev.* **72**, 49 (2014).
- [240] B. Geers, I. Lentacker, N. N. Sanders, J. Demeester, S. Meairs, and S. C. De Smedt, *J. Control. Release Off. J. Control. Release Soc.* **152**, 249 (2011).
- [241] D. Fukumura and R. K. Jain, *J. Cell. Biochem.* **101**, 937 (2007).
- [242] E. A. Neuwelt, M. Glasberg, E. Frenkel, and P. Barnett, *Ann. Neurol.* **14**, 316 (1983).
- [243] A. Kondo, T. Inoue, H. Nagara, J. Tateishi, and M. Fukui, *Brain Res.* **412**, 73 (1987).
- [244] R. Zhang, R. Saito, Y. Mano, M. Kanamori, Y. Sonoda, T. Kumabe, and T. Tominaga, *J. Neurosci. Methods* **222**, 131 (2014).
- [245] K. Hynynen, *Med. Phys.* **18**, 1156 (1991).
- [246] W. J. Elias, D. Huss, T. Voss, J. Loomba, M. Khaled, E. Zadicario, R. C. Frysinger, S. A. Sperling, S. Wylie, S. J. Monteith, J. Druzgal, B. B. Shah, M. Harrison, and M. Wintermark, *N. Engl. J. Med.* **369**, 640 (2013).
- [247] A. C. Stan, S. Casares, D. Radu, G. F. Walter, and T. D. Brumeanu, *Anticancer Res.* **19**, 941 (1999).
- [248] S. Voulgaris, M. Partheni, M. Karamouzis, P. Dimopoulos, N. Papadakis, and H. P. Kalofonos, *Am. J. Clin. Oncol.* **25**, 60 (2002).
- [249] S. Ananda, A. K. Nowak, L. Cher, A. Dowling, C. Brown, J. Simes, M. A. Rosenthal, and Cooperative Trials Group for Neuro-Oncology (COGNO), *J. Clin. Neurosci. Off. J. Neurosurg. Soc. Australas.* **18**, 1444 (2011).
- [250] H. von Holst, E. Knochenhauer, H. Blomgren, V. P. Collins, L. Ehn, M. Lindquist, G. Norén, and C. Peterson, *Acta Neurochir. (Wien)* **104**, 13 (1990).
- [251] T. Hekmatara, C. Bernreuther, A. S. Khalansky, A. Theisen, J. Weissenberger, 183

- J. Matschke, S. Gelperina, J. Kreuter, and M. Glatzel, *Clin. Neuropathol.* **28**, 153 (2009).
- [252] T. Siegal, A. Horowitz, and A. Gabizon, *J. Neurosurg.* **83**, 1029 (1995).
- [253] S. C. J. Steiniger, J. Kreuter, A. S. Khalansky, I. N. Skidan, A. I. Bobruskin, Z. S. Smirnova, S. E. Severin, R. Uhl, M. Kock, K. D. Geiger, and S. E. Gelperina, *Int. J. Cancer J. Int. Cancer* **109**, 759 (2004).
- [254] S. Wohlfart, A. S. Khalansky, C. Bernreuther, M. Michaelis, J. Cinatl Jr, M. Glatzel, and J. Kreuter, *Int. J. Pharm.* **415**, 244 (2011).
- [255] R. Zhou, R. Mazurchuk, and R. M. Straubinger, *Cancer Res.* **62**, 2561 (2002).
- [256] P. J. Gaillard, C. C. M. Appeldoorn, R. Dorland, J. van Kregten, F. Manca, D. J. Vugts, B. Windhorst, G. A. M. S. van Dongen, H. E. de Vries, D. Maussang, and O. van Tellingen, *PloS One* **9**, e82331 (2014).
- [257] F.-Y. Yang, M.-C. Teng, M. Lu, H.-F. Liang, Y.-R. Lee, C.-C. Yen, M.-L. Liang, and T.-T. Wong, *Int. J. Nanomedicine* **7**, 965 (2012).
- [258] I. Brigger, J. Morizet, L. Laudani, G. Aubert, M. Appel, V. Velasco, M.-J. Terrier-Lacombe, D. Desmaële, J. d' Angelo, P. Couvreur, and G. Vassal, *J. Control. Release Off. J. Control. Release Soc.* **100**, 29 (2004).
- [259] B. Uziely, S. Jeffers, R. Isacson, K. Kutsch, D. Wei-Tsao, Z. Yehoshua, E. Libson, F. M. Muggia, and A. Gabizon, *J. Clin. Oncol. Off. J. Am. Soc. Clin. Oncol.* **13**, 1777 (1995).
- [260] R. F. Barth and B. Kaur, *J. Neurooncol.* **94**, 299 (2009).
- [261] M. C. Chamberlain, *J. Neurooncol.* **101**, 319 (2011).
- [262] P.-C. Chu, W.-Y. Chai, H.-Y. Hsieh, J.-J. Wang, S.-P. Wey, C.-Y. Huang, K.-C. Wei, and H.-L. Liu, *BioMed Res. Int.* **2013**, 627496 (2013).
- [263] E. Nance, K. Timbie, G. W. Miller, J. Song, C. Louttit, A. L. Klibanov, T.-Y. Shih, G. Swaminathan, R. J. Tamargo, G. F. Woodworth, J. Hanes, and R. J. Price, *J. Control. Release Off. J. Control. Release Soc.* (2014).

- [264] L. H. Treat, N. McDannold, N. Vykhodtseva, Y. Zhang, K. Tam, and K. Hynynen, *Int. J. Cancer* **121**, 901 (2007).
- [265] M. Kinoshita, N. McDannold, F. A. Jolesz, and K. Hynynen, *Proc. Natl. Acad. Sci. U. S. A.* **103**, 11719 (2006).
- [266] E. A. Neuwelt, M. Pagel, P. Barnett, M. Glassberg, and E. P. Frenkel, *Cancer Res.* **41**, 4466 (1981).
- [267] A. J. Primeau, A. Rendon, D. Hedley, L. Lilge, and I. F. Tannock, *Clin. Cancer Res. Off. J. Am. Assoc. Cancer Res.* **11**, 8782 (2005).

Appendix

- I. **M. Aryal**, C. D. Arvanitis, P. M. Alexander, N. McDannold, “*Ultrasound-mediated blood-brain barrier disruption for targeted drug delivery in the central nervous system*”, *Advanced Drug Delivery Reviews*, 72,94-109 (2014)/DOI 10.1016/j.addr.2014.01.008

Material from this manuscript is included in Chapter 1 in this thesis. I would like to thank my coauthors for their permission to include text that they contributed to this work.

- II. **M. Aryal**, N. Vykhodtseva, Y. Z. Zhang, J. Park, N. McDannold, “Multiple treatments with liposomal doxorubicin and ultrasound-induced disruption of blood–tumor and blood–brain barriers improve outcomes in a rat glioma model”, *J. Control. Release* 169, 103–111 (2013)/ DOI 10.1016/j.jconrel.2013.04.007

This manuscript describes the experiments presented in Chapter 5..

- III. **M. Aryal**, J. Park, N. Vykhodtseva, Y. Z. Zhang, N. McDannold, “Enhancements in blood-tumor barrier permeability and delivery of liposomal doxorubicin using focused ultrasound and microbubbles: evaluation during tumor progression in a rat glioma model”, (submitted)

This manuscript describes the experiments presented in Chapter 6..

- IV. **M. Aryal**, N. Vykhodtseva, Y. Z. Zhang, N. McDannold, “*Multiple use of ultrasound to deliver liposomal doxorubicin after blood-brain barrier disruption*”, A safety study (submitted)

This manuscript describes the experiments presented in Chapter 4.

- V. J. Park, **M. Aryal**, N. Vykhodtseva, Y. Z. Zhang, N. McDannold, “Increased blood-tumor barrier permeability and enhanced doxorubicin delivery into rat glioma by MRI guided focused ultrasound and microbubbles”, (under preparation)

Appendix I

Ultrasound-mediated blood–brain barrier disruption for targeted drug delivery in the central nervous system

Muna Aryal, Costas D. Arvanitis , Phillip M. Alexander and Nathan McDannold
Adv Drug Deliv Rev. 2014 Jun;72:94-109



Contents lists available at ScienceDirect

Advanced Drug Delivery Reviews

journal homepage: www.elsevier.com/locate/addr

Ultrasound-mediated blood–brain barrier disruption for targeted drug delivery in the central nervous system ^{☆☆☆}

Muna Aryal ^{a,b}, Costas D. Arvanitis ^b, Phillip M. Alexander ^{b,c}, Nathan McDannold ^{b,*}

^a Department of Physics, Boston College, Chestnut Hill, USA

^b Department of Radiology, Brigham & Women's Hospital, Harvard Medical School, Boston, USA

^c Institute of Biomedical Engineering, Department of Engineering Science, and Brasenose College, University of Oxford, Oxford, UK

ARTICLE INFO

Article history:
Accepted 14 January 2014
Available online xxxx

Keywords:
Brain
Drug delivery
Ultrasound
Microbubbles

ABSTRACT

The physiology of the vasculature in the central nervous system (CNS), which includes the blood–brain barrier (BBB) and other factors, complicates the delivery of most drugs to the brain. Different methods have been used to bypass the BBB, but they have limitations such as being invasive, non-targeted or requiring the formulation of new drugs. Focused ultrasound (FUS), when combined with circulating microbubbles, is a noninvasive method to locally and transiently disrupt the BBB at discrete targets. This review provides insight on the current status of this unique drug delivery technique, experience in preclinical models, and potential for clinical translation. If translated to humans, this method would offer a flexible means to target therapeutics to desired points or volumes in the brain, and enable the whole arsenal of drugs in the CNS that are currently prevented by the BBB.

© 2014 Elsevier B.V. All rights reserved.

Contents

1. Introduction	0
2. Methods for drug delivery in the brain	0
2.1. Invasive approaches to brain drug delivery	0
2.2. Transvascular brain drug therapy: Biopharmaceutical approaches	0
2.3. Transvascular brain drug therapy: BBB disruption	0
3. Focused ultrasound	0
4. Ultrasound-induced BBB disruption	0
4.1. Effect of ultrasound parameters and other factors on BBB disruption	0
4.2. Optimal parameters?	0
4.3. Potential mechanisms	0
4.4. Bioeffects induced by FUS and microbubbles	0
4.5. Delivery of imaging/therapeutic agents and tests in animal disease models	0
4.5.1. Delivery of therapeutics	0
4.5.2. Disease models	0
4.6. Methods to plan, monitor, and evaluate FUS-induced BBB disruption	0
4.6.1. Treatment planning	0
4.6.2. Treatment monitoring and control	0
4.6.3. Treatment evaluation	0
5. Going forward	0
6. Conclusion	0
References	0

[☆] This review is part of the Advanced Drug Delivery Reviews theme issue on “Ultrasound triggered drug delivery”.

^{☆☆} Support: This work was supported by NIH grants P01CA174645, P41EB015898, P41RR019703, and R25CA089017.

* Corresponding author at: 75 Francis Street, Boston, MA 02115, USA. Tel.: +1 617 278 0605; fax: +1 617 525 7450.

E-mail address: njm@bwh.harvard.edu (N. McDannold).

1. Introduction

The blood–brain barrier (BBB) is a specialized non-permeable barrier in cerebral microvessels consisting of endothelial cells connected together by tight junctions, a thick basement membrane, and astrocytic endfeet. The tight junctions between the endothelial cells, together with

an ensemble of enzymes, receptors, transporters, and efflux pumps of the multidrug resistance (MDR) pathways, control and limit access of molecules in the vascular compartment to the brain by paracellular or transcellular pathways [1]. The BBB normally protects the brain from toxins, and helps maintain the delicate homeostasis of the neuronal microenvironment. However, it also excludes 98% of small-molecule drugs and approximately 100% of large-molecule neurotherapeutics from the brain parenchyma [2,3]. Only small-molecule drugs with high lipid solubility and a molecular mass under 400–500 Da can cross the BBB in pharmacologically significant amounts, resulting in effective treatments for only a few diseases such as depression, affective disorders, chronic pain, and epilepsy. Given the paucity of small-molecule drugs effective for CNS disorders, it is clear that the BBB is a primary limitation for the development and use of drugs in the brain. Overcoming this hindrance could mean potential therapies for a wide range of disorders, including Alzheimer's and Huntington's diseases, amyotrophic lateral sclerosis (ALS), neuro-AIDS, stroke, brain or spinal cord trauma, autism, lysosomal storage disorders, fragile X syndrome, inherited ataxias, and blindness.

Tumors, particularly those in the brain also face challenges for effective drug delivery. While the blood vessels in most primary and metastatic brain tumors are often somewhat permeable from the lack of a fully formed BBB, infiltrating cancer cells at the tumor margins and small metastatic seeds may be protected by the BBB of surrounding normal tissue [4]. Glioblastomas in particular are highly infiltrative, and commonly recur after localized treatments such as conformal radiotherapy or surgery. Relapse usually occurs within a few centimeters of the treatment site [5–7]. Furthermore, their vascular permeability is heterogeneous, and additional barriers to drug delivery include increased interstitial pressures [8] and drug efflux pumps that contribute to their multidrug resistance phenotype [9]. As for metastatic tumors, work in mice suggests that the blood–tumor barrier (BTB) is only partially compromised in breast adenocarcinoma brain metastases, and that toxic concentrations of chemotherapy are only achieved in a small subset of tumors that are highly permeable [10]. Also, systemic drug accumulation in brain metastases can be substantially less than in extracranial metastases [10]. Thus, the BTB is a hindrance to effective drug delivery similarly to the BBB.

2. Methods for drug delivery in the brain

In order to overcome these limitations, it is necessary to either bypass these vascular barriers altogether, or to facilitate passage across it via controlled exploitation of endogenous transport mechanisms. Different methods have been explored to bypass the BBB (or the BTB) (Table 1) [11–13]. While these methods are promising, they also have limitations.

2.1. Invasive approaches to brain drug delivery

High local drug concentrations can be achieved by inserting a needle or catheter into the brain and directly injecting or infusing drugs or by

implanting drug-exuding devices. With such techniques, therapeutic benefits have been shown for brain tumors and other disorders [14–17]. However, because of their invasiveness, there are some risks of infection or brain trauma, and they may not be amenable for repeated treatments or for drug delivery to large areas of the brain. It can also be a challenge to control the drug distribution, as drug concentrations decrease exponentially from the injection or implantation site [18]. When convection-enhanced diffusion is used, the infused agents are delivered preferentially along white matter tracts [19], which may not be desirable.

Another approach for bypassing the BBB is to introduce drugs into the cerebrospinal fluid (CSF) via intrathecal or intraventricular routes. It then follows the flow patterns of the CSF and enters the brain parenchyma via diffusion. This approach has been successful in cases where the target is in the subarachnoid space [20], but drug diffusion drops off exponentially from the brain surface and penetration into the brain parenchyma can be limited [11]. It is also possible to deliver drugs transnasally from the submucosal space into the olfactory CSF [21–24]. This approach has advantages of being noninvasive and being relatively easy to administer. However, only small drug volumes can be delivered and interindividual variability and other factors may pose challenges to this procedure [24]. Nevertheless, the technique is a promising route to bypass the BBB and is currently being investigated by numerous researchers.

2.2. Transvascular brain drug therapy: Biopharmaceutical approaches

A number of approaches have been investigated to develop or modify drugs that can cross the BBB. While these methods are highly promising and offer the ability to easily administer drugs to the CNS as in other organs, they do require the expense and time of developing new agents, and they result in drugs being delivered to the entire brain, which may not always be desirable.

Converting water-soluble molecules that would not ordinarily cross the BBB into lipid-soluble ones is one approach to brain drug therapy. This can be achieved by the addition of lipid groups, or functional groups such as acetate to block hydrogen bonding. The molecule would then undergo passive diffusion across the BBB. An example of this is the conversion of morphine to heroin by the acetylation of two hydroxyl groups, which results in the removal of the molecule from hydrogen bonding with its aqueous environment [25]. Although utilized by the pharmaceutical industry, this approach has limited applicability to drugs greater than 400–450 Da [12,26].

Another approach involves utilizing the large variety of solute carrier proteins (SLC) on the endothelial surface that specifically transport many essential polar and charged nutrients such as glucose, amino acids, vitamins, small peptides, and hormones transcellularly across the BBB [27]. These transporters move the solute into the cytoplasm where they await another SLC at the opposite cell membrane to exocytose them into the brain parenchyma. An example of SLC used for brain drug therapy is the large neutral amino acid transporter type 1 (LAT1),

Table 1
Different methods investigated to get around the BBB to deliver drugs to the brain.

Method	Advantages	Disadvantages
Direct injection, convection-enhanced delivery, implantable devices	High local drug concentrations can be achieved; systemic administration avoided.	Invasive; side effects; challenging to control; not readily repeatable.
Intrathecal, intraventricular injection	Effectively delivers drugs to subarachnoid space, brain surface.	Little drug penetration beyond brain surface; invasive.
Trans-nasal delivery	Noninvasive; easy to administer; repeatable.	Small volume of drug delivered; interindividual variability.
BBB disruption via arterial injection of osmotic solution or other agents	Effectively delivers drugs to large brain regions; large clinical experience.	Invasive; requires general anesthesia; side effects; not readily repeatable.
Modification of drugs to cross barrier through endogenous transport mechanisms	Easily administered; delivered to whole brain.	Requires systemic administration; expensive; each drug requires new development; clinical data lacking.
BBB disruption via FUS and microbubbles	Noninvasive; readily repeatable; can target drug delivery to desired volumes; can control "magnitude" of disruption; can be combined with drug-loaded microbubbles or magnetic particles for additional targeting.	Requires systemic administration; currently technically challenging; large volume/whole brain disruption unproven; no clinical data.

which transports the amino acid Parkinson's drug L-dopa across the BBB. Once across, it is converted to dopamine by aromatic amino acid decarboxylase, and can then bind to its target receptor. Dopamine being water-soluble cannot cross the BBB [26,28].

Finally, the molecular targeting of endothelial-surface receptors, colloquially termed the “Trojan Horse” approach, is yet another paradigm in drug transport across the BBB. This involves using a targeting ligand such as a serum protein, monoclonal antibody, or other high affinity targeting molecule that binds to its receptor and activates endocytosis of the complex into a vesicle that is transported across to, and released from the opposite pole (i.e., transcytosis). In theory, if the ligand is chemically linked to a drug or drug carrier, it too is transported across the BBB. Over the last two decades, a number of animal studies have suggested the transport of antineoplastic drugs, fusion proteins, genetic therapies (plasmid vectors, siRNA), liposomes, and nanoparticles by this mechanism [29–32]. For transcytosis to occur, it requires that the endosome not fuse with lysosomes while in the cytoplasm, which would degrade the internalized macromolecules. Unlike other tissues, endothelial cells in brain capillaries appear to have low levels of endosome fusion with lysosomes, facilitating transport of necessary substances through the transcellular route [33–35].

2.3. Transvascular brain drug therapy: BBB disruption

Others have investigated methods to temporarily disrupt the BBB to enable CNS delivery of circulating agents. One such technique investigated intensively for several decades is the intraarterial injection of hyperosmotic solutions such as mannitol. This procedure causes shrinkage of endothelial cells and consequent stretching of tight junctions [36–39] through which drugs may pass. This method has been shown repeatedly to enhance delivery of therapeutic agents to brain tumors, and several promising clinical trials have been performed [40–45]. Other agents such as bradykinin have also been investigated [46–49]. While such methods can be an effective means to deliver drugs to large brain regions, they are invasive procedures that require general anesthesia, and can have side effects. For example, one study reported focal seizures in 5% of patients who received osmotic BBB disruption [40], and others have noted vasovagal response with bradycardia and hypotension [39]. Having a less-invasive way to achieve this disruption would be desirable.

The use of ultrasound, when combined with circulating microbubbles, offers a potential way to disrupt the BBB in a targeted, noninvasive, and repeatable manner to deliver a wide range of drugs to the brain and to brain tumors. Below, we review the literature on this technique, (i) describing how it is performed, (ii) how different parameters effect the BBB disruption, (iii) what has been delivered in preclinical studies, and (iv) methods that can be used to guide the procedure. While to date the technique has only been performed in animals, it is clear that it holds great promise for the treatment of a wide range of CNS disorders. If successfully translated to the clinic, it offers a means to target drugs, biomolecular therapies, and perhaps cellular therapies to desired brain regions while sparing the rest of the brain from unnecessary uptake. The technique also offers the potential to control the “magnitude” of BBB disruption at each focal target through modification of the ultrasound parameters, enabling a level of control over drug delivery that is not available with other technologies. This flexibility, along with its noninvasiveness, lack of need for general anesthesia, and amenability to be readily repeated make FUS a potentially transformative technology.

3. Focused ultrasound

An ultrasound field can be noninvasively focused deep into the body and used to induce a broad range of bioeffects through thermal or mechanical mechanisms. FUS has been investigated since the 1940's for noninvasive ablation in the brain, as a potential alternative to surgical

resection and radiosurgery [50–53]. Until recently, clinical testing required a craniotomy to allow for ultrasound propagation into the brain [54,55] because of ultrasonic heating of the skull, and beam aberration caused by the skull's irregular shape and large acoustic impedance.

In the past decade, FUS thermal ablation systems have been developed that overcome these obstacles produced by the skull [56]. They reduce skull heating through active cooling of the scalp and a transducer design with a large aperture to distribute the ultrasound energy over a large skull region, and they correct for beam aberrations using a phased array transducer design. When combined with methods that use acoustic simulation based on CT scans of the skull bone to determine the phase and amplitude corrections for the phased array [57,58] and MR temperature imaging (MRTI) to monitor the heating [59], a completely noninvasive alternative to surgical resection in the brain becomes possible. These systems use very high intensities to enable thermal ablation through the human skull, and are currently in initial human trials [60–63].

The effects of FUS can be enhanced by combining the ultrasound exposures (“sonications”) with preformed microbubbles that are commercially available as ultrasound imaging contrast agents. They consist of semi-rigid lipid or albumin shells that encapsulate a gas (typically a perfluorocarbon), range in size from about 1–10 μm , and are constrained to the vasculature. The microbubbles concentrate the ultrasound effects to the microvasculature, greatly reducing the FUS exposure levels needed to produce bioeffects. Thus, with microbubbles one can apply FUS transcranially without significant skull heating.

When microbubbles interact with an ultrasound field, a range of biological effects have been observed [64]. Depending on their size, the bubbles can oscillate within the ultrasound field, and they can grow in size via rectified diffusion. They can interact with the vessel wall through oscillatory and radiation forces [65,66]. They also can exert indirect shear forces induced by micro-streaming in the fluid that surrounds them [67]. At higher acoustic pressures, they can collapse during the positive pressure cycle, a phenomenon known as inertial cavitation, producing shock waves and high-velocity jets [65], free radicals [68], and high local temperatures [69,70]. The microbubbles used in ultrasound contrast agents can presumably exhibit these behaviors, either with their shells intact or after being broken apart by the ultrasound beam and their gas contents released.

4. Ultrasound-induced BBB disruption

Since the early years of investigation into ultrasound bioeffects on the brain, several studies have noted localized BBB disruption, either accompanied with tissue necrosis or without evident tissue damage [52,71–76]. None of these early studies however, elucidated sonication parameters that could repeatedly and reliably produce BBB disruption without occasionally producing lesions or necrosis.

In 2000 our laboratory found that if short ultrasound bursts are preceded by an intravenous injection of microbubble contrast agent, the BBB can be consistently opened without the production of lesions or apparent neuronal damage [77]. The circulating microbubbles appear to concentrate the ultrasound effects to the blood vessel walls, causing BBB disruption through widening of tight junctions and activation of transcellular mechanisms, with little effect on the surrounding parenchyma [78]. Furthermore, the opening occurs at acoustic power level orders of magnitude lower than was previously used, making this method substantially easier to apply through the intact skull. For BBB disruption, the sonications have been typically applied as short (~1–20 ms) bursts applied at a low duty cycle (1–5%) for 0.5–1 min. With a few simple modifications to enable low-intensity bursts, existing clinical brain FUS systems can be used for BBB disruption [79]. Clinical translation may also be possible using simpler FUS systems [80].

Fig. 1 shows examples of targeted BBB disruption in a macaque from our institution using a clinical transcranial MRI-guided FUS system (ExAblate, InSightec, Haifa, Israel) [79]. The device uses a hemispherical

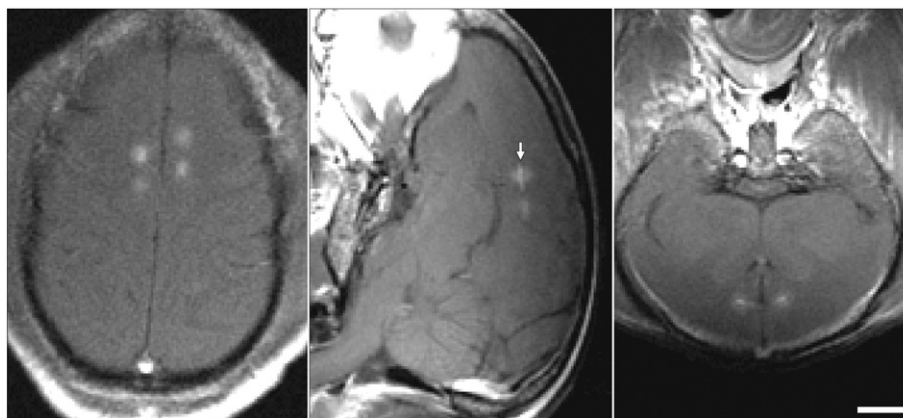


Fig. 1. Contrast-enhanced T1-weighted MRI of the brain of a rhesus macaque showing enhancement at four focal targets in the cingulate cortex after injection of Gd-DTPA. (Left image: Axial; middle: Sagittal; right: Coronal). Enhancement of this MRI contrast agent, which normally does not extravasate into the brain, indicates areas with BBB disruption. Four targets were sonicated using a 220 kHz clinical MRI-guided FUS system along with an infusion of Definity microbubbles. The dimensions of the disrupted spots were approximately 3 mm wide and 4 mm long. Note the leakage of contrast agent into the cingulate sulcus evident in the sagittal image (arrow). These images were obtained in a study evaluating passive cavitation mapping during microbubble-enhanced FUS [176] (bar: 1 cm).

1024-element phased array operating at 220 kHz, and is integrated with a 3T MRI scanner. The focal region can be electronically steered to different locations using this array without physically moving the transducer. Volumes can be targeted by systematically steering the focal point to different targets, enabling one to deliver drugs to desired brain regions. Fig. 2 shows an example of such “volumetric” FUS-induced BBB disruption. BBB disruption was evaluated using two MRI contrast agents and with the vital dye trypan blue. Note the lack of contrast enhancement in white matter despite evident staining with the dye. This difference is presumably due to the lower vascular density in white matter compared to gray matter.

4.1. Effect of ultrasound parameters and other factors on BBB disruption

A number of sonication parameters can be varied in ultrasonic BBB disruption. Each parameter variation may impact the threshold pressure amplitude needed to disrupt the BBB, the magnitude of its disruption, and the resultant drug quantity delivered to the brain parenchyma. As determined from a number of studies, parameter variations and their effects are listed in Table 2. These studies used an MRI contrast agent, fluorescent probe, or drug to evaluate the BBB disruption. Given the large parameter space, and different techniques and criteria used to evaluate the disruption (each with different sensitivities), it can be challenging to compare results from different laboratories. Such comparisons are additionally confounded by uncertain accuracies in estimates of acoustic pressure amplitude when sonicating through the skull [81]. However, general trends can be observed.

For a fixed set of parameters, as one increases the pressure amplitude, the magnitude of the BBB disruption increases, and at some level it appears to saturate [82–84]. Below some value, no disruption is detected, and at some higher pressure threshold, vascular damage is produced along with the disruption (see below). Such studies repeated while varying a different parameter have shown that the threshold for BBB disruption depends strongly on the ultrasound frequency [85] and burst length [86]. Most experiments have been done with commercially-available ultrasound contrast agents that consist of microbubbles with a wide range of diameters. Experiments with microbubbles with narrow size distributions suggest that the BBB disruption threshold can also be reduced by using larger microbubbles [87–89].

By fixing the pressure amplitude and varying each parameter, one can evaluate their effects on the magnitude of the disruption. The magnitude has been found to increase with the burst length up to a duration of approximately 10 ms, with further increases in burst length having little or no effect [77,81,86,90,90–92]. Several groups have shown that the disruption magnitude may be increased by using a larger dose of

ultrasound contrast agent [83,93–95] (although other works have shown little or no effect [86,90]) or by using larger microbubbles [87–89]. Pulse repetition frequency can also influence the magnitude of disruption up to a point [90,91], but other studies have seen no dependence [86]. Finally, the magnitude of the disruption can be increased by increasing the sonication duration [84] or by repeating the sonication after some delay [96,97], but excessive durations may result in tissue damage [84,97]. Factors such as using an infusion instead of a bolus injection of microbubbles [98] and choice of anesthesia protocol [99] may also influence the resulting disruption. Other factors such as the delay between the microbubble injection and the start of sonication, and whether the drug or tracer is administered before or after the sonication may also be expected to have an effect. Additive effects have been observed when FUS-induced BBB disruption is combined with agents that affect vascular permeability [100–102].

These trends observed in parametric studies are difficult to interpret with confidence since the exact mechanism by which microbubble-enhanced FUS induces BBB disruption is currently unknown (see below). They are perhaps consistent with the following notions. First, for BBB disruption to occur, the microbubbles oscillations may need to reach a certain minimal radius, which can be achieved by increasing the pressure amplitude or by using larger microbubbles, and assuming the bubbles grow during each burst via rectified diffusion, by decreasing the ultrasound frequency or increasing the burst length. Next, in addition to depending on the bubble size during its oscillation, the magnitude of the disruption depends on the number of sites on which the microbubbles interact with the vasculature. The number of these sites can be increased by increasing the microbubble dose, or by increasing the sonication duration and/or number of bursts. Data showing a strong dependence on burst length may also suggest that the threshold and magnitude of the disruption depend on the amount of time the microbubbles interact with the blood vessels during each burst. Pulse repetition frequency may have an influence if the microbubbles are being fragmented or destroyed – time may be needed to replenish them if that is the case [103]. Finally, it appears that the magnitude of the disruption can saturate at some level, and increasing the different parameters has no additional effect.

4.2. Optimal parameters?

Overall, these studies have made it clear that BBB disruption is possible over a wide range of exposure parameters. Disruption has been demonstrated at frequencies between 28 kHz [104] and 8 MHz [92], burst lengths as low as a few ultrasound cycles [90,91,98] up to 100 ms [77], and over a range of pulse repetition frequencies,

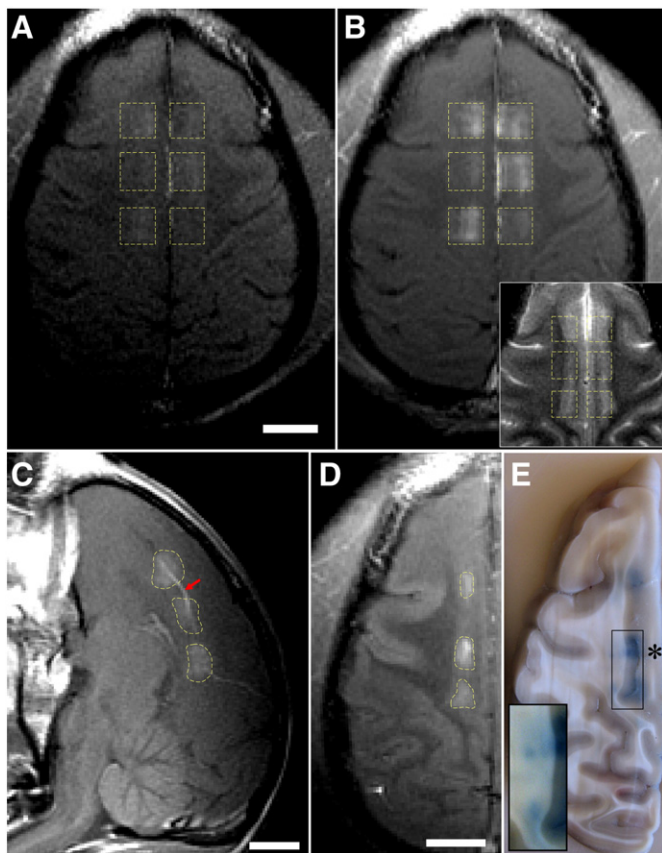


Fig. 2. Demonstration of FUS-induced BBB disruption using contrast enhanced MRI and trypan blue. (A–C) Contrast-enhanced T1-weighted MRI after BBB disruption at six volumes in the cingulate cortex. At each volume, the focal region was steered electronically in sequence to nine targets in a 3×3 grid using a phased array. (A) Low-level enhancement observed with gadofosveset trisodium, an MR contrast agent that binds to albumin in the blood (MW of albumin: ~67 kDa); it was administered before sonication. (B) Enhancement after injection of Gd-DTPA (MW: 938 Da). The inset in (B) shows the same view in T2-weighted imaging. The enhancement patterns correspond to regions of cortical gray matter visible in T2-weighted imaging. (C) Sagittal view of Gd-DTPA enhancement, which included leakage of agent into a sulcus (arrow). (D–E) Volumetric BBB disruption at three targets centered on the boundary between the cingulate cortex and white matter; from another experimental session in this animal. (D) T1-weighted MRI showing Gd-DTPA extravasation in the cingulate cortex, but not in the white matter. (E) Photograph of formalin-fixed brain showing trypan blue extravasation into both the cingulate cortex and white matter. This differential enhancement between gray and white matter presumably reflects differences in vascular density. The white matter component of two of these targets is shown with increased image contrast in the inset to better visualize low-level trypan blue extravasation. (Scale bars: 1 cm). Reprinted from *Cancer Research* 2012; 72:3652–3663; © 2012 American Association for Cancer Research. (For interpretation of the references to color in this figure legend, the reader is referred to the web version of this article.)

microbubble doses, and sonication times. It is not clear what the “optimal” parameters are, or what criteria to use to establish them. In our view, the primary consideration could be to find parameters that

maximize the window in acoustic pressure amplitude where robust BBB disruption is possible without producing vascular damage. It will be challenging to precisely estimate the pressure amplitude in the human brain after transcranial sonication, and having the widest safety margin possible will be desirable for clinical translation. How close the FUS frequency is to the “resonant size” of the microbubbles may have an impact on the width of this safety window. Additional important criteria would be to optimize the frequency and transducer geometry to produce the desired focal spot size, to effectively focus through the skull with minimal distortion, and if a phased array transducer is used, to be able to steer the focal region throughout the brain. It may also be desirable to find parameters that enable BBB disruption in the shortest possible sonication time so that multiple targets can be targeted in a reasonable amount of time, and to maintain a safe dose of microbubbles.

4.3. Potential mechanisms

Even though FUS exposures combined with microbubbles have been investigated to disrupt the BBB in numerous studies, the exact mechanism to open BBB still remains unknown. It does appear that two known effects that can be induced by FUS, bulk heating and inertial cavitation, are not responsible. Initial studies on the method utilized MRI-based temperature imaging [77] during the sonications, and no measurable heating was observed. Studies that recorded the acoustic emissions during the sonications [105–107] have found that BBB disruption can be achieved without wideband acoustic emission, which is a signature for inertial cavitation [53]. It also may not be the same mechanism utilized for so-called “sonoporation”, where transient pores in cell membranes created by sonication with microbubbles enable drugs to enter [108]. Those pores are rapidly resolved, while FUS-induced BBB disruption lasts for several hours.

Fundamentally, we do not know if the FUS/microbubble interactions physically modify the vessel walls, or if they are triggering a physiological response that includes temporary BBB breakdown. As described below, electron microscopy studies have shown delivery of tracers through widened tight junctions [78,109], which could be consistent with a direct physical force pulling them apart, as well as active transport [78,110]. Other work has shown the sonications can induce vascular spasm [111,112]. While the role of this spasm is not clear, it does make clear that the sonications can trigger a physiological response.

In the absence of bulk heating and inertial cavitation, we are left with mechanical effects induced during the microbubble oscillations in the ultrasound field. A number of effects are produced with potential to induce the observed BBB disruption. Microbubbles tend to move in the direction of the wave propagation via acoustic radiation force [66], which will bring them in contact with vessel endothelium. During oscillation, the shell of the microbubble can break, the bubbles can be fragmented into smaller bubbles, and they can grow via rectified diffusion. Microstreaming due to microbubble oscillations can induce biologically-significant shear stresses on the neighboring endothelium, and the oscillations produce inward forces that in extreme cases can

Table 2

Reported effects of different parameters on BBB disruption via FUS and microbubbles.

Parameter	Effect on BBB disruption
Pressure amplitude	Increase in BBB disruption magnitude as pressure amplitude increases; saturation at some point [82–84]; vascular damage produced at high pressure amplitudes.
Ultrasound frequency	Decrease in BBB disruption threshold as frequency decreases; some evidence of improved safety for lower frequencies [85].
Burst length	For burst lengths less than 10 ms, BBB disruption threshold increases and BBB disruption magnitude decreases as burst length is reduced [86,90–92]; little or no increase in disruption magnitude for longer bursts [77,81,90].
Pulse repetition frequency	BBB disruption magnitude increases as repetition frequency increases up to a point [90]. Other works have observed no effect on BBB disruption magnitude [86].
Ultrasound contrast agent dose	Magnitude of BBB disruption increases with dose [83,90,94,188]; other experiments have reported no effect [86].
Sonication duration	Longer durations [84] or repeated sonication [96,97] increase magnitude of BBB disruption; damage reported with excessive sonication [84,97].
Microbubble diameter	Threshold for BBB disruption lower for larger microbubbles; disruption magnitude increased with larger microbubbles [87–89].
Ultrasound contrast agent	Similar outcomes reported for Optison® and Definity® microbubbles [189]. Sonovue® microbubbles and research agents are also commonly used.

pull the vessel wall inward [113]. Clearly, the behavior of a microbubble in an acoustic field is complex, and it can be different in free fluid than when constrained within a capillary [114].

4.4. Bioeffects induced by FUS and microbubbles

The BBB disruption can occur almost immediately with sonication [112] and appears to decay exponentially over several hours thereafter [77,82,96,115]. The amount of agent delivered across the barrier appears to be much larger in gray matter than in white matter, presumably due to differences in vascular density [79]. Several studies have found that the barrier appears to be largely restored in approximately 4–6 h [77,82,96,109,115,116]; other experiments have observed low-level disruption at 24 h after sonication or longer [89]. The source of this discrepancy is not clear, but it could be simply that more sensitive detection methods such as high-field MRI combined with large doses of MRI contrast agent are capable of detecting low-level disruption missed in other works. The duration of the opening to different tracers appears to be reduced for larger tracers [115].

This window in time where the barrier is open is thought to be good for the prospect of delivering even long-circulating drugs, but not so long as to produce concern of toxicity arising from chronic BBB breakdown. Indeed, the appearance of the brain after BBB disruption in light microscopy appears to be normal [117], even after repeated weekly sessions [79]. Example histology obtained after BBB disruption is shown in Fig. 3. The only major feature that has been observed in many studies is the presence of tiny clusters of extravasated red blood cells (petechiae) [118,119]. It is thought that these petechiae are formed during inertial cavitation, and experiments where no wideband emissions (a signature for inertial cavitation) were observed, no such extravasations were observed [105]. Some have suggested that wideband emissions can be observed without producing such petechiae [106]. While the presence of these petechiae is undesirable, their impact on the brain may be minimal. Investigations looking for apoptosis or ischemia, which may be expected if serious vascular damage were occurring,

failed to observe anything more than a few individual damaged neurons, and long-term effects have not found evidence of neuronal damage with such sonications [118,120]. At excessive exposure levels, more severe vascular damage, parenchymal damage, and neuronal loss can occur [77,121].

Transmission electron microscopy (TEM) investigations have demonstrated an increase of cytoplasmic vesicles in endothelium and pericytes (suggestive of transcytosis), formation of trans-endothelial fenestrae, widened tight junctions, and transport of serum components across the BBB [78]. The use of a 44 kDa tracer molecule helped elucidate arterioles as the major sight of trans-endothelial vesicle transport (followed by capillaries then venules), and showed extensive tracer deposition in the endothelial paracellular space, basement membrane, and surrounding brain parenchyma [110]. Finally, using immunogold labeling, the disappearance of tight junction (TJ) proteins occludin, claudin-5, and ZO-1 were shown, along with opened endothelial junctions and tracer leakage at 1–4 h post-sonication [109]. The TJ proteins reappeared at 6 and 24 h. Examples showing tracer penetration across the BBB through widened tight junctions and vesicular transport are shown in Fig. 4. Other work has shown down-regulation of the same TJ proteins along with their mRNA, and recovery to normal levels at 12 h post-sonication [122]. Reorganization of connexin gap junction proteins have also been reported [123]. An increase of endothelial vesicles in normal [124] and tumor microvessels [125] have also been observed on TEM with an up-regulation of caveolin proteins/mRNA, suggesting that caveolae-mediated transcytosis (CMT) as a contributing mechanism for permeability. These researchers also found increased phosphorylation of Src and caveolin-1/2, noting that Src-induced phosphorylation of caveolins is a trigger for CMT [126].

Intracellular signaling cascades in response to mechanical stimulation by FUS-induced BBB disruption is likely, but has only recently been addressed. Increased phosphorylation of Akt and its downstream molecule GSK3 β has been shown in neurons flanking the BBB disruption at 24 h, well after tight junction reassembly [127]. Akt phosphorylation has been implicated in neuroprotection after stroke [128], while

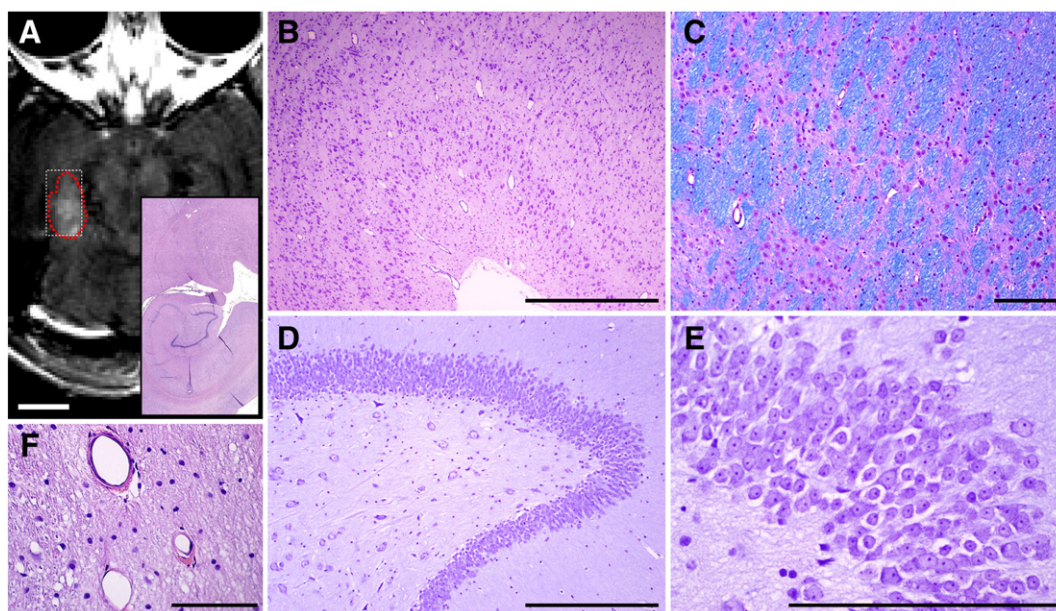


Fig. 3. Normal-appearing histology after FUS-induced BBB disruption. This example was obtained after volumetric sonication to induce BBB disruption in the hippocampus and lateral geniculate nucleus (LGN) in macaque. This target was sonicated approximately 2 h before the animal was sacrificed and in seven prior sessions over several months. (A) Axial contrast-enhanced T1-weighted MRI showing BBB disruption induced by sonicating nine targets in a 3 × 3 grid. Inset: Low-magnification microphotograph showing histology in the hippocampus/LGN. (B–C) High-magnification view showing normal-appearing layers in the LGN. (D–E) High-magnification views of hippocampus showing the granular cell layer (D) and the pyramidal layers (E). (F) Blood vessels in the LGN with a few extravasated red blood cells, presumably from the last sonication session. Only a very small number of such extravasations were found. (B, F: H&E; C: H&E–Luxol fast blue; D–E: Nissl; scale bars: A: 1 cm, B, D: 1 mm, C, E–F: 200 μ m). Reprinted from *Cancer Research* 2012; 72:3652–3663; © 2012 American Association for Cancer Research.

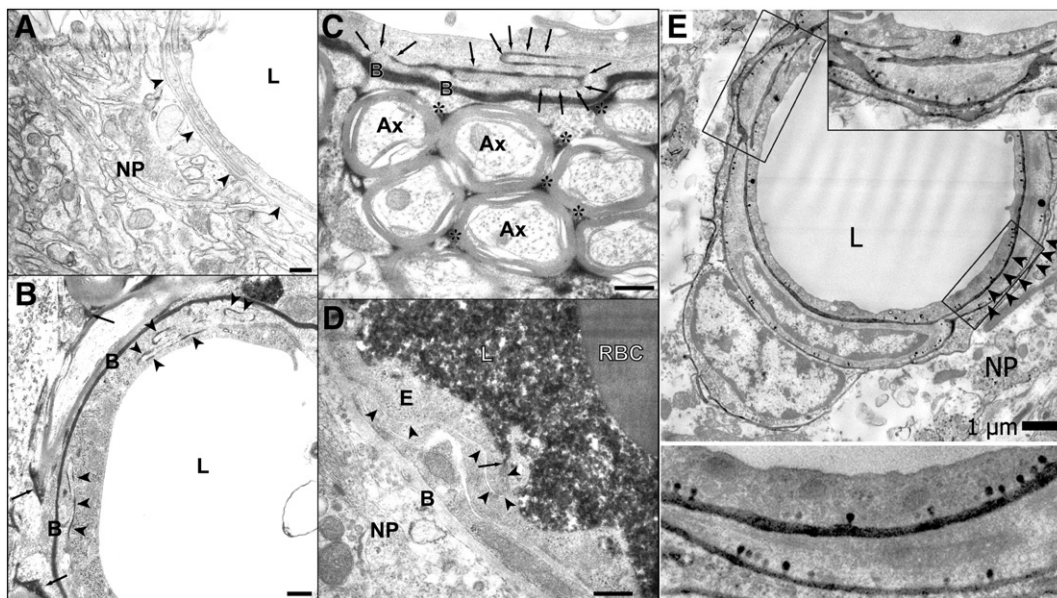


Fig. 4. BBB permeability for horseradish peroxidase (HRP). (A) Photomicrograph showing part of a cross-sectioned microvessel and the surrounding nerve tissue from a nonsonicated area. No HRP passage to the basement membrane (arrowheads) or the neuropil [NP] can be seen. The lumen [L] appears empty because the tracer was washed out during perfusion fixation. (B) A portion of a microvessel with adjacent nerve tissue from a sample obtained 1 h after sonication. Passage of HRP (black color) through several interendothelial clefts is indicated by arrowheads. The tracer has infiltrated the basement membrane [B] and the interstitial space (arrows) in the neuropil. (C) A portion of longitudinally sectioned capillary in a sample obtained 2 h after sonication. The tracer is present in the junctional cleft (arrows), the basement membrane [B] and the interstitial spaces (asterisks) between myelinated axons [Ax]. (D) Full restoration of the tight junctional barrier function 4 h after sonication. Immersion fixation (instead of perfusion fixation) was used in this brain and permits visualization of the tracer (black) filling the lumen [L] and being stopped at the first tight-junction (arrow). No penetration can be seen in the rest of the junctional cleft (arrowheads), nor in the basement membrane [B] or neuropil [NP]. E: endothelial cell cytoplasm; RBC: red blood cell in the lumen. Scale bars: 200 nm. Modified from *Ultrasound in Med. & Biol.*, Vol. 34, No. 7, pp. 1093–1104, 2008; Copyright © 2008 World Federation for Ultrasound in Medicine & Biology. (E) Electron micrograph of an arteriole 1 h after sonication at 0.26 MHz. An intense vesicular transport is demonstrated by the increased number of HRP-positive caveolae (arrows). Significantly fewer vesicles were observed in capillaries and venules. L: lumen. Modified from *Ultrasound in Med. & Biol.*, Vol. 32, No. 9, pp. 1399–1409, 2006; Copyright © 2006 World Federation for Ultrasound in Medicine & Biology.

activation of the p38 JNK MAP kinases promotes neuronal apoptosis [129,130]. Alonso et al. showed increased protein ubiquitination in neurons not glia post sonication, no increase in heat shock proteins, and limited neuronal apoptosis at 24 h in areas staining positive for extravasated albumin [131]. Ca^{2+} signaling has also been suggested as being stimulated by FUS-induced BBB disruption. Specifically, temporary disruption of the endothelial plasma membrane (i.e., sonoporation) can induce immediate transient changes of intracellular Ca^{2+} concentration in cells with direct contact with microbubbles, and delayed fluctuations in nearby cells [132]. When factoring in fluid shear induced in an *in vitro* flow channel (intended to mimic cerebral vessels), the membrane disruption and Ca^{2+} transients were much lower [133].

Multiphoton microscopy (MPM) has provided useful insights into the bioeffects of FUS-induced BBB disruption. Initial work with this technique demonstrated arteriolar vasospasm in 14/16 mice lasting up to 5 min (Fig. 5), and interrupted cerebral blood flow [111]. Although this could cause ischemic injury, it has been noted that mice have enhanced vasomotor excitability over other rodents, such as rats [134]. Indeed, a similar study in rats showed vasospasm in only 25% of the vessels examined [112]. Initial work has also noted two forms of vessel dye leakage, rapid focal microdisruptions (3–9 s) that were prevalent at vessel bifurcations and slow disruptions that were observed as a gradual increase in extravascular signal intensity [111]. Subsequent work noted three rather than two leakage types: (1) fast, characterized

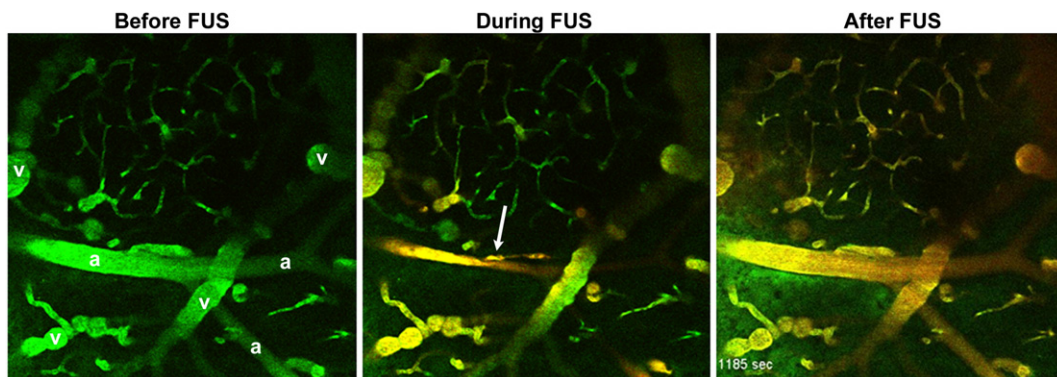


Fig. 5. Vascular effects observed in real time during FUS-induced BBB disruption using *in vivo* multiphoton microscopy. Each frame is a $615 \times 615 \mu\text{m}$ image acquired using a mouse before, during, and approximately 20 min after sonication. Arterioles and veins (determined by dye transit) are marked 'a' and 'v' respectively, in the first frame. The animal received 0.1 mL (2 mg/mL) 10 kDa, dextran-conjugated Alexa Fluor 488 intravenously ~5 mins before imaging (green in images). Immediately after the first frame was taken, a 45-sec US exposure was initiated and a 0.1 mL bolus (10 mg/mL) of 70 kDa, dextran-conjugated Texas Red was delivered intravenously (red in images). Almost total occlusion of the large vessel in the center of the field occurred 12 s after the initiation of US (arrow). Beginning at 60 s and by 305 s, leakage in the green channel is apparent in the lower left of the field, and around the central vessel. (For interpretation of the references to color in this figure legend, the reader is referred to the web version of this article.) Modified from *Journal of Cerebral Blood Flow & Metabolism* 2007;27(2):393–403; Copyright © 2006 ISCBFM.

by rapid increase to peak intensity and rapid decrease, (2) sustained, described as rapid increase to peak which persisted for up to an hour, and (3) slow, a gradual increase to peak intensity [112]. The authors noted that differing vessel calibers have preferences for different leakage types, and interestingly, that distinct peak negative pressures also show preference for leakage types. Continuing work suggested correlation between fast leakage, common with high pressure amplitudes, and detachment of astrocyte endfeet from the vessel walls [135].

4.5. Delivery of imaging/therapeutic agents and tests in animal disease models

One advantage of this method for targeted drug delivery in the brain is that it appears to be “drug neutral” – that is, it appears that many agents with a wide range of properties can be successfully delivered across the BBB and/or the BTB. A large number of imaging tracers (Table 3) and therapeutic agents (Table 4) which normally do not cross the BBB have been delivered to the brain or to brain tumor models with FUS and microbubbles. The amount of substance delivered and the distance from the blood vessels that it penetrates appears to depend on its size. This is evident in the examples shown in Fig. 2, where less delivery of an albumin-bound MRI contrast agent (MW: ~67 kDa) was evident compared to a standard agent (MW: 928 Da) in a macaque. This is even more clear in the example shown in Fig. 6, where delivery of fluorescent dextrans with different molecular weights was examined after sonication in the mouse hippocampus. For 3000 Da dextrans, a relatively uniform fluorescence was observed; for the larger 70 kDa tracer, it was more concentrated near the blood vessels, and a 2000 kDa was found not to penetrate at all [136]. This result points to a need for close examination of how the delivery of large agents occurs – it may not be enough to look for the presence of the agent, but to also investigate whether it is delivered far enough from the vasculature at a high enough concentration to reach the desired target at a therapeutic level. Low-resolution methods such as MRI may not be sufficient for this purpose. It may be possible, for example, for agents to make it past the endothelial cells but get trapped at the basement membrane [137].

4.5.1. Delivery of therapeutics

A large number of therapeutic agents have also been delivered to the brain and to brain tumor models (Table 4). Many of the studies so far have investigated the delivery of chemotherapy agents, such as BCNU [138], doxorubicin [96], methotrexate [139], cytarabine [140], and temozolomide [141]. Enhanced delivery of chemotherapy packaged in liposomes [83,142], targeted liposomes [143] and magnetic particles [144–146], which allow for MRI-based tracking and enhanced delivery via magnetic targeting, have also been demonstrated (Fig. 7). Other

works have shown Trastuzumab, an antibody-based agent used for HER2-positive breast cancer [147,148], and boronophenylalanine, which is used for boron neutron capture therapy, can be delivered to the brain and to brain tumor models [149,150]. FUS-induced BBB disruption has also been shown to improve the delivery of natural killer cells in a brain tumor model [151]. Finally, a number of experiments have loaded chemotherapy and other agents into the microbubbles used for the disruption [146,152–155], which offers the possibility of achieving even higher local payload at the targeted region.

Delivering agents for neurodegenerative diseases, such as Alzheimer's, Huntington's, and Parkinson's disease, have also been an active area of research by several groups. A number of therapies for neurodegenerative diseases such as neuroprotective agents [153,156], antibodies [157,158], plasmid DNA [154], and siRNA [135] have all been successfully delivered across the BBB using FUS and microbubbles. Other investigations have shown that circulating neural progenitor cells [159] or viral vectors for gene therapy [160–162] can be delivered to the sonicated regions after FUS-induced BBB disruption. An example of delivery of adeno-associated virus serotype 9 via FUS-induced BBB disruption to the different cell populations in the mouse brain is shown in Fig. 8.

4.5.2. Disease models

While delivery of these agents is promising, one also needs to demonstrate that the amount of drug delivered – and the drug penetration – is sufficient to produce a therapeutic response. In some cases it is also important to demonstrate that the drug reaches the desired target and is active after it is delivered [156]. Several studies have shown that FUS enhancement of the BTB can slow tumor growth and/or improve survival in orthotopic murine models of primary or metastatic brain tumors [138,141,142,144,145,148,163]. While in some cases the response has been modest, several of these studies have seen substantial improvements. Using multiple treatments may be necessary to achieve a pronounced improvement [142]. One factor that has not been investigated in depth so far is to confirm that drugs can successfully be delivered to infiltrating tumor cells, which are a major feature in glioma and other primary tumors, and to metastatic “seeds”. Both can be protected by the normal BBB. The orthotopic models investigated so far do generally not have large infiltrating zones, and the benefit observed in studies so far may have been primarily due to FUS-enhanced permeability of the BTB. It may be challenging to get therapeutic levels to distant regions that are protected by the BBB. Some agents may have neurotoxic effects on the normal brain that may limit this ability.

Beyond brain tumors, a study by Jordão et al. showed that delivery of antibodies targeted to amyloid plaques can reduce the plaque burden in Alzheimer's disease model mice [158]. While the decrease was modest, with multiple treatment sessions this may be an effective treatment strategy. In an intriguing follow-up study, the same group recently

Table 3
Example different tracers that have been delivered across the BBB.

Agent	Size	Use
Lanthanum chloride	139 Da	Electron microscopy tracer [109]
^{99m} Tc-diethylenetriaminepentaacetic pentaacetate	492 Da	SPECT agent [190]
Omniscan® (Gd-DTPA-BMA)	574 Da	MRI contrast agent [89]
Magnevist® (Gd-DTPA)	928 Da	MRI contrast agent [77]
Trypan blue, Evans blue	~67 kDa	Tissue dyes (binds to albumin) [79,191]
Ablavar® (gadofosveset trisodium)	~67 kDa	MRI contrast agent (binds to albumin) [79]
Horseradish peroxidase	40 kDa	Electron microscopy tracer [78]
Dextran	3–70 kDa	Fluorescent tracer [136]
Immunoglobulin G	~150 kDa	Endogenous antibodies [157]
pCMV-EGFP ^a	?	Plasmid DNA [192]
MION-47	20 nm	MRI contrast agent [120]
Gold nanoparticles	50 nm	Carrier for drugs or imaging [193]
Gold nanorods	10 × 40 nm	Photoacoustic imaging contrast agent [194]
Dotarem, P846, P792, P904, P03680	1–65 nm	MRI contrast agents [115]

^a Loaded into a microbubble.

Table 4

Example therapeutic agents that have been delivered across the BBB or BTB.

Therapeutic agent	Size	Use	Delivered to
Temozolomide	194 Da	Chemotherapy	Glioma model (9L) ^a [141]
1,3-bis(2-chloroethyl)-1-nitrosourea (BCNU) ^b	214 Da	Chemotherapy	Glioma model (C6) ^a [138,152]
Cytarabine	243 Da	Chemotherapy	Normal brain [140]
Boronophenylalanine	330 Da	Agent for boron neutron capture therapy	Glioma models (GBM 8401 [149]; 9L [150])
Doxorubicin	540 Da	Chemotherapy	Normal brain [96]
Methotrexate	545 Da	Chemotherapy	Normal brain [139]
siRNA	~13 kDa	Huntington's disease therapy	Normal brain [135]
Glial cell line-derived neurotrophic factor (GDNF) ^b	24 kDa	Neuroprotective agent	Normal brain [153]
Brain-derived neurotrophic factor (BDNF)	27 kDa	Neuroprotective agent	Normal brain ^c [156]
Herceptin (trastuzumab)	148 kDa	Anti-cancer antibody	Normal brain [147]; breast cancer brain met. model (BT474) ^a [148]
BAM-10 A β targeted antibodies	~150 kDa	Therapeutic antibody for Alzheimer's disease	TgCrND8 Alzheimer's model mice ^a [158]
BCNU-VEGF ^b	~150 kDa	Antiangiogenic-targeted chemotherapy	Glioma model (C6) ^a [155]
Plasmid DNA (pBDNF-EGFP) ^b	~3600 kDa ^d	Gene therapy	Normal brain [154]
Epirubicin in magnetic nanoparticles	~12 nm	Magnetic targeted chemotherapy	Glioma model (C6) ^a [144]
Doxorubicin in magnetic nanoparticles ^b	~6–10 nm	Magnetic targeted chemotherapy	Glioma model (C6) [146]
BCNU in magnetic nanoparticles	~10–20 nm	Magnetic targeted chemotherapy	Glioma model (C6) ^a [145]
Adeno-associated virus (AAV)	~25 nm	Gene therapy vector	Normal brain [160–162]
Liposomal doxorubicin (Lipo-DOX)	90 nm	Chemotherapy	Normal brain [83]; Glioma model (9L) ^a [142,163]
Interleukin-4 receptor targeted Lipo-DOX	100–120 nm	Chemotherapy	Glioma model (8401) [143]
Neural progenitor cells	7–10 μ m	Stem cell	Normal brain [159]
Natural killer cells (NK-92)	~10 μ m	Cell therapy for brain tumor	Breast cancer brain met. model (MDA-MB-231-HER2) [151]

^a Also showed improved outcomes with FUS-induced BBB disruption.^b Used drug-loaded microbubbles.^c Also showed drug activity after delivery.^d Assumed 660 Da per base pair (bp), 760 bp for BDNF, and 4700 bp for pEGFP-N1.

showed that FUS-induced BBB disruption *alone* can reduce the size of the plaques, perhaps through the delivery of endogenous antibodies [164]. We anticipate that these studies are only the beginning, and that FUS has a large potential for Alzheimer's disease and other neurodegenerative disorders. Issues regarding the feasibility and safety of disrupting the BBB in large brain regions (or the whole brain – perhaps repeatedly) may be need further investigation, however.

4.6. Methods to plan, monitor, and evaluate FUS-induced BBB disruption

As described above, FUS-induced BBB disruption utilizes the mechanical interactions between microbubbles oscillating in the ultrasound field and the vasculature. These interactions critically depend on the exposure parameters as well as the vascular density and perhaps other properties of the vascular bed. The latter, can affect the local concentration of microbubbles, how they interact with the ultrasound field [114], and, more importantly, how much drug will be delivered to the brain [79]. Unfortunately, many of these parameters are difficult to predict and are expected to vary significantly across different patients and diseases. Thus, methods are needed to (i) determine what parameters to use (treatment planning), (ii) refine them during sonication to

ensure BBB disruption without overexposure (treatment monitoring), and (iii) evaluate the treatment effects (treatment evaluation).

4.6.1. Treatment planning

In most cases, experiments evaluating FUS-induced BBB disruption in animal models have used a fixed set of acoustic parameters determined from prior experience and simple, geometrically-focused transducers. In general, accurate targeting can be achieved with such systems using stereotactic frames [165] if image-guidance is not available, and fairly repeatable results can be obtained with sonication through the thin skull in mice and rats, or in larger animals through a craniotomy. Methods to avoid standing waves [81] and that take into account variations in skull thickness [166] can improve repeatability in small animal studies where transcranial sonication is used.

Such approaches may be challenging to translate to human subjects, where the thicker skull is complex (a layer of trabecular bone surrounded by layers of cortical bone) and can vary substantially between individuals (3.5–9.5 mm [167]). The skull, which has a substantially higher acoustic impedance than soft tissue, will reflect most of the ultrasound beam, and the amount transmitted will depend strongly on the angle between the bone and the face of the transducer [168]. Its irregular shape can also deflect and distort the beam, and

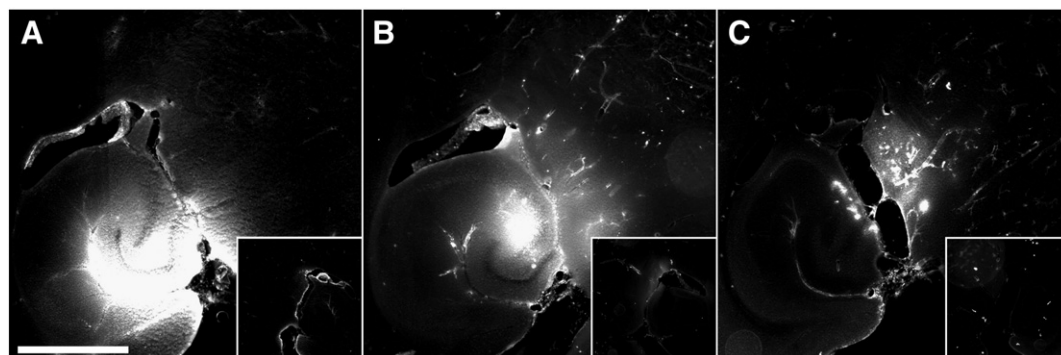


Fig. 6. Delivery of fluorescent dextrans with different sizes across the BBB in a mouse using FUS and microbubbles (A: 3 kDa; B: 10 kDa; C: 70 kDa; bar: 1 mm). Diffuse fluorescence regions can be observed for all dextrans, whereas spots of high fluorescence are observed only with the 70-kDa dextran.

Modified from Proc Natl Acad Sci U S A 2011; 108: 16539–16544; © 2011 by The National Academy of Sciences of the USA.

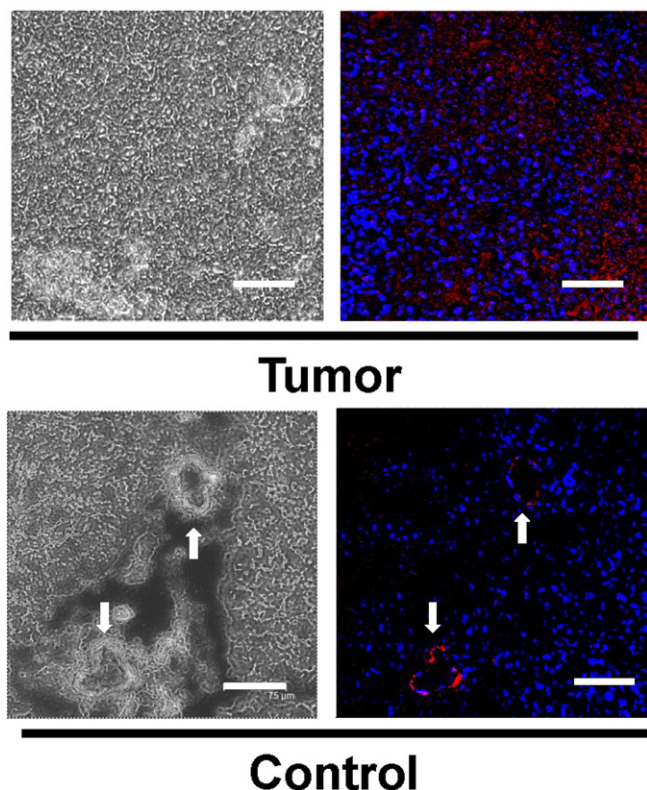


Fig. 7. Confocal micrographs of tissue from tumor after FUS-induced BTB permeabilization followed by magnetic targeting and contralateral brain regions after delivery of magnetic nanoparticles (MNPs) loaded with epirubicin. Dark structures in the phase micrographs show MNPs (left); fused fluorescence images (right) indicate the presence of epirubicin (red) and DAPI-stained nuclei (blue). Arrows indicate the capillaries; epirubicin occurs in the capillary beds but does not penetrate into the brain parenchyma. (For interpretation of the references to color in this figure legend, the reader is referred to the web version of this article.)

Modified from Proc Natl Acad Sci U S A 2010; 107: 15205–15210; © 2011 by The National Academy of Sciences of the USA.

reflections within the skull cavity need to be taken into account. To correct for beam-aberrations introduced by thick skulls, phased arrays composed of more than 1000 elements combined with skull aberration correction algorithms that utilize CT data are employed [57,58]. These arrays can also be programmed to rapidly steer the beam electronically to multiple targets enabling coverage of tissue volumes [79], and different portions of the array can be disabled to reduce internal reflections or exclude certain structures.

While these approaches that use acoustic simulations and CT scans are effective in restoring the focusing of the array after transmission through the skull, clinical experience with them for thermal ablation have shown that one still needs to correct for small errors (~1–2 mm) in targeting [60,63]. To achieve this correction, one needs to be able to visualize the focal region at exposure levels that do not induce damage or other unwanted effects. Currently, this can be achieved using MRI-based methods that can visualize low-level (1–2 °C) focal heating [59,169] or map small tissue displacements of a few microns induced by radiation force [170].

Ensuring accurate targeting will be most important if one aims to precisely disrupt the BBB at discrete locations. In addition, since the strength of the total microbubble activity, as well as magnitude of the disruption will depend on the vascularity of the targeted tissue (gray vs. white matter, for example [79]), it will be important to know exactly where the target is located. It might also be desirable to avoid direct sonication on large blood vessels. If one is uncertain about the targeting of the focal region, it may be challenging to understand whether a poor or unexpected result is due to an incorrect exposure level or to mistargeting. Pre-treatment imaging delineating vascularity, perfusion,

or other vascular properties may prove useful for planning the treatment. It may also be useful to combine these measurements with models of the microbubble oscillations within the microvasculature [114,171].

Accurate control of the focal pressure is critical to ensure BBB disruption is produced while preventing inertial cavitation. The thick and complex human skull makes accurate focal pressure estimations extremely challenging. While the acoustic modeling methods developed for aberration correction may provide estimates of the focal pressure amplitude, it has not been validated to our knowledge. It may be possible to use the MRI-based methods mentioned above that can visualize focal displacements or heating to ensure a predictable focal pressure amplitude. Marty et al., for example, used MR acoustic radiation force imaging to ensure a consistent exposure level between subjects in BBB disruption experiments in rats [115]. However, one needs to take the underlying tissue properties (which may be unknown for tumors or other abnormalities) into account or test it in proximal normal brain locations.

4.6.2. Treatment monitoring and control

Given the challenges in predicting the focal pressure amplitude when sonicating transcranially, we anticipate that effective monitoring of the procedure will be important if this technology is to be translated to clinical use. At minimum, such monitoring should provide an indication that the exposure level is sufficient to induce BBB disruption and alert the user if inertial cavitation is occurring. One could use MRI methods for this purpose. Contrast-enhanced imaging can be used to visualize when the disruption occurs, and T2*-weighted or susceptibility-weighted MRI can be used to detect petechiae produced by inertial cavitation [77,119]. These methods could be used now for control over the procedure in initial clinical tests of FUS-induced BBB disruption with experienced users. However, performing multiple MRI acquisitions would be time-consuming and might require excessive amounts of both ultrasound and MRI contrast agents. Real-time and, perhaps, more direct methods are likely necessary for widespread clinical implementation.

For real-time monitoring and control, a number of studies have investigated the use of piezoelectric receivers operated in passive mode (i.e. only listening) to record and analyze the diverging pressure waves (i.e. acoustic emissions) emitted by oscillating microbubbles during FUS-induced BBB disruption [105–107,172,173]. The spectral content and strength of the recorded emissions is sufficient to characterize and subsequently control the microbubble oscillations. Inertial cavitation is manifested in the frequency domain of the acoustic emission as a broadband signal [53], and has generally been associated with the production of vascular damage during BBB disruption [105,107], although other studies have suggested that it can occur without damage [106]. Harmonic and/or sub- and ultra-harmonic acoustic emissions in the absence of broadband signal are indicative of stable volumetric oscillations, which consistently have been associated with safe BBB disruption [105–107]. Therefore, depending on the spectral content and strength of the emissions the output of the device can be increased until strong harmonic, subharmonic, or ultraharmonic emissions are observed, and decreased if broadband emissions are detected. O'Reilly et al. demonstrated a closed-loop controller built around the detection of ultraharmonic emissions to automatically select an acoustic exposure that could produce BBB disruption with little or no petechiae [173]. We have been exploring the strength of the harmonic emissions as a basis for such a controller, as we have found that we can reliably detect it before inertial cavitation occurs and that it is correlated with the magnitude of the BBB disruption measured via MRI contrast enhancement [105,107]. An example of this correlation observed during transcranial BBB disruption in macaques using a clinical brain FUS system is shown in Fig. 9A.

If one can integrate a large number of receivers into the FUS system, one can use passive reconstruction methods [174,175] to create two- or even three-dimensional maps of the microbubble activity to ensure that it is occurring at the expected location. Examples from experiments in

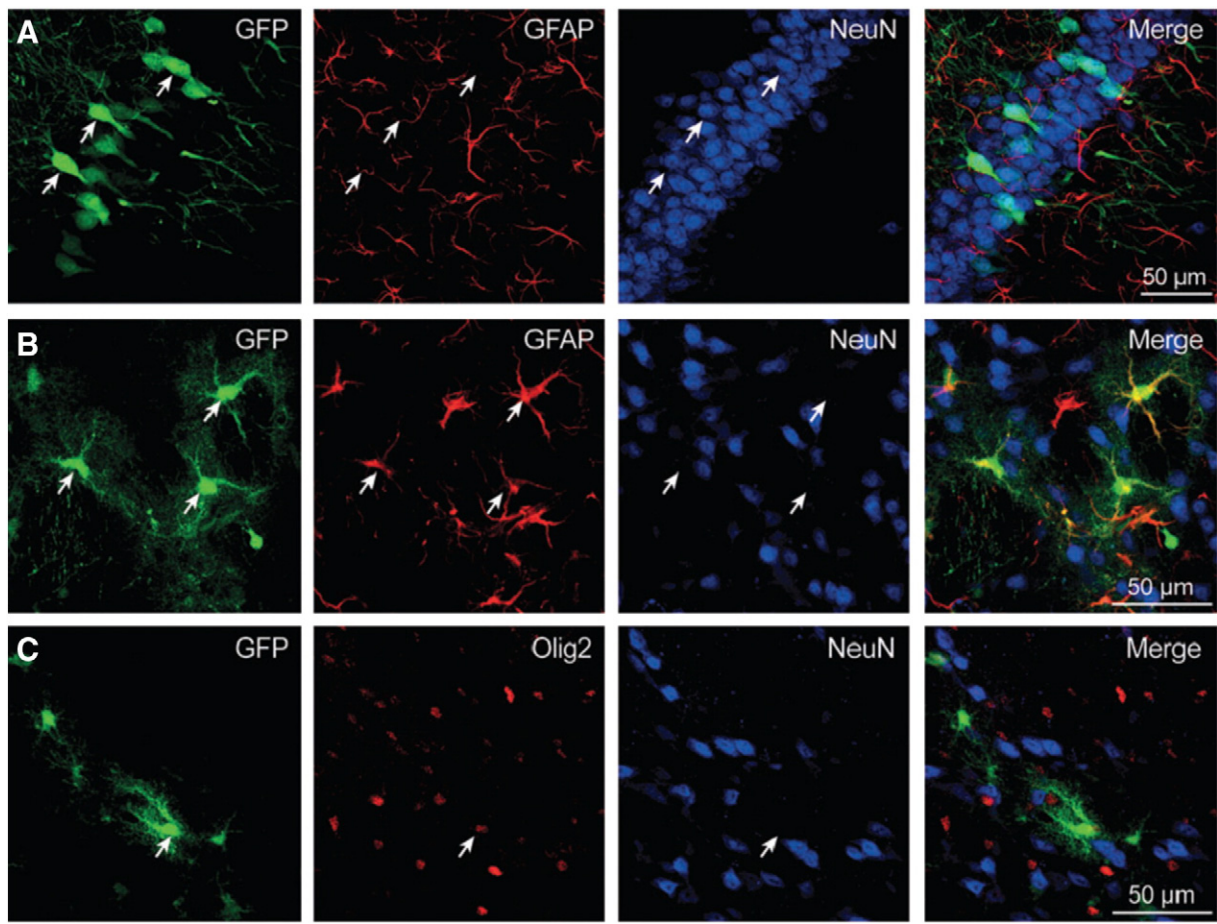


Fig. 8. Gene transfer to neurons, astrocytes, and oligodendrocytes after delivery of adeno-associated virus serotype 9 carrying the green fluorescent protein (GFP) to the mouse brain via FUS-induced BBB disruption. Immunohistochemistry was used to detect GFP expression in hippocampus for (A) NeuN-positive cells (neurons, white arrows), and striatum for (B) GFAP-positive cells (astrocytes, white arrows) and (C) Olig2-positive cells (oligodendrocytes, white arrow).

Modified from Human Gene Therapy 23:1144–1155 (November 2012); © 2012 Mary Ann Liebert, Inc.

our laboratory in macaques using a linear receiver array integrated into a clinical brain FUS system are shown in Fig. 9B–C. In these experiments, we found that the cavitation activity in the passive acoustic maps (red area in Fig. 9B–C) was co-localized with the resulting BBB disruption [176].

4.6.3. Treatment evaluation

As described above, contrast-enhanced imaging and T2* or susceptibility-weighted imaging can be used to verify that BBB disruption has occurred and whether significant vascular damage has occurred, respectively. For tumors, it may be necessary to compare the signal enhancement after contrast injection to measurements obtained before FUS. Other imaging modalities may also be useful [177]. If the contrast-enhanced imaging is obtained before the therapeutic agent is injected, one can confirm that the BBB disruption is only occurring at the targeted locations before administering the drug, providing another level of control to ensure that drugs are delivered only to desired regions.

Post-treatment imaging could be more useful if one could use it to estimate drug uptake and penetration in the brain. This can be achieved directly by labeling the drug with a contrast agent for MRI or other modality [146]. It might also be possible to use a standard contrast agent as a surrogate measurement. A number of studies have related signal intensity changes of contrast-enhanced MRI at the end of the sonication with tissue drug concentrations [83,147,178]. More quantitative and repeatable techniques, such as estimating contrast agent concentrations via T1-mapping [115,179] or vascular transfer coefficients via analysis of dynamic contrast-enhanced MRI (DCE-MRI) [180] have

been used to perform spatial and temporal characterization of BBB permeability. DCE-MRI can also predict the resulting payload of drugs to the brain [96] and in some cases, in tumors [179]. Examples showing DCE-MRI evaluation of BBB disruption and its subsequent restoration over time, and its relationship to concentrations of doxorubicin are shown in Fig. 10. If one understands the relationship between the concentrations of the therapeutic and the imaging contrast agent, which can perhaps be established in animals, one might be able to titrate the drug administration to achieve a desired level in the brain. However, this may be challenging in tumors, where the vascular permeability can change over time [179].

5. Going forward

Based on the extensive preclinical experience described above, along with recent studies in non-human primates [79,80] demonstrating that the method can be “scaled up” without producing evident tissue damage or functional deficits even after repeated sessions [79], this method for targeted drug delivery in the brain is ready in our view for initial safety tests in humans, where it will hopefully reveal its enormous potential. Clinical transcranial MRI-guided FUS systems [60,63] and commercially-available ultrasound contrast agents are available and can be used for these tests. Given the huge clinical need and the existence of available approved anticancer agents that are expected to be effective if they could be adequately delivered, brain tumors may be an appropriate target for these initial tests.

Given MRI’s high cost and complexity, coupled with the need in many cases to administer therapeutics over multiple sessions, it would

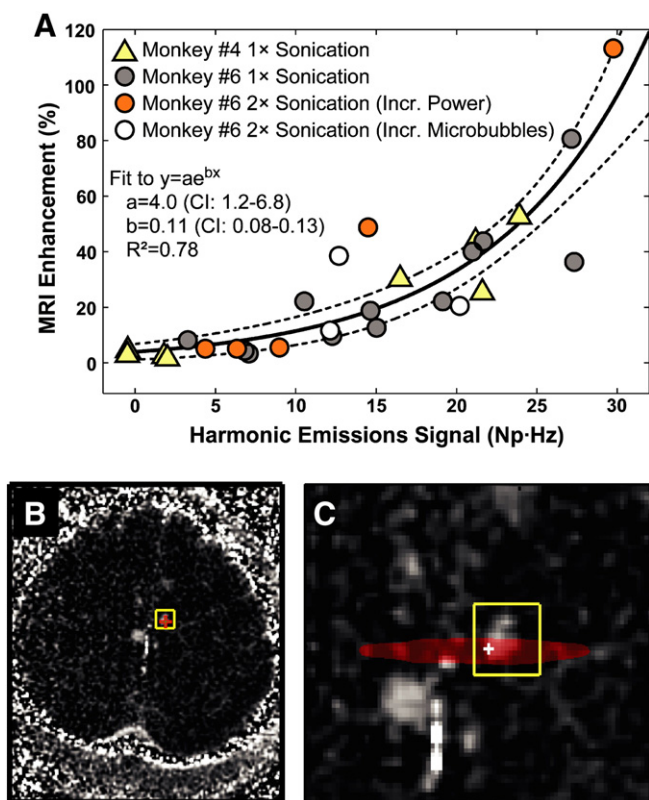


Fig. 9. Comparison of MRI signal enhancement with microbubble acoustic emissions. (A) MRI signal enhancement after Gd-DTPA injection plotted as a function of the harmonic emissions signal strength measured with single-element detectors. A clear relationship between the two measurements was observed with a good fit to an exponential. The agreement appeared to hold among different animals and in cases where targets with low-level harmonic emissions were sonicated a second time with either a higher power level or an increased dose of microbubbles. Reprinted from PLoS ONE 7(9): e45783. <http://dx.doi.org/10.1371/journal.pone.0045783>; © 2012 Arvanitis et al. (B–C) Comparison between MRI signal enhancement and passive cavitation mapping. (B) Map showing the enhancement relative to a pre-contrast image. (C) Fusion of passive cavitation map with the T1-weighted MRI from (B). The red region shows the pixels in the cavitation map within 95% of the maximum value. This region overlapped with the contrast enhancement. The pixel with the maximum cavitation activity is noted with a "+". The enhancement from other targets sonicated in the same session is visible. (For interpretation of the references to color in this figure legend, the reader is referred to the web version of this article.) Modified from Phys Med Biol 58.14 (2013): 4749–61; © 2013 Institute of Physics and Engineering in Medicine.

be desirable in the long run to develop systems to provide FUS-induced BBB outside of the MRI environment. Passive cavitation monitoring and/or mapping may be the enabling technology for this translation away from MRI guidance. One can envision systems that use pre-treatment MRI and CT (to delineate different tissue structures and skull density, respectively), along with “frameless” navigation and cavitation monitoring to provide routine BBB disruption in an outpatient facility. A number of technical developments, such as reducing targeting error during transcranial sonication, finding methods to easily register the position of the skull within the FUS device without a stereotactic frame, and developing methods to better quantify acoustic emissions measurements obtained through the thicker human skull, are needed to reach this goal. In our opinion, all of these things are achievable. It would also be desirable to remove the need to shave the head, which is currently needed to allow for acoustic coupling. Attenuation should not prevent this [181].

The potential of this technique to manipulate the amount of drug delivered to each point in the brain can provide a level of control that is not readily available with existing technologies. This control can be achieved by modulating the acoustic parameters to control the “level”

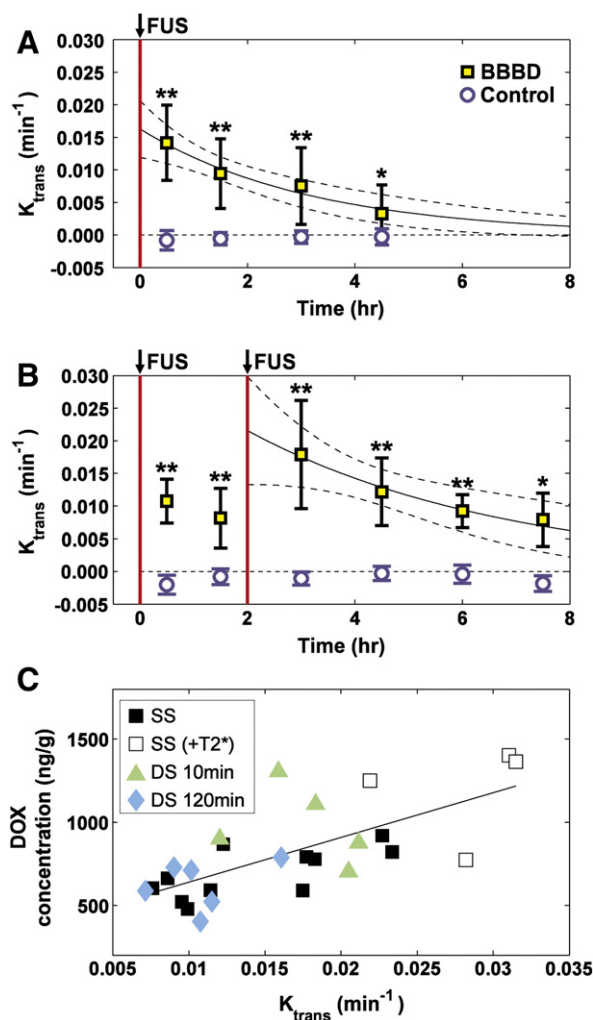


Fig. 10. Using DCE-MRI to evaluate FUS-BBB disruption. (A–B) Mean K_{trans} values measured vs. time from DCE-MRI in regions of interest at sonicated locations and in corresponding non-sonicated structures in the contralateral hemisphere. The decay of K_{trans} , which occurred due to restoration of the BBB, was fit to an exponential decay (solid line; dotted lines: 95% CI). (A) Decay after a single sonication. (B) Time course after two sonications separated by 120 min. The second sonication increased the amount of time the barrier was disrupted. Values were significantly higher than in control locations in the contralateral hemisphere (** $P < 0.01$ and * $P < 0.05$). (C) DOX concentration achieved at the sonicated locations as a function of K_{trans} measured using DCE-MRI 30 min after sonication. The DOX concentration was measured approximately 16 h later for brain targets in single sonication (SS), single sonication with hyperintense spots in T2* weighted image (SS (+T2*)), double sonication with 10 min interval (DS 10 min), and double sonication with 120 min interval (DS 120 min). The solid line shows a linear regression of the data (slope: 28,824 ng/g DOX per change in K_{trans} in min^{-1} ; intercept: 377 ng/g DOX; $R: 0.7$). Modified from Journal of Controlled Release 2012;162:134–142; © 2012 Elsevier B.V.

of the disruption, by analyzing the post-sonication contrast enhancement before injecting the drug and titrating the drug dose, or by repeating sonication at select areas after some delay to lengthen the time the barrier is disrupted [96]. It might even be possible to tailor the sonication parameters and BBB disruption to the molecular weight of the therapeutic agent. These methods may enable “dose painting” that can give clinicians new flexibility in how drugs are used in the CNS to maximize efficacy and minimizing side effects. Further targeting and control can be achieved by loading drugs into microbubbles [146,152–155] or by using magnetic targeting after FUS-induced BBB disruption [144–146].

It will also be important to establish the feasibility and safety of targeting very large volumes. Many promising applications of this technology (brain tumors, Alzheimer's disease, etc.) will require sonication over large portions of the brain for greatest effect. This can be achieved

by systematically focusing the ultrasound beam to a large number of individual targets. It should be possible to target the hundreds or thousands of focal points needed to achieve such large-scale BBB disruption in a reasonable amount of time. Given the low duty cycle and minimal acoustic exposure levels needed to induce the effect, many targets can be sonicated simultaneously. For example, with the low duty cycle needed to induce BBB disruption (1% or less), we can target 100 targets or more with electronic beam steering with a phased array in the same amount of time it currently takes to disrupt one location with the simple system we use for small animal experiments. While again this will require technical improvements and more safety tests, we expect that achieving controlled, large volume BBB disruption is achievable.

It would be helpful if the physical and/or physiological mechanisms by which the mechanical effects of FUS and microbubbles induce BBB disruption were elucidated. Without knowledge of the mechanism, one can only speculate on how one can optimize the procedure, and we are left with performing time-consuming parametric studies. Given the large parameter space in variables that can influence the magnitude of the BBB disruption, it is possible that we have not stumbled upon parameters that can further improve upon the safe window where BBB disruption is possible. Multidisciplinary approaches are very likely to prove fruitful and could potentially identify a unique physiologic mechanism, perhaps with interesting implications on the structure and function of the vasculature in the CNS.

Other tissues have barriers similar to the BBB and could benefit from similar microbubble-enhanced sonications or prove to be simpler models to study the aforementioned interactions. There is data demonstrating that disruption of the blood–retinal [182] and blood–spinal cord [183] barriers can be disrupted by FUS, and that the glomerular function in the kidney can be enhanced, presumably through changes in the “blood–urine barrier” [184]. Also, using pressure amplitudes higher than are needed for FUS-induced BBB disruption, one can use microbubble-enhanced sonications for ablation [185], thrombolysis [186], or radiosensitization [187]. One can potentially combine one of these microbubble-enhanced therapies with BBB disruption to produce a synergistic effect or to deliver therapeutics in the surrounding tissues.

The clinical need for new approaches to bypass the BBB in order to increase the number of drugs that can be used effectively in the CNS is tremendous. In addition to CNS disorders such as brain tumors, stroke, trauma, and genetic neurodegenerative disorders, opportunities may exist for a wide range of other applications. Examples include pain management, and psychological disorders such as addiction, both of which may benefit from a technology that permits drug transport to precise targets in the brain. Existing drugs for these conditions can have severe side effects that limit their use. With an ever-growing knowledge of brain function and dysfunction, precise drug targeting in the CNS may prove to be particularly important. Technical improvements that are achievable in our view could enable FUS to be used on a wide scale for routine targeted drug delivery to the CNS.

6. Conclusion

FUS is a unique technology that can induce BBB or BTB permeabilization that is targeted, noninvasive and transient. Extensive work in preclinical studies has demonstrated that it can enable the delivery of therapeutics that normally do not reach the brain, and enhance their delivery to brain tumors. The sonications do not appear to have any deleterious effects on the brain, and the method is readily repeatable. MRI and acoustic methods to plan, monitor, and evaluate the treatment offer the possibility of having control over where drugs are delivered and in what concentration. Given the availability of clinical FUS devices capable of focusing ultrasound through the intact human skull, along with recent safety studies demonstrating the method can be performed safely in nonhuman primates, it appears that the method is ready for initial clinical tests.

References

- [1] E.A. Neuwelt, B. Bauer, C. Fahlke, G. Fricker, C. Iadecola, D. Janigro, L. Leybaert, Z. Molnar, M.E. O'Donnell, J.T. Povlishock, N.R. Saunders, F. Sharp, D. Stanimirovic, R.J. Watts, L.R. Drewes, Engaging neuroscience to advance translational research in brain barrier biology, *Nat. Rev. Neurosci.* 12 (2011) 169–182.
- [2] N.J. Abbott, I.A. Romero, Transporting therapeutics across the blood–brain barrier, *Mol. Med. Today* 2 (1996) 106–113.
- [3] W.M. Pardridge, Molecular biology of the blood–brain barrier, *Mol. Biotechnol.* 30 (2005) 57–70.
- [4] A.F. Eichler, E. Chung, D.P. Kodack, J.S. Loeffler, D. Fukumura, R.K. Jain, The biology of brain metastases—translation to new therapies, *Nat. Rev. Clin. Oncol.* 8 (2011) 344–356.
- [5] G. Minniti, D. Amelio, M. Amichetti, M. Salvati, R. Muni, A. Bozzao, G. Lanzetta, S. Scarpino, A. Arcella, R.M. Enrici, Patterns of failure and comparison of different target volume delineations in patients with glioblastoma treated with conformal radiotherapy plus concomitant and adjuvant temozolomide, *Radiother. Oncol.* 97 (2010) 377–381.
- [6] M.C. Dobbels, O.L. Burnett, R.A. Nordal, L.B. Nabors, J.M. Markert, M.D. Hyatt, J.B. Fiveash, Patterns of failure for glioblastoma multiforme following concurrent radiation and temozolomide, *J. Med. Imaging Radiat. Oncol.* 55 (2011) 77–81.
- [7] M.C. Chamberlain, Radiographic patterns of relapse in glioblastoma, *J. Neurooncol.* 101 (2011) 319–323.
- [8] D. Fukumura, R.K. Jain, Tumor microenvironment abnormalities: causes, consequences, and strategies to normalize, *J. Cell. Biochem.* 101 (2007) 937–949.
- [9] A. Regina, M. Demeule, A. Laplante, J. Jodoin, C. Dagenais, F. Berthelet, A. Moghrabi, R. Beliveau, Multidrug resistance in brain tumors: roles of the blood–brain barrier, *Cancer Metastasis Rev.* 20 (2001) 13–25.
- [10] P.R. Lockman, R.K. Mittapalli, K.S. Taskar, V. Rudraraju, B. Gri, K.A. Bohn, C.E. Adkins, A. Roberts, H.R. Thorsheim, J.A. Gaasch, S. Huang, D. Palmieri, P.S. Steeg, Q.R. Smith, Heterogeneous blood–tumor barrier permeability determines drug efficacy in experimental brain metastases of breast cancer, *Clin. Cancer Res.* 16 (2010) 5664–5678.
- [11] D.R. Groothuis, The blood–brain and blood–tumor barriers: a review of strategies for increasing drug delivery, *Neuro Oncol.* 2 (2000) 45–59.
- [12] W.M. Pardridge, Blood–brain barrier delivery, *Drug Discov. Today* 12 (2007) 54–61.
- [13] J.P. Blumling, G.A. Silva, Targeting the brain: advances in drug delivery, *Curr. Pharm. Biotechnol.* 13 (2012) 2417–2426.
- [14] T. Tomita, Interstitial chemotherapy for brain tumors: review, *J. Neurooncol.* 10 (1991) 57–74.
- [15] R.H. Bobo, D.W. Laske, A. Akbasak, P.F. Morrison, R.L. Dedrick, E.H. Oldfield, Convection-enhanced delivery of macromolecules in the brain, *Proc. Natl. Acad. Sci. U. S. A.* 91 (1994) 2076–2080.
- [16] C. Guerin, A. Olivi, J.D. Weingart, H.C. Lawson, H. Brem, Recent advances in brain tumor therapy: local intracerebral drug delivery by polymers, *Invest. New Drugs* 22 (2004) 27–37.
- [17] H. Brem, P. Gabikian, Biodegradable polymer implants to treat brain tumors, *J. Control. Release* 74 (2001) 63–67.
- [18] L.K. Fung, M. Shin, B. Tyler, H. Brem, W.M. Saltzman, Chemotherapeutic drugs released from polymers: distribution of 1,3-bis(2-chloroethyl)-1-nitrosourea in the rat brain, *Pharm. Res.* 13 (1996) 671–682.
- [19] J. Voges, R. Reszka, A. Gossmann, C. Dittmar, R. Richter, G. Garlip, L. Kracht, H.H. Coenen, V. Sturm, K. Wienhard, W.D. Heiss, A.H. Jacobs, Imaging-guided convection-enhanced delivery and gene therapy of glioblastoma, *Ann. Neurol.* 54 (2003) 479–487.
- [20] G. Fleischhack, U. Jaehde, U. Bode, Pharmacokinetics following intraventricular administration of chemotherapy in patients with neoplastic meningitis, *Clin. Pharmacokinet.* 44 (2005) 1–31.
- [21] L. Illum, Nasal drug delivery—possibilities, problems and solutions, *J. Control. Release* 87 (2003) 187–198.
- [22] L. Illum, Nasal drug delivery: new developments and strategies, *Drug Discov. Today* 7 (2002) 1184–1189.
- [23] M.I. Ugwoke, R.U. Agu, N. Verbeke, R. Kinget, Nasal mucoadhesive drug delivery: background, applications, trends and future perspectives, *Adv. Drug Deliv. Rev.* 57 (2005) 1640–1665.
- [24] A. Pires, A. Fortuna, G. Alves, A. Falcao, Intranasal drug delivery: how, why and what for? *J. Pharm. Pharm. Sci.* 12 (2009) 288–311.
- [25] W.H. Oldendorf, S. Hyman, L. Braun, S.Z. Oldendorf, Blood–brain barrier: penetration of morphine, codeine, heroin, and methadone after carotid injection, *Science* 178 (1972) 984–986.
- [26] N.J. Abbott, A.A. Patabendige, D.E. Dolman, S.R. Yusof, D.J. Begley, Structure and function of the blood–brain barrier, *Neurobiol. Dis.* 37 (2010) 13–25.
- [27] E.Y. Zhang, G.T. Knipp, S. Ekins, P.W. Swaan, Structural biology and function of solute transporters: implications for identifying and designing substrates, *Drug Metab. Rev.* 34 (2002) 709–750.
- [28] W.M. Pardridge, Blood–brain barrier drug targeting: the future of brain drug development, *Mol. Interv.* 3 (2003) 90–105(51).
- [29] W.M. Pardridge, Drug targeting to the brain, *Pharm. Res.* 24 (2007) 1733–1744.
- [30] P. Blasi, S. Giovagnoli, A. Schoubben, M. Ricci, C. Rossi, Solid lipid nanoparticles for targeted brain drug delivery, *Adv. Drug Deliv. Rev.* 59 (2007) 454–477.
- [31] J.C. Olivier, Drug transport to brain with targeted nanoparticles, *NeuroRx* 2 (2005) 108–119.
- [32] A. Snyder, J. Huwyler, Drug transport to brain with targeted liposomes, *NeuroRx* 2 (2005) 99–107.
- [33] R.D. Broadwell, B.J. Balin, M. Salzman, Transcytotic pathway for blood-borne protein through the blood–brain barrier, *Proc. Natl. Acad. Sci. U. S. A.* 85 (1988) 632–636.

- [34] I. Mellman, Endocytosis and molecular sorting, *Annu. Rev. Cell Dev. Biol.* 12 (1996) 575–625.
- [35] S. Mukherjee, R.N. Ghosh, F.R. Maxfield, Endocytosis, *Physiol. Rev.* 77 (1997) 759–803.
- [36] S.I. Rapoport, Effect of concentrated solutions on blood–brain barrier, *Am. J. Physiol.* 219 (1970) 270–274.
- [37] S.I. Rapoport, Advances in osmotic opening of the blood–brain barrier to enhance CNS chemotherapy, *Expert. Opin. Investig. Drugs* 10 (2001) 1809–1818.
- [38] R.A. Kroll, E.A. Neuwelt, Outwitting the blood–brain barrier for therapeutic purposes: osmotic opening and other means, *Neurosurgery* 42 (1998) 1083–1099.
- [39] M.A. Bellavance, M. Blanchette, D. Fortin, Recent advances in blood–brain barrier disruption as a CNS delivery strategy, *AAPS J.* 10 (2008) 166–177.
- [40] N.D. Doolittle, M.E. Miner, W.A. Hall, T. Siegal, E. Jerome, E. Osztie, L.C. McAllister, J.S. Bubalo, D.F. Kraemer, D. Fortin, R. Nixon, L.L. Muldoon, E.A. Neuwelt, Safety and efficacy of a multicenter study using intraarterial chemotherapy in conjunction with osmotic opening of the blood–brain barrier for the treatment of patients with malignant brain tumors, *Cancer* 88 (2000) 637–647.
- [41] W.A. Hall, N.D. Doolittle, M. Daman, P.K. Bruns, L. Muldoon, D. Fortin, E.A. Neuwelt, Osmotic blood–brain barrier disruption chemotherapy for diffuse pontine gliomas, *J. Neurooncol.* 77 (2006) 279–284.
- [42] K. Jahnke, D.F. Kraemer, K.R. Knight, D. Fortin, S. Bell, N.D. Doolittle, L.L. Muldoon, E.A. Neuwelt, Intraarterial chemotherapy and osmotic blood–brain barrier disruption for patients with embryonal and germ cell tumors of the central nervous system, *Cancer* 112 (2008) 581–588.
- [43] L. Angelov, N.D. Doolittle, D.F. Kraemer, T. Siegal, G.H. Barnett, D.M. Peereboom, G. Stevens, J. McGregor, K. Jahnke, C.A. Lacy, N.A. Hedrick, E. Shalom, S. Ference, S. Bell, L. Sorenson, R.M. Tyson, M. Haluska, E.A. Neuwelt, Blood–brain barrier disruption and intra-arterial methotrexate-based therapy for newly diagnosed primary CNS lymphoma: a multi-institutional experience, *J. Clin. Oncol.* 27 (2009) 3503–3509.
- [44] J.A. Boockvar, A.J. Tsioris, C.P. Hofstetter, I. Kovanlikaya, S. Fralin, K. Kesavabhotla, S.M. Seedial, S.C. Pannullo, T.H. Schwartz, P. Stieg, R.D. Zimmerman, J. Knopman, R.J. Scheff, P. Christos, S. Vallabhajosula, H.A. Riina, Safety and maximum tolerated dose of superselective intraarterial cerebral infusion of bevacizumab after osmotic blood–brain barrier disruption for recurrent malignant glioma. Clinical article, *J. Neurosurg.* 114 (2011) 624–632.
- [45] D.J. Guillaume, N.D. Doolittle, S. Gahramanov, N.A. Hedrick, J.B. Delashaw, E.A. Neuwelt, Intra-arterial chemotherapy with osmotic blood–brain barrier disruption for aggressive oligodendroglial tumors: results of a phase I study, *Neurosurgery* 66 (2010) 48–58.
- [46] T. Inamura, T. Nomura, K. Ikezaki, M. Fukui, G. Pollinger, K.L. Black, Intracarotid histamine infusion increases blood tumour permeability in RG2 glioma, *Neurol. Res.* 16 (1994) 125–128.
- [47] M. Gutman, R. Laufer, A. Eisenthal, G. Goldman, A. Ravid, M. Inbar, J.M. Klausner, Increased microvascular permeability induced by prolonged interleukin-2 administration is attenuated by the oxygen-free-radical scavenger dimethylthiourea, *Cancer Immunol. Immunother.* 43 (1996) 240–244.
- [48] K.L. Black, C.C. Chio, Increased opening of blood–tumour barrier by leukotriene C4 is dependent on size of molecules, *Neurol. Res.* 14 (1992) 402–404.
- [49] H.E. de Vries, M.C. Blom-Roosemalen, M. van Oosten, A.G. de Boer, T.J. van Berkel, D.D. Breimer, J. Kuiper, The influence of cytokines on the integrity of the blood–brain barrier in vitro, *J. Neuroimmunol.* 64 (1996) 37–43.
- [50] J.G. Lynn, T.J. Putnam, Histology of cerebral lesions produced by focused ultrasound, *Am. J. Pathol.* 20 (1944) 637–652.
- [51] W.J. Fry, F.J. Fry, Fundamental neurological research and human neurosurgery using intense ultrasound, *IRE Trans. Med. Electron.* ME-7 (1960) 166–181.
- [52] H.T. Ballantine, E. Bell, J. Manlapaz, Progress and problems in the neurological applications of focused ultrasound, *J. Neurosurg.* 17 (1960) 858–876.
- [53] P.P. Lele, Effects of ultrasound on “solid” mammalian tissues and tumors in vivo, in: M.H. Repacholi, M. Grondolfo, A. Rindi (Eds.), *Ultrasound: Medical Applications, Biological Effects and Hazard Potential*, Plenum Pub. Corp, New York, 1987, pp. 275–306.
- [54] R. Meyers, W.J. Fry, F.J. Fry, L.L. Dreyer, D.F. Shultz, R.F. Noyes, Early experiences with ultrasonic irradiation of the pallidifugal and nigral complexes in hyperkinetic and hypertonic disorders, *J. Neurosurg.* 16 (1959) 32–54.
- [55] R.F. Heimbürger, Ultrasound augmentation of central nervous system tumor therapy, *Indiana Med. J.* 78 (1985) 469–476.
- [56] K. Hynynen, N. McDannold, MRI guided and monitored focused ultrasound thermal ablation methods: a review of progress, *Int. J. Hyperthermia* 20 (2004) 725–737.
- [57] G.T. Clement, K. Hynynen, A non-invasive method for focusing ultrasound through the human skull, *Phys. Med. Biol.* 47 (2002) 1219–1236.
- [58] J.F. Aubry, M. Tanter, M. Pernot, J.L. Thomas, M. Fink, Experimental demonstration of noninvasive transskull adaptive focusing based on prior computed tomography scans, *J. Acoust. Soc. Am.* 113 (2003) 84–93.
- [59] Y. Ishihara, A. Calderon, H. Watanabe, K. Okamoto, Y. Suzuki, K. Kuroda, A precise and fast temperature mapping using water proton chemical shift, *Magn. Reson. Med.* 34 (1995) 814–823.
- [60] N. McDannold, G.T. Clement, P. Black, F. Jolesz, K. Hynynen, Transcranial magnetic resonance imaging-guided focused ultrasound surgery of brain tumors: initial findings in 3 patients, *Neurosurgery* 66 (2010) 323–332.
- [61] N. Lipsman, M.L. Schwartz, Y. Huang, L. Lee, T. Sankar, M. Chapman, K. Hynynen, A.M. Lozano, MR-guided focused ultrasound thalamotomy for essential tremor: a proof-of-concept study, *Lancet Neurol.* 12 (2013) 462–468.
- [62] W.J. Elias, D. Huss, T. Voss, J. Loomba, M. Khaled, E. Zadicario, R.C. Frysiinger, S.A. Sperling, S. Wylie, S.J. Monteith, J. Druzgal, B.B. Shah, M. Harrison, M. Wintermark, A pilot study of focused ultrasound thalamotomy for essential tremor, *N. Engl. J. Med.* 369 (2013) 640–648.
- [63] E. Martin, D. Jeanmonod, A. Morel, E. Zadicario, B. Werner, High-intensity focused ultrasound for noninvasive functional neurosurgery, *Ann. Neurol.* 66 (2009) 858–861.
- [64] W.L. Nyborg, P.L. Carson, E.L. Carstensen, F. Dunn, D.L. Miller, M.W. Miller, H.E. Thompson, M.C. Ziskin, R.E. Apfel, C.C. Church, L.A. Crum, Exposure Criteria for Medical Diagnostic Ultrasound: II. Criteria Based on All Known Mechanisms (NCRP Report No. 140), National Council on Radiation Protection and Measurements, Bethesda, Maryland, 2002.
- [65] T.G. Leighton, *The Acoustic Bubble*, Academic Press Limited, San Diego, CA, 1994.
- [66] P. Dayton, A. Klibanov, G. Brandenburger, K. Ferrara, Acoustic radiation force in vivo: a mechanism to assist targeting of microbubbles, *Ultrasound Med. Biol.* 25 (1999) 1195–1201.
- [67] D.L. Miller, Particle gathering and microstreaming near ultrasonically activated gas-filled micropores, *J. Acoust. Soc. Am.* 84 (1988) 1378–1387.
- [68] P.D. Edmonds, K.M. Sancier, Evidence for free radical production by ultrasonic cavitation in biological media, *Ultrasound Med. Biol.* 9 (1983) 635–639.
- [69] H.G. Flynn, Generation of transient cavities in liquids by microsecond pulses of ultrasound, *J. Acoust. Soc. Am.* 72 (1982) 1926–1932.
- [70] R.E. Apfel, Acoustic cavitation: a possible consequence of biomedical uses of ultrasound, *Br. J. Cancer Suppl.* 45 (1982) 140–146.
- [71] L. Bakay, T.F. Hueter, H.T. Ballantine, D. Sosa, Ultrasonically produced changes in the blood–brain barrier, *Arch. Neurol.* 76 (1956) 457–467.
- [72] N. Vykhodtseva, Effects of high intensity pulsed ultrasound on brain tissues, *The 5th International Symposium on Ultrasound in Biol. Med.* Puschino, Russia, 1981, pp. 95–97.
- [73] J.T. Patrick, M.N. Nolting, S.A. Goss, K.A. Dines, J.L. Clendenon, M.A. Rea, R.F. Heimbürger, Ultrasound and the blood–brain barrier, *Adv. Exp. Med. Biol.* 267 (1990) 369–381.
- [74] N.I. Vykhodtseva, K. Hynynen, C. Damianou, Histologic effects of high intensity pulsed ultrasound exposure with subharmonic emission in rabbit brain in vivo, *Ultrasound Med. Biol.* 21 (1995) 969–979.
- [75] A.H. Mesivala, L. Farrell, H.J. Wenzel, D.L. Silbergeld, L.A. Crum, H.R. Winn, P.D. Mourad, High-intensity focused ultrasound selectively disrupts the blood–brain barrier in vivo, *Ultrasound Med. Biol.* 28 (2002) 389–400.
- [76] N. McDannold, N. Vykhodtseva, F.A. Jolesz, K. Hynynen, MRI investigation of the threshold for thermally induced blood–brain barrier disruption and brain tissue damage in the rabbit brain, *Magn. Reson. Med.* 51 (2004) 913–923.
- [77] K. Hynynen, N. McDannold, N. Vykhodtseva, F.A. Jolesz, Noninvasive MR imaging-guided focal opening of the blood–brain barrier in rabbits, *Radiology* 220 (2001) 640–646.
- [78] N. Sheikov, N. McDannold, N. Vykhodtseva, F. Jolesz, K. Hynynen, Cellular mechanisms of the blood–brain barrier opening induced by ultrasound in presence of microbubbles, *Ultrasound Med. Biol.* 30 (2004) 979–989.
- [79] N. McDannold, C.D. Arvanitis, N. Vykhodtseva, M.S. Livingstone, Temporary disruption of the blood–brain barrier by use of ultrasound and microbubbles: safety and efficacy evaluation in rhesus macaques, *Cancer Res.* 72 (2012) 3652–3663.
- [80] F. Marquet, Y.S. Tung, T. Teichert, V.P. Ferrera, E.E. Konofagou, Noninvasive, transient and selective blood–brain barrier opening in non-human primates in vivo, *PLoS One* 6 (2011) e22598.
- [81] M.A. O'Reilly, Y. Huang, K. Hynynen, The impact of standing wave effects on transcranial focused ultrasound disruption of the blood–brain barrier in a rat model, *Phys. Med. Biol.* 55 (2010) 5251–5267.
- [82] K. Hynynen, N. McDannold, N.A. Sheikov, F.A. Jolesz, N. Vykhodtseva, Local and reversible blood–brain barrier disruption by noninvasive focused ultrasound at frequencies suitable for trans-skull sonications, *Neuroimage* 24 (2005) 12–20.
- [83] L.H. Treat, N. McDannold, Y. Zhang, N. Vykhodtseva, K. Hynynen, Targeted delivery of doxorubicin to the rat brain at therapeutic levels using MRI-guided focused ultrasound, *Int. J. Cancer* 121 (2007) 901–907.
- [84] R. Chopra, N. Vykhodtseva, K. Hynynen, Influence of exposure time and pressure amplitude on blood–brain-barrier opening using transcranial ultrasound exposures, *ACS Chem. Neurosci.* 1 (2010) 391–398.
- [85] N. McDannold, N. Vykhodtseva, K. Hynynen, Blood–brain barrier disruption induced by focused ultrasound and circulating preformed microbubbles appears to be characterized by the mechanical index, *Ultrasound Med. Biol.* 34 (2008) 834–840.
- [86] N. McDannold, N. Vykhodtseva, K. Hynynen, Effects of acoustic parameters and ultrasound contrast agent dose on focused-ultrasound induced blood–brain barrier disruption, *Ultrasound Med. Biol.* 34 (2008) 930–937.
- [87] J.J. Choi, J.A. Feshitan, B. Baseri, S. Wang, Y.S. Tung, M.A. Borden, E.E. Konofagou, Microbubble-size dependence of focused ultrasound-induced blood–brain barrier opening in mice in vivo, *IEEE Trans. Biomed. Eng.* 57 (2010) 145–154.
- [88] F. Vlachos, Y.S. Tung, E. Konofagou, Permeability dependence study of the focused ultrasound-induced blood–brain barrier opening at distinct pressures and microbubble diameters using DCE-MRI, *Magn. Reson. Med.* 66 (2011) 821–830.
- [89] G. Samiotaki, F. Vlachos, Y.S. Tung, E.E. Konofagou, A quantitative pressure and microbubble-size dependence study of focused ultrasound-induced blood–brain barrier opening reversibility in vivo using MRI, *Magn. Reson. Med.* 67 (2012) 769–777.
- [90] J.J. Choi, K. Selert, Z. Gao, G. Samiotaki, B. Baseri, E.E. Konofagou, Noninvasive and localized blood–brain barrier disruption using focused ultrasound can be achieved at short pulse lengths and low pulse repetition frequencies, *J. Cereb. Blood Flow Metab.* 31 (2011) 725–737.
- [91] J.J. Choi, K. Selert, F. Vlachos, A. Wong, E.E. Konofagou, Noninvasive and localized neuronal delivery using short ultrasonic pulses and microbubbles, *Proc. Natl. Acad. Sci. U. S. A.* 108 (2011) 16539–16544.
- [92] K.F. Bing, G.P. Howles, Y. Qi, M.L. Palmeri, K.R. Nightingale, Blood–brain barrier (BBB) disruption using a diagnostic ultrasound scanner and Definity in mice, *Ultrasound Med. Biol.* 35 (2009) 1298–1308.

- [93] F.Y. Yang, W.M. Fu, R.S. Yang, H.C. Liou, K.H. Kang, W.L. Lin, Quantitative evaluation of focused ultrasound with a contrast agent on blood–brain barrier disruption, *Ultrasound Med. Biol.* 33 (2007) 1421–1427.
- [94] J.C. Weng, S.K. Wu, W.L. Lin, W.Y. Tseng, Detecting blood–brain barrier disruption within minimal hemorrhage following transcranial focused ultrasound: a correlation study with contrast-enhanced MRI, *Magn. Reson. Med.* 65 (2011) 802–811.
- [95] J.C. Weng, S.K. Wu, F.Y. Yang, W.L. Lin, W.Y. Tseng, Pulse sequence and timing of contrast-enhanced MRI for assessing blood–brain barrier disruption after transcranial focused ultrasound in the presence of hemorrhage, *J. Magn. Reson. Imaging* 31 (2010) 1323–1330.
- [96] J. Park, Y. Zhang, N. Vykhotseva, F.A. Jolesz, N.J. McDannold, The kinetics of blood brain barrier permeability and targeted doxorubicin delivery into brain induced by focused ultrasound, *J. Control. Release* 162 (2012) 134–142.
- [97] F.Y. Yang, Y.S. Lin, K.H. Kang, T.K. Chao, Reversible blood–brain barrier disruption by repeated transcranial focused ultrasound allows enhanced extravasation, *J. Control. Release* 150 (2011) 111–116.
- [98] M.A. O'Reilly, A.C. Waspe, M. Ganguly, K. Hynynen, Focused-ultrasound disruption of the blood–brain barrier using closely-timed short pulses: influence of sonication parameters and injection rate, *Ultrasound Med. Biol.* 37 (2011) 587–594.
- [99] N. McDannold, Y. Zhang, N. Vykhotseva, Blood–brain barrier disruption and vascular damage induced by ultrasound bursts combined with microbubbles can be influenced by choice of anesthesia protocol, *Ultrasound Med. Biol.* 37 (2011) 1259–1270.
- [100] J.E. Wang, Y.H. Liu, L.B. Liu, C.Y. Xia, Z. Zhang, Y.X. Xue, Effects of combining low frequency ultrasound irradiation with papaverine on the permeability of the blood–tumor barrier, *J. Neurooncol.* 102 (2) (2010) 213–224.
- [101] Z. Zhang, C. Xia, Y. Xue, Y. Liu, Synergistic effect of low-frequency ultrasound and low-dose bradykinin on increasing permeability of the blood–tumor barrier by opening tight junction, *J. Neurosci. Res.* 87 (2009) 2282–2289.
- [102] Z. Zhang, Y. Xue, Y. Liu, X. Shang, Additive effect of low-frequency ultrasound and endothelial monocyte-activating polypeptide II on blood–tumor barrier in rats with brain glioma, *Neurosci. Lett.* 481 (2010) 21–25.
- [103] D.E. Goertz, C. Wright, K. Hynynen, Contrast agent kinetics in the rabbit brain during exposure to therapeutic ultrasound, *Ultrasound Med. Biol.* 36 (2010) 916–924.
- [104] H.L. Liu, C.H. Pan, C.Y. Ting, M.J. Hsiao, Opening of the blood–brain barrier by low-frequency (28-kHz) ultrasound: a novel pinhole-assisted mechanical scanning device, *Ultrasound Med. Biol.* 36 (2010) 325–335.
- [105] N. McDannold, N. Vykhotseva, K. Hynynen, Targeted disruption of the blood–brain barrier with focused ultrasound: association with cavitation activity, *Phys. Med. Biol.* 51 (2006) 793–807.
- [106] Y.S. Tung, F. Vlachos, J.J. Choi, T. Deffieux, K. Selert, E.E. Konofagou, In vivo transcranial cavitation threshold detection during ultrasound-induced blood–brain barrier opening in mice, *Phys. Med. Biol.* 55 (2010) 6141–6155.
- [107] C.D. Arvanitis, M.S. Livingstone, N. Vykhotseva, N. McDannold, Controlled ultrasound-induced blood–brain barrier disruption using passive acoustic emissions monitoring, *PLoS One* 7 (2012) e45783.
- [108] C.X. Deng, F. Sieling, H. Pan, J. Cui, Ultrasound-induced cell membrane porosity, *Ultrasound Med. Biol.* 30 (2004) 519–526.
- [109] N. Sheikov, N. McDannold, S. Sharma, K. Hynynen, Effect of focused ultrasound applied with an ultrasound contrast agent on the tight junctional integrity of the brain microvascular endothelium, *Ultrasound Med. Biol.* 34 (2008) 1093–1104.
- [110] N. Sheikov, N. McDannold, F. Jolesz, Y.Z. Zhang, K. Tam, K. Hynynen, Brain arterioles show more active vesicular transport of blood-borne tracer molecules than capillaries and venules after focused ultrasound-evoked opening of the blood–brain barrier, *Ultrasound Med. Biol.* 32 (2006) 1399–1409.
- [111] S.B. Raymond, J. Skoch, K. Hynynen, B.J. Backsai, Multiphoton imaging of ultrasound/Optison mediated cerebrovascular effects in vivo, *J. Cereb. Blood Flow Metab.* 27 (2007) 393–403.
- [112] E.E. Cho, J. Drazic, M. Ganguly, B. Stefanovic, K. Hynynen, Two-photon fluorescence microscopy study of cerebrovascular dynamics in ultrasound-induced blood–brain barrier opening, *J. Cereb. Blood Flow Metab.* 31 (2011) 1852–1862.
- [113] H. Chen, W. Kreider, A.A. Brayman, M.R. Bailey, T.J. Matula, Blood vessel deformations on microsecond time scales by ultrasonic cavitation, *Phys. Rev. Lett.* 106 (2011) 034301.
- [114] E. Sassaroli, K. Hynynen, Resonance frequency of microbubbles in small blood vessels: a numerical study, *Phys. Med. Biol.* 50 (2005) 5293–5305.
- [115] B. Marty, B. Larrat, M. Van Landeghem, C. Robic, P. Robert, M. Port, D. Le Bihan, M. Pernot, M. Tanter, F. Lethimonnier, S. Meriaux, Dynamic study of blood–brain barrier closure after its disruption using ultrasound: a quantitative analysis, *J. Cereb. Blood Flow Metab.* 32 (2012) 1948–1958.
- [116] G.P. Howles, K.F. Bing, Y. Qi, S.J. Rosenzweig, K.R. Nightingale, G.A. Johnson, Contrast-enhanced in vivo magnetic resonance microscopy of the mouse brain enabled by noninvasive opening of the blood–brain barrier with ultrasound, *Magn. Reson. Med.* 64 (2010) 995–1004.
- [117] B. Baseri, J.J. Choi, Y.S. Tung, E.E. Konofagou, Multi-modality safety assessment of blood–brain barrier opening using focused ultrasound and Definity microbubbles: a short-term study, *Ultrasound Med. Biol.* 36 (2010) 1445–1459.
- [118] N. McDannold, N. Vykhotseva, S. Raymond, F.A. Jolesz, K. Hynynen, MRI-guided targeted blood–brain barrier disruption with focused ultrasound: histological findings in rabbits, *Ultrasound Med. Biol.* 31 (2005) 1527–1537.
- [119] H.L. Liu, Y.Y. Wai, W.S. Chen, J.C. Chen, P.H. Hsu, X.Y. Wu, W.C. Huang, T.C. Yen, J.J. Wang, Hemorrhage detection during focused-ultrasound induced blood–brain-barrier opening by using susceptibility-weighted magnetic resonance imaging, *Ultrasound Med. Biol.* 34 (2008) 598–606.
- [120] K. Hynynen, N. McDannold, N. Vykhotseva, S. Raymond, R. Weissleder, F.A. Jolesz, N. Sheikov, Focal disruption of the blood–brain barrier due to 260-kHz ultrasound bursts: a method for molecular imaging and targeted drug delivery, *J. Neurosurg.* 105 (2006) 445–454.
- [121] H.L. Liu, Y.Y. Wai, P.H. Hsu, L.A. Lyu, J.S. Wu, C.R. Shen, J.C. Chen, T.C. Yen, J.J. Wang, In vivo assessment of macrophage CNS infiltration during disruption of the blood–brain barrier with focused ultrasound: a magnetic resonance imaging study, *J. Cereb. Blood Flow Metab.* 30 (2010) 674.
- [122] X. Shang, P. Wang, Y. Liu, Z. Zhang, Y. Xue, Mechanism of low-frequency ultrasound in opening blood–tumor barrier by tight junction, *J. Mol. Neurosci.* 43 (2011) 364–369.
- [123] A. Alonso, E. Reinz, J.W. Jenne, M. Fatar, H. Schmidt-Glenewinkel, M.G. Hennerici, S. Meairs, Reorganization of gap junctions after focused ultrasound blood–brain barrier opening in the rat brain, *J. Cereb. Blood Flow Metab.* 30 (2010) 1394–1402.
- [124] J. Deng, Q. Huang, F. Wang, Y. Liu, Z. Wang, Z. Wang, Q. Zhang, B. Lei, Y. Cheng, The role of caveolin-1 in blood–brain barrier disruption induced by focused ultrasound combined with microbubbles, *J. Mol. Neurosci.* 46 (2012) 677–687.
- [125] C.Y. Xia, Y.H. Liu, P. Wang, Y.X. Xue, Low-frequency ultrasound irradiation increases blood–tumor barrier permeability by transcellular pathway in a rat glioma model, *J. Mol. Neurosci.* 48 (1) (2012) 281–290.
- [126] A.N. Shajahan, C. Tiruppathi, A.V. Smrcka, A.B. Malik, R.D. Minshall, Gbetagamma activation of Src induces caveolae-mediated endocytosis in endothelial cells, *J. Biol. Chem.* 279 (2004) 48055–48062.
- [127] S. Jalali, Y. Huang, D.J. Dumont, K. Hynynen, Focused ultrasound-mediated BBB disruption is associated with an increase in activation of Akt: experimental study in rats, *BMC Neurol.* 10 (2010) 114.
- [128] H. Zhao, R.M. Sapolsky, G.K. Steinberg, Phosphoinositide-3-kinase/Akt survival signal pathways are implicated in neuronal survival after stroke, *Mol. Neurobiol.* 34 (2006) 249–270.
- [129] R. Nath, K. McGinnis, S. Dutta, B. Shivers, K.K. Wang, Inhibition of p38 kinase mimics survival signal-linked protection against apoptosis in rat cerebellar granule neurons, *Cell. Mol. Biol. Lett.* 6 (2001) 173–184.
- [130] J. Harada, M. Sugimoto, An inhibitor of p38 and JNK MAP kinases prevents activation of caspase and apoptosis of cultured cerebellar granule neurons, *Jpn. J. Pharmacol.* 79 (1999) 369–378.
- [131] A. Alonso, E. Reinz, M. Fatar, J. Jenne, M.G. Hennerici, S. Meairs, Neurons but not glial cells overexpress ubiquitin in the rat brain following focused ultrasound-induced opening of the blood–brain barrier, *Neuroscience* 169 (2010) 116–124.
- [132] J. Park, Z. Fan, R.E. Kumon, M.E. El Sayed, C.X. Deng, Modulation of intracellular Ca²⁺ concentration in brain microvascular endothelial cells in vitro by acoustic cavitation, *Ultrasound Med. Biol.* 36 (2010) 1176–1187.
- [133] J. Park, Z. Fan, C.X. Deng, Effects of shear stress cultivation on cell membrane disruption and intracellular calcium concentration in sonoporation of endothelial cells, *J. Biomech.* 44 (2011) 164–169.
- [134] C. Ayata, H.K. Shin, S. Salomone, Y. Ozdemir-Gursoy, D.A. Boas, A.K. Dunn, M.A. Moskowitz, Pronounced hypoperfusion during spreading depression in mouse cortex, *J. Cereb. Blood Flow Metab.* 24 (2004) 1172–1182.
- [135] A. Burgess, Y. Huang, W. Querbes, D.W. Sah, K. Hynynen, Focused ultrasound for targeted delivery of siRNA and efficient knockdown of Htt expression, *J. Control. Release* 163 (2012) 125–129.
- [136] J.J. Choi, S. Wang, Y.S. Tung, B. Morrison III, E.E. Konofagou, Molecules of various pharmacologically-relevant sizes can cross the ultrasound-induced blood–brain barrier opening in vivo, *Ultrasound Med. Biol.* 36 (2010) 58–67.
- [137] L.L. Muldoon, M.A. Pagel, R.A. Kroll, S. Roman-Goldstein, R.S. Jones, E.A. Neuwelt, A physiological barrier distal to the anatomic blood–brain barrier in a model of transvascular delivery, *AJNR Am. J. Neuroradiol.* 20 (1999) 217–222.
- [138] H.L. Liu, M.Y. Hua, P.Y. Chen, P.C. Chu, C.H. Pan, H.W. Yang, C.Y. Huang, J.J. Wang, T.C. Yen, K.C. Wei, Blood–brain barrier disruption with focused ultrasound enhances delivery of chemotherapeutic drugs for glioblastoma treatment, *Radiology* 255 (2010) 415–425.
- [139] J. Mei, Y. Cheng, Y. Song, Y. Yang, F. Wang, Y. Liu, Z. Wang, Experimental study on targeted methotrexate delivery to the rabbit brain via magnetic resonance imaging-guided focused ultrasound, *J. Ultrasound Med.* 28 (2009) 871–880.
- [140] H.Q. Zeng, L. Lu, F. Wang, Y. Luo, S.F. Lou, Focused ultrasound-induced blood–brain barrier disruption enhances the delivery of cytarabine to the rat brain, *J. Chemother.* 24 (2012) 358–363.
- [141] K.C. Wei, P.C. Chu, H.Y. Wang, C.Y. Huang, P.Y. Chen, H.C. Tsai, Y.J. Lu, P.Y. Lee, I.C. Tseng, L.Y. Feng, P.W. Hsu, T.C. Yen, H.L. Liu, Focused ultrasound-induced blood–brain barrier opening to enhance temozolomide delivery for glioblastoma treatment: a preclinical study, *PLoS One* 8 (2013) e58995.
- [142] M. Aryal, N. Vykhotseva, Y.Z. Zhang, J. Park, N. McDannold, Multiple treatments with liposomal doxorubicin and ultrasound-induced disruption of blood–tumor and blood–brain barriers improve outcomes in a rat glioma model, *J. Control. Release* 169 (2013) 103–111.
- [143] F.Y. Yang, T.T. Wong, M.C. Teng, R.S. Liu, M. Lu, H.F. Liang, M.C. Wei, Focused ultrasound and interleukin-4 receptor-targeted liposomal doxorubicin for enhanced targeted drug delivery and antitumor effect in glioblastoma multiforme, *J. Control. Release* 160 (3) (2012) 652–658.
- [144] H.L. Liu, M.Y. Hua, H.W. Yang, C.Y. Huang, P.C. Chu, J.S. Wu, I.C. Tseng, J.J. Wang, T.C. Yen, P.Y. Chen, K.C. Wei, Magnetic resonance monitoring of focused ultrasound/magnetic nanoparticle targeting delivery of therapeutic agents to the brain, *Proc. Natl. Acad. Sci. U. S. A.* 107 (2010) 15205–15210.
- [145] P.Y. Chen, H.L. Liu, M.Y. Hua, H.W. Yang, C.Y. Huang, P.C. Chu, L.A. Lyu, I.C. Tseng, L.Y. Feng, H.C. Tsai, S.M. Chen, Y.J. Lu, J.J. Wang, T.C. Yen, Y.H. Ma, T. Wu, J.P. Chen, J.J. Chuang, J.W. Shin, C. Hsueh, K.C. Wei, Novel magnetic/ultrasound focusing system enhances nanoparticle drug delivery for glioma treatment, *Neuro Oncol.* 12 (2010) 1050–1060.

- [146] C.H. Fan, C.Y. Ting, H.J. Lin, C.H. Wang, H.L. Liu, T.C. Yen, C.K. Yeh, SPIO-conjugated, doxorubicin-loaded microbubbles for concurrent MRI and focused-ultrasound enhanced brain-tumor drug delivery, *Biomaterials* 34 (2013) 3706–3715.
- [147] M. Kinoshita, N. McDannold, F.A. Jolesz, K. Hynynen, Noninvasive localized delivery of Herceptin to the mouse brain by MRI-guided focused ultrasound-induced blood–brain barrier disruption, *Proc. Natl. Acad. Sci. U. S. A.* 103 (2006) 11719–11723.
- [148] E.J. Park, Y.Z. Zhang, N. Vykhodtseva, N. McDannold, Ultrasound-mediated blood–brain/tumor barrier disruption improves outcomes with trastuzumab in a breast cancer brain metastasis model, *J. Control. Release* (2012), <http://dx.doi.org/10.1016/j.jconrel.2012.09.007>.
- [149] F.Y. Yang, Y.W. Chen, F.I. Chou, S.H. Yen, Y.L. Lin, T.T. Wong, Boron neutron capture therapy for glioblastoma multiforme: enhanced drug delivery and antitumor effect following blood–brain barrier disruption induced by focused ultrasound, *Future Oncol.* 8 (2012) 1361–1369.
- [150] R.D. Alkins, P.M. Brodersen, R.N. Sodhi, K. Hynynen, Enhancing drug delivery for boron neutron capture therapy of brain tumors with focused ultrasound, *Neuro Oncol.* 15 (9) (2013) 1225–1235.
- [151] R. Alkins, A. Burgess, M. Ganguly, G. Francia, R. Kerbel, W.S. Wels, K. Hynynen, Focused ultrasound delivers targeted immune cells to metastatic brain tumors, *Cancer Res.* 73 (2013) 1892–1899.
- [152] C.Y. Ting, C.H. Fan, H.L. Liu, C.Y. Huang, H.Y. Hsieh, T.C. Yen, K.C. Wei, C.K. Yeh, Concurrent blood–brain barrier opening and local drug delivery using drug-carrying microbubbles and focused ultrasound for brain glioma treatment, *Biomaterials* 33 (2012) 704–712.
- [153] F. Wang, Y. Shi, L. Lu, L. Liu, Y. Cai, H. Zheng, X. Liu, F. Yan, C. Zou, C. Sun, J. Shi, S. Lu, Y. Chen, Targeted delivery of GDNF through the blood–brain barrier by MRI-guided focused ultrasound, *PLoS One* 7 (2012) e52925.
- [154] Q. Huang, J. Deng, F. Wang, S. Chen, Y. Liu, Z. Wang, Z. Wang, Y. Cheng, Targeted gene delivery to the mouse brain by MRI-guided focused ultrasound-induced blood–brain barrier disruption, *Exp. Neurol.* 233 (2012) 350–356.
- [155] C.H. Fan, C.Y. Ting, H.L. Liu, C.Y. Huang, H.Y. Hsieh, T.C. Yen, K.C. Wei, C.K. Yeh, Antiangiogenic-targeting drug-loaded microbubbles combined with focused ultrasound for glioma treatment, *Biomaterials* 34 (2013) 2142–2155.
- [156] B. Baseri, J.J. Choi, T. Deffieux, G. Samiotaki, Y.S. Tung, O. Olumolade, S.A. Small, B. Morrison, E.E. Konofagou, Activation of signaling pathways following localized delivery of systemically administered neurotrophic factors across the blood–brain barrier using focused ultrasound and microbubbles, *Phys. Med. Biol.* 57 (2012) N65–N81.
- [157] S.B. Raymond, L.H. Treat, J.D. Dewey, N. McDannold, K. Hynynen, B.J. Bacskaï, Ultrasound enhanced delivery of molecular imaging and therapeutic agents in Alzheimer's disease mouse models, *PLoS One* 3 (2008) e2175.
- [158] J.F. Jordao, C.A. Ayala-Grosso, K. Markham, Y. Huang, R. Chopra, J. McLaurin, K. Hynynen, I. Aubert, Antibodies targeted to the brain with image-guided focused ultrasound reduces amyloid-beta plaque load in the TgCRND8 mouse model of Alzheimer's disease, *PLoS One* 5 (2010) e10549.
- [159] A. Burgess, C.A. Ayala-Grosso, M. Ganguly, J.F. Jordao, I. Aubert, K. Hynynen, Targeted delivery of neural stem cells to the brain using MRI-guided focused ultrasound to disrupt the blood–brain barrier, *PLoS One* 6 (2011) e27877.
- [160] E. Thevenot, J.F. Jordao, M.A. O'Reilly, K. Markham, Y.Q. Weng, K.D. Foust, B.K. Kaspar, K. Hynynen, I. Aubert, Targeted delivery of self-complementary adeno-associated virus serotype 9 to the brain, using magnetic resonance imaging-guided focused ultrasound, *Hum. Gene Ther.* 23 (2012) 1144–1155.
- [161] A. Alonso, E. Reinz, B. Leuchs, J. Kleinschmidt, M. Fatar, B. Geers, I. Lentacker, M.G. Hennerici, S.C. de Smedt, S. Meairs, Focal delivery of AAV2/1-transgenes into the rat brain by localized ultrasound-induced BBB opening, *Mol. Ther. Nucleic Acids* 2 (2013) e73.
- [162] P.H. Hsu, K.C. Wei, C.Y. Huang, C.J. Wen, T.C. Yen, C.L. Liu, Y.T. Lin, J.C. Chen, C.R. Shen, H.L. Liu, Noninvasive and targeted gene delivery into the brain using microbubble-facilitated focused ultrasound, *PLoS One* 8 (2013) e57682.
- [163] L.H. Treat, N. McDannold, Y. Zhang, N. Vykhodtseva, K. Hynynen, Improved anti-tumor effect of liposomal doxorubicin after targeted blood–brain barrier disruption by MRI-guided focused ultrasound in rat glioma, *Ultrasound Med. Biol.* 38 (2012) 1716–1725.
- [164] J.F. Jordao, E. Thevenot, K. Markham-Coultes, T. Scarcelli, Y.Q. Weng, K. Khima, M. O'Reilly, Y. Huang, J. McLaurin, K. Hynynen, I. Aubert, Amyloid-beta plaque reduction, endogenous antibody delivery and glial activation by brain-targeted, transcranial focused ultrasound, *Exp. Neurol.* 248 (2013) 16–29.
- [165] J.J. Choi, M. Pernot, S.A. Small, E.E. Konofagou, Noninvasive, transcranial and localized opening of the blood–brain barrier using focused ultrasound in mice, *Ultrasound Med. Biol.* 33 (2007) 95–104.
- [166] M.A. O'Reilly, A. Muller, K. Hynynen, Ultrasound insertion loss of rat parietal bone appears to be proportional to animal mass at submegahertz frequencies, *Ultrasound Med. Biol.* 37 (2011) 1930–1937.
- [167] S. Pichardo, V.W. Sin, K. Hynynen, Multi-frequency characterization of the speed of sound and attenuation coefficient for longitudinal transmission of freshly excised human skulls, *Phys. Med. Biol.* 56 (2011) 219–250.
- [168] P.J. White, G.T. Clement, K. Hynynen, Longitudinal and shear mode ultrasound propagation in human skull bone, *Ultrasound Med. Biol.* 32 (2006) 1085–1096.
- [169] K. Hynynen, N.I. Vykhodtseva, A.H. Chung, V. Sorrentino, V. Colucci, F.A. Jolesz, Thermal effects of focused ultrasound on the brain: determination with MR imaging, *Radiology* 204 (1997) 247–253.
- [170] N. McDannold, S.E. Maier, Magnetic resonance acoustic radiation force imaging, *Med. Phys.* 35 (2008) 3748–3758.
- [171] N. Hosseinkhah, K. Hynynen, A three-dimensional model of an ultrasound contrast agent gas bubble and its mechanical effects on microvessels, *Phys. Med. Biol.* 57 (2012) 785–808.
- [172] Y.S. Tung, F. Marquet, T. Teichert, V. Ferrera, E.E. Konofagou, Feasibility of noninvasive cavitation-guided blood–brain barrier opening using focused ultrasound and microbubbles in nonhuman primates, *Appl. Phys. Lett.* 98 (2011) 163704.
- [173] M.A. O'Reilly, K. Hynynen, Blood–brain barrier: real-time feedback-controlled focused ultrasound disruption by using an acoustic emissions-based controller, *Radiology* 263 (2012) 96–106.
- [174] V.A. Salgaonkar, S. Datta, C.K. Holland, T.D. Mast, Passive cavitation imaging with ultrasound arrays, *J. Acoust. Soc. Am.* 126 (2009) 3071–3083.
- [175] M. Gyongy, C.C. Coussios, Passive cavitation mapping for localization and tracking of bubble dynamics, *J. Acoust. Soc. Am.* 128 (2010) EL175–EL180.
- [176] C.D. Arvanitis, M.S. Livingstone, N. McDannold, Combined ultrasound and MR imaging to guide focused ultrasound therapies in the brain, *Phys. Med. Biol.* 58 (2013) 4749–4761.
- [177] F.Y. Yang, H.E. Wang, G.L. Lin, M.C. Teng, H.H. Lin, T.T. Wong, R.S. Liu, Micro-SPECT/CT-based pharmacokinetic analysis of ^{99m}Tc-diethylenetriaminepentaacetic acid in rats with blood–brain barrier disruption induced by focused ultrasound, *J. Nucl. Med.* 52 (2011) 478–484.
- [178] F.Y. Yang, S.C. Horng, Y.S. Lin, Y.H. Kao, Association between contrast-enhanced MR images and blood–brain barrier disruption following transcranial focused ultrasound, *J. Magn. Reson. Imaging* 32 (2010) 593–599.
- [179] P.C. Chu, W.Y. Chai, H.Y. Hsieh, J.J. Wang, S.P. Wey, C.Y. Huang, K.C. Wei, H.L. Liu, Pharmacodynamic analysis of magnetic resonance imaging-monitored focused ultrasound-induced blood–brain barrier opening for drug delivery to brain tumors, *Biomed. Res. Int.* 2013 (2013) 627496.
- [180] V. Vlachos, Y.S. Tung, E.E. Konofagou, Permeability assessment of the focused ultrasound-induced blood–brain barrier opening using dynamic contrast-enhanced MRI, *Phys. Med. Biol.* 55 (2010) 5451–5466.
- [181] S.B. Raymond, K. Hynynen, Acoustic transmission losses and field alterations due to human scalp hair, *IEEE Trans. Ultrason. Ferroelectr. Freq. Control* 52 (2005) 1415–1419.
- [182] J. Park, Y. Zhang, N. Vykhodtseva, J.D. Akula, N.J. McDannold, Targeted and reversible blood–retinal barrier disruption via focused ultrasound and microbubbles, *PLoS One* 7 (2012) e42754.
- [183] J. Wachsmuth, R. Chopra, K. Hynynen, Feasibility of transient image-guided blood–spinal cord barrier disruption, *Proceedings of the 8th International Symposium on Therapeutic Ultrasound*, Minneapolis, MN, AIP Conf. Proc., 1113, 2008, pp. 256–259.
- [184] K. Fischer, N.J. McDannold, Y. Zhang, M. Kardos, A. Szabo, A. Szabo, G.S. Reusz, F.A. Jolesz, Renal ultrafiltration changes induced by focused US, *Radiology* 253 (2009) 697–705.
- [185] N.J. McDannold, N.I. Vykhodtseva, K. Hynynen, Microbubble contrast agent with focused ultrasound to create brain lesions at low power levels: MR imaging and histologic study in rabbits, *Radiology* 241 (2006) 95–106.
- [186] M.J. Borrelli, W.D. O'Brien Jr., E. Hamilton, M.L. Oelze, J. Wu, L.J. Bernock, S. Tung, H. Rokadia, W.C. Culp, Influences of microbubble diameter and ultrasonic parameters on in vitro sonothrombolysis efficacy, *J. Vasc. Interv. Radiol.* 23 (2012) 1677–1684.
- [187] G.J. Czarnota, R. Karshafian, P.N. Burns, S. Wong, A. Al Mahrouki, J.W. Lee, A. Caissie, W. Tran, C. Kim, M. Furukawa, E. Wong, A. Giles, Tumor radiation response enhancement by acoustical stimulation of the vasculature, *Proc. Natl. Acad. Sci. U. S. A.* 109 (2012) E2033–E2041.
- [188] F.Y. Yang, W.M. Fu, W.S. Chen, W.L. Lin, Quantitative evaluation of the use of microbubbles with transcranial focused ultrasound on blood–brain-barrier disruption, *Ultrasound. Sonochem.* 15 (2008) 636–643.
- [189] N. McDannold, N. Vykhodtseva, K. Hynynen, Use of ultrasound pulses combined with Definity for targeted blood–brain barrier disruption: a feasibility study, *Ultrasound Med. Biol.* 33 (2007) 584–590.
- [190] K.J. Lin, H.L. Liu, P.H. Hsu, Y.H. Chung, W.C. Huang, J.C. Chen, S.P. Wey, T.C. Yen, I.T. Hsiao, Quantitative micro-SPECT/CT for detecting focused ultrasound-induced blood–brain barrier opening in the rat, *Nucl. Med. Biol.* 36 (2009) 853–861.
- [191] F.Y. Yang, H.E. Wang, G.L. Lin, H.H. Lin, T.T. Wong, Evaluation of the increase in permeability of the blood–brain barrier during tumor progression after pulsed focused ultrasound, *Int. J. Nanomedicine* 7 (2012) 723–730.
- [192] Q. Huang, J. Deng, Z. Xie, F. Wang, S. Chen, B. Lei, P. Liao, N. Huang, Z. Wang, Z. Wang, Y. Cheng, Effective gene transfer into central nervous system following ultrasound-microbubbles-induced opening of the blood–brain barrier, *Ultrasound Med. Biol.* 38 (2012) 1234–1243.
- [193] A.B. Etame, R.J. Diaz, M.A. O'Reilly, C.A. Smith, T.G. Mainprize, K. Hynynen, J.T. Rutka, Enhanced delivery of gold nanoparticles with therapeutic potential into the brain using MRI-guided focused ultrasound, *Nanomedicine* 8 (7) (2012) 1133–1142.
- [194] P.H. Wang, H.L. Liu, P.H. Hsu, C.Y. Lin, C.R. Wang, P.Y. Chen, K.C. Wei, T.C. Yen, M.L. Li, Gold-nanorod contrast-enhanced photoacoustic micro-imaging of focused-ultrasound induced blood–brain-barrier opening in a rat model, *J. Biomed. Opt.* 17 (2012) 061222.

Appendix II

Multiple treatments with liposomal doxorubicin and ultrasound induced disruption of blood-tumor and blood-brain barriers improves outcomes in a rat glioma

Muna Aryal, Natalia Vykhodtseva, Yong-Zhi Zhang, Juyoung Park, Nathan McDannold
J Control Release. 2013 July 10; 169(0): 103–111



Multiple treatments with liposomal doxorubicin and ultrasound-induced disruption of blood–tumor and blood–brain barriers improve outcomes in a rat glioma model[☆]

Muna Aryal^{a,b,*}, Natalia Vykhodtseva^b, Yong-Zhi Zhang^b, Juyoung Park^b, Nathan McDannold^b

^a Department of Physics, Boston College, Chestnut Hill, USA

^b Department of Radiology, Brigham & Women's Hospital, Harvard Medical School, Boston, USA

ARTICLE INFO

Article history:

Received 2 January 2013

Accepted 10 April 2013

Available online 18 April 2013

Keywords:

Focused ultrasound

Brain

Drug delivery

Glioma

Blood–brain barrier

Chemotherapy

ABSTRACT

The blood–brain–barrier (BBB) prevents the transport of most anticancer agents to the central nervous system and restricts delivery to infiltrating brain tumors. The heterogeneous vascular permeability in tumor vessels, along with several other factors, creates additional barriers for drug treatment of brain tumors. Focused ultrasound (FUS), when combined with circulating microbubbles, is an emerging noninvasive method to temporarily permeabilize the BBB and the “blood–tumor barrier”. Here, we tested the impact of three weekly sessions of FUS and liposomal doxorubicin (DOX) in 9L rat glioma tumors. Animals that received FUS + DOX (N = 8) had a median survival time that was increased significantly (P < 0.001) compared to animals who received DOX only (N = 6), FUS only (N = 8), or no treatment (N = 7). Median survival for animals that received FUS + DOX was increased by 100% relative to untreated controls, whereas animals who received DOX alone had only a 16% improvement. Animals who received only FUS showed no improvement. No tumor cells were found in histology in 4/8 animals in the FUS + DOX group, and in two animals, only a few tumor cells were detected. Adverse events in the treatment group included skin toxicity, impaired activity, damage to surrounding brain tissue, and tissue loss at the tumor site. In one animal, intratumoral hemorrhage was observed. These events are largely consistent with known side effects of doxorubicin and with an extensive tumor burden. Overall this work demonstrates that multiple sessions using this FUS technique to enhance the delivery of liposomal doxorubicin have a pronounced therapeutic effect in this rat glioma model.

© 2013 Elsevier B.V. All rights reserved.

1. Introduction

The blood–brain barrier (BBB) and other challenges prevent the effective use of most systemically-administered chemotherapeutic agents in patients with brain tumors. The BBB restricts transport of practically all agents to the brain parenchyma due to its selective permeability, which is based on lipid solubility, molecular size and charge [1,2]. Infiltrating tumor cells and metastatic “seeds” in the central nervous system are protected by the intact BBB and are excluded from the therapeutic effects of most drugs. Tumor blood vessels, which often lack an intact BBB, will allow some agent to extravasate and reach the vascular portion of the tumor. However, the permeability of the tumor vasculature is heterogeneous, and factors such as increased interstitial pressure [3] limit how far from the vasculature the drugs can penetrate. Furthermore, efflux pumps, which are present at

the BBB and in many tumors, extrude cytotoxic drugs that usually enter cells by passive diffusion [4]. Methods to overcome these barriers to drug delivery are needed if effective brain tumor therapies are to be developed.

Because of these challenges, the treatment of glioblastoma multiforme (GBM), an aggressive, high-grade brain tumor, is difficult [5]. This tumor is highly infiltrative, and recurrence after localized treatments such as conformal radiotherapy or surgery is common. This relapse usually occurs within a few cm of the treated region [6–8]. The introduction of temozolomide, a small molecule chemotherapy agent that has some penetration across the BBB, has improved clinical outcomes [9], but this improvement has been modest. A technique that can deliver larger agents across the “blood–tumor barrier” (BTB) and the BBB in the surrounding brain could enable the use of a wide range of anticancer agents for GBM and other brain tumors.

The use of focused ultrasound (FUS) combined with a circulating microbubble agent is an emerging technique to disrupt the BBB temporarily in a localized and non-invasive manner [10]. The microbubbles, which are constrained to the vasculature, interact strongly with even low-intensity ultrasound, producing mechanical forces on the endothelium that result in transient disassembly of tight junctional complexes

[☆] Conflict of interest: The last author holds two patents on the ultrasound technique evaluated in this work. The other authors have no conflicts of interest to report.

* Corresponding author at: 221 Longwood Avenue, Boston, MA 02115, USA. Tel.: +1 617 732 5920; fax: +1 617 525 7450.

E-mail address: muna@bwh.harvard.edu (M. Aryal).

and the induction of active transport processes [11,12]. No significant adverse effects have been observed resulting from this temporary BBB disruption [13–15]. The barrier is restored in a few hours [10], providing a time-window to deliver even long-circulating agents. Prior work in animals has demonstrated delivery of a wide range of imaging and therapeutic agents, even large agents such as antibodies, nanoparticles, and liposomally-encapsulated drugs [16–19]. The method can increase the delivery of agents to brain tumors [20,21], and several studies have shown that it can improve outcomes in animal brain tumor models [20,22–24]. These results, along with recent work demonstrating safety in a large animal model using a clinical brain FUS system [13] make it a promising approach for the treatment of GBM and other brain tumors. Volumetric BBB disruption can be achieved with such devices by rapidly steering the ultrasound focal point to different locations [13].

This method has several potential advantages over other approaches tested to overcome the BBB and the BTB [25]. FUS-induced BBB disruption is a noninvasive and targeted procedure, and the effect can be localized to only desired volumes in the brain. The method is also compatible with currently-available drugs, removing the need to develop new agents. Importantly, since FUS is noninvasive and can presumably be applied without general anesthesia, it is expected to be a relatively benign procedure that can be readily repeated to match a patient's drug schedule.

The purpose of this work was to evaluate whether multiple treatment sessions can effectively improve the therapeutic effect of liposomal doxorubicin in a rat glioma model. Previous work has shown that a single treatment with FUS-enhanced delivery of this agent to orthotopically-implanted 9L rat gliosarcoma model had a modest improvement in survival and tumor growth [24]. Here we examined whether three weekly sessions can provide a more pronounced treatment effect in this tumor model. We also utilized low-frequency FUS to better match an existing clinical FUS device [26].

2. Materials and methods

2.1. Sonication system

An air-backed, single element, 690 kHz focused piezoelectric transducer (diameter/radius of curvature: 100/80 mm) generated the ultrasound field. It was driven by an arbitrary waveform generator (model 395, Wavetek) and RF amplifier (240L, ENI); electric power was measured with a power meter (E4419B, Agilent) and a dual-directional coupler (C5948-10, Werlatone). Reported exposure levels are absolute peak negative pressure amplitudes measured in water with a membrane hydrophone (Marconi; 0.5 mm diameter). Attenuation by the brain and rat skull is expected to reduce the pressure amplitude by ~30% at this frequency [27] with additional uncertainty arising from standing waves within the skull and increases in skull thickness as the animal ages [27]. The pressure distribution of the transducer was mapped using a 0.2 mm needle hydrophone (Onda, Sunnyvale, CA); its half-maximum diameter and length were 2.3 and 12 mm, respectively. The transducer efficiency was measured using a radiation force-balance.

2.2. Experimental setup

The sonication system was operated within a clinical 3 T MRI scanner (Signa; GE Healthcare). The transducer was immersed in a small tank of degassed, deionized water and attached to an MRI-compatible, manually-operated positioning system (Fig. 1A). The animal was laid supine on a tray above this tank, with a water bag providing an acoustic path to the dorsal surface of the head. Images were obtained with a 7.5 cm-diameter transmit/receive MRI surface coil. The animal's body temperature was maintained with a heated water pad. Before treatment, we visualized heating in a silicone phantom using temperature-sensitive MRI to localize the acoustic focal point in the MRI space.

Accurate targeting *in vivo* was confirmed before the tumor sonications in select animals (typically the first animal treated each week) by sonicating a spot in the brain outside the tumor and checking that the resulting MRI contrast extravasation was at the desired target.

2.3. Animals

The experiments were approved by our institutional animal committee. Tests were performed in 40 male Sprague–Dawley rats (Charles River Laboratories; ~250 g). Before each procedure, the animals were anesthetized *via* intraperitoneal injections of Ketamine (80 ml/kg/h) and Xylazine (10 ml/kg/h). A catheter was placed in the tail vein, and the hair on the scalp was removed with clippers and depilatory cream.

9L rat gliosarcoma cells (passage number 3, obtained from the Neurosurgery Tissue Bank at UCSF) were grown in Minimum Essential Medium (1×) with Earle's salts, supplemented with 10% fetal bovine serum, 1% L-glutamine, 1% MEM nonessential amino acids, and 0.1% gentamicin in a 5% CO₂ chamber held at 37 °C. After preparing the skin, a 5-mm skin incision was made and a 1-mm burr hole was drilled into the skull 1 mm anterior to the bregma and 2 mm lateral to the midline. A 4 µl volume of cell suspension (1 × 10⁵ cells) was injected into the right caudate putamen at a depth of 3.5 mm relative to the dural surface using a 10 µl gas-tight syringe (Hamilton). Cells were injected over five minutes; two minutes later the needle was retracted slowly over another 5 min, and the skin was sutured. The sutures were removed 5 days later, and treatment began on day 7 or 8, at which point the tumor had an MRI-evident diameter between 1 and 3 mm.

The animals were monitored regularly to evaluate the treatment effects on survival and tumor growth. Animals surviving 6 weeks after treatment were considered long-term survivors. However, some were followed for longer periods for later histological examination, as they appeared healthy. The animals were euthanized if they exhibited severely impaired activity, weight loss exceeding 20% within one week, tumor dimensions exceeding 10–11 mm, or if treatment-related severe adverse events occurred that caused pain or distress and that could not be ameliorated. The animals were euthanized *via* transcardial perfusion with saline followed by 10% phosphate-buffered formalin while under deep anesthesia. The brain was removed and immersed in 10% phosphate-buffered formalin for histological preparation. To avoid skin infections that were observed in two animals (see below), animals receiving FUS and chemotherapy were treated with an antibiotic Baytril (Bayer; 2.5 mg/kg).

2.4. Treatment

The rats were randomly assigned to one of four groups: (1) no treatment (Control) (N = 7), (2) three weekly treatments with FUS-induced BBB/BTB permeabilization (FUS-Only) (N = 8), (3) three weekly treatments with liposomal doxorubicin (DOX-only) (N = 6), and (4) three weekly treatments with FUS and concurrent chemotherapy (FUS + DOX) (N = 8). After determining the coordinates of the focal point within the MRI space, treatment planning MRI was acquired, and the focal region was positioned within the tumor. Ultrasound bursts were then applied at multiple points in and around the tumor at pressure amplitudes ranging from 0.55 to 0.81 MPa (burst length: 10 ms, pulse repetition frequency: 1 Hz, duration: 60 s). The pressure amplitude was initially set based on a prior study in rats with this device [28]. It was increased based on the age and weight of the animals to achieve a consistent level of BBB disruption. This observation was made in our initial treatments and is similar to previous reports [27]. Before each sonication, ultrasonic contrast agent (DEFINITY, Lantheus Medical Imaging; 0.01 ml/kg) was administered intravenously. To facilitate the injections of such a small volume, the agent was diluted to 0.1× normal concentration in PBS. It was injected as a bolus

approximately 9 s before each sonication, followed by a 0.2 ml saline flush. The sonications were delivered at 5 min intervals in a grid pattern (spacing: 1 or 1.5 mm, depending on tumor volume) to 5–20 targets with the number of locations increasing over the three weeks as the tumor volume increased. We aimed to permeabilize the BBB in the entire tumor and the BBB in a surrounding rim of at least 1 mm.

For chemotherapy, 5.67 mg/kg of doxorubicin hydrochloride encapsulated in long-circulating pegylated liposomes was administered

intravenously. This dosage was selected based on prior work testing this agent in rats [29]. In our initial experiments (5 rats in DOX-Only group; 5 in FUS + DOX group), we used DOXIL (Centocor Ortho-Biotech). Due to a national shortage of this agent that occurred during these experiments, we used Lipo-DOX (TTY Biopharm) for the remaining animals (1 rat in the DOX-Only group; 3 in the FUS + DOX group). Previous work has shown that doxorubicin can be released from liposomes by ultrasound if microbubbles are in close vicinity [30], and we speculated that such may occur in these treatments. Thus for the FUS + DOX group, chemotherapy was administered over multiple slow injections administered just before each sonication. This scheme aimed to ensure a high drug concentration in the bloodstream during every sonication. For the DOX-only group, the agent was administered over 5 slow injections at 5 min intervals. Each injection was followed by a 0.2 ml saline flush.

2.5. Magnetic resonance imaging

T2-Weighted imaging was used to plan the treatments and measure tumor volumes. BBB/BBT disruption was evaluated using T1-weighted imaging acquired before and after administration of the MRI contrast agent gadopentatate dimeglumine (Magnevist Gd-DTPA; Bayer Healthcare; 0.25 ml/kg). T2*-Weighted imaging was used to confirm that petechiae, which are produced by excessive FUS exposures, did not occur [10] and to evaluate hemorrhagic regions in the tumors. Detailed imaging parameters are listed in Supplemental Methods.

2.6. Image analysis

Non-contrast MRI imaging was performed weekly (± 1 –3 days depending on MRI availability). Tumor boundaries were manually segmented in axial T2-weighted images using ImageJ; the volume was calculated by the sum of the areas multiplied by the image thickness. In weeks 1–2, the tumors appeared as clearly circumscribed volumes which were sometimes surrounded by hyperintense regions (presumably edema). These boundaries were sometimes not evident at later times in the FUS + DOX group, and it was not clear whether MRI abnormalities were residual/recurring tumor or treatment-related effects. To be conservative, such cases were included in the volume calculations.

2.7. Histology

Representative examples from the Control (4/7 animals) and FUS-Only (5/8 animals) groups were selected for histological examination. The treatment response varied for animals in the DOX-Only and FUS + DOX groups (see below), and all brains from these animals were examined. Tissue blocks containing the tumor were embedded

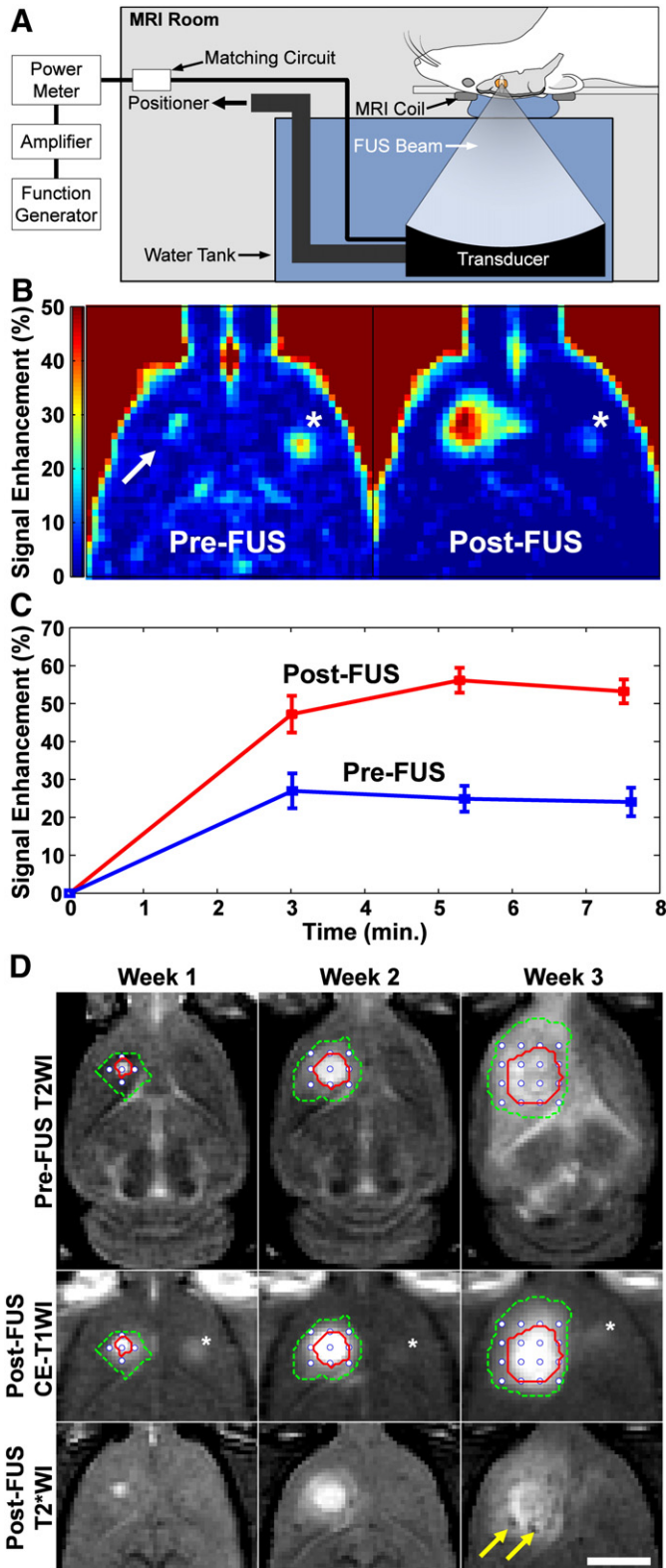
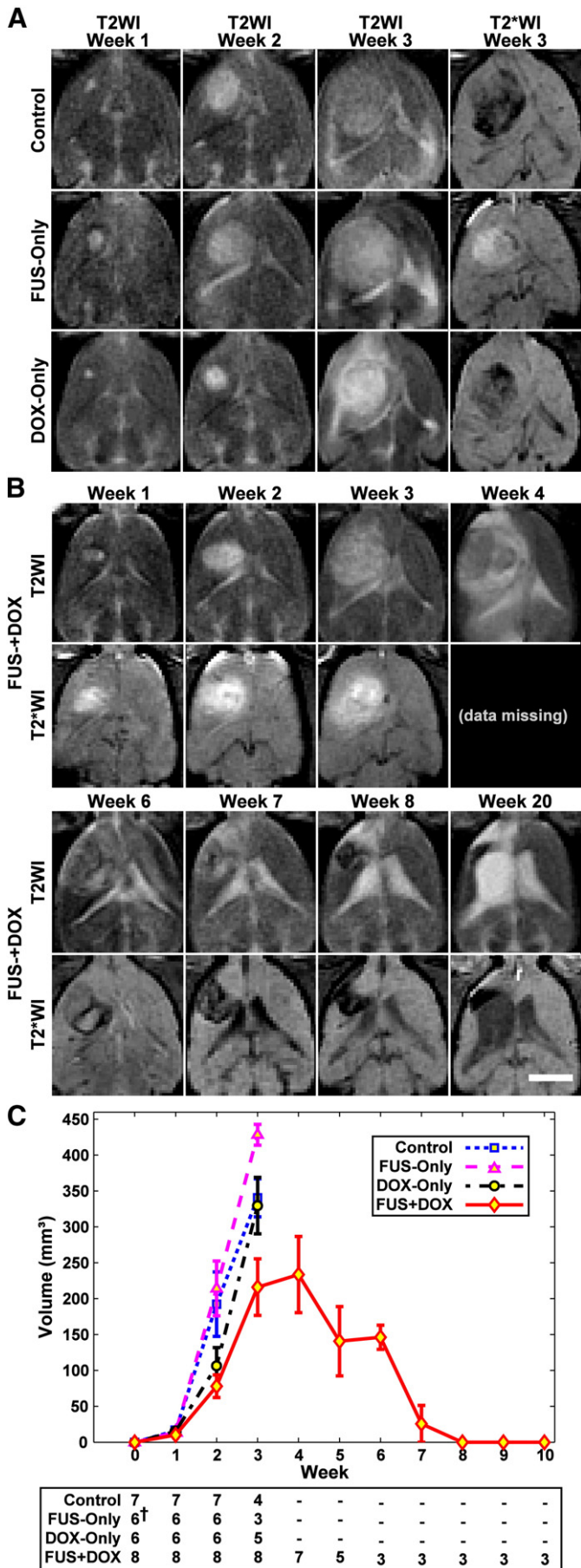


Fig. 1. Experimental setup and treatment overview. (A) Schematic of the MRI-guided focused ultrasound system used in this work. The function generator, amplifier, and power meter were located outside the MRI room (B). Axial images acquired before (left) and after (right) the first FUS + DOX treatment showing the signal enhancement in T1-weighted MRI after Gd-DTPA injection. Before FUS, the tumor was a small enhancing area (arrow). The magnitude and extent of this enhancement were increased after FUS. (C) Signal enhancement in this example as a function of time. (D) T2-weighted imaging (T2WI) used for treatment planning, contrast-enhanced T1-weighted imaging (CE-T1WI) used to verify the BBB/BBT permeabilization, and post-FUS T2*-weighted imaging (T2*WI) used to verify the BBB/BBT permeabilization, and post-FUS T2*-weighted imaging (T2*WI). The location of the tumor in treatment planning is indicated by the solid line, and the extent of MRI contrast enhancement is indicated by the dotted line. The coordinates of the sonication targets are also noted (white circles). Two hypointense spots (arrows) were evident after the third treatment in T2*-weighted imaging. The enhancing area evident in the other hemisphere in (B) and (D) (asterisk) was a location in the brain that was sonicated before the first Gd-DTPA injection to confirm the accurate targeting of the FUS beam. Bars: 5 mm.



in paraffin and cut into 4–6 μm serial sections perpendicular to the direction of ultrasound propagation. Sections with the largest evident tumor were stained with Hematoxylin and Eosin (H&E) for examination in light microscopy.

2.8. Statistical analysis

Tumor volumes for the four groups were compared using one-way ANOVA. The Kaplan–Meier method was used to compare survival of animals in each group. Significance was calculated by using log-rank test with Yates' correction. These analyses were performed using Matlab (MathWorks) and Microsoft Excel. The Bonferroni method was used to compare multiple pairs of groups [31]. With four treatment groups (including controls) and with six possible paired comparisons, pair-wise P values less than the Bonferroni-corrected threshold of 0.05/6 = 0.0083 were considered statistically significant.

3. Results

3.1. Tumor progression

BBB/BTB permeabilization and a lack of significant FUS-induced tissue damage were confirmed using contrast-enhanced and T2*-weighted MRI, respectively (Fig. 1B). A higher pressure amplitude (0.81 vs. 0.55 MPa) was needed for the third treatment to induce consistent BBB/BTB permeabilization, presumably because of an increase in skull or dura thickness as the rats grew [27]. To confirm that the sonications increased the vascular permeability in the tumor, we performed contrast-enhanced imaging before and after the sonications in several animals (Fig. 1B–C). Sonication targets were applied in a grid to cover the tumor evident in T2-weighted imaging plus a surrounding margin (Fig. 1D). Weekly MRI examination was used to monitor the tumor progression. Representative examples from each experimental group over the first three weeks and the tumor volume measurements are shown in Fig. 2.

In most animals in the three control groups, the tumor grew rapidly over this time (Fig. 2A), resulting in significant midline shift and compression of the lateral ventricles. Hypointense regions were often evident within the tumor in T2*-weighted imaging in all groups. Eleven of fifteen rats (73%) in these groups either died or were euthanized before the third treatment due either to tumor dimensions exceeding 10–11 mm or poor health conditions (weight loss exceeding 20% or severely impaired activity). The rest died or were euthanized for these reasons before week 4. One rat in the DOX-Only group was euthanized before the third treatment; the rest were euthanized shortly after week 3.

All animals in the FUS + DOX group received all three treatments, and no rat in this group was euthanized before week 4 (Fig. 2B–C). The tumor volume reached a maximum at weeks 3 or 4, after which

Fig. 2. MRI appearance of the tumors and their growth over time. (A) MRI for the three control groups for weeks 1–3. The rapid growth that was observed in most of the rats in these groups is evident in T2-weighted imaging (T2WI). Hypointense areas were often observed within the tumor in T2*-weighted MRI (T2*WI). (B) Serial MRI for a long-term survivor in the FUS + DOX group (Rat 4 in Table 1) showing rapid tumor growth and subsequent resolution. The volume was maximum at week four, at which time it covered a significant portion of one hemisphere. It then began to shrink, and from week 8 onwards it was no longer evident. Brain tissue loss at the former site was evident, and the lateral ventricle was enlarged and filled much of this space. Tissue adjacent to the former tumor mass was highly hyperintense in T2-weighted imaging, and presumably damaged. A hypointense region was observed at the former tumor site in T2*-weighted imaging starting at weeks 6–7, which slowly shrunk over time. Imaging between weeks 8 and 20 was mostly similar. Note that the T2*-weighted imaging in the FUS-Only and FUS + DOX animals was acquired after Gd-DTPA in weeks 1–3; contrast enhancement was observed in the tumor and surrounding brain. Bar: 5 mm. (C) MRI-measured tumor volumes as a function of time for each experimental group. Tumors were implanted at week 0. The number of surviving animals at each week is noted below the plot (†MRI from two animals in the FUS-Only group was not included in this analysis due to poor image quality). Mean ± S.E. is shown.

they began to shrink. The outcomes for the eight animals in this group varied and are summarized in Table 2. The maximum tumor volume varied substantially, with some tumors reaching volumes similar to the control group, and others never reaching 100 mm³. The mean tumor volume in the FUS + DOX group was less than in the three control groups at weeks 2–3 (Fig. 2C). However the differences were not significant.

The first two rats treated in the FUS + DOX group (Rats 1 and 2 in Table 1) exhibited local skin toxicity (inflammation, peeling; minor bleeding) on the scalp and the front and hind paws beginning on or after week two. These two animals developed a skin infection and were euthanized at days 34 and 35. In their last imaging session, one of these animals had no tumor evident in MRI, and the other had a small tumor that appeared to be responding to the treatment. Subsequent animals were treated prophylactically with antibiotics. While skin irritation or mild inflammation was observed, they did not develop infections.

Three animals (Rats 3, 4 and 8 in Table 1) did not exhibit any evident morbidity. They gained weight and behaved normally. These animals were followed for 9 or more weeks, at which time they were euthanized for histological examination. One of these long-term survivors was euthanized at day 66; the other two were observed for longer periods (136 and 142 days). Tumors in these animals grew to a substantial volume (greater than 300 mm³) before they began to resolve. MRI from one of these animals is shown in Fig. 2B. After the tumors disappeared, brain tissue loss at the former tumor site was evident in MRI, along with damage in adjacent tissues and enlarged ventricles. Tissue damage appeared as highly hyperintense regions in T2-weighted imaging. In some regions, within this damaged area, discrete hyperintense zones in both T2* and T2-weighted imaging were seen.

Two animals in the FUS + DOX group (Rats 5 and 7 in Table 1) were euthanized due to poor health at days 32 and 36, respectively. At the time of sacrifice, one of these animals exhibited only a small hyperintense region in T2-weighted imaging, and no tumor was evident in histology (see below). The other had an extensive hyperintense area in T2-weighted imaging, but only a small cluster containing a few tumor cells was found in histology. Finally, in one animal (Rat 6 in Table 1), a large hypointense region was observed in T2*-weighted imaging at week 4 that was assumed to be intratumoral hemorrhage. This animal also exhibited impaired activity and was euthanized at this time.

3.2. Histological findings

Tumors in the Control and FUS-Only groups appeared at days 15–23 as solid masses that replaced large amounts of brain tissue (Fig. 3A). The tumor bulk consisted of viable and rapidly dividing spindle-shaped cells interspersed with multiple small necrotic sites.

Table 1
Outcomes in FUS + DOX group.

Rat	Survival (days)	Maximum vol. in MRI (mm ³)	Vol. in MRI at euthanasia (mm ³)	Tumor found in histology	Outcome
1	34	244	63	Yes	Skin infection, euthanized
2	35	52	0	No	Skin infection, euthanized
3	66	358	0	No	Long-term survivor
4	142	365	0	No	Long-term survivor
5	32	424 ²	424 ²	Yes ¹	Poor health, euthanized
6	31	312	312	Yes	Intratumoral hemorrhage, euthanized
7	36	96	40	No	Poor health, euthanized
8	136	312	0	Yes ¹	Long-term survivor

¹ Only a small cluster containing a few tumor cells was found.

² A well-defined tumor margin was not evident in T2-weighted MRI at weeks 3–4 in this animal; only a large hyperintense region was observed (see Fig. 4F). The volume of this hyperintense region was included in the volume measurements, as we could not determine if this region was tumor or edema.

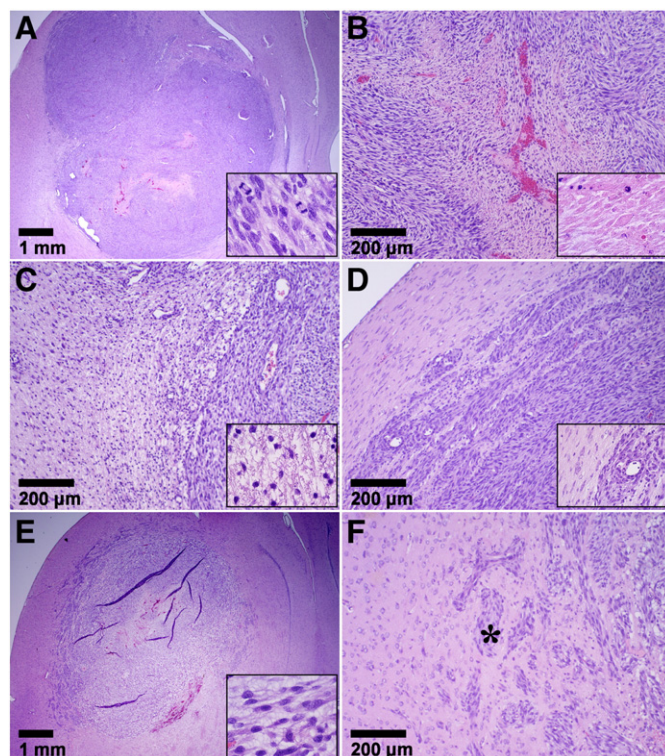


Fig. 3. Appearance of 9L gliosarcoma in the three control groups in histology. Animals receiving no treatment or FUS-Only (A–D) all had a similar appearance. The tumor appeared as a solid mass that replaced large volumes of brain tissue (A). The bulk of the tumors consisted of viable and rapidly dividing spindle-shaped cells (inset in A). Congested blood vessels were observed throughout, surrounded by necrotic tissue (B). Some regions of adjacent brain tissue were severely damaged, presumably from ischemia (C). There was a rim of infiltrating cells at the margin (D). Most tumors in the DOX-Only group (E–F) were also large masses of tumor cells with an infiltrating margin (E). However, unlike the other two control groups, they had a lower cellularity, unhealthy tumor cells, and intensely vacuolated matrix (inset in E). Tumor cell invasions along perivascular tracts and tumor cell clusters were observed at distant sites up to 2 mm from the edge of the solid tumor. The vacuolation evident in the tumor mass was often not observed in the infiltrating margin (* in F).

Microvessels that were necrotic, dilated, and congested with erythrocytes were observed throughout and were surrounded by necrotic zones (Fig. 3B). Small hemorrhagic regions were also found. Blood cells in these regions and in congested blood vessels were consistent with the hypointense regions observed in T2*-weighted imaging. In the largest tumors, numerous necrotic and hemorrhagic areas accompanied by cell necrosis and apoptosis were found scattered throughout the tumor mass. Rapid tumor growth and invasion displaced and compressed the surrounding brain tissue, resulting in ischemia and cell death (infarction) in some adjacent brain regions (Fig. 3C). A narrow (0.5–1 mm) band of invading/infiltrating cells was evident at the tumor margin (Fig. 3D).

The tumor appearance in the DOX-only group varied. Although viable and dividing cells were generally present, a reduced cellularity compared to the other control groups, along with unhealthy-appearing tumor cells and an intensely vacuolated matrix was evident in this group (Fig. 3E). Large regions of necrosis were observed in some cases, but some viable tumor cells were always found within these necrotic areas. Substantial hemorrhage was evident at the periphery of some tumors, accompanied by infarction in the surrounding brain. Tumor cell invasion along perivascular tracts and tumor cell clusters were observed at sites as far as 1–2 mm from the edge of the solid tumor mass (Fig. 3F). In one animal (euthanized at day 26 due to impaired activity), no tumor cells were found in histology.

In contrast to the controls, all but one of the animals in the FUS + DOX group exhibited a strong treatment response, with no tumor mass detected in 6/8 animals. However, in two of these animals a few residual or recurrent tumor cells were found in the former tumor site. In one rat, which was euthanized due to skin infection at day 34, a tumor was found to be shrunken compared to its maximum size in MRI and partly destroyed. The central area contained a viable tumor mass, and a surrounding rim of tissue appeared to be damaged. Only one animal (Rat 6 in Table 1) had a large tumor like most rats in the control groups. This animal, in which intratumoral bleeding was suspected in MRI, was euthanized at week 4. Histological examination confirmed hemorrhagic infarction in a region of tumor necrosis. This region was restricted to the tumor mass; no blood was found inside the adjacent ventricular space.

Example histological findings from the FUS + DOX group are shown in Fig. 4. In the three long-term survivors, where the tumors grew to a substantial volume before beginning to resolve, brain tissue loss was evident at the former tumor site (Fig. 4A). The adjacent lateral ventricle was significantly enlarged and filled this missing area. A region in the adjacent brain was necrotic, with an appearance consistent with infarct (Fig. 4B). A small cyst was observed within this necrotic zone. The hypointense regions evident in MRI contained hemosiderin – either in clusters or taken up by macrophages (inset in Fig. 4B). In one long-term survivor, a small cluster of recurring or residual tumor cells was found.

Findings from two animals from the FUS + DOX group that were euthanized for impaired activity are shown in Fig. 4C–H. In one case (euthanized at day 36) only a small necrotic area with macrophage infiltration was found at the former tumor site (Fig. 4C–E). In the second animal (euthanized at day 32), a larger necrotic area was found at the former tumor site, and affected or damaged tissue was observed in the surrounding brain that was hyperintense in T2-weighted MRI (Fig. 4F–H). A tiny cluster of tumor cells was found in this example (inset in Fig. 4G).

3.3. Survival analysis

Kaplan–Meier survival analysis is shown in Fig. 5; the corresponding statistical data are summarized in Table 2. The median survival time for the animals in both the Control and FUS-Only groups was about 18 days. For animals in the DOX-only group, it was 20.3 days – a 16% improvement over the animals in the Control group. However, this difference was not significant ($P = 0.16$). In contrast, the animals in the FUS + DOX group showed a significant survival benefit ($P < 0.001$) compared to the other three groups. The median survival time was 35 days, a 100% and 72% improvement over the Control and DOX-Only groups, respectively. Note that this analysis did not censor the two animals euthanized early due to skin infection. If one assumes those animals did not die from their tumor and censors them, the estimated median survival of the FUS + DOX group would be longer than 142 days, as more than 50% of the remaining animals survived until this time.

4. Discussion

Doxorubicin is a commonly-used anticancer drug for treatment of a wide range of cancers. While its effectiveness against glioma has been shown *in vitro* [32] and *in vivo* when injected directly into the tumor [33,34], systemic administration has not been effective clinically [35], presumably reflecting insufficient delivery [2]. A number of drug formulations have been developed to enhance the delivery of doxorubicin in animal glioma models [36–40] and at least one clinical trial is ongoing with such an agent [41]. Here, we demonstrated that ultrasound and microbubbles can effectively improve outcomes in a rat glioma model using an existing liposomal agent, removing

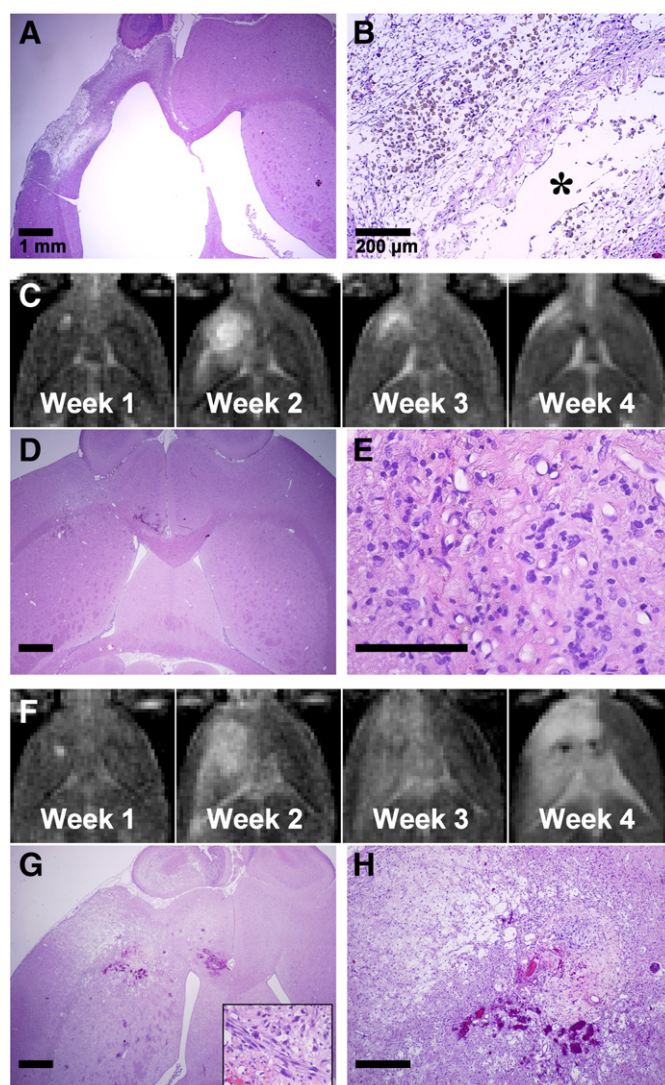


Fig. 4. Histological appearance of the brain in three of the animals from the FUS + DOX group. (A–B) Long-term survivor (see Fig. 2B for MRI). No tumor cells were found. Brain tissue loss at the former tumor site was evident, and the lateral ventricle was enlarged and filled this space. Tissue necrosis (infarct) was observed in the adjacent tissue, presumably from ischemia. Hemosiderin, either in clusters or inside macrophages was observed within the necrotic area. A small cyst (*) was also observed. (C–E) Example from an animal, whose tumor was resolved, but the animal was euthanized at day 36 due to poor health. (C) T2-weighted MRI showing tumor growth and shrinkage. At week 4, only a small hyperintense region was visible. (D–E) A small necrotic area with macrophage infiltration was found at the former tumor site. (F–H) Another animal with a strong treatment response, but that was euthanized due to poor health at day 32. In this animal, the tumor grew to a relatively large size over weeks 1–2. At week 4, an extensive hyperintense area was observed in T2-weighted imaging (F). A necrotic area with micro-hemorrhages was found in histology at the former tumor site (G–H). Damaged or necrotic brain tissue was evident in the area that was hyperintense in T2-weighted imaging. A small cluster of tumor cells remained (inset in G).

the need to develop and test new drug formulations. The method is noninvasive and restricts the drug delivery only to desired brain regions. While more work is needed to optimize the treatment and to better understand its safety profile, these results are promising for the development of new treatment options for glioma patients. They join several other studies that showed this FUS method can enhance drug delivery and improve outcomes in brain tumor models [18,20–24,42].

This study also demonstrates the importance of multiple treatments. Previously, a modest survival improvement (24%) compared to untreated controls was observed with a single treatment in this tumor model [24]. With three weekly treatments, median survival

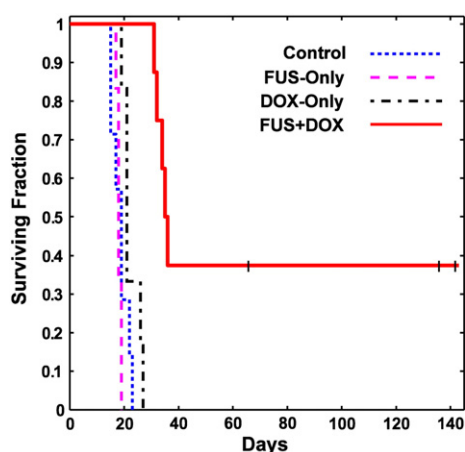


Fig. 5. Kaplan–Meier survival curves for the four experimental groups. Three long-term survivors, who did not exhibit impaired activity, were euthanized at different times (tick marks). Afterwards they were censored.

was increased by 100% compared to the controls, and we observed a 72% survival improvement compared to treatment with chemotherapy only. While the drug alone produced some treatment effects, it did not significantly improve survival or stop tumor proliferation in most cases. Histological examination of the tumors in this group showed a heterogeneous response to the treatment, with necrotic areas interspersed with viable tumor cells – perhaps consistent with heterogeneous vascular permeability and insufficient drug delivery to some regions. It also appeared that perhaps the drug did not reach the infiltrating tumor cells, as the matrix vacuolation evident in the tumor mass was not seen around the tumor cells at the tumor margin. In contrast, all but one of the tumors in the FUS + DOX group exhibited a strong treatment effect.

Several adverse events were observed. Three rats with little or no tumor evident in histology – one in the DOX-Only group and two in the FUS + DOX group – were euthanized due to impaired activity after three treatments. This finding may suggest that we used an aggressive treatment schedule that may not be tolerated by all subjects. Doxorubicin, even when encapsulated, has multiple known side effects, some of them severe. Use of medications to reduce the symptoms of these side effects may help to avoid the impairment we observed. In one animal (shown in Fig. 4F–H), damaged brain tissue was evident over a large portion of the treated hemisphere. We also observed brain tissue loss and necrosis in the surrounding brain in the three long-term survivors in the FUS + DOX group. We do not know whether these effects were due to the FUS + DOX treatment or to the extensive tumor burden that could have damaged the surrounding brain due to mass effects. While previous work did not find severe damage after one FUS + DOX treatment in normal rat brain [19], it is possible that cumulative effects from the three treatments, along with known neurotoxic effects of doxorubicin [43,44], produced this damage. If that is the case, attempting to aggressively

Table 2
Survival analysis.

Treatment group	N animals	Max. survival (days)	Median survival (days)	IST _{median} (%)	Mean survival ± S.D. (days)	P-Value, hazard ratio
Control	7	23	17.5	...	18.6 ± 3	...
FUS-Only	8	21	18.0	2.9	18.9 ± 1	0.85, 1.16
DOX-Only	6	27	20.3	16.2	22.5 ± 3	0.16, 1.18
FUS + DOX	8	>142	35.0	100.0	64.0 ± 48	0.00031, 5.36

Note – Increase in Survival Time [IST_{median} (%)], P-value, and Hazard ratio are relative to the Control group.

P-Value and Hazard ratio from Log-Rank test between FUS + DOX and Dox-Only group are 0.00057 and 4.52 respectively.

target infiltrating tumor cells with this agent may be contraindicated, and it may be necessary to either reduce the dosage delivered to the surrounding brain or to only target the vascular part of the tumor. Future work should evaluate the effects of multiple FUS + DOX treatments in the brain.

A potentially significant adverse event was the extensive intratumoral hemorrhagic area that occurred in one animal one week after the last FUS + DOX treatment. While we did not observe frank bleeding (such as into the ventricles), vascular risks associated the treatment should be examined in more detail. This hemorrhage may have resulted from necrosis of the vessel wall in a large tumor vessel. Others have reported hemorrhages in this tumor model with different doxorubicin formulations [40,45]. We also observed skin toxicity, a finding that may not be surprising since such toxicity, particularly in the hands and feet, is a known side effect of doxorubicin [46]. However, it might be prudent to confirm that the sonications do not increase drug delivery into the scalp. The focal region of our transducer overlapped the small rat skull, and the intensity on the scalp may have been relatively high. While the intensity on the scalp is expected to be less in humans, this issue might still be important, as large tumors may require sonication at hundreds of individual targets, and any low-level effects may accumulate. Reflections from the skull bone can exacerbate this effect.

This study had several limitations. First, due to a national shortage of DOXIL, we used a different drug formulation in some animals. While they had similar liposome properties, there may have been differences unknown to us that may have impacted our results. The sample size was also relatively small, and more work is needed to better characterize the effectiveness of the treatment and the rate of adverse events. More consistent results may be obtained using online methods to optimize the exposure levels. While we did modify the exposure levels based on the animal age and weight, we did not go back and re-treat regions where MRI contrast enhancement was poor to attempt to achieve a uniform level of enhancement. We anticipate that monitoring the microbubble dynamics in real-time using online acoustic emission monitoring [47,48] and re-treating areas with poor contrast enhancement can improve the local delivery and perhaps allow for a reduced systemic dose. Here, we evaluated only one dose of liposomal doxorubicin. We expect that by utilizing post-treatment MRI contrast imaging, which can be correlated to drug concentrations [19,49], along with online methods to control the exposures, we can optimize the drug dose delivered to the tumor and the surrounding brain tissue. Since liposomal doxorubicin has a long circulation time, we can sonicate regions where a higher dose is desired (such as the vascular portion of the tumor) repeatedly after a delay to extend the duration of BBB/BBB permeabilization [49] without increasing the dose to the surrounding brain tissue. It would also be interesting to investigate whether the sonications can release the doxorubicin from the liposomes, as has been observed by others with liposome-coated microbubbles [30].

Another limitation was our tumor model. While the 9L rat gliosarcoma model is highly aggressive and the robust survival improvement observed here is certainly encouraging, future work is needed with models that are genetically similar to human GBM and that have similar growth patterns. The 9L glioma model is not considered to be highly infiltrating [50] and we observed only a relatively narrow infiltrating zone. The disruption of the BBB in the surrounding brain tissue may not have played as large a role in our outcomes as might be anticipated clinically. Targeting infiltration is anticipated to be critically important with human GBM, and based on clinical patterns of recurrence [6–8], a margin extending several centimeters into the “normal” brain may require BBB disruption for effective therapy. Additional work in a more infiltrating tumor model is needed to ensure that we can safely and effectively target such regions. Finally, this model has been reported to be immunogenic [50], which may have led to more improved outcomes than would be achieved in non-immunogenic tumor model.

Despite these limitations, the favorable outcome of these tests continues to support the development of this drug delivery technology for brain tumors and confirms the notion that a significant improvement in outcome can be achieved using multiple treatments. Going forward, we aim to validate these results in an infiltrating human GBM line and to integrate advanced methods for treatment planning, online monitoring, and post-treatment evaluation to maximize both the treatment efficacy and safety profile.

5. Conclusions

This work demonstrates that multiple sessions using this FUS technique to enhance the delivery of liposomal doxorubicin to tumors and the surrounding brain can have a pronounced therapeutic effect in this rat glioma model. A strong treatment effect was observed in 7/8 animals in our FUS + DOX group, with no tumor mass found in histology in six of the animals. Median survival was increased by 100% and 72% compared to control animals that received no treatment and DOX-Only, respectively. Adverse events, including damage to surrounding brain tissue, impaired activity, skin toxicity, and in one case, an extensively hemorrhagic tumor, were observed along with these treatment effects. While these events are consistent with known side effects of doxorubicin and with an extensive tumor burden, future work should be performed to examine the effects of multiple FUS + DOX sessions.

Acknowledgments

This work was supported by NIH grants P41EB015898, P41RR019703, and R01EB003268 and from a gift from Brudnick family. We are grateful to Dr. Hao-Li Liu and Dr. Kuo-Chen Wei for supplying us with Lipo-DOX and Chanikarn Power for her technical help on the tumor implantation.

Appendix A. Supplementary data

Supplementary data to this article can be found online at <http://dx.doi.org/10.1016/j.jconrel.2013.04.007>.

References

- W.M. Pardridge, Drug and gene delivery to the brain: the vascular route, *Neuron* 36 (4) (2002) 555–558.
- H. von Holst, E. Knochenhauer, H. Blomgren, V.P. Collins, L. Ehn, M. Lindquist, G. Noren, C. Peterson, Uptake of adriamycin in tumour and surrounding brain tissue in patients with malignant gliomas, *Acta Neurochir. (Wien)* 104 (1–2) (1990) 13–16.
- D. Fukumura, R.K. Jain, Tumor microenvironment abnormalities: causes, consequences, and strategies to normalize, *J. Cell. Biochem.* 101 (4) (2007) 937–949.
- F.M. Kievit, F.Y. Wang, C. Fang, H. Mok, K. Wang, J.R. Silber, R.G. Ellenbogen, M. Zhang, Doxorubicin loaded iron oxide nanoparticles overcome multidrug resistance in cancer in vitro, *J. Control. Release* 152 (1) (2011) 76–83.
- T.S. Surawicz, F. Davis, S. Freels, E.R. Laws Jr., H.R. Menck, Brain tumor survival: results from the National Cancer Data Base, *J. Neurooncol.* 40 (2) (1998) 151–160.
- M.C. Chamberlain, Radiographic patterns of relapse in glioblastoma, *J. Neurooncol.* 101 (2) (2011) 319–323.
- M.C. Dabelbower, O.L. Burnett Iii, R.A. Nordal, L.B. Nabors, J.M. Markert, M.D. Hyatt, J.B. Fiveash, Patterns of failure for glioblastoma multiforme following concurrent radiation and temozolomide, *J. Med. Imaging Radiat. Oncol.* 55 (1) (2011) 77–81.
- G. Minniti, D. Amelio, M. Amichetti, M. Salvati, R. Muni, A. Bozzao, G. Lanzetta, S. Scarpino, A. Arcella, R.M. Enrici, Patterns of failure and comparison of different target volume delineations in patients with glioblastoma treated with conformal radiotherapy plus concomitant and adjuvant temozolomide, *Radiother. Oncol.* 97 (3) (2010) 377–381.
- R. Stupp, M.E. Hegi, W.P. Mason, M.J. van den Bent, M.J. Taphoorn, R.C. Janzer, S.K. Ludwin, A. Allgeier, B. Fisher, K. Belanger, P. Hau, A.A. Brandes, J. Gijtenbeek, C. Marosi, C.J. Vecht, K. Mokhtari, P. Wesseling, S. Villa, E. Eisenhauer, T. Gorlia, M. Weller, D. Lacombe, J.G. Cairncross, R.O. Mirimanoff, Effects of radiotherapy with concomitant and adjuvant temozolomide versus radiotherapy alone on survival in glioblastoma in a randomised phase III study: 5-year analysis of the EORTC-NCIC trial, *Lancet Oncol.* 10 (5) (2009) 459–466.
- M. Hynynen, N. McDannold, N. Vykhodtseva, F.A. Jolesz, Noninvasive MR imaging-guided focal opening of the blood–brain barrier in rabbits, *Radiology* 220 (3) (2001) 640–646.
- X. Shang, P. Wang, Y. Liu, Z. Zhang, Y. Xue, Mechanism of low-frequency ultrasound in opening blood–tumor barrier by tight junction, *J. Mol. Neurosci.* 43 (3) (2011) 364–369.
- N. Sheikov, N. McDannold, N. Vykhodtseva, F. Jolesz, K. Hynynen, Cellular mechanisms of the blood–brain barrier opening induced by ultrasound in presence of microbubbles, *Ultrasound Med. Biol.* 30 (7) (2004) 979–989.
- N. McDannold, C. Arvanitis, N. Vykhodtseva, M. Livingstone, Temporary disruption of the blood–brain barrier by use of ultrasound and microbubbles: safety and efficacy evaluation in rhesus macaques, *Cancer Res.* 27 (2012) 3652–3663.
- N. McDannold, N. Vykhodtseva, S. Raymond, F.A. Jolesz, K. Hynynen, MRI-guided targeted blood–brain barrier disruption with focused ultrasound: histological findings in rabbits, *Ultrasound Med. Biol.* 31 (11) (2005) 1527–1537.
- Y.S. Tung, F. Vlachos, J.J. Choi, T. Deffieux, K. Selert, E.E. Konofagou, In vivo transcranial cavitation threshold detection during ultrasound-induced blood–brain barrier opening in mice, *Phys. Med. Biol.* 55 (20) (2010) 6141–6155.
- J.F. Jordao, C.A. Ayala-Grosso, K. Markham, Y. Huang, R. Chopra, J. McLaurin, K. Hynynen, I. Aubert, Antibodies targeted to the brain with image-guided focused ultrasound reduces amyloid-beta plaque load in the TgCRND8 mouse model of Alzheimer's disease, *PLoS One* 5 (5) (2010) e10549.
- M. Kinoshita, N. McDannold, F.A. Jolesz, K. Hynynen, Noninvasive localized delivery of Herceptin to the mouse brain by MRI-guided focused ultrasound-induced blood–brain barrier disruption, *Proc. Natl. Acad. Sci. U. S. A.* 103 (31) (2006) 11719–11723.
- H.L. Liu, M.Y. Hua, H.W. Yang, C.Y. Huang, P.C. Chu, J.S. Wu, I.C. Tseng, J.J. Wang, T.C. Yen, P.Y. Chen, K.C. Wei, Magnetic resonance monitoring of focused ultrasound/magnetic nanoparticle targeting delivery of therapeutic agents to the brain, *Proc. Natl. Acad. Sci. U. S. A.* 107 (34) (2010) 15205–15210.
- L.H. Treat, N. McDannold, N. Vykhodtseva, Y. Zhang, K. Tam, K. Hynynen, Targeted delivery of doxorubicin to the rat brain at therapeutic levels using MRI-guided focused ultrasound, *Int. J. Cancer* 121 (4) (2007) 901–907.
- H.L. Liu, M.Y. Hua, P.Y. Chen, P.C. Chu, C.H. Pan, H.W. Yang, C.Y. Huang, J.J. Wang, T.C. Yen, K.C. Wei, Blood–brain barrier disruption with focused ultrasound enhances delivery of chemotherapeutic drugs for glioblastoma treatment, *Radiology* 255 (2) (2010) 415–425.
- J. Mei, Y. Cheng, Y. Song, Y. Yang, F. Wang, Y. Liu, Z. Wang, Experimental study on targeted methotrexate delivery to the rabbit brain via magnetic resonance imaging-guided focused ultrasound, *J. Ultrasound Med.* 28 (7) (2009) 871–880.
- P.Y. Chen, H.L. Liu, M.Y. Hua, H.W. Yang, C.Y. Huang, P.C. Chu, L.A. Lyu, I.C. Tseng, L.Y. Feng, H.C. Tsai, S.M. Chen, Y.J. Lu, J.J. Wang, T.C. Yen, Y.H. Ma, T. Wu, J.P. Chen, J.I. Chuang, J.W. Shin, C. Hsueh, K.C. Wei, Novel magnetic/ultrasound focusing system enhances nanoparticle drug delivery for glioma treatment, *Neuro Oncol.* 12 (10) (2010) 1050–1060.
- E.J. Park, Y.Z. Zhang, N. Vykhodtseva, N. McDannold, Ultrasound-mediated blood–brain/blood–tumor barrier disruption improves outcomes with trastuzumab in a breast cancer brain metastasis model, *J. Control. Release* 163 (3) (2012) 277–284.
- L.H. Treat, N. McDannold, Y. Zhang, N. Vykhodtseva, K. Hynynen, Improved anti-tumor effect of liposomal doxorubicin after targeted blood–brain barrier disruption by MRI-guided focused ultrasound in rat glioma, *Ultrasound Med. Biol.* 38 (10) (2012) 1716–1725.
- W. Pardridge, Blood–brain barrier delivery, *Drug Discov. Today* 12 (2007) 54–61.
- N. McDannold, G.T. Clement, P. Black, F. Jolesz, K. Hynynen, Transcranial magnetic resonance imaging-guided focused ultrasound surgery of brain tumors: initial findings in 3 patients, *Neurosurgery* 66 (2) (2010) 323–332, (discussion 332).
- M.A. O'Reilly, A. Muller, K. Hynynen, Ultrasound insertion loss of rat parietal bone appears to be proportional to animal mass at submegahertz frequencies, *Ultrasound Med. Biol.* 37 (11) (2011) 1930–1937.
- M. Pilatou, N. Vykhodtseva, N.J. McDannold, Blood–Brain Barrier Disruption in Rats Induced by Focused Ultrasound Under MRI Guidance: A Safety Study, MR-Guided Focused Ultrasound Symposium, Washington, DC, 2008.
- Robert D. Arnold, Donald E. Mager, Jeanine E. Slack, Robert M. Straubinger, Effect of repetitive administration of doxorubicin-containing liposomes on plasma pharmacokinetics and drug biodistribution in a rat brain tumor model, *Clin. Cancer Res.* 11 (2005) 8856–8865.
- B. Geers, I. Lentacker, N.N. Sanders, J. Demeester, S. Meairs, S.C. De Smedt, Self-assembled liposome-loaded microbubbles: the missing link for safe and efficient ultrasound triggered drug-delivery, *J. Control. Release* 152 (2) (2011) 249–256.
- J.M. Bland, D.G. Altman, Multiple significance tests: the Bonferroni method, *BMJ* 310 (6973) (1995) 170.
- A.C. Stan, S. Casares, D. Radu, G.F. Walter, T.D. Brumeanu, Doxorubicin-induced cell death in highly invasive human gliomas, *Anticancer Res.* 19 (2A) (1999) 941–950.
- K.A. Walter, R.J. Tamargo, A. Olivi, P.C. Burger, H. Brem, Intratumoral chemotherapy, *Neurosurgery* 37 (6) (1995) 1128–1145.
- S. Voulgaris, M. Partheni, M. Karamouzis, P. Dimopoulos, N. Papadakis, H.P. Kalofonos, Intratumoral doxorubicin in patients with malignant brain gliomas, *Am. J. Clin. Oncol.* 25 (1) (2002) 60–64.
- S. Ananda, A.K. Nowak, L. Cher, A. Dowling, C. Brown, J. Simes, M.A. Rosenthal, Phase 2 trial of temozolomide and pegylated liposomal doxorubicin in the treatment of patients with glioblastoma multiforme following concurrent radiotherapy and chemotherapy, *J. Clin. Neurosci.* 18 (11) (2011) 1444–1448.
- T. Hekmatara, C. Bernreuther, A.S. Khalansky, A. Theisen, J. Weissenberger, J. Matsche, S. Gelperina, J. Kreuter, M. Glatzel, Efficient systemic therapy of rat glioblastoma by nanoparticle-bound doxorubicin is due to antiangiogenic effects, *Clin. Neuropathol.* 28 (3) (2009) 153–164.

- [37] T. Siegal, A. Horowitz, A. Gabizon, Doxorubicin encapsulated in sterically stabilized liposomes for the treatment of a brain tumor model: biodistribution and therapeutic efficacy, *J. Neurosurg.* 83 (6) (1995) 1029–1037.
- [38] S.C. Steiniger, J. Kreuter, A.S. Khalansky, I.N. Skidan, A.I. Bobruskin, Z.S. Smirnova, S.E. Severin, R. Uhl, M. Kock, K.D. Geiger, S.E. Gelperina, Chemotherapy of glioblastoma in rats using doxorubicin-loaded nanoparticles, *Int. J. Cancer* 109 (5) (2004) 759–767.
- [39] S. Wohlfart, A.S. Khalansky, C. Bernreuther, M. Michaelis, J. Cinatl Jr., M. Glatzel, J. Kreuter, Treatment of glioblastoma with poly(isohexyl cyanoacrylate) nanoparticles, *Int. J. Pharm.* 415 (1–2) (2011) 244–251.
- [40] R. Zhou, R. Mazurchuk, R.M. Straubinger, Antivasculature effects of doxorubicin-containing liposomes in an intracranial rat brain tumor model, *Cancer Res.* 62 (9) (2002) 2561–2566.
- [41] P. Gaillard, W. Gladdines, C. Appeldoorn, J. Rip, W. Boogerd, J. Beijnen, D. Brandsma, Olaf van Tellingen, Development of glutathione pegylated liposomal doxorubicin (2B3-101) for the treatment of brain cancer, *Cancer Res.* 72 (8) (2012).
- [42] F. Yang, M.-C. Teng, M. Lu, H.-F. Liang, Y.-R. Lee, C.-C. Yen, M.-L. Liang, T.-T. Wong, Treating glioblastoma multiforme with selective high-dose liposomal doxorubicin chemotherapy induced by repeated focused ultrasound, *Int. J. Nanomedicine* 7 (2012) 965–974.
- [43] E.A. Neuwelt, M. Glasberg, E. Frenkel, P. Barnett, Neurotoxicity of chemotherapeutic agents after blood–brain barrier modification: neuropathological studies, *Ann. Neurol.* 14 (3) (1983) 316–324.
- [44] A. Kondo, T. Inoue, H. Nagara, J. Tateishi, M. Fukui, Neurotoxicity of adriamycin passed through the transiently disrupted blood–brain barrier by mannitol in the rat brain, *Brain Res.* 412 (1) (1987) 73–83.
- [45] I. Brigger, J. Morizet, L. Laudani, G. Aubert, M. Appel, V. Velasco, M.J. Terrier-Lacombe, D. Desmaele, J. d'Angelo, P. Couvreur, G. Vassal, Negative preclinical results with stealth nanospheres-encapsulated doxorubicin in an orthotopic murine brain tumor model, *J. Control. Release* 100 (1) (2004) 29–40.
- [46] B. Uziely, S. Jeffers, R. Isacson, K. Kutsch, D. Wei-Tsao, Z. Yehoshua, E. Libson, F.M. Muggia, A. Gabizon, Liposomal doxorubicin: antitumor activity and unique toxicities during two complementary phase I studies, *J. Clin. Oncol.* 13 (7) (1995) 1777–1785.
- [47] N. McDannold, N. Vykhodtseva, K. Hynynen, Targeted disruption of the blood–brain barrier with focused ultrasound: association with cavitation activity, *Phys. Med. Biol.* 51 (4) (2006) 793–807.
- [48] M.A. O'Reilly, K. Hynynen, Blood–brain barrier: real-time feedback-controlled focused ultrasound disruption by using an acoustic emissions-based controller, *Radiology* 263 (1) (2012) 96–106.
- [49] J. Park, Y. Zhang, N. Vykhodtseva, F.A. Jolesz, N.J. McDannold, The kinetics of blood brain barrier permeability and targeted doxorubicin delivery into brain induced by focused ultrasound, *J. Control. Release* 162 (1) (2012) 134–142.
- [50] R.F. Barth, B. Kaur, Rat brain tumor models in experimental neuro-oncology: the C6, 9L, T9, RG2, F98, BT4C, RT-2 and CNS-1 gliomas, *J. Neurooncol.* 94 (3) (2009) 299–312.